

Spin and charge relaxation in graphene

Inauguraldissertation

zur
Erlangung der Würde eines Doktors der Philosophie
vorgelegt der
Philosophisch-Naturwissenschaftlichen Fakultät
der Universität Basel

von

Simon Zihlmann
aus Hergiswil bei Willisau LU, Schweiz

Basel, 2018

Genehmigt von der Philosophisch-Naturwissenschaftlichen Fakultät
auf Antrag von
Prof. Dr. Christian Schönenberger
Prof. Dr. Bart J. van Wees
Prof. Dr. Christoph Stampfer

Basel, 27.03.2018

Prof. Dr. Martin Spiess
Dekan

Contents

Introduction	ix
1. Outline of this thesis	xi
1. Theoretical background	1
1.1. Graphene basics	2
1.1.1. Lattice structure, Brillouin zone and band structure of graphene	2
1.1.2. Pseudospin and Berry-phase	6
1.1.3. Bilayer graphene	7
1.1.4. Spin-orbit coupling in pristine graphene	9
1.1.5. Spin-orbit coupling in graphene on TMDCs	10
1.2. Charge transport in graphene	13
1.2.1. Field effect	13
1.2.2. Phase coherent effects	16
1.2.3. Hall effect and quantum Hall effect	21
1.3. Spin transport in graphene	22
1.3.1. Ferromagnetism and magnetic anisotropies	22
1.3.2. Electrical spin injection in non-magnetic materials	25
1.3.3. Conductivity mismatch	25
1.3.4. Spin diffusion equation	27
1.3.5. Non-local spin valve	27
1.3.6. Hanle effect	30
1.3.7. Spin relaxation mechanisms in graphene	31
1.4. Spin Hall and inverse spin Hall effect	34
1.4.1. Spin hall injection and inverse spin Hall detection	35
1.5. Thermal transport in graphene	35
1.5.1. Heat diffusion equation	37
1.5.2. Cooling by phonons	39
2. Experimental methods	43
2.1. Sample fabrication	44
2.1.1. Exfoliation	44
2.1.2. vdW-heterostructures	44
2.1.3. Suspended graphene samples	47
2.1.4. CVD materials	49
2.2. Electrical measurements	51

3. Investigation of building blocks: Ferromagnetic contacts and CVD hBN	55
3.1. Introduction	56
3.2. Characterization of ferromagnetic contacts	57
3.2.1. Magnetization mapping of Py and Co contacts	59
3.2.2. Magnetic force microscopy	60
3.3. Role of CVD hBN in protecting ferromagnetic nanostructures from oxidation	61
3.3.1. Discussion and interpretation of the oxidation of ferromagnetic contacts	67
3.4. Characterization of CVD hBN	69
3.5. Discussion, conclusion and outlook	71
4. Non-equilibrium properties of graphene probed by superconducting tunnel spectroscopy	73
4.1. Sample overview and fabrication	74
4.2. Working principle of superconducting tunnel spectroscopy . . .	75
4.3. Temperature dependence	78
4.4. Hot electron regime	80
4.5. Phonon cooling	84
4.6. Hint of double step	85
4.7. Discussion	87
4.7.1. Deviation from hot electron regime	87
4.7.2. Electron-phonon coupling strength	88
4.7.3. Discussion of the presence of a double-step distribution function	89
4.7.4. General remarks	89
4.8. Conclusion and outlook	89
5. Spin transport in graphene spin valves	91
5.1. Spin transport in two-layer CVD hBN/graphene/hBN heterostructures	92
5.1.1. Discussion and interpretation of the spin transport properties	95
5.2. Proposal of a measurement scheme to detect the influence of magnetic moments on spin transport	103
5.2.1. Room temperature characterization of a two-layer CVD hBN/multilayer graphene spin valve	104
5.2.2. Low temperature spin transport - signatures of magnetic moments?	105
5.3. Discussion on magnetic moments	108
5.4. Conclusion and outlook	109

6. Spin pumping into graphene	111
6.1. Introduction into dynamical spin injection into graphene	112
6.2. Working principle of spin pumping	113
6.2.1. Device fabrication and implementation	114
6.2.2. Measurement technique	116
6.3. Ferromagnetic resonance condition	117
6.4. Inverse spin Hall voltage	119
6.4.1. Influence of spurious effects	121
6.4.2. Power dependence of the voltage at the Pt electrode . .	121
6.5. Discussion and interpretation	122
6.6. Conclusion and outlook	123
7. Spin-orbit coupling in graphene/WSe₂ heterostructures	125
7.1. Introduction	126
7.2. Fabrication and characterization of hBN/Gr/WSe ₂ heterostruc- tures	126
7.3. SOC characterization through weak antilocalization measure- ments	128
7.3.1. Fitting	130
7.3.2. Density dependence	132
7.3.3. In-plane magnetic field dependence	133
7.4. Interpretation and discussion of WAL measurements	134
7.4.1. Spin-orbit scattering times and their anisotropy	136
7.4.2. $z \rightarrow -z$ symmetric SOC (τ_{sym})	137
7.4.3. $z \rightarrow -z$ asymmetric SOC (τ_{asy})	138
7.4.4. Band structure analysis	138
7.5. Non-local resistances in hBN/graphene/WSe ₂ heterostructures	141
7.5.1. Density and electric field dependence of the non-local signal	142
7.5.2. Temperature dependence of non-local signal	143
7.5.3. Magnetic field dependence and Hanle measurements . .	144
7.5.4. Screening of back gate	148
7.6. Alternative WSe ₂ source and influence of WSe ₂ quality	149
7.6.1. Fully WSe ₂ encapsulated graphene	151
7.7. Conclusion	153
8. Quantum capacitance and dissipation in graphene pn-junctions	155
8.1. Introduction	156
8.2. Device layout	156
8.2.1. Measurement principle	158
8.3. Reflectance results	159
8.3.1. Quantum capacitance	161
8.3.2. Charge relaxation resistance	162

8.4. Discussion	164
8.5. Conclusion and outlook	164
9. Diamonds in suspended bilayer graphene	167
9.1. Device structure and basic characterization	168
9.1.1. Quantum Hall effect	169
9.1.2. Gate-gate maps at finite magnetic field	169
9.2. Possible explanations	173
9.2.1. Edge state equilibration	173
9.2.2. Conductance along domain walls in bilayer graphene . .	178
9.2.3. Additional conductance channels along the edge	180
9.3. Evidence of a spontaneous gap formation and Lifshitz transition	181
9.4. Further bilayer devices	185
9.5. Discussion, conclusion and outlook	186
10. Summary and outlook	189
10.1. Outlook	190
Bibliography	193
A. Fabrication Recipes	211
A.1. Fabrication of vdW-heterostructures	211
A.1.1. Cleaning the wafer for exfoliation	211
A.1.2. Markers on Si ⁺⁺ /SiO ₂ chip (~300 nm oxide)	211
A.1.3. Assembly of vdW-heterostructures	211
A.2. E-beam lithography and development	212
A.2.1. PMMA resist for contacts and etching (negative mask) .	212
A.2.2. PMMA/HSQ resist for etching (positive mask)	212
A.3. Reactive ion etching	213
A.3.1. CHF ₃ :O ₂ plasma	213
A.3.2. SF ₆ :Ar:O ₂ plasma	213
A.3.3. O ₂ plasma	213
A.4. Cr/Au leads	214
A.4.1. Metal top gates on Hall bar devices	214
A.4.2. ZEP resist for ferromagnetic contacts	214
A.5. Fabrication of freely suspended graphene samples using the LOR technique	215
A.5.1. Bottom gate structures	215
A.5.2. LOR coating and opening of bonding pads	215
A.5.3. Lithography on LOR	216
A.5.4. Suspension of graphene	216
A.5.5. ZEP based lithography on LOR for Py contacts	216
A.6. Fabrication of niobium resonators	216

B. Details on the fabrication and XAS analysis of ferromagnetic contacts	217
B.1. Fabrication details	217
B.2. Fitting procedure of XAS data	218
C. Further data and discussions of WSe₂/Gr-heterostructures	221
C.1. Fitting of magneto conductivity over larger magnetic field range	221
C.2. Fitting of magneto conductivity data from device B	222
C.3. Electric field dependence of the spin-orbit scattering rates . . .	223
C.4. Spin relaxation anisotropy	224
C.5. Estimate of valley-Zeeman SOC strength	226
C.6. Data from device D	227
C.7. WL in hBN/Gr/hBN heterostructures	229
D. Further information on the superconducting tunnel spectroscopy	231
D.1. Details on the numerical extraction of the energy distribution function	231
D.2. Influence of the finite width of the superconducting electrode .	233
E. Further information on Quantum capacitance and dissipation in graphene pn-junctions	235
E.1. Reflectance measurements of device C	235
E.2. Details on the parameter extraction for different circuit losses .	237
Curriculum Vitae	239
Publications	241
Acknowledgements	245

Introduction

Computation has changed our lives dramatically. This all started by the invention and the first realization of the transistor back in 1947 by Bardeen, Brattain and Shockley [1]. Continuous improvement in fabrication techniques lead to transistors on the size of a few tens of nanometres that are currently used in our computers and smart phones. Their incredible small size allows to pack millions onto a small chip leading to extremely large computation power even in hand-held devices [2]. However, the ongoing miniaturization will unavoidably be stopped by physical limits such as the size of an atom ($\sim 1 \text{ \AA}$). Already at larger length scales quantum mechanical effects come into play and will limit further miniaturization. In order to fulfil the demand of the society for ever faster computers, new computation concepts have to be invoked.

The realization of quantum computers, where the information is stored in a quantum bit (qubit), is a revolutionary step in the field of electronics and computation. Their working principle is fundamentally different from classical computers and therefore new computation schemes have to be implemented. A qubit can not only be in an off or on state (0 or 1) as a classical bit, but it can also be in any superposition of these two states at the same time. This conceptual difference paired with the possibility of entanglement between several qubits leads to advantages of a quantum computer over classical computers.

In general, a qubit can be realized by any quantum mechanical two-level system. Many possible systems have been proposed and implemented in small numbers so far. Discrete electron levels in trapped ions [3], or superconducting qubits relying on charge [4], phase [5] or flux [6] have been successfully implemented in small numbers. Today, everyone can freely access a quantum computer with 16 superconducting qubits already [7]. Whereas all these implementations work very well for single or a few number of qubits, the upscaling to more qubits has proven to be challenging. Spin qubits have been proposed as a versatile tool for quantum computation [8] with the possibility for easier upscaling. In addition, spin qubits realized in silicon [9, 10] could be realized in CMOS compatible architecture [11], bringing classical and quantum computers closer together.

Whereas it is not clear when quantum computers based on spin qubits will be realized, the electron spin can already be used for information storage and processing using novel device architectures. This field is called spintronics, which is a growing field where the control and manipulation of electron spins give the basis of solid-state electronic circuits [12]. It was the discovery of the

Giant Magneto-Resistance (GMR) effect by Albert Fert and Peter Grünberg in the end of the 1980's [13, 14] that lead to the first realization of spintronics concepts. Nowadays, the GMR effect in conventional hard drives is replaced by a similar, but yet more sensitive effect called Tunnelling Magneto-Resistance (TMR) effect. Both effects rely on the fact that the resistance through a device consisting of two ferromagnets and a non-magnetic material (either a normal metal or an insulator) heavily depends on the relative alignment of the two ferromagnets, making it therefore a perfect sensor for classical bits realized on magnetic hard drives.

It has been recently found that two-dimensional materials offer a new platform for spintronics devices, owing to their wealth of unusual physical phenomena and great diversity [15]. The first of these materials was graphene [16], which has proven ideal for spin transport [15] with spin relaxation lengths of $24\text{ }\mu\text{m}$ [17] and spin lifetimes on the order of 10 ns [18] at room temperature. The small spin-orbit coupling in graphene, that is due to the low atomic mass, and the absence of a nuclear spin in the most abundant isotope of carbon (^{12}C), leads to very long spin lifetimes theoretically predicted in graphene [15, 19, 20]. Continuous improvement of device quality and contact optimization led to the truly outstanding state of the art spin transport properties stated above.

Since the discovery of graphene by Geim and Novoselov in 2004 [21], many more two-dimensional materials have been predicted, exfoliated and characterized with very different properties. Among them are metals such as graphene, insulators such as hexagonal boron nitride (hBN) or semiconductors with black phosphorous or the large family of the transition metal dichalcogenides (TMDCs) that includes WSe_2 . Furthermore, more exotic materials such as superconductors as NbSe_2 [22, 23] is one, ferromagnets such as CrI_3 [24] or topological insulators in the monolayer limit of WTe_2 [25] have been reported. The assembly of them into so called van-der Waals (vdW) heterostructures can result in new device functionalities and properties that are not existing in a single material [26]. These designer materials can be used for future spintronics devices (e.g. vertical TMR devices) with enhanced performance, but can also be used to explore new device concepts and material properties.

As an example the physical properties of graphene can be altered by placing it in proximity to other materials, including the formation of minibands [27–30], magnetic ordering [31, 32], and superconductivity [33, 34]. Special interest has been paid to the enhancement of spin-orbit coupling (SOC) in graphene since a topological state, a quantum spin Hall phase, was theoretically shown to emerge [35]. In addition, significant electric field tunable SOC could enable fast and efficient spin manipulation by electric fields for possible spintronics applications, such as spin-filters [36] or spin-orbit valves [37, 38]. This is complemented by large spin-Hall angles predicted in graphene/TMDC heterostructures [39] that could be used as a source or as a detector of spin currents in graphene-based spintronic devices. Graphene/TMDC heterostruc-

tures are a very promising candidate to enhance the intrinsically weak SOC in graphene [40], while preserving graphene's exceptional charge transport properties [15, 41, 42].

In order to be able to use any material for spintronics applications or for possible implementations for quantum computation its basic properties have to be understood. In particular, novel materials such as graphene or other 2D materials need to be characterized with respect to their charge and spin transport properties. Therefore, the aim of this thesis was set to investigate spin and charge relaxation in graphene in various devices using standard transport techniques but also novel high frequency approaches.

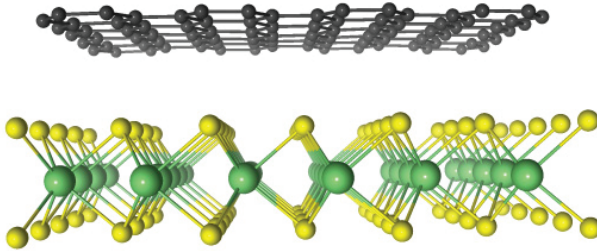
1. Outline of this thesis

In the beginning of the thesis in **chapter 1** an introduction to graphene and its properties is given. The unique band structure is introduced and possible spin-orbit terms are discussed, which can arise when graphene is put in proximity to a TMDC layer. Apart from charge and spin transport in graphene, a basic introduction on thermal transport is also given, focussing on low temperatures. **Chapter 2** gives an overview of the most important fabrication techniques used to prepare the devices studied in this thesis. The fundamental cornerstones of electrical transport measurements and set-up specific information are also shown. In **chapter 3**, nanomagnets are characterized using magnetic force microscopy and photoemission electron microscopy. In addition to the characterization of the magnetic domain structure, the latter technique is also used to study the role of a chemical vapour deposited hBN layer in protecting the ferromagnetic nanostructures from oxidation. In the end of the chapter, the CVD hBN itself is characterized employing various techniques. Throughout this thesis CVD hBN is used as a tunnel barrier for two purposes. As a first example superconducting tunnel spectroscopy of graphene is presented in **chapter 4**. This technique, that gives access to the energy distribution function is used to study electron thermal transport in the electron and phonon cooled regime. In **chapter 5** the CVD hBN is used as a tunnel barrier for electrical spin injection into graphene. The spin transport properties of graphene devices are studied at room and low temperatures, where similar contribution of the Dyakonov-Perel and Elliott-Yafet spin relaxation mechanism were found. In addition, high resistance tunnel contact show opposite spin injection polarizations, which are tunable by bias voltage. In the end of the chapter a possible route to characterize the influence of magnetic moments on the spin transport is presented. An alternative method to create a spin current in graphene is presented in **chapter 6**. High frequency magnetic fields are used to excite a ferromagnetic contact into ferromagnetic resonance, where a spin current is injected into the graphene channel. The inverse spin-

Hall effect in platinum is used to detect the spin current travelling through the graphene channel. Our approach of a transmission line allows simple on-chip integration and a broadband excitation. The low spin-orbit coupling in graphene is ambivalent as it on one side allows for very long spin relaxation times but at the same time graphene lacks a strong electric field tunability of spin relaxation time. In addition to spintronics applications, topological states have been predicted in graphene due to spin-orbit coupling. In **chapter 7**, the spin-orbit coupling arising from the proximity of a WSe₂ crystal is investigated using quantum interference phenomena. A strong valley-Zeeman SOC is found in these structure, that leads to a strong asymmetry in spin relaxation of in-plane and out-of-plane spins. A novel contactless characterization method is presented in **chapter 8**. An encapsulated pn-junction is capacitively coupled to a superconducting resonator operating at high frequency. As an example we used this scheme to extract the quantum capacitance and the charge relaxation resistance of a graphene pn-junction without the need for electrical contacts. Quantum-Hall measurements on a bilayer graphene pnp-junction presented in **chapter 9** shed light onto equilibration phenomena of different Landau levels, revealing spin dependent edge state equilibration.

Finally, the main findings of this thesis are revisited and put into a broader context in **chapter 10**, where also a brief outlook is given.

1 Theoretical background



This chapter covers the most important theoretical concepts that are used throughout this thesis. First, the unique band structure is introduced and all possible spin-orbit terms that can arise when graphene is put in proximity to a TMDC layer are discussed. Furthermore, the basic concepts of charge, spin and heat transport in graphene are introduced. Charge transport concepts are discussed in more detail focussing on coherent effects such as universal conductance fluctuations and weak (anti)localization. Starting from electrical spin injection into graphene, non-local spin transport in graphene is discussed as well and the most important spin relaxation mechanisms are introduced in the end of this section. Apart from charge and spin transport in graphene, a basic introduction is given about thermal transport in graphene focussing on low temperatures. The first part of this chapter follows partially the references [43–45], whereas the spin transport part follows partially the references [12, 46].¹

¹The image showing graphene on top of WSe₂ was taken from Ref. [47].

1.1. Graphene basics

Graphene is a two-dimensional sheet of carbon atoms arranged in a honeycomb structure as shown in Fig. 1.1 (a). There are two stable isotopes of carbon, namely ^{12}C with an abundance of 98.9% and zero nuclear spin and ^{13}C with an abundance of 1.1% and a nuclear spin of 1/2. In principle this allows to synthesize isotopically pure ^{12}C or ^{13}C graphene.

The electronic configuration of a free carbon atom is $1s^2 2s^2 2p^2$ with a total of six electrons. The core electrons in the $1s^2$ orbital are inert and do not contribute to any chemical bonds. In the case of graphene, the four valence electrons will occupy three sp^2 orbitals and the p_z orbital instead of the normal $2s$ and $2p$ orbitals. The p_z orbital is perpendicular to the plane spanned by the three sp^2 orbitals that form a trigonal planar configuration. Whereas the sp^2 orbitals form well localized σ -bonds the p_z orbitals form delocalized π -bonds that form the π -bands in graphene crystals. In the following a simple tight-binding model will be used to describe the low energy spectrum of graphene that results from the p_z orbitals.

1.1.1. Lattice structure, Brillouin zone and band structure of graphene

The Bravais lattice of graphene is triangular with a two atom basis (A and B atom) with the lattice vectors

$$\vec{a}_1 = \frac{a_0}{2} \begin{pmatrix} 3 \\ \sqrt{3} \end{pmatrix} \quad \text{and} \quad \vec{a}_2 = \frac{a_0}{2} \begin{pmatrix} 3 \\ -\sqrt{3} \end{pmatrix}, \quad (1.1)$$

where $a_0 = 1.42 \text{ \AA}$ is the inter-atomic distance, which lies between a single C–C bond and a double C=C bond [45]. The nearest-neighbour vectors in real space are given by

$$\vec{d}_1 = a_0 \begin{pmatrix} 1 \\ 0 \end{pmatrix} \quad \text{and} \quad \vec{d}_2 = \frac{a_0}{2} \begin{pmatrix} -1 \\ -\sqrt{3} \end{pmatrix} \quad \text{and} \quad \vec{d}_3 = \frac{a_0}{2} \begin{pmatrix} -1 \\ \sqrt{3} \end{pmatrix}. \quad (1.2)$$

All nearest neighbours of an A atom are B atoms and vice-versa, see Fig. 1.1 (a).

The first Brillouin zone is shown in Fig. 1.1 (b) with the two reciprocal lattice vectors

$$\vec{b}_1 = \frac{2\pi}{3a_0} \begin{pmatrix} 1 \\ \sqrt{3} \end{pmatrix} \quad \text{and} \quad \vec{b}_2 = \frac{2\pi}{3a_0} \begin{pmatrix} 1 \\ -\sqrt{3} \end{pmatrix} \quad (1.3)$$

that are obtained by the relation $\vec{a}_i \vec{b}_j = 2\pi \delta_{ij}$.

In a tight-binding calculation the electrons are thought to be well localized in atomic orbitals at the site of each atom. Furthermore, they are allowed to

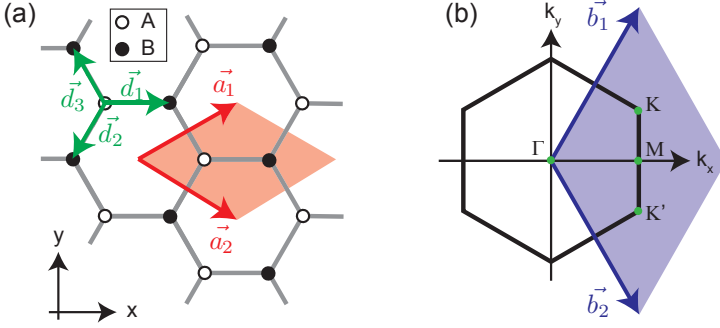


Figure 1.1. Graphene lattice in real and reciprocal space: (a) The real space lattice of graphene is spanned by the two lattice vectors \vec{a}_1 and \vec{a}_2 that form the unit cell containing two atoms (A, B). (b) The first Brillouin zone in reciprocal space is spanned by the unit vectors \vec{b}_1 and \vec{b}_2 and contains the two inequivalent valleys K and K' . Figure adapted from Ref. [48].

hop between neighbouring atoms. In a more advance calculation, also next-nearest neighbour hopping or higher terms can be included. However, in most cases the nearest neighbour hopping describes the physics accurate enough and therefore we focus here only on nearest neighbour hopping. As mentioned above, only the electrons in the p_z orbitals will contribute to the low energy spectrum and we therefore take the p_z orbitals of the A and B atoms $|\phi_A\rangle$ and $|\phi_B\rangle$ as the basis for the tight-binding calculation and we arrive at the following ansatz for the Bloch functions:

$$\psi_{A,B}(\vec{r}) = \frac{1}{\sqrt{N}} \sum_{\vec{R}_{A,B}} e^{i\vec{q}\vec{R}_{A,B}} \phi_{A,B}(\vec{r} - \vec{R}_{A,B}), \quad (1.4)$$

where N is the number of unit cells that the sum is running over, \vec{q} is the wave vector and $\vec{R}_{A,B}$ is the location of the atom. The Hamiltonian takes the form of a 2×2 matrix

$$H = \begin{pmatrix} H_{AA} & H_{AB} \\ H_{BA} & H_{BB} \end{pmatrix}, \quad (1.5)$$

where $H_{AA} = H_{BB} = \epsilon$ because of sublattice symmetry and $H_{AB} = H_{BA}^*$. Without loss of generality we can set the on-site energy $\epsilon = 0$ eV. The off-diagonal term is given by

$$H_{AB} = t \cdot \left(e^{i\vec{q}\vec{d}_1} + e^{i\vec{q}\vec{d}_2} + e^{i\vec{q}\vec{d}_3} \right) = t \cdot f(\vec{q}), \quad (1.6)$$

where $t = \langle \phi_A(\vec{r}) | H | \phi_B(\vec{r}) \rangle \sim -2.7 \text{ eV}$ is the nearest neighbour hopping energy [43]. The eigenvalues are readily obtained as $E_{\pm} = \pm |t| \sqrt{|f(\vec{q})|^2}$, where the $+$ ($-$) accounts for the conduction (valence) band. An explicit expression in \vec{q} is found by plugging in the nearest neighbour vectors from Eq. 1.2 and one obtains:

$$E_{\pm}(\vec{q}) = \pm t \sqrt{1 + 4 \cos\left(\frac{3}{2} q_y a_0\right) \cos\left(\frac{\sqrt{3}}{2} q_x a_0\right) + 4 \cos\left(\frac{\sqrt{3}}{2} q_y a_0\right)^2}, \quad (1.7)$$

which is plotted in Fig. 1.2 (a) for the first Brillouin zone².

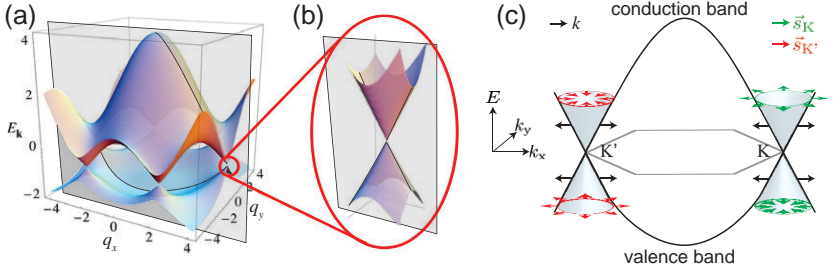


Figure 1.2. Band structure of graphene: (a) shows the energy spectrum (in units of t) for $t = -2.7 \text{ eV}$ and $t' = -0.2 t$, which parametrizes next-nearest neighbour hopping. Figure adapted from Ref. [43]. (b) Low-energy spectrum near a Dirac-point. (c) Cut for $q_y = 0$ as indicated in (a) and (b) with the black, semi-transparent plane. The orientation of the pseudospin ($\vec{s}_{K,K'}$) is parallel (anti-parallel) to \vec{k} in valence (conduction) band at K. The opposite chirality is found at K'. Figure adapted from Ref. [48].

The valence and conduction band touch each other at the six corners of the first Brillouin zone, that are often called Dirac points. Only two of the six Dirac points are not equivalent and are called K and K' valley. The two valleys are a consequence of the triangular Bravais lattice and are only indirectly linked to the two atomic basis. In undoped graphene, the Fermi energy lies at zero energy and therefore the Fermi surface consists of six points. Therefore, graphene is a zero-gap semiconductor that distinguishes it from conventional semiconductors and metals. At small energies the band structure is linear whereas at larger energies a saddle point between the K and K' valley is reached. This leads to van Hove singularities in the density of states at an energy that is comparable to the hopping term $t \sim 2.7 \text{ eV}$.

²The calculations leading to Fig. 1.2 include next-nearest neighbour hopping that leads to an asymmetry in valence and conduction band.

At low energies the dispersion relation can be expanded around the K point with $\vec{q} = \vec{K} + \vec{k}$, where $|\vec{k}| \ll |\vec{K}|$ is the quasi-momentum measured from the K point. Similarly, this can be done at the K' point. A Taylor expansion of Eq. 1.7 around \vec{K} leads to

$$E_{\pm}(\vec{k}) = \pm \hbar v_F |\vec{k}|, \quad (1.8)$$

where \hbar is the reduced Planck constant, $v_F = 3ta_0/(2\hbar) \sim 1 \times 10^6 \text{ m s}^{-1}$ is the Fermi velocity and the \pm -sign accounts for the conduction and valence band. The linearised Hamiltonian that describing both valleys takes the following form:

$$H_0 = \hbar v_F (\kappa k_x \hat{\sigma}_x - k_y \hat{\sigma}_y), \quad (1.9)$$

where $\kappa = \pm$ stands for the K and K' valley and $\hat{\sigma}_i$ are the Pauli matrices acting on the sublattice space that is also called pseudospin. The Hamiltonian is identical to the Dirac Hamiltonian for massless relativistic particles with velocity v_F and therefore charge carriers in graphene are commonly referred to as "Dirac particles".

Since the two valleys (K and K') are energetically degenerate but inequivalent the charge carriers in graphene have an additional degree of freedom next to the normal magnetic spin. The density of states (DoS) in graphene depends linearly on energy since the dispersion relation is linear in \vec{k} :

$$DoS(E) = \frac{g_s g_v E}{2\pi(\hbar v_F)^2}, \quad (1.10)$$

where $g_s = g_v = 2$ are the degeneracies due to spin and valley. This energy dependence of the DoS is in stark contrast to conventional 2-dimensional semiconductors that have a constant DoS due to the conventional parabolic dispersion relation.

The rather low DoS of graphene allows to tune the Fermi energy by applying a gate voltage (see section 1.2) but this implies that when the charge carrier density is changed the chemical potential also changes. If dN electrons (a total charge of $dQ = edN$) are added to the graphene, the chemical potential changes by $d\mu = dN/DoS(E)$, which can be expressed as a voltage $dV = d\mu/e = dQ/(e^2 DoS(E))$. Using the definition of a capacitor $C = Q/V$, one arrives at the definition of the quantum capacitance:

$$C_Q(E) = e^2 DoS(E). \quad (1.11)$$

Here, $C_Q(E)$ is given per unit area. The quantum capacitance has to be added in series to the gate capacitance but is neglected in most experiments as it has a marginally effect on the induced charge carrier density. However, in very clean graphene systems, where the chemical potential can be tuned very close to the Dirac point, the quantum capacitance can become dominant.

The relation $|\vec{k}| = k_F = \sqrt{\pi n}$ allows to express the Fermi energy as a function of density:

$$E(n) = \hbar v_F \sqrt{\frac{4\pi n}{g_s g_v}}. \quad (1.12)$$

1.1.2. Pseudospin and Berry-phase

As a consequence of the two atom basis of the graphene lattice, the charge carriers in graphene are described by an additional quantum number, called pseudospin. It describes the relative weight of the two orbital wave functions $|\phi_A\rangle$ and $|\phi_B\rangle$ in the solution of the linear low energy Hamiltonian. An analogy to a spin 1/2 can be drawn.

Eq. 1.9 can be rewritten using $k_x + ik_y = k_F e^{i\theta}$ with $\theta = \arctan(k_y/k_x)$:

$$H = \hbar v_F k_F \begin{pmatrix} 0 & \pm e^{\mp i\theta} \\ \pm e^{\pm i\theta} & 0 \end{pmatrix}, \quad (1.13)$$

where the \pm -signs account for the two solutions at the K and K' valley. θ describes the angle between \vec{k}_F , which is proportional to the momentum, and k_x . The eigenvectors of Eq. 1.13 for the conduction ($|EV_C\rangle$) and valence band ($|EV_V\rangle$) are

$$|EV_C\rangle = \frac{1}{\sqrt{2}} \begin{pmatrix} e^{\mp i\theta/2} \\ e^{\pm i\theta/2} \end{pmatrix} \quad \text{and} \quad |EV_V\rangle = \frac{1}{\sqrt{2}} \begin{pmatrix} e^{\mp i\theta/2} \\ -e^{\pm i\theta/2} \end{pmatrix}, \quad (1.14)$$

where the \pm -sign accounts for the K and K' valley. These two solutions can be generalized by introducing the parameter s , which accounts for the valence band (holes, $s = -1$) and for the conduction band (electrons, $s = +1$):

$$|s\rangle = \frac{1}{\sqrt{2}} \begin{pmatrix} e^{\mp i\theta/2} \\ s e^{\pm i\theta/2} \end{pmatrix}. \quad (1.15)$$

The absolute square of the two components of the vector in Eq. 1.15 give the probability of finding the wave function on sublattice A or B. The spinor rotation around the z-axis by an angle θ is given as:

$$R(\theta) = e^{-i\theta/2\sigma_z} = \begin{pmatrix} e^{-i\theta/2} & 0 \\ 0 & e^{i\theta/2} \end{pmatrix}. \quad (1.16)$$

Eq. 1.16 directly leads to the conclusion that the wave function picks up a phase of π if a rotation of 2π is performed, which is equivalent to a charge carrier encircling the K or K' point. This phase is called Berry phase.

It follows that the pseudospin is parallel to \vec{k} in the conduction band and anti-parallel to \vec{k} in the valence band for the K valley. In K' valley this relation is inverted, which is shown in Fig. 1.2 (c). The helicity, which is the projection

of the pseudospin onto the momentum is a conserved quantity at low energy. Therefore, backscattering (inverting momentum and thus \vec{k}) is not allowed within a valley since this would require to change the helicity of the charge carrier. Backscattering is thus only allowed by intervalley scattering, which requires a large $\vec{k} \sim \vec{K} \sim 1/a_0$. Such scattering events can only happen at the edge, at atomic defects or at very small wrinkles.

1.1.3. Bilayer graphene

In bilayer graphene two single layer graphene sheets are stacked on top of each other. In the case of AB stacking, which is the most common one, the A atom of the upper layer sits directly above the B atom of the lower layer, see Fig. 1.3 (a). The most relevant hopping terms are also indicated by γ_i . The interlayer hopping between A1 (A2) and B1 B(2) in the lower (upper) layer corresponds to the nearest neighbour hopping in single layer graphene and therefore we write $\gamma_0 = t = -2.7 \text{ eV}$. All other relevant hopping terms describe the coupling between the two layers with $\gamma_1 = -0.4 \text{ eV}$ connecting the A1 and the B2 atom sitting directly above each other. A2 and B1 are linked by $\gamma_2 = -0.3 \text{ eV}$, which is also called skew coupling. The last term connecting the B1 to the B2 atom is characterized by $\gamma_4 = -0.04 \text{ eV}$ [49].

The band structure of bilayer graphene can be derived in a tight binding approximation similar to single layer as shown above. Here we will only give the resulting dispersion relation. Considering only γ_0 and γ_1 , the energy dispersion relation for the valence (-) and conduction (+) band is found as:

$$E_{\pm}^{\alpha} = \pm \left[V^2 + \hbar^2 v_F^2 \vec{k}^2 + \frac{\gamma_1^2}{2} + (-1)^{\alpha} \sqrt{4V^2 \hbar^2 v_F^2 \vec{k}^2 + \gamma_0 \hbar^2 v_F^2 \vec{k}^2 + \frac{\gamma_1^4}{2}} \right], \quad (1.17)$$

where $v_F = 1 \times 10^6 \text{ ms}^{-1}$ is the Fermi velocity of single layer graphene and V describes a possible difference of the electrochemical potential of the two layers that can, for example, arise in an external perpendicular electric field [44]. The parameter α is needed to describe the two subbands in the conduction and valence band, which are shifted by γ_1 away from zero energy in the case of $V = 0$. In the case of $V = 0$, Eq. 1.17 can be simplified to:

$$E_{\pm}^{\alpha} = (-1)^{\alpha} \cdot \frac{\gamma_1}{2} \pm \frac{\gamma_1}{2} \sqrt{1 + \left(\vec{k} \cdot \frac{3\gamma_0 a_0}{\gamma_1} \right)}. \quad (1.18)$$

For small \vec{k} , Eq. 1.18 describes a parabolic dispersion relation with an effective mass $m = \frac{\gamma_1}{2v_F^2} \sim 0.03m_e$, where m_e is the mass of a free electron. At larger \vec{k} , the dispersion relation changes from parabolic to linear, which happens around a charge carrier density of $5 \times 10^{12} \text{ cm}^{-2}$.

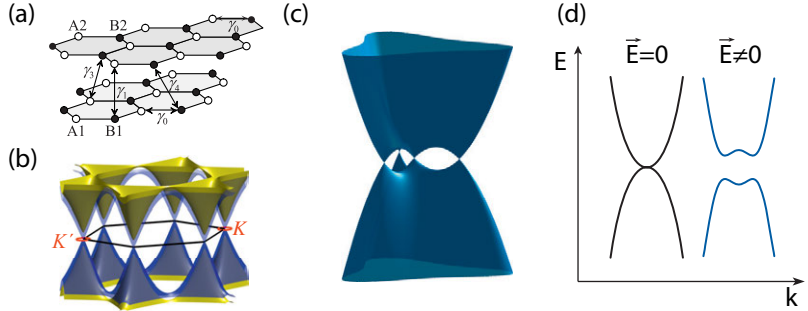


Figure 1.3. Band structure of bilayer graphene: (a) shows the real space lattice of a AB stacked bilayer graphene with all relevant hopping terms indicated by γ_i , image adapted from Ref. [44]. (b) shows the energy spectrum of bilayer graphene on an energy scale of 3 eV measured from the Dirac point that is marked by the black hexagon representing the first Brillouin zone. The blue (yellow) surfaces show the low-energy (split) bands and the two inequivalent but degenerate valleys are indicated. Image adapted from Ref. [50]. (c) Low energy spectrum at the K valley taking into account trigonal warping. Image adapted from Ref. [50]. (d) shows effect of a perpendicular electric field on the band structure without taking into account trigonal warping. A finite electric field opens a gap. Image adapted from Ref. [51].

The band structure is shown in Fig. 1.3 (b), where the two coloured surfaces represent the two split bands. The influence of an external electric field on the low energy spectrum is schematically shown in Fig. 1.3 (d). Taking into account the other interlayer hopping terms γ_2 and γ_3 , the low energy spectrum changes from parabolic to four mini Dirac cones as shown in Fig. 1.3 (d) [50]. This effect is commonly called trigonal warping as it deforms the band structure into a trigonal shape. It is important to note that the energy of the Lifshitz transition, where the topology of the Fermi surface changes from a single circle to four disconnected circles, is around 1 meV.

Similar to single layer graphene, the quasiparticle in bilayer graphene are also chiral, meaning that the momentum is locked to the sublattice space. The chirality has opposite sign in the two valleys. However, the Berry phase is 2π [44, 52].

Due to the parabolic dispersion relation, the density of states of bilayer graphene is independent of energy [44]:

$$DoS(E) = \frac{4m^*}{2\pi\hbar^2}, \quad (1.19)$$

where the factor 4 accounts for spin and valley degree of freedom.

1.1.4. Spin-orbit coupling in pristine graphene

As seen in the previous section, the charge carriers in graphene move with constant velocity leading to a zero mass and absence of a band gap. Therefore, an analogy with massless Dirac fermions is often drawn, that makes graphene a solid-state toy to investigate relativistic quantum mechanics (such as Klein tunnelling). Ironically, this nice analogy is broken by a relativistic effect itself: spin-orbit coupling, which gives the electrons in graphene a finite mass and opens an energy gap in the band structure.

In pristine graphene, only one, namely a spin-conserving next-nearest neighbour hopping spin-orbit coupling is allowed by symmetry [53], which can be written as the following effective Hamiltonian:

$$H_I = \kappa\lambda_I\hat{\sigma}_z\hat{s}_z. \quad (1.20)$$

Here \hat{s}_z is the spin Pauli matrix, $\hat{\sigma}_z$ is the pseudospin Pauli matrix and $\kappa = +1(-1)$ for the K (K' valley). In combination with the orbital part of the graphene Hamiltonian, see Eq. 1.9, the energy spectrum reads:

$$E_{\pm} = \pm\sqrt{\hbar^2v_F^2(k_x^2 + k_y^2) + 2\lambda_I}, \quad (1.21)$$

where \pm accounts for the conduction and valence band. Here, the K and K' valleys are degenerate as we have seen above. The valence and conduction band are split by $2|\lambda_I|$ and are spin degenerate as required by space inversion

and time reversal symmetry. The influence of H_I on the band structure can be seen in Fig. 1.4 (a). The strength of the spin-orbit coupling comes from the hybridization of the p_z orbitals that form the Dirac cones with d and higher carbon orbitals [54]. First principles calculations found λ_I to be 12 μeV [54]. Kane and Mele have shown that graphene with the intrinsic spin-orbit coupling is a topological insulator [35], hosting edge states at the boundary of the sample while the bulk of the sample is insulating.

As soon as the graphene is placed on a substrate, or an electric field perpendicular to the graphene plane is applied, the inversion symmetry is broken and a Rashba type SOC is allowed. This term spin-splits the band by 10 $\mu\text{eV V}^{-1} \text{ nm}$ in intrinsic graphene [54]. In the next section, graphene on a TMDC layer is considered, which also includes Rashba SOC.

1.1.5. Spin-orbit coupling in graphene on TMDCs

Placing graphene on top of a TMDC substrate reduces the symmetries in the system and this allows for more spin-orbit coupling terms next to the intrinsic spin-orbit coupling [53]. An enhancement of the spin-orbit coupling can be understood by the hybridization of the graphene orbitals with the TMDC orbitals. For the case of the Dirac cones lying in the band gap of the TMDC, virtual hopping terms can be used to incorporate an enhanced spin-orbit coupling. In detail, the low-energy Hamiltonian of graphene on a single layer TMDC is given by $H = H_0 + H_\Delta + H_I^{A,B} + H_R + H_{PIA}^{A,B}$ [47, 53], which includes all symmetry allowed spin-orbit coupling terms. H_0 is the Hamiltonian of pristine graphene as derived above. H_Δ represents an orbital gap that arises from a staggered sublattice potential that leads to an on-site energy of the A atom that is different from the on-site energy of the B atom. $H_I^{A,B}$ represents the intrinsic spin-orbit coupling, which is allowed to be different for the two sublattices as the inversion symmetry is not present. Similarly, $H_{PIA}^{A,B}$ represents the sublattice resolved pseudospin inversion asymmetry spin-orbit coupling, which is permitted by broken z/z symmetry [53]. Finally, H_R represents the Rashba spin-orbit coupling that is induced by a perpendicular electric field [35, 54]. The different terms can be written as follows:

$$\begin{aligned}
H_0 &= \hbar v_F (\kappa k_x \hat{\sigma}_x - k_y \hat{\sigma}_y) \cdot \hat{s}_0 \\
H_\Delta &= \Delta \hat{\sigma}_z \cdot \hat{s}_0 \\
H_I &= \frac{1}{2} [\lambda_I^A (\hat{\sigma}_z + \hat{\sigma}_0) + \lambda_I^B (\hat{\sigma}_z - \hat{\sigma}_0)] \cdot \kappa \hat{s}_z \\
H_{PIA} &= \frac{a_0}{2} [\lambda_{PIA}^A (\hat{\sigma}_z + \hat{\sigma}_0) + \lambda_{PIA}^B (\hat{\sigma}_z - \hat{\sigma}_0)] \cdot (\kappa_x \hat{s}_y - \kappa_y \hat{s}_x) \\
H_R &= \lambda_R (\kappa \hat{\sigma}_x \cdot \hat{s}_y - \hat{\sigma}_y \cdot \hat{s}_x).
\end{aligned} \tag{1.22}$$

Here, \hbar is the reduced Planck constant, v_F is the Fermi velocity, $\kappa = +1(-1)$ stands for the K and (K') valley, $\hat{\sigma}_i(\hat{s}_i)$ are the sublattice (spin) Pauli matrices.

ces, k_i are the wave vector components measured relative to K or K', a_0 is the graphene lattice constant, Δ is the staggered sublattice potential and λ_i represent different spin-orbit coupling strengths. The notation in eq. 1.22 is particularly useful for tight binding calculations. However, from an analytical point of view it is more transparent to combine sublattice dependent terms, resulting in $H = H_0 + H_\Delta + H_I + H_{VZ} + H_R + H_{PIA} + H_{\Delta_{PIA}}$ with [36]:

$$\begin{aligned}
 H_I &= \lambda_I \kappa \hat{\sigma}_z \cdot \hat{s}_z, & \lambda_I &= \frac{1}{2} (\lambda_I^A + \lambda_I^B) \\
 H_{VZ} &= \lambda_{VZ} \kappa \hat{\sigma}_0 \cdot \hat{s}_z, & \lambda_{VZ} &= \frac{1}{2} (\lambda_I^A - \lambda_I^B) \\
 H_{PIA} &= a_0 \lambda_{PIA} \hat{\sigma}_z \cdot (k_x \hat{s}_y - k_y \hat{s}_x), & \lambda_{PIA} &= \frac{1}{2} (\lambda_{PIA}^A + \lambda_{PIA}^B) \\
 H_{\Delta_{PIA}} &= a_0 \Delta_{PIA} \hat{\sigma}_0 \cdot (k_x \hat{s}_y - k_y \hat{s}_x), & \Delta_{PIA} &= \frac{1}{2} (\lambda_{PIA}^A - \lambda_{PIA}^B).
 \end{aligned} \tag{1.23}$$

Here, H_I is the usual intrinsic spin-orbit coupling in graphene that opens a topological gap of $2|\lambda_I|$. In addition, a valley Zeeman term H_{VZ} , which locks valley to spin, emerges from the difference of the intrinsic spin-orbit coupling in the two sublattices. This term polarizes the spins out of plane with opposite orientation in the K and K' valley, which is a property inherited from the TMDC substrate. H_{PIA} normalizes the Fermi velocity independent of the spin, whereas $H_{\Delta_{PIA}}$ renormalizes the Fermi velocity depending on the spin. This term therefore leads to a $|\vec{k}|$ -linear spin splitting of the bands. The influence of each term individually on the pristine graphene band structure is shown in Fig. 1.4 for the K valley. Since H_{PIA} and $H_{\Delta_{PIA}}$ scale linearly with $|\vec{k}|$ their influence is negligible at low energies as one can easily see in Fig. 1.4 (e) and (f) where five order of magnitude larger Hamiltonian parameters were used compared to the other terms to have a similar effect on the band structure.

z/-z symmetry and its implications

It is the loss of horizontal mirror symmetry (e.e. mirroring the graphene plane perpendicular to z-axis) that allows Rhasba and PIA spin-orbit coupling in graphene. The other spin-orbit coupling terms in the Hamiltonian presented in eq. 1.23 are symmetric in z/-z mirroring. This can easily be seen that only H_R , H_{PIA} and $H_{\Delta_{PIA}}$ contain $\hat{s}_{x,y}$ that are not invariant upon inversion of the z-direction. For example, s_x transforms into $-s_x$ if z is mirrored to $-z$. This means that no spin polarizaiton in s_x or s_y can be present if the $z/-z$ -symmetry is present, as it is in pristine graphene. Therefore, only $\hat{s}_{z,0}$ -terms are allowed in a Hamiltonian preserving this symmetry [53].

This classification into symmetric and asymmetric spin-orbit coupling with respect to horizontal mirror symmetry is useful in the discussion of spin-orbit scattering rates extracted from weak anti-localization measurements. In such

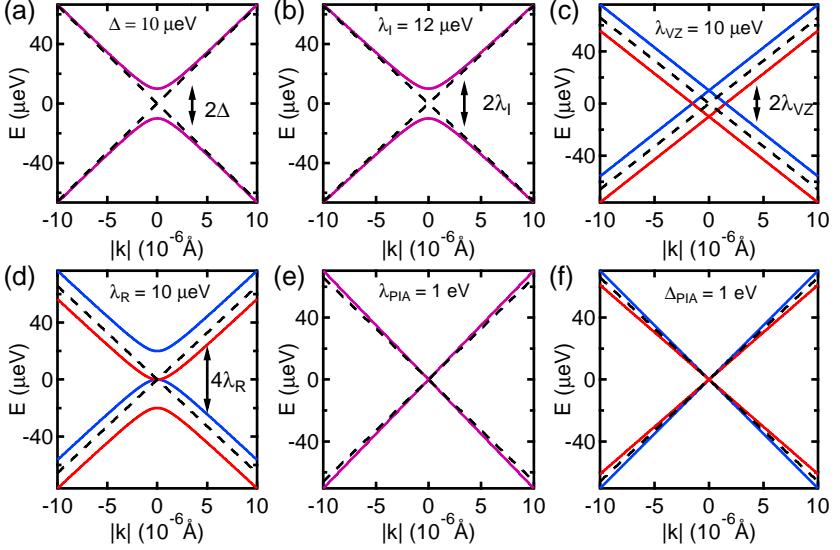


Figure 1.4. Spin-orbit coupling in graphene for the K valley: The band structure of pristine graphene is shown as black dashed line. Purple solid lines indicate spin degenerate bands whereas blue and red solid lines indicate spin resolved bands. The spin expectation value is different though between the valley-Zeeman SOC and Rashba SOC. A staggered sublattice potential (a) opens a gap of 2Δ close to the Dirac point, leaving the valence and conduction band spin degenerate. Similarly the intrinsic spin-orbit coupling (b) opens a topological gap of $2\lambda_I$ at the Dirac points. In contrast to (a), (b) host spin polarized edge currents. A valley-Zeeman term (c) spin splits the band by $2\lambda_{VZ}$, keeping the linear dispersion relation. A Rashba spin-orbit coupling (d) also spin splits the band but introduces in addition a finite mass. The PIA terms renormalise the Fermi velocities. λ_{PIA} (e) is spin independent whereas Δ_{PIA} (f) leads to spin dependent Fermi velocities and therefore to a k-linear splitting of the bands. Since the PIA terms depend on momentum, it is clear that in order to have an effect at very low energy scales, very large values for λ_{PIA} and Δ_{PIA} are needed. In other words, for realistic SOC terms, the PIA SOC only has an influence at very large doping and it is therefore irrelevant around the Dirac point.

measurements, two different spin-orbit scattering rates can be obtained, a symmetric τ_{sym} and an asymmetric τ_{asy} . Therefore, the asymmetric spin relaxation rate contains information about H_R , H_{PIA} and $H_{\Delta_{PIA}}$, whereas the symmetric spin relaxation rate contains information about H_I and H_{VZ} .

1.2. Charge transport in graphene

In order to discuss charge transport in graphene it is helpful to define some length scales first. For a two-dimensional conductor the device width W and the device length L define the size of the system. Another important length scale is the mean free path l_{mfp} , which is the distance the charge carriers can travel before a momentum scattering happens. Different transport regimes can occur depending on the ratio of $l_{mfp}/W, L$. If $l_{mfp} \ll W, L$, which is called the diffusive regime, the charge carriers scatter many times while travelling through the device and therefore fully randomize their momentum. On the other hand, if $l_{mfp} \sim W, L$ the ballistic regime is entered. In suspended or hBN/TMDC-encapsulated graphene, l_{mfp} can be on the order of several μm , whereas it is on the order of 10 nm for conventional graphene devices on SiO_2 substrate.

Charge carriers in graphene do not only carry information in the form of charge, but they also contain viable information in their spin, valley and the electron's phase that are relevant for transport phenomena. All these quantities are randomized over their own characteristic length scale: the momentum over the mean free path l_{mfp} , the spin over the spin relaxation length λ_s , the valley over the valley scattering length l_{iv} , and the phase over the phase coherence length λ_ϕ . All length scales can also be expressed in their corresponding time scales: momentum relaxation time τ_p , spin relaxation time τ_s , valley scattering time τ_{iv} and phase coherence time τ_ϕ .

In the following the basics of diffusive charge transport is explained, followed by an introduction to spin transport in graphene.

1.2.1. Field effect

Most of the graphene devices investigated in this thesis have at least two electrodes (source and drain) and at least one gate (mostly global back gate). This configuration allows for straightforward transport experiments. If a voltage V_{SD} across source and drain is applied, a current I_{SD} will flow and the conductance $G = I_{SD}/V_{SD}$ can be measured as a function of several parameters. A finite voltage difference between the graphene channel and the gate electrode will induce a charge carrier density proportional to the gate capacitance:

$$C = \epsilon_0 \epsilon_r \frac{A}{d}, \quad (1.24)$$

which in most cases is very well approximated by a plate capacitor with area A and with a dielectric of thickness d with a relative dielectric constant ϵ_r . As mentioned above, the charge carrier density in graphene is not solely defined by the geometric gate capacitance but the quantum capacitance has to be added in series, see section 1.1.1. However, in most cases this is a minor correction and can therefore be neglected. The induced density will lead to a shift of the Fermi energy in the graphene. Since graphene is a zero-gap semiconductor, electron and hole conduction are both accessible by changing the sign of the gate voltage. Such an ambipolar field effect is shown in Fig. 1.5 (a). By changing the gate voltage from negative to positive values, the Fermi energy is shifted from the hole band through the Dirac point into the valence band. While it is possible to shift the Fermi energy to the Dirac point in an ideal graphene device, small potential fluctuations prevent this in real devices. A homogeneous doping across the device is not possible for low doping levels and the device then breaks up into random electron and hole regions, also called puddles. Therefore, people often refer to the Dirac point as charge neutrality point (CNP) as this is a more accurate description. The residual doping n^* , which is the lowest doping level that can homogeneously be realized in a device, characterises the device quality in terms of how close the Fermi energy can be tuned to the Dirac point. It can also be thought of the "width" of the CNP. The residual doping can be extracted from a log-log plot of the conductance versus the density, see Fig. 1.5 (b).

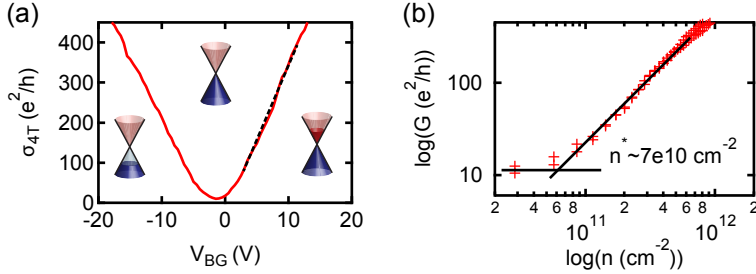


Figure 1.5. Field effect in graphene: (a) Gate dependence of the graphene conductivity showing ambipolar field effect. The insets show schematically the different doping levels. The field effect mobility is extracted from the slope of the conductivity with gate (density) and is on the order of $100\,000\text{ cm}^2\text{ V}^{-1}\text{ s}^{-1}$ for this device. (b) Extraction of the residual doping with a log-log plot.

In a semi-classical Drude model, the conductivity in graphene is given as

$$\sigma = \frac{n e^2 \tau_p}{m} = \frac{2 e^2 \tau_p v_F \sqrt{n \pi}}{h}, \quad (1.25)$$

where $m = |\vec{p}|/v_F = \hbar k_F/v_F$ was used as the charge carrier mass. Depending on the relation of τ_p on k_F different regimes are possible. Usually, the charge impurity scattering with $\tau_p \propto k_F$ [55] dominates and a linear relation of the conductivity with density is obtained:

$$\sigma \sim n e \mu, \quad (1.26)$$

where μ is a density independent charge carrier mobility. This allows to extract a field effect mobility by fitting the slope in conductivity measurements, see also Fig. 1.5 (a). An additional estimate of the mobility can be obtained by the magnetic field at which Shubnikov-de Haas (SdH) oscillations appear for the first time. SdH oscillations occur once charge carriers can complete a full cyclotron orbit, which is the case if $\omega_c \tau_e \geq 1$. Here, $\omega_c = e B v_F / (\hbar k_F)$ is the cyclotron frequency and τ_e is the elastic scattering time including short range scattering (small angle scattering) that does not lead to momentum relaxation ($\tau_e \leq \tau_p \sim l_{mfp}/v_F$). Therefore, the so-called quantum mobility is obtained as $\mu \sim 1/B$, where B is the magnetic field at which SdH oscillations appear.

Using the Einstein relation, the conductivity can be related to the density of states with the diffusion constant D as the proportionality factor:

$$\sigma = e^2 D o S \cdot D. \quad (1.27)$$

This expression is in particular useful as it allows to estimate the diffusion constant that is then used to relate spin and phase relaxation lengths to their corresponding times scales through $\lambda_{s,\phi} = \sqrt{D \tau_{s,\phi}}$.

If l_{mfp} approaches W, L , the above mentioned diffusive formulas do not hold. In a pure ballistic graphene channel the conductance is given by the number of modes carrying each a conductance of $4e^2/h$ due to spin and valley degeneracy. The number of modes is given by the width of the graphene channel and one obtains the total conductance

$$G = \frac{4e^2}{h} \frac{W}{\lambda_F/2} = \frac{4e^2}{h} W \sqrt{n/\pi}, \quad (1.28)$$

where $\lambda_F = 2\pi/k_F$ was used. Ballistic transport in graphene constrictions [56] as well as quantized conductance [57] was recently observed.

pn-junctions

So far only homogeneous doping was considered. As shown above, graphene can be smoothly tuned from hole conducting to electron conducting. It is

furthermore possible to laterally dope the graphene to different charge carrier densities by multiple electrostatic gates. Between such differently gated regions so called pn or nn' junctions are formed, which can either be operated in the unipolar regime where both regions have the same charge carrier polarity (nn' or pp') or in the bipolar regime where the two regions have opposite charge carrier polarity (pn or np). It is important to note that in the case of pn-junctions (opposite polarity) a zero density region separating the two regions will be present. However, as the spectrum of graphene is gapless, no gap is present as it would be the case in conventional semiconductor. A remarkable consequence of the pseudospin in graphene is the fact that charge carriers will transmit a pn-junction with unity probability under perpendicular incident, which is called Klein tunnelling [58, 59].

Semi-transparent pn-junctions were recently introduced as building blocks for electron optics in graphene, where Fabry-Pérot cavities were formed [60, 61]. We also showed guiding of electrons in gate defined channels [62], where we also observed mode filling. In addition, beamsplitter behaviour was demonstrated [63] as well as negative refraction [64] leading to the realization of a Veselago lens [65].

1.2.2. Phase coherent effects

If the phase coherence length $\lambda_\phi \geq L, W$, then charge transport is phase coherent. This means that the quantum mechanical phase is preserved during multiple scattering events and interference effects can dominate transport. This does not mean that phase coherence effects are negligible in the regime $\lambda_\phi \ll L, W$ since some interference effects are even observable for macroscopic samples. In the first case, universal conductance fluctuations are expected for example, whereas weak (anti-)localization can be observed even the second case. Both effects are introduced in the following.

Universal conductance fluctuations

In a diffusive conductor, the different trajectories of the charge carriers added up phase coherently and lead to a constructive or destructive interference at certain places. This results in a deviation from the classically expected conductance. If $\lambda_\phi \sim L, W$, then the amplitude of the fluctuations around the mean value of the conductance is on the order of e^2/h [66], independent of device size and disorder strength, which made people call the fluctuations universal [67].

In optics the interference pattern can be changed by changing the path length or the wavelength. In analogy to optics, the charge carrier wavelength λ_F or their trajectories can be changed. The trajectories can be modified by a magnetic field that bends the charge carrier trajectories. In addition, changing

the disorder potential (e.g. by gating) the path of the charge carriers will be modified. The wavelength λ_F can be changed by changing the gate voltage, which results in a change of the Fermi energy. Therefore, the conductance is expected to fluctuate around the mean value by changing the magnetic field or by changing a gate voltage.

When the device dimensions are larger than the phase coherence length, it can be viewed as independent pieces of size $\sim \lambda_\phi^2$ that all display fluctuations that are uncorrelated. Therefore, the overall UCF amplitude reduces for larger devices. On the other hand if $\lambda_\phi = \sqrt{\tau_\phi D}$ is reduced, the amplitude of the UCF reduces as well as the overall conductor can be separated in more uncorrelated areas. The increase of temperature reduces τ_ϕ and hence λ_ϕ , which suppresses UCF. In addition an ensemble averaging over density or magnetic field can be performed to reduce the UCF amplitude further. In contrast to UCF, weak localisation and weak anti-localization are not averaged out if $W, L \gg \lambda_\phi$. More about this phenomena is shown in the next section.

If the disorder potential is gradually removed, the conductor goes from a diffusive regime to a ballistic regime. Interferences due to multiple paths can still occur but for the limit of a ballistic sample scattering is only possible at the edge or at electrostatic defined boundaries. Changing the density or the magnetic field will now affect the interference conditions in a regular way and Fabry-Pérot interferences, similar to optical cavities, can occur in the ballistic limit.

Weak localization and weak anti-localization

In a diffusive conductor, the charge carrier trajectories can form closed loops after several scattering events, see Fig. 1.6. The presence of time-reversal symmetry leads to two identical paths denoted by solid lines (forward) and dashed lines (reversed), which return to the common starting point. The complex quantum mechanical amplitudes of the two paths can be described by A^+ and A^- . Then the probability of returning to the starting point is

$$|A^+ + A^-|^2 = |A^+|^2 + |A^-|^2 + A^+ A^{-*} + A^{+*} A^-, \quad (1.29)$$

where the first two terms describe the classical contributions to backscattering (captured in the Drude formalism presented above). The last two terms arise due to the interference effect of both paths which is neglected in the classical incoherent Drude formalism. Time-reversal symmetry requires $A^+ = A^- \equiv A$. This then leads straightforwardly to the classical backscattering probability $P_{cl} = 2|A|^2$ and to the enhanced quantum mechanical backscattering probability $P_{qm} = 4|A|^2$. This effect is called weak localization (WL) [67].

The weak localization can be suppressed by an out-of-plane magnetic field. The wave function will pick up an additional Aharonov-Bohm phase ϕ_{AB} , that is opposite for the two paths. The quantum mechanical amplitudes are

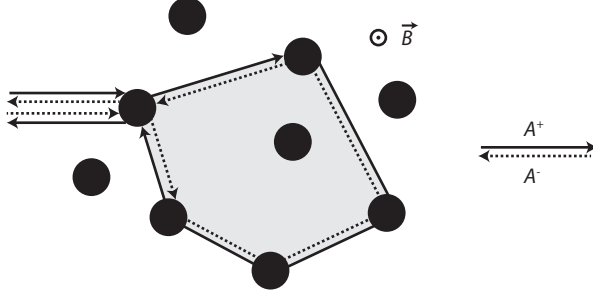


Figure 1.6. Closed loop interference of WL. Closed loops due to multiple scattering events lead to an interference condition at the starting point. If time reversal symmetry is present, the forward and the reversed path will interfere constructive at the starting point and an enhanced backscattering probability results. A perpendicular magnetic field \vec{B} through the loop area (grey shaded region) suppresses the interference condition.

therefore depending on magnetic field, $A^\pm(B) = Ae^{\pm i\phi_{AB}}$. The interference condition at the starting point will now be a periodic function of magnetic field: $P_{qm} = 2|A|^2 + 2|A|^2 \cos(4e\pi BS/h)$, where S is the area of the closed loop, see also Fig. 1.6. Since many closed loops with different area will contribute to the overall conductance, a coherent effect is only observed around zero magnetic field whereas at larger magnetic fields the oscillation in the interference conditions will average out. As a result, the conductance increases with magnetic field. This correction is commonly known as quantum correction to the magneto conductivity.

In the case of graphene, the quantum correction to the magneto conductivity $\Delta\sigma$ in the absence of SOC is given by:

$$\Delta\sigma(B) = \frac{e^2}{\pi h} \left[F\left(\frac{\tau_B^{-1}}{\tau_\phi^{-1}}\right) - F\left(\frac{\tau_B^{-1}}{\tau_\phi^{-1} + 2\tau_{iv}^{-1}}\right) - 2F\left(\frac{\tau_B^{-1}}{\tau_\phi^{-1} + \tau_*^{-1}}\right) \right], \quad (1.30)$$

where $F(x) = \ln(x) + \Psi(1/2 + 1/x)$, with $\Psi(x)$ being the digamma function, $\tau_B^{-1} = 4eDB/\hbar$, where D is the diffusion constant, τ_ϕ is the phase coherence time, τ_{iv} is the intervalley scattering time and $\tau_* = (1/\tau_{iv} + 1/\tau_z + 1/\tau_w)^{-1}$, where τ_z is the intravalley scattering time and τ_w is a scattering time associated with trigonal warping [52]. In principle, Eq. 1.30 can describe weak localization or weak anti-localization depending on the relative value of the involved time scales. In the limit of $\tau_\phi > \tau_{iv}$, the quantum correction to the

magnetoconductivity displays a WL behaviour, which is commonly observed [68–71], see also section C.7. On the other hand if $\tau_{iv,*} \geq \tau_\phi$, a WAL behaviour is obtained. This transition has been shown experimentally by Tikhonenko et al. [69]. The influence of τ_ϕ and τ_{iv} on the quantum correction to the magneto conductivity are shown in Fig. 1.7.

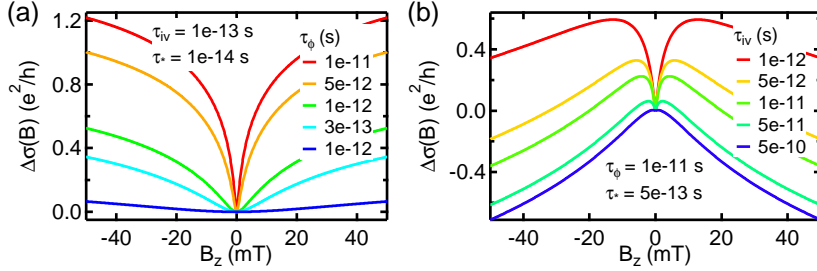


Figure 1.7. $\Delta\sigma(B)$ for different phase coherent and intervalley scattering times: WL and WAL is obtained from Eq. 1.30 by using $D = 0.118 \text{ m}^2 \text{ s}^{-1}$ and various combinations of τ_ϕ and τ_{iv} . (a) shows the influence of τ_ϕ , which is responsible for the suppression of the WL signal with shorter τ_ϕ . (b) shows the influence of τ_{iv} , which can change the curve shape from a clear WL signature to a broad WAL signature.

In principle, the charge carriers in graphene should show a WAL behaviour as they possess an additional quantum number, the pseudospin. Therefore, the wave function picks up an additional phase of π in closed loops, see also section 1.1.2. However, intervalley scattering (τ_{iv}) prevents the wave function from picking up a phase of π as the chirality in the K valley is opposite to the K' valley. Strong intervalley scattering will therefore lead to the recovery of WL.

In analogy to the pseudospin that is coupled to momentum by the chirality, the magnetic spin can be coupled to the momentum through SOC (e.g. Rashba SOC). Therefore, strong SOC in graphene will also lead to WAL. The WAL signature of a spin 1/2 in strong spin-orbit materials has been shown by Bergmann in an illustrative way [72]. In the case of strong SOC in graphene, the quantum correction to the magneto conductivity $\Delta\sigma$ is given by:

$$\Delta\sigma(B) = -\frac{e^2}{2\pi h} \left[F\left(\frac{\tau_B^{-1}}{\tau_\phi^{-1}}\right) - F\left(\frac{\tau_B^{-1}}{\tau_\phi^{-1} + 2\tau_{asy}^{-1}}\right) - 2F\left(\frac{\tau_B^{-1}}{\tau_\phi^{-1} + \tau_{asy}^{-1} + \tau_{sym}^{-1}}\right) \right], \quad (1.31)$$

where τ_{asy} is the spin-orbit scattering time due to SOC terms that are asymmetric upon z/-z inversion (H_R , H_{PIA}) and τ_{sym} is the spin-orbit scattering time due to SOC terms that are symmetric upon z/-z inversion (H_I , H_{VZ}) [73]. Eq. 1.31 holds only in the limit where τ_{iv} is shorter than τ_ϕ , τ_{asy} and τ_{sym} . Otherwise the influence of τ_{iv} and τ_* have to be taken into account, see section C.6 for a complete formula. Again, different limits with WL and WAL are possible depending on the relative magnitude of the time scales.

In the limit of very weak asymmetric but strong symmetric SOC ($\tau_{asy} \gg \tau_\phi \gg \tau_{sym}$), Eq. 1.31 describes reduced WL since the first two terms cancel and therefore a positive magneto conductivity results. Contrary to that, in the limit of very weak symmetric but strong asymmetric SOC ($\tau_{sym} \gg \tau_\phi \gg \tau_{asy}$) a clear WAL peak is obtained. If both time scales are shorter than τ_ϕ , the ratio τ_{asy}/τ_{sym} will determine the quantum correction of the magneto conductivity. In the limit of total weak SOC ($\tau_{asy}, \tau_{sym} \gg \tau_\phi$) the normal WL in graphene is obtained, see above. The influence of τ_{asy} and τ_{sym} on $\Delta\sigma(B)$ is shown in Fig. 1.8.

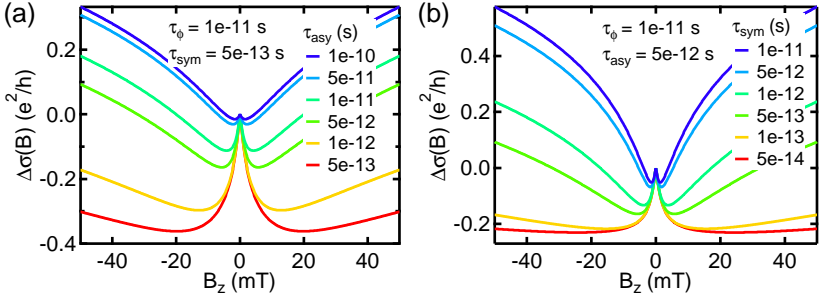


Figure 1.8. $\Delta\sigma(B)$ for different spin-orbit scattering rates: Various shapes of $\Delta\sigma(B)$ are obtained from Eq. 1.31 using $D = 0.118 \text{ m}^2 \text{ s}^{-1}$ and the time scales indicated in the figure. (a) shows the influence of τ_{asy} , which is responsible for the transition from a clear WAL peak at $\tau_{asy} = 5 \times 10^{-13} \text{ s}$ to a (mostly) WL feature at $\tau_{asy} = 5 \times 10^{-10} \text{ s}$. (b) shows the influence of τ_{sym} , which mostly only changes the background at large magnetic field. The central WAL peak height depends weakly on τ_{sym} for $\tau_{sym} \ll \tau_{asy}$.

There is an upper limit of the field scale (the so-called transport field B_{tr}) at which the theory of WL/WAL breaks down. The size of the shortest closed loops that can be formed in a diffusive sample is on the order of l_{mfp}^2 , where l_{mfp} is the mean-free path of the charge carriers. Fields that are larger than Φ_0/l_{mfp}^2 , where $\Phi_0 = h/e$ is the flux quantum, are not meaningful in the

framework of diffusive transport.

In general τ_ϕ is the longest time scale and is therefore responsible for the sharpest feature around zero magnetic field. Even though Eq. 1.30 and 1.31 can both reproduce clear WL and WAL signatures, the WAL due to SOC is characterized by a sharp peak around zero magnetic field, whereas the WAL due to the pseudospin is much broader with a sharp dip around zero magnetic field. Therefore, the quantum correction to the magneto conductivity can reveal the presence and strength of the SOC.

1.2.3. Hall effect and quantum Hall effect

Charge carriers in graphene experience a Lorentz force when a perpendicular magnetic field is applied [74]. This leads to a deflection of the charge carriers, which in turn leads to a voltage appearing between opposite edges of the graphene (Hall voltage) given by [67]: $V_H = IB/(en)$, where I is the applied current. Therefore, the Hall effect allows to determine the charge carrier density in the graphene. Furthermore, a parabolic magnetoconductance is expected in a two-terminal measurements, whose exact shape is determined by the τ_p and the charge carrier density n [67].

For very large magnetic fields the charge carriers in graphene can form closed loops and quantum effects start to play a role. In high-mobility 2-dimensional electron gases (2DEGs) at low temperatures the longitudinal resistance R_{xx} drops to zero, whereas the Hall resistance $R_{xy} = h/(e^2\nu)$ with $\nu = 1, 2, 3, \dots$ becomes quantized [75]. In this phase, the quantum Hall phase, the bulk of the sample is gapped, whereas dissipationless edge channels carry the current, resulting in the quantized Hall conductance. The quantum Hall effect appears if two main criterion are met. First the charge carriers need to be able to perform full cyclotron orbits without being scattered and second the temperature must be small enough such that $k_B T \ll E_N$, where E_N is the LL energy.

The LL energies in graphene are obtained by solving the Dirac equation in a perpendicular magnetic field resulting in:

$$E_N = \text{sign}(N)v_F\sqrt{2e\hbar B|N|}. \quad (1.32)$$

It is evident from Eq. 1.32 that the lowest LL is at zero energy, being half filled by electrons and half filled by holes. The square-root dependence on B results in non-equidistant LL gaps (in contrast to conventional semiconductors) with a very large LL gap between the first two LL, which lead to the observation of the QHE in graphene at room temperature [76]. The Hall conductivity takes the form

$$\sigma_{xy} = \frac{g_s g_v e^2}{h} (N + 1/2) \quad (1.33)$$

The two factors of $g_s = g_v = 2$ resembles the spin and valley degeneracy whereas the additional $1/2$ comes from the Berry phase picked up by closed loops. Whenever the Hall conductivity is quantized to the values described in Eq. 1.33, the longitudinal resistance R_{xx} will go to zero indicating dissipation less edge channels. Due to electron-electron interactions [77], the spin and valley degeneracy can be lifted and quantized conductance at all integer values of e^2/h can be observed. In the absence of interaction driven symmetry breaking, the spin-splitting of the quantum Hall states could be used to investigate the SOC strength [78].

In two terminal device G_{xy} and R_{xx} cannot be measured independently but only a combination of both depending on the aspect ratio W/L . For $W/L \sim 1$ well defined plateaus at the values given in Eq. 1.33 develop [79, 80].

Since the charge carrier in bilayer graphene are massive, the Landau level spacing is nearly equidistance and discribed by [81]:

$$E_N = \pm \hbar \omega \sqrt{N(N-1)}. \quad (1.34)$$

A direct consequence of this formula is that the Landau level $N=0$ and $N=1$ both lie at zero energy leading to an eightfold degeneracy, whereas the other Landau levels are fourfold degenerate. As in single layer graphene, this Landau level is half-filled by holes and half-filled by electrons. The Hall conductance is quantized in steps of $\pm 4, \pm 8, \pm 12 \dots$ [81].

1.3. Spin transport in graphene

Ferromagnetic contacts are one of the most common ways to inject a spin polarized current into a non-magnetic material (NM), including graphene. Before discussing spin transport in graphene, a basic introduction to ferromagnetism is given, followed by the concept of electrical spin injection.

1.3.1. Ferromagnetism and magnetic anisotropies

Metallic ferromagnetism (e.g. in Fe, Ni, Co) is well described by the Sonter model [82, 83]. Spontaneous ferromagnetic ordering occurs if the Stoner criterion $U \cdot \text{DoS}(E_F) \geq 1$ is met. In general, a large exchange interaction U and a large density of states at the Fermi energy $\text{DoS}(E_F)$ is required. The 3d bands of the transition metals Fe, Ni and Co fulfil these conditions [82]. A spin-splitting of the bands by the exchange splitting ΔE_{ex} and a spontaneous magnetization $M \propto (n_\uparrow - n_\downarrow)$, proportional to the total number of spin-up n_\uparrow and spin-down n_\downarrow electrons, occurs even in the absence of an external magnetic field. This is shown in Fig. 1.9 (a).

While the microscopic origin of the magnetization \vec{M} is described by the Stoner model, it fails to describe the local variations of $\vec{M}(\vec{r})$ and its anisotropy in

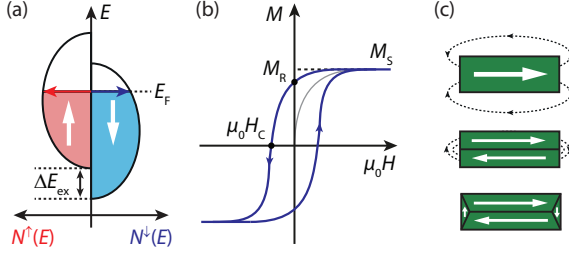


Figure 1.9. Ferromagnetism: (a) shows a schematic of the spin-split bands shifted by the exchange energy ΔE_{ex} in the Stoner model. Different DoS N^\uparrow (red arrow), DoS N^\downarrow (blue arrow), and a spontaneous magnetization $M \propto (n_\uparrow - n_\downarrow)$ result. (b) Magnetization as a function of external magnetic field $\mu_0 H$ of a multi-domain ferromagnet. (c) shows the stray field generated by rectangular ferromagnets and the reduction of the stray field by forming multiple domains, including closure domains at the ends. Adapted from Ref. [84].

bulk ferromagnets. This can be captured by minimizing the ferromagnet's total free energy $G = \int_V dV g_{tot}(\vec{M}(\vec{r}), \vec{H})$, considering all relevant energy terms and magnetic anisotropies of the system [83, 85]. Anisotropies are for example responsible that the magnetization \vec{M} aligns along a preferred direction, so called easy axis, in the absence of an external magnetic field \vec{H} . In this case, the system's total free energy G is minimal. On the other hand, a hard axis is called an orientation of the magnetization that leads to a maximum in G . The most relevant energy terms contributing to the total energy density $g_{tot} = f_{ex} + f_Z + f_{mc} + f_d$ are discussed briefly in the following based on Refs. [83, 85].

The short range internal exchange energy term $f_{ex} \propto (\nabla \vec{M})^2$ accounts for the microscopic ferromagnetic ordering, that favours parallel orientation between magnetic moments. The Zeeman energy term $f_Z = -\mu_0 \vec{H} \vec{M}$ accounts for the interaction of the magnetization with an external field that favours parallel orientation. The magneto crystalline anisotropy energy f_{mc} accounts for the alignment of the magnetic moments with respect to a crystallographic easy axis. The microscopic origin of this interaction is the spin-orbit interaction that couples spins to the anisotropic orbitals in crystalline structures [83]. In permalloy (Py = $\text{Ni}_{80}\text{Fe}_{20}$) the magneto crystalline anisotropy of Ni and Fe nearly cancel, which results in a material with a very small crystal anisotropy. The dipole energy term $f_d = -\mu_0 \vec{H}_d \vec{M}(\vec{r})$ describes the dipole-dipole interaction of the magnetization with the demagnetization field \vec{H}_d (in the sample) or stray field (outside the sample) that is created by the ferromag-

netic material itself. This term tries to minimize the stray field. The preferred in-plane magnetization of a thin ferromagnetic film is due to this term. Furthermore, it is also the driving force for domain formation [83], which can reduce the stray field as depicted in Fig. 1.9 (b). One often also speaks about shape anisotropy since a given shape of a ferromagnet will prefer a certain direction of the magnetization. A typical magnetization curve as a function of external field is shown in Fig. 1.9 (b) for a multi-domain ferromagnet. In an increasing external magnetic field the domains with a magnetic moment parallel to the external field will grow until all moment are aligned with the external magnetic field and the saturation magnetization M_S is reached. In this case, the ferromagnet is in a single domain state. At zero external magnetic field, a non-zero (remanent) magnetization M_R remains. The coercive field $\mu_0 H_C$ is required to overcome this ferromagnetic ordering and to reverse the sign of the magnetization. Ferromagnets with a small H_C are called soft magnets, whereas ferromagnets with large H_C are called hard magnets [82].

In the case of very small ferromagnetic samples (≤ 100 nm to 500 nm [86]) the energy cost for a domain wall formation is larger than the gain due to the stray field reduction and a single domain will result, see also Fig. 1.9 (c), top. In this case, the magnetization direction will be determined by a competition of the shape and crystal anisotropy. For thin ferromagnetic strips with the width being much smaller than the length, an in-plane magnetization along the longest direction is observed commonly for Co and Py.

As shown above the magnetization in a nanoscale ferromagnet can be uniform (e.g. single domain). Therefore, we describe the magnetization dynamics in the following for a classical macro-spin \vec{M} . The magnetization dynamics of a ferromagnet in an effective magnetic field \vec{H}_{eff} is governed by the Landau-Lifshitz-Gilbert equation [87, 88]

$$\frac{d\vec{M}}{dt} = \gamma \vec{H}_{eff} \times \vec{M} + \alpha \vec{M} \times \frac{d\vec{M}}{dt}, \quad (1.35)$$

where $\gamma = g\mu_B/\hbar$ is the gyromagnetic ratio with g the Landé g-factor and $\mu_B = e\hbar/(2m_e)$ the Bohr magneton and α the Gilbert damping constant. Driving the magnetization with an external high-frequency magnetic field can lead to a stable resonance condition when the driving power equals the damping power. This situation is called ferromagnetic resonance (FMR). The resonance frequency depends on the effective field \vec{H}_{eff} that is a sum of several influences (e.g. external field, shape and crystal anisotropy fields). The Gilbert damping, characterizing the loss of the system, can have several origins. It was predicted [89] and observed that the damping term substantially increases if the ferromagnet is in contact with a non-magnetic material that can absorb a spin current emitted from the ferromagnet [90–93]. This situation corresponds to spin pumping that will be discussed in chapter 6.

1.3.2. Electrical spin injection in non-magnetic materials

Ferromagnetic contacts are one of the most common ways to inject a spin polarized current into a non-magnetic material (NM). The two spin-dependent bands are shifted in energy due to exchange interaction and hence the density of states in a ferromagnet is different for the two spin species (here called "spin up" and "spin down"). This leads to a magnetization that is a measure of the difference of total spin up and spin down electrons in the system. Usually for transport measurements, the density of states at the Fermi energy is relevant. It is obvious to see that in the case of a half-metal (where only one spin species is allowed at the Fermi energy) the current will be spin polarized. Therefore, a current passed from a half-metal into a non-magnetic metal will lead to a net spin current in the normal metal. In reality half-metals are scarce and therefore normal ferromagnets are used. Their spin dependent density of states leads to spin dependent conductivities, which in a diffusive system can be written with the use of Einstein's relation as

$$\sigma_{\uparrow\downarrow} = e^2 \rho_{\uparrow\downarrow}(E_F) D_{\uparrow\downarrow}, \quad (1.36)$$

where e is the electron charge, $D_{\uparrow\downarrow}$ is the spin dependent diffusion constant and $\rho_{\uparrow\downarrow}(E_F)$ is the spin dependent density of states at the Fermi energy (E_F). In a non-magnetic material $D_{\uparrow\downarrow}$ can be replaced with the D_c (this holds as long as spin is coupled to charge, which is mostly the case). This leads to spin polarized currents in the ferromagnetic material with a polarization

$$P = \frac{\sigma_{\uparrow} - \sigma_{\downarrow}}{\sigma_{\uparrow} + \sigma_{\downarrow}}, \quad (1.37)$$

where the overall conductance is given by $\sigma = \sigma_{\uparrow} + \sigma_{\downarrow}$.

Driving now a current across a FM/NM interface will lead to a spin imbalance in the NM as the current is spin polarized as seen above. This spin imbalance will decay over distance with a characteristic length scale λ_s and it will finally vanish at distances very far away from the interface as no net spin polarization is allowed to exist there (equilibrium condition in a NM). The spin imbalance is called spin accumulation, which can be expressed by the difference of the chemical potential of the spin up and spin down electrons: $\mu_s = (\mu_{\uparrow} - \mu_{\downarrow})$. In a diffusive picture, the spin relaxation length λ_s can be related to the spin relaxation time τ_s using the spin diffusion constant D_s : $\lambda_s = \sqrt{D_s \tau_s}$.

1.3.3. Conductivity mismatch

As mentioned in the previous section, a spin accumulation will develop if a current is driven across the FN/NM interface, which is given as:

$$\mu_{s,NM}(0) = -ejP_i R_{NM}, \quad (1.38)$$

where e is the electric charge, $\mu_{s,NM}$ is the spin accumulation in the normal metal at the interface ($x=0$), j is the current driven across the interface, P_i is the injection efficiency and $R_{NM} = \frac{\lambda_{s,NM}}{\sigma_{NM}}$ is the effective resistance of the normal metal. Often this resistance is also called spin resistance as it describes the resistance of one spin channel over the characteristic length scale λ_s . The magnitude of $\mu_{s,NM}$ crucially depends on the involved materials and interface properties as this defines the injection efficiency P_i , which is given as [94]:

$$P_i = \frac{R_{FM}P_{FM} + R_C P_C}{R_{FM} + R_C + R_{NM}}, \quad (1.39)$$

where $R_{FM,NM,C}$ are the effective resistances of the FM, NM and contact respectively and $P_{FM,C}$ are the spin polarizations of the FM and contact respectively [94]. Here, P_{FM} means the bulk polarization of the FM, whereas P_C is the polarization associated with the contact interface of the FM to the NM. Two limiting cases can be distinguished:

$$P_i = \begin{cases} \frac{R_{FM}P_{FM}}{R_{NM}+R_{FM}} & R_C \ll R_{FM}, R_{NM} \rightarrow \text{transparent contact} \\ P_C & R_C \gg R_{FM}, R_{NM} \rightarrow \text{tunnel contact} \end{cases}, \quad (1.40)$$

depending on the relative magnitude of R_C to R_{NM} and R_{FM} .

In the case of a transparent contact, the ratio of R_{FM} to R_{NM} will finally determine the spin injection efficiency. For $R_{FM} \sim R_{NM}$, meaning the FN and NM are equally conducting³, a large spin injection efficiency $P_i \simeq P_{FM}$ can be reached. This is the situation usually the case for all metallic spin valves or for the injection of a spin polarized current from a ferromagnetic semiconductor to a normal semiconductor. If on the other hand $R_{NM} \gg R_{FM}$, which would correspond to the injection from a ferromagnetic metal to a non-magnetic semiconductor or to a low dimensional conductor (e.g. graphene), the spin injection efficiency is small $P_i \simeq \frac{R_{FM}}{R_{NM}} P_{FM}$. This situation is well known as the conductivity mismatch problem [95].

In the case of a highly resistive contact ($R_C \gg R_{FM}, R_{NM}$, e.g. a tunnel contact), the spin injection efficiency P_i is given by P_C , which can be large. In this case the contact acts as a spin filter. Obviously, the question is what determines P_C . In a general form, where no further assumptions are made about the contact, one can write $P_C = \frac{\Sigma_{\uparrow} - \Sigma_{\downarrow}}{\Sigma_{\uparrow} + \Sigma_{\downarrow}}$, where $\Sigma_{\uparrow,\downarrow}$ are the spin conductances of the contact. The spin dependent conductances of the contact $\Sigma_{\uparrow,\downarrow}$ can be given by a spin-filtering effect of the contact, or by the spin dependent density of states of the FM in the case of a tunnel contact for example.

In a tunnel contact, the tunnelling current is given as a convolution of the occupied states of the FM with the empty states in the NM within the bias

³Equally conducting means here that the effective resistances are similar, which depend on the conductivities and spin relaxation lengths.

window. Since the occupied states in the FM depend on the density of states at the Fermi energy, which itself is spin dependent, a spin dependent term enters the contact resistance. Therefore, a large difference in density of states for spin up and down at the Fermi energy is beneficial, which is the case for iron and cobalt whereas there is only a small splitting for nickel [96, 97]. Therefore, a tunnel barrier between the FM and the NM is a solution to the conductivity mismatch problem and allows for large spin polarizations and accumulations in the NM. Alternatively, a spin filtering at the interface of a highly resistive contact could be another way to inject spin polarized currents efficiently into a NM.

1.3.4. Spin diffusion equation

As seen above, a spin accumulation can be created in a NM at the interface to a FM contact. The motion of the spins in the NM (e.g. graphene) can be described by the spin diffusion equation in steady state [94]:

$$\frac{d\vec{\mu}_s}{dt} = 0 = D_s \nabla^2 \vec{\mu}_s - \frac{\vec{\mu}_s}{\tau_s}, \quad (1.41)$$

where $\vec{\mu}_s = (\mu_s^x, \mu_s^y, \mu_s^z)$ is the spin accumulation in three dimensions. The first term on the right represents diffusion and the second term describes relaxation with the spin relaxation time τ_s . In the case of a 1D system (e.g. infinitely long narrow graphene strip), the solution of the differential equation is $\mu_s(x) = \mu_{s,0} e^{-|x|/\lambda_s}$. This describes an exponential decay of the spin accumulation to the equilibrium condition $\mu(x = \pm\infty) = 0$ with the characteristic length scale $\lambda_s = \sqrt{D\tau_s}$, where D is the diffusion constant, and with $\mu_{s,0}$ given above.

1.3.5. Non-local spin valve

A non-local spin valve as depicted in Fig. 1.10 (a) is an ideal platform to study the spin properties of the channel material (e.g. graphene). In this configuration the current path is spatially separated from the voltage detection. This is a big advantage as it allows to separate any magnetoresistance effect present in local spin valves (e.g. anisotropic magnetoresistance of the FM) from the pure spin transport signal. The non-local spin valve uses the fact that a spin accumulation below the injecting contacts leads to the diffusion of spins away from this point. The voltage detection circuit starting at distance L from the injector contact thus probes only the spin accumulation due to diffusion of the spin away from the injector contact.

A typical non-local spin valve consists of four ferromagnetic contacts (actually only contact 2 and 3 need to be ferromagnetic), as shown in Fig. 1.10 (a). If a current is passed from contact 2 to contact 1, a spin accumulation builds up in the graphene as shown in (b). If all contacts are magnetized parallel to each

other, as shown on the top, contact 2 injects spins, whereas contact 1 extracts spin of the same polarization. This leads to the opposite spin accumulation below contact 2 and contact 1. If contact 2 and contact 1 are magnetized anti-parallel to each other, then the spin accumulation has the same sign below both contacts and it adds up. Therefore, an anti-parallel configuration leads to an overall larger spin accumulation than a parallel configuration (see also the difference between the dashed grey lines (individual contribution) and the blue solid lines (combined contribution)). This effect only plays a significant role if contact 1 is close to the other contacts.⁴

Contact 3 and 4 probe preferentially the spin resolved chemical potential, as indicated by black circles in Fig. 1.10 (b). This effect is known as *Silsbee-Johnson spin charge coupling* and was first proposed by Silsbee [98] and experimentally demonstrated by Johnson and Silsbee [99] in the first electrical spin injection experiments. In a simplified picture, the chemical potential of a FM will adjust with the spin up chemical potential in the graphene (depending on the magnetization). Therefore, a finite voltage between the FM and the mean chemical potential in graphene will develop that can be measured. This leads to a voltage difference between contact 3 and 4 that can be measured with a voltmeter. This non-local voltage $V_{NL} = P_3 \frac{\mu_s(x_3)}{e} - P_4 \frac{\mu_s(x_4)}{e}$, where $P_{3,4}$ are the injection/detection efficiencies of the contacts⁵ and $x_{3,4}$ are the locations of the contacts, depends solely on the spin accumulation μ_s . By changing the magnetization direction of contact 3, the opposite spin chemical potential is sensed and the non-local voltage will change sign. Since the contact polarization is not 100%, every FM contact will not purely sense one spin resolved chemical potential but rather both weighted by the contact polarization. This contact polarization depends on the nature of the contact as explained above and is ideally given by the polarization associated with the contact polarization P_C .

If the contacts 1 and 4 are far away ($|x_2 - x_1|, |x_3 - x_4| \gg \lambda_s$), only the distance $|x_2 - x_3| = L$ plays a role and the non-local voltage can be expressed as:

$$V_{NL} = \frac{I R_{sq} \lambda_s}{2w} P_3 P_4 e^{-L/\lambda_s}. \quad (1.42)$$

Here, the effective resistance of the NM was replaced by $R_{NM} = \frac{R_{sq} \lambda_s}{w}$ for the special case of a 2D material such as graphene. R_{sq} is the sheet resistance of the graphene. The non-local resistance can be normalized by the injecting current and one obtains the non-local resistance $R_{NL} = V_{NL}/I$. This non-local resistance is not a dissipative resistance. It should rather be interpreted as a

⁴Close means that the distance $|x_2 - x_1|$ is comparable to λ_s as the spin accumulation falls off exponentially: $e^{|x_2 - x_1|/\lambda_s}$.

⁵The above defined injection efficiency P_i is commonly referred to as contact polarization. However, one should not confuse it with the contact polarization P_C defined above, which for tunnel contacts equals P_i .

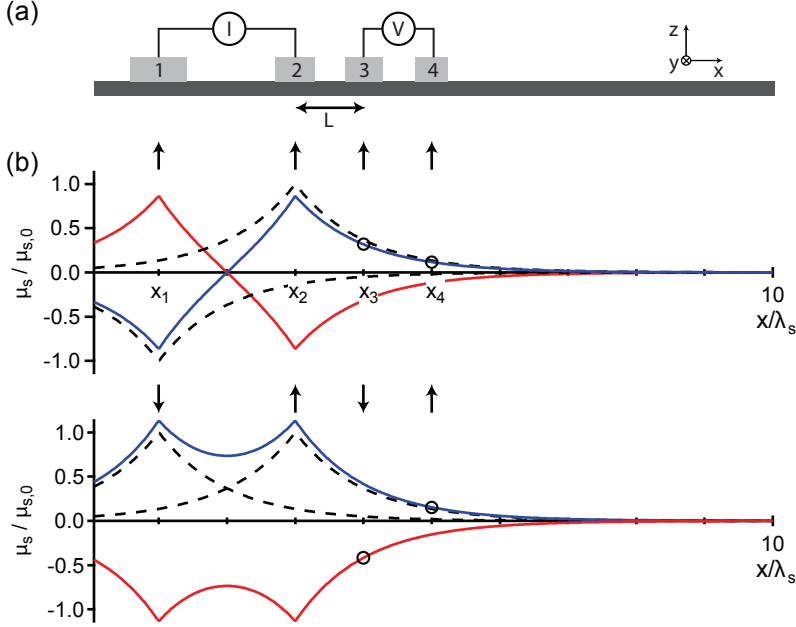


Figure 1.10. Schematics of a non-local spin valve. (a) shows the device schematics with four ferromagnetic contacts labelled 1 to 4 in contact to the channel material below. The electrical circuit to inject and detect spins is shown as well. (b) shows the spin accumulation (e.g. chemical potential for spin up (blue) and down (red)) for the case where all electrodes are aligned parallel (top) and for the case where they are aligned anti-parallel (bottom). The black dashed lines show the spin accumulation of spin up for each injecting contact separately. The channel material is assumed to extend in both direction to infinity (e.g. no boundary effects are included).

normalized measure of the spin accumulation in the graphene and therefore, also negative R_{NL} are possible. R_{NL} can be written in a more compact way using assuming $P_2 = P_3 = P$

$$R_{NL} = \pm \frac{R_{sq}\lambda_s}{2w} P^2 e^{-L/\lambda_s}. \quad (1.43)$$

Here the \pm sign accounts for parallel and anti-parallel configuration of the injector (contact 2) and detector (contact 3) electrode. Eq. 1.43 predicts sudden jumps in the non-local resistance if the magnetizations of contact 2 and 3 are switched from parallel to anti-parallel.

1.3.6. Hanle effect

In principle, a spin valve measurement contains all important information about the channel material (λ_s). With the help of the diffusion constant, the spin relaxation time $\tau_s = \sqrt{D\lambda_s}$ could be calculated. However, this method is greatly affected by the contact polarization P as one can see in Eq. 1.43.

A more accurate way to obtain the spin transport parameters from the channel material is by the use of the Hanle effect [94]. A magnetic field applied perpendicular to the spin direction (collinear with the magnetization of the ferromagnetic contacts) will lead to a precession of the spin around this field (Larmor precession). Since the electrons and hence the spins as well, move diffusively in the graphene, not a full coherent rotation of the spin ensemble but rather a decrease of net spin polarization with time is the result. The modulation of the non-local resistance is given as:

$$R_{NL}(B) = \pm \frac{P^2 R_{sq} D_s}{w} \int_0^\infty \frac{1}{\sqrt{4\pi D_s t}} e^{-L^2/(4D_s t)} \cdot \cos(\omega_L t) \cdot e^{-t/\tau_s} dt, \quad (1.44)$$

where $\omega_L = \frac{g\mu_B}{\hbar} B$ is the Larmor precession frequency with g being the Landé g -factor and μ_B the Bohr magneton and \hbar the reduced Planck constant. The first term in the integral $\frac{1}{\sqrt{4\pi D_s t}} e^{-L^2/(4D_s t)}$ describes the probability of a spin arriving at the detector after time t in a diffusive picture. During this time t , the spin will precess around the magnetic field B , which results in the second term $\cos(\omega_L t)$. To account for spin relaxation during this time t , the factor e^{-t/τ_s} is introduced. This integral can be solved and one arrives at the analytical formula:

$$R_{NL}(B) = \pm \frac{P^2 R_{sq} D_s}{w} Re \left\{ \frac{1}{\sqrt{D_s}} \frac{e^{-L\sqrt{\lambda_s^{-2} - i\frac{\omega}{D_s}}}}{\sqrt{\tau_s^{-1} - i\omega}} \right\}. \quad (1.45)$$

Eq. 1.45 describes how the non-local resistance depends on a magnetic field perpendicular to the spin axis and distance between injector and detector

electrode. The magnetization is assumed not to be influenced by the magnetic field, which is a valid assumption for fields much smaller than the coercive field. D_s and τ_s can be extracted by fitting the measured R_{NL} with eq. 1.45, assuming $g = 2$. The extracted D_s should correspond to D_c that can be extracted independently from charge transport measurements.

In order to remove any spin unrelated background signals (e.g. Hall effect), the Hanle curve can be measured in parallel (R_P) and anti-parallel (R_{AP}) configuration of the injector and detector electrode. The difference of this two measurements $R_s = (R_P - R_{AP})/2$ is only due to spin.

1.3.7. Spin relaxation mechanisms in graphene

There are three fundamental principles leading to spin relaxation. First, spins can be relaxed by the presence of spin-orbit coupling, leading to Dyakonov-Perel and Elliot-Yafet spin relaxation mechanism. Second, the spin polarization can be lost due to hyperfine interactions with the nuclear spins. Lastly, spins can be scattered by localized magnetic moments that lead to the loss of spin polarization.

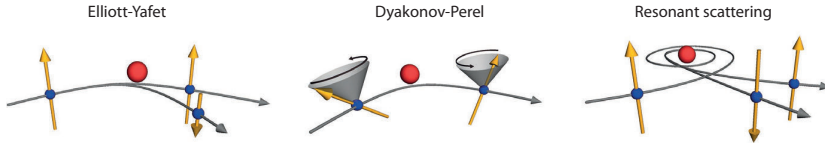


Figure 1.11. Spin relaxation mechanism: Schematics of the Elliott-Yafet, Dyakonov-Perel and the resonant scattering mechanisms are shown. Figure adapted from Ref. [15].

In the following, I will touch upon the uniform spin-orbit coupling and show how spin relaxation rates, which are accessible in experiments, can be linked to uniform SOC strengths. This includes the two most important spin-relaxation mechanisms: Elliott-Yafet and Dyakonov-Perel. In addition the relaxation due to resonant magnetic scatters is also discussed. Depending on the individual contribution of each mechanism the spin relaxation anisotropy can be distinctively different, which will be discussed in the end.

Elliott-Yafet mechanism

Elliott [100] and Yafet [101] found that ordinary momentum scattering can lead to spin relaxation if SOC is present. This can be understood since the SOC mixes the pure spin states and therefore there exists a finite (but small)

probability at each scattering event to flip the spin. This leads to

$$\tau_s = \frac{\tau_p}{\alpha}, \quad (1.46)$$

where τ_s is the spin lifetime, τ_p the momentum scattering time and α a proportionality constant.

In the case of graphene, this proportionality constant relating a given SOC to the spin relaxation time has been shown to depend on the ratio of the Fermi energy to the SOC strength and takes the following form for intrinsic SOC (α_I) and Rashba SOC (α_R) [19, 102]:

$$\begin{aligned} \alpha_I &= \left(\frac{\lambda_I}{2E_F} \right)^2 \\ \alpha_R &= \left(\frac{4\lambda_R}{E_F} \right)^2. \end{aligned} \quad (1.47)$$

Here, the SOC strengths are defined in the Hamiltonian shown in Eq. 1.23. Since the spin relaxation time scales inversely with the ration of λ/E_F , the influence of Elliott-Yafet mechanism is greatly reduced for E_F much larger than the SOC strength. Furthermore, a long τ_p will lead long spin relaxation times. Using reasonable numbers for pristine graphene ($\lambda_I \simeq 10 \mu\text{eV}$ [54], $E_F \simeq 100 \text{ meV}$ and $\tau_p \simeq 10 \text{ fs}$) yields a spin relaxation time of the order of $1 \mu\text{s}$.

Dyakonov-Perel mechanism

If the SOC can be viewed as an uniform spin-orbit magnetic field (though k-dependence can still be present), spins can precess around this effective magnetic field between scattering events. In a k-dependent spin-orbit field, such as it is the case for Rashba type SOC, the spin precession axis will depend on the k vector. After multiple scattering events different electrons will have experience different spin-orbit fields and hence will have a different spin orientation. This leads to spin relaxation. If the the momentum time is short the spins have only little time to precess around the effective spin-orbit field and only small precession angles result. Since small rotations commute the order of which the spin experiences the different spin-orbit field does not matter and the spin relaxation time is longer. This effect is also called motional narrowing. It can be shown that

$$\tau_s = \left(\frac{\hbar}{2\lambda_R} \right)^2 \tau_p^{-1} \quad (1.48)$$

describes the spin relaxation time τ_s in the presence of a Rashba type SOC of strength λ_R .

Not only can the Rashba SOC lead to spin relaxation mediated by the Dyakonov-Perel mechanism, but also further SOC terms can lead to Dyakonov-Perel mediated spin relaxation. Recently, Cummings et al. have shown that the valley-Zeeman can relax in-plane spins [36]. The effective spin-orbit magnetic field is independent of \vec{k} in the case of valley-Zeeman SOC. However, intervalley scattering can randomize the direction of the spin-orbit field seen by the charge carriers. Therefore, the above derived spin relaxation in the motional narrowing takes the following form

$$\tau_s = \left(\frac{\hbar}{2\lambda_{VZ}} \right)^2 \tau_{iv}^{-1}, \quad (1.49)$$

where the momentum scattering time τ_p is replaced by the intervalley scattering time τ_{iv} .

Resonant magnetic moments

Experiments on weak localization and universal conductance fluctuations in graphene in strong in-plane magnetic fields have found a significant contribution to dephasing from magnetic moments [103]. Magnetic moments in graphene can form due to carbon vacancies or chemisorbed hydrogen, leading to a sp^3 hybridization [104–107]. Such localized magnetic moments can lead to spin precession of the electron spins and hence to spin relaxation. However, the interaction time of an electron spin with a localized magnetic moments is too short to lead to significant spin precession and therefore cannot lead to an efficient spin relaxation [108]. This picture completely changes if the magnetic moments are resonant scatterers meaning that the energy level of the scatterer matches the Fermi energy and hence the energy of the electrons. This leads to a much longer interaction time of the electron spin with the magnetic moment. If the interaction time is on the order of the precession frequency the probability of spin flip is large. This leads to an efficient spin relaxation [108]. Similar effects have been proposed for bilayer graphene [109].

Spin relaxation anisotropy

The spin lifetime anisotropy $\xi = \tau_{\perp}/\tau_{\parallel}$, defined as the ratio between the out-of-plane spin relaxation time τ_{\perp} to the in-plane spin relaxation time τ_{\parallel} , can give valuable insights into the dominating nature of spin relaxation mechanism. Here, out-of-plane means perpendicular and in-plane means parallel to the graphene plane. The anisotropy is given by the preferential direction of the spin-orbit field that lead to spin relaxation [15]. Spin-orbit fields in the graphene plane (e.g. Rashba or PIA) will lead to an anisotropy $\xi < 1$ [19, 94, 110]. In a conventional 2D Rashba system a spin-life time anisotropy of 1/2 is expected. On the other hand, out-of-plane spin-orbit fields (e.g. valley-Zeeman

[36], ripples[19] or flexural distortions [111] will result in $\xi > 1$. Therefore, ξ is a good measure to identify the symmetry of the the dominant spin-orbit term. The presence of local magnetic moments with random orientation, due to hydrogen adatoms for example, can dominate over the spin-orbit mediated spin relaxation and this will result in $\xi = 1$. Overall, the spin-life anisotropy is a good figure of merit to characterize the limiting factor in spin-life time.

1.4. Spin Hall and inverse spin Hall effect

The spin Hall effect (SHE) and the inverse spin Hall effect (ISHE) are two relativistic spin-orbit phenomena that relate electrical currents to pure spin currents and vice-versa. In the SHE, an unpolarized charge current leads to a transverse pure spin current, see Fig. 1.12 on the left. On the contrary in the ISHE, a pure spin current leads to a transverse charge current, see Fig. 1.12 on the right [112].

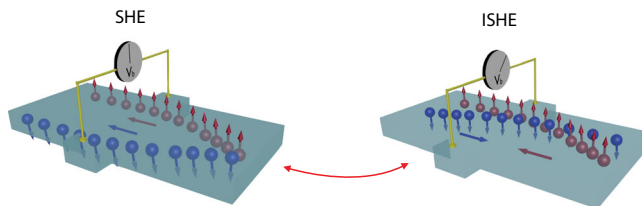


Figure 1.12. Spin Hall and inverse spin Hall effect: In the SHE, an unpolarized charge current leads to a transverse pure spin current. In the ISHE, a pure spin current leads to a transverse charge current. Image adapted from Ref. [112].

SHE and ISHE are classified according to their origin into extrinsic and intrinsic effect. The extrinsic effects includes skew scattering and side-jump scattering, which are both spin dependent scattering mechanisms. These effects can be described in the framework of Mott scattering [113], that is also the basis for the description of the anomalous Hall effect (AHE) in ferromagnetic materials [112]. On the other hand, the intrinsic effect has a clearly distinct origin. It arises from a spin dependent transverse velocity that is due to the spin-orbit fields. Therefore, this effect is also present in perfect crystals without scattering [112].

First experimental detection of the SHE relied on optical read-out of the spin polarization of semiconductors with strong SOC [114, 115]. First reports of the ISHE were based on spin-pumping [116], electrical spin injection [117] or optical methods [118]. Since the first qualitative reports, many more and more

quantitative studies were performed on various material systems [112]. One of the most studied system for SHE and ISHE is platinum since it is a very heavy element that possesses strong SOC. This is an important ingredient in efficient spin-to-charge conversion. The efficiency of spin-to-charge conversion (or the reverse) is commonly described by the spin Hall angle θ_{SH} . In this framework, the charge current density \vec{j}_c and the spin current density \vec{j}_s are related through θ_{SH} in the following way:

$$\vec{j}_c = \theta_{SH} \frac{2e}{\hbar} \vec{j}_s \times \vec{\sigma}, \quad (1.50)$$

where σ is the spin polarization [112]. It is clear from this equation that the vector product has sever implications on the SHE and ISHE. These effects can only occur in if the spin polarization is perpendicular to both the charge current and the spin current density. Therefore, only an out-of-plane spin polarization can lead to SHE or ISHE within two dimensional materials. A very recent theoretical study investigated the SHE in graphene in proximity to a TMDC layer. Due to a sizeable valley-Zeeman SOC term, considerable spin Hall angles were found [39].

1.4.1. Spin hall injection and inverse spin Hall detection

The combination of SHE and ISHE in a single device allows for simple generation and detection of a pure spin current. Such a device structure is shown in Fig. 1.13 and was first proposed by Hankiewicz et al. [119].

A charge current driven through the left leg of the H structure shown in Fig. 1.13 leads to a transverse spin current due to the SHE. This spin current propagates in the horizontal direction and leads therefore to a charge current in the right leg due to the ISHE. In an open-circuit configuration this charge current flows until the potential difference is large enough to counteract this charge current. The charge voltage on the right leg normalized to the charge current in the left leg is called the non-local resistance is proportional to θ_{SH}^2 .

1.5. Thermal transport in graphene

For the investigation of non-equilibrium temperature profiles appearing in graphene we shall give a short intro introduction into thermal transport.

In graphene, thermal transport can happen through the electronic system but also through phonons. The very large optical phonon energies on the order of 100 meV render them negligible at low temperatures. On the other hand, the weak interaction of the electrons with the acoustic phonons, given by a small electron-phonon coupling, allows for high intrinsic carrier mobilities up to room temperature [120, 121]. In the following a short introduction into

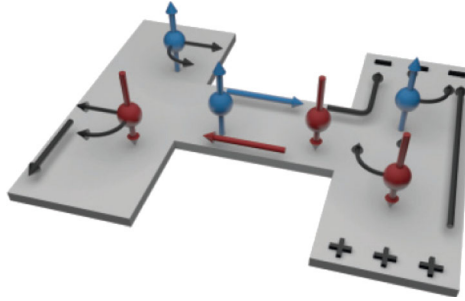


Figure 1.13. H-bar device for non-local detection: A H-bar device, proposed by Hankiewicz et al. [119], to study the SHE and the ISHE in a single device with in-situ spin current generation and detection. A vertical charge current in the left leg leads to a transverse spin current (horizontal) due to the SHE. This spin current leads then to a charge current (vertical) in the right lead due to the ISHE. In an open-circuit configuration, a charge voltage can be measured. Image adapted from Ref. [112].

thermal transport in graphene is given in several transport limits. In addition, electron-phonon coupling is discussed.

In most cases, including this thesis, thermal transport in graphene is studied in a quasi 1-dimensional system, see Fig. 1.14 (a). Generally, the graphene channel is connected to two normal metal contacts (N1 and N2) that can be biased to different potentials. Such a bias U can lead to Joule heating, that locally heats the electron system. Both contacts can be viewed as ideal reservoirs, where all incoming electrons are absorbed and only electrons with an energy distribution function given by a Fermi-Dirac distribution at the reservoir temperature are emitted. In most studies, an effective electron temperature in the graphene channel is measured by noise thermometry [122–125] or a secondary thermometer, such as the difference between the switching current and the retrapping current in a Josephson junction [126] or simply the temperature dependence of the graphene resistance itself [127] is used. An alternative approach relies on the measurement of the temperature locally with an additional contact, denoted by S in Fig. 1.14 (a).

Not only does charge transport depend crucially on different length scales, but also do characteristic lengths scale dominate the thermal transport. A peculiar situation is reached if only elastic scattering among charge carriers happens. This means that the device dimensions L, W are much shorter than the inelastic electron-electron scattering length l_{e-e} and electron-phonon scattering length l_{e-ph} . In this case no Joule heating is produced inside the graphene and a double-step energy distribution function as shown in Fig. 1.15 (a)

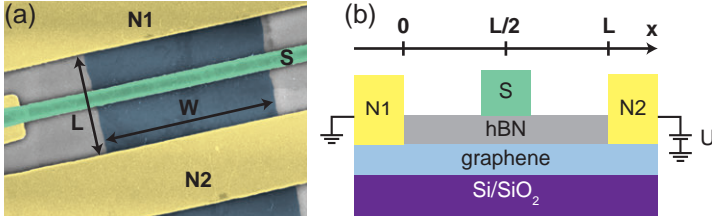


Figure 1.14. Experimental layout to study thermal transport in graphene: The temperature in the middle of the graphene device can be measured with the additional contact S . A false colour scanning electron micrograph is shown in (a), where $L = 2.5 \mu\text{m}$ and $W = 4 \mu\text{m}$. (b) shows a schematic cross section of the device. N1 is grounded whereas N2 is put at an electrical potential U to apply a Joule heating power.

results. If the device is large, such that $L_{e-e} < L, W < l_{e-ph}$, electron-electron scattering leads to Joule heating dissipated only into the electron system. This regime is also called hot electron regime and the corresponding energy distribution function inside the graphene is shown in Fig. 1.15 (b). The energy distribution function is well described by a Fermi-Dirac distribution at an effective electron temperature that depends on the position in x -direction. In very long graphene channels, where $L > l_{e-ph}$ the electron and lattice temperature equilibrate by phonon emission and most of the Joule power is dissipated to the lattice. Here, the electron-phonon coupling is the bottleneck in cooling to the substrate [128]. In this regime, the energy distribution function is also described by a Fermi-Dirac distribution with (nearly) constant temperature along the graphene channel, see Fig. 1.15 (c).

1.5.1. Heat diffusion equation

Thermal transport can be described by the continuity equation for heat, which relates the difference of the change of energy density (here heat) over time and the gradient of the heat current to the local sources and sinks:

$$\rho c_p \frac{\partial T_e(x, t)}{\partial t} - \frac{\partial}{\partial x} \left(\kappa \frac{\partial T_e(x, t)}{\partial x} \right) = P - P_{ph}, \quad (1.51)$$

where ρ is the mass density, c_p is the specific heat capacity, $T_e(x, t)$ is the electron temperature, κ is the heat conductivity, P is the Joule heating power per unit area and P_{ph} is the cooling power per unit area of the phonons. In steady state, $\frac{\partial T_e(x, t)}{\partial t} = 0$, and using the Joule heating $P = U^2/R$ and the

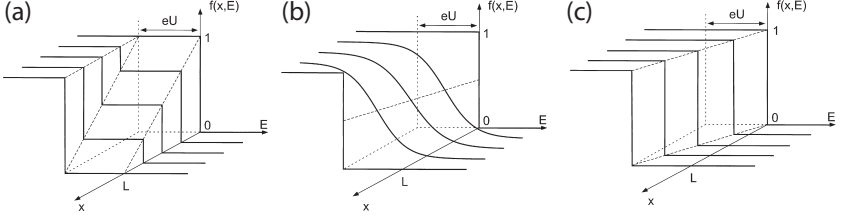


Figure 1.15. Non-equilibrium distribution functions: Different distribution functions are found in a 1-dimensional wire placed between two reservoirs at different electrical potential. **(a)** shows the distribution function in the absence of inelastic scattering, where the total energy of each quasiparticle is conserved along the 1-dimensional channel and relaxation only occurs in the reservoirs. Here, neither the electron temperature nor the electrochemical potential is defined. **(b)** shows the distribution function in the case of strong quasiparticle scattering where local thermal equilibrium is achieved but phonon scattering is negligible. **(b)** In the case of very strong phonon scattering, the quasiparticles thermalize with the phonons and a constant temperature along the 1-dimensional wire is found. Adapted from Pothier et al. [129, 130].

device dimensions W, L as defined in Fig. 1.14 one arrives at

$$\frac{U^2}{R} = -LW \frac{\partial}{\partial x} \left(\kappa_{WF}(x) \frac{\partial T_e(x)}{\partial x} \right) + LW \cdot \Sigma_{ep} (T_e(x)^\delta - T_0^\delta), \quad (1.52)$$

where the Joule heating on the left side is balanced by cooling through electron diffusion (first term on the right) and cooling through electron-phonon coupling (second term on the right). Here, U is the heating bias applied across the device resistance R and T_0 is the phonon temperature. Furthermore, the electron cooling is connected to the Joule heating through the Wiedemann-Franz law $\kappa_{WF}(x) = \mathcal{L}_0 T_e(x) L / (WR)$, where $\mathcal{L}_0 = \frac{\pi^2 k_B^2}{3e^2}$ is the Lorenz number. The electron-phonon cooling can be parametrized through the coupling constant Σ_{ep} and the exponent δ , which can depend on temperature and device properties as shown below. If the explicit form of the Wiedemann-Franz law is plugged into Eq. 1.52, one arrives at the following relation

$$\frac{\partial^2 T_e(x)}{\partial x^2} = \frac{1}{T_e(x)} \left[-\frac{U^2}{L^2 \mathcal{L}_0} + \frac{RW}{L \mathcal{L}_0} \Sigma_{ep} (T_e(x)^\delta - T_0^\delta) - \left(\frac{\partial T_e(x)}{\partial x} \right)^2 \right], \quad (1.53)$$

which can be used to numerically solve for $T_e(x)$.

In the absence of phonon cooling (e.g. $T_e(x) \sim T_0$ or $\Sigma_{ep} \rightarrow 0$), the above

equation reduces to

$$\frac{\partial^2 T_e(x)}{\partial x^2} = \frac{1}{T_e(x)} \left[-\frac{U^2}{L^2 \mathcal{L}_0} - \left(\frac{\partial T_e(x)}{\partial x} \right)^2 \right], \quad (1.54)$$

which has the analytical solution

$$T_e(x) = \sqrt{T_0^2 + \frac{x}{L} \left(1 - \frac{x}{L} \right) \frac{U^2}{L_0}}, \quad (1.55)$$

where the temperature at the electrodes $T_e(x=0) = T_e(x=L) = T_0$ is used as a boundary condition. The electron temperature given in Eq. 1.55 corresponds to the effective electron temperature that describes the energy distribution functions shown in Fig. 1.15 (b).

On the other hand if electron cooling is negligible (e.g. very large contact resistance or superconducting contact materials that suppress cooling through electron diffusion) Eq. 1.52 reduces to

$$\frac{U^2}{R} = \frac{RW}{L\mathcal{L}_0} \Sigma_{ep} (T_e(x)^\delta - T_0^\delta), \quad (1.56)$$

which has the very simply solution

$$T_e(x) = \sqrt[\delta]{\frac{U^2}{RLW\Sigma_{ep}} - T_0^\delta}, \quad (1.57)$$

that is independent of x . In this case, there will be a discontinuity of the temperature across the contact to the graphene. In a simple case where $T_0 \rightarrow 0$ K and assuming $\delta = 4$ (clean limit, see below), the transition between electron cooling and phonon cooling happens at a bias voltage $U_\Sigma = \mathcal{L}_0 / \sqrt{4RLW\Sigma_{ep}}$ [131]. For typical devices with dimensions on the order of μm , device resistance of $\text{k}\Omega$ and an electron-phonon coupling of around $30 \text{ mWK}^{-4} \text{ m}^{-2}$ [125] the crossover voltage is on the order of mV .

1.5.2. Cooling by phonons

In the following, the coupling of the electronic system to the lattice is discussed for low temperature, where only acoustic phonons need to be considered as the optical phonon energy is on the order of 100 meV [132]. The total heat flux between the electrons and longitudinal acoustic phonons takes the general form

$$P(T_e, T_0) = A\Sigma(T_e^\delta - T_0^\delta), \quad (1.58)$$

where A is the area of the graphene, Σ is the coupling constant between the electrons and the phonons and T_e and T_0 are the temperature of the electrons

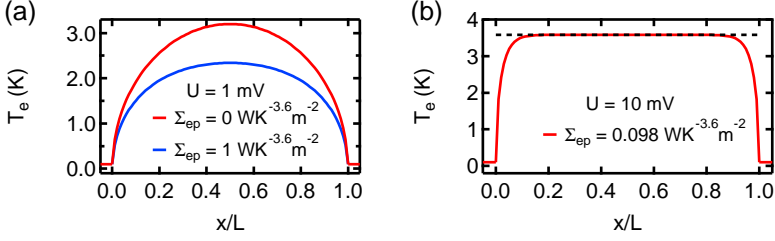


Figure 1.16. Temperature profiles: Numerical solutions to Eq. 1.53 are shown for different limits. (a) shows the hot electron regime, where the red solid line corresponds to the analytical solution shown in Eq. 1.55. A finite electron-phonon coupling reduces T_e . Here, $R = 4.1 \text{ k}\Omega$, $W = 2 \text{ }\mu\text{m}$, $L = 3.4 \text{ }\mu\text{m}$ and $\delta = 3.6$ was used. (b) shows the T_e in the phonon-cooled regime, where $R = 17.2 \text{ k}\Omega$, $W = 6 \text{ }\mu\text{m}$, $L = 100 \text{ }\mu\text{m}$ and $\delta = 3.6$ were used in the numerical calculation. The black dashed line corresponds to the temperature given by Eq. 1.57.

and phonons, respectively [133]. In the limit of $T_e \gg T_0$, the cooling power takes the approximate form of $P \approx \Sigma T_e^\delta$, that allows to extract the power δ and electron-phonon coupling Σ easily. The form of δ and Σ depend on temperature of the electron system with a crossover at the Bloch-Grüneisen temperature $T_{BG} = 2s\hbar\sqrt{\pi n}/k_B$, where $s = 2 \times 10^4 \text{ m s}^{-1}$ is the speed of sound in graphene, n is the carrier density and k_B is Boltzmann's constant. For a reasonable doping of $n \sim 1 \times 10^{12} \text{ cm}^{-2}$, T_{BG} is estimated to be around 50 K. Below T_{BG} the most energetic thermal phonons have a momentum, which is much smaller than $\hbar k_F$ and therefore scattering events of electrons with phonons can only lead to small angle scattering. On the other hand, large angle scattering, leading to momentum relaxation can occur at temperature above T_{BG} . This will also modify how energy is transferred from the electron to the phonon system and vice versa. In the following we only focus on the regime $T < T_{BG}$.

The electron-phonon coupling can strongly be modified by electronic disorder if the wavelength of the thermal phonons become comparable to (or longer than) the electronic mean free path. This condition results in two regimes; the clean limit where the mean free path is much longer than the phonon wavelength and the dirty limit where the mean free path is much short than the phonon wave length.

Here, we focus only on $T < T_{BG}$ as the experiments in chapter 4 were carried out at cryogenic temperatures ($T \sim 1 \text{ K}$). In the clean limit and assuming a weak screening, the total cooling power due to electron-phonon interaction is

given as [133]

$$P(T_e, T_0) = A\Sigma_1(T_e^4 - T_0^4), \quad \Sigma_1 = \frac{\pi^2 D^2 |E_F| k_B^4}{15\rho_M \hbar^5 v_F^3 s^3}. \quad (1.59)$$

Here, D is the deformation potential that characterized the strength of the electron-phonon coupling, $\rho_M = 7.6 \times 10^{-7} \text{ kg m}^{-2}$ is the mass density of graphene and the other symbols as defined above. In contrast to that, the cooling power due to the electron-phonon interaction in the dirty limit is [133]

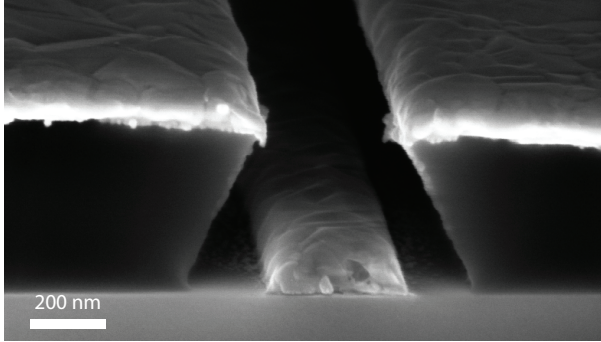
$$P(T_e, T_0) = A\Sigma_2(T_e^3 - T_0^3), \quad \Sigma_2 = \frac{2\zeta(3)D^2 |E_F| k_B^3}{\pi^2 \rho_M \hbar^4 v_F^3 s^2 l_{mfp}}. \quad (1.60)$$

Here, $\zeta(n)$ is the Riemann zeta function with $\zeta(3) \approx 1.2$. In the dirty limit, the power law of the cooling power is reduced by one and the electron-phonon coupling is changed accordingly. The crossover between these two regimes is characterized by T_x , at which the cooling power of the clean and dirty limit is equal. This temperature is given by

$$T_x = \frac{30\hbar s \zeta(3)}{\pi^4 k_B l_{mfp}}. \quad (1.61)$$

Graphene samples on SiO_2 substrate generally show a mean free path on the order of 30 nm, which leads to a crossover temperature $T_x \sim 1 \text{ K}$. Experimentally, the different cooling regimes can be accessed by varying the electron temperature and the heating power (e.g. Joule heating) applied to the electronic system. The power law can easily be extracted by a log-log plot, where the heating power is plotted as a function of electron temperature. The slope of this corresponds to the power δ in Eq.1.58.

2 Experimental methods



This chapter is devoted to the description of a few important experimental methods. First, the concepts of the most important fabrication techniques are introduced. The second part focusses on the electrical measurements. The key features of the cryogenic set-ups that were used are described and a typical measurement scheme is presented¹.

¹An SEM image of a cross section of a Pd/Pb/In-test evaporation with ZEP resist is shown.

2.1. Sample fabrication

The sample fabrication is the start of every project within this thesis. None of the presented measurements would have been possible without previous fabrication of a suitable sample. In the following sections, the most important fabrication techniques are introduced. First, the isolation of thin 2-dimensional materials is described. Then their assembly into vdW-heterostructures is presented followed by a short introduction to the fabrication of suspended samples. As a last part CVD materials and the related fabrication techniques are presented. To complete a device, standard nanofabrication procedures have been used such as electron beam lithography, UV-lithography, reactive ion etching, metallization with thermal, e-gun and sputter deposition as well as wet chemical processes. It would go beyond the scope of this thesis to cover all these techniques in detail. All the detailed fabrication recipes can be found in the appendix A.

2.1.1. Exfoliation

The basis for many results described in this thesis is the isolation of various 2D materials in the form of thin layers down to the single layer limit (one atom thick). The break-through in the isolation of single layer graphene in 2004 by Novoselov and Geim et al. [21] started the whole field of 2D materials. Soon after the discovery of graphene the family of 2D materials was extended to hBN, TMDCs and complex oxides [134].

Fig. 2.1 shows example exfoliations of graphene, hBN and WSe₂. In general Nitto² tape was used for exfoliation. Graphene was either exfoliated from highly-oriented pyrolytic graphite (HOPG) grade ZYA³ or from natural graphite flakes⁴. The hBN was exfoliated from high quality crystals grown by K. Watanabe and T. Tanaguchi [135]. WSe₂ was exfoliated from commercially available sources⁵. Whereas the determination of the thickness by optical contrast (e.g. number of layers) works very well for graphene and WSe₂ down to the single layer limit, thin hBN flakes are invisible on 300 nm SiO₂ atop Si. Special tricks, such as the usage of thinner SiO₂ layers or the usage of colour filters, have to be used [136]. Contrast enhancement was also used for graphene flakes exfoliated on top of polymer layers (e.g. PMMA or LOR).

2.1.2. vdW-heterostructures

The fabrication process of vdW-heterostructures is schematically shown in Fig. 2.2 and is based on the technique introduced by Wang et al. [137] and

²SPV 224P, Nitto Europe NV

³Obtained from hq graphene.

⁴Obtained from NGS.

⁵Obtained from hQ graphene or Nanosurf, see section 7.6 for a comparison.

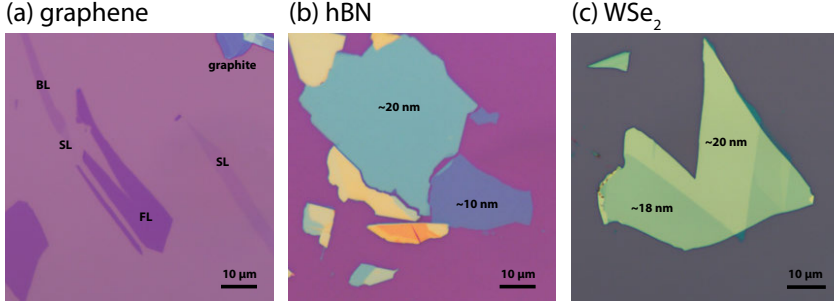


Figure 2.1. Exfoliation of 2D materials: (a) to (c) show different 2D materials exfoliated onto Si wafers with 300 nm of SiO_2 being responsible for the interference contrast. Graphene is easily visible down to a single layer (SL). Bilayer (BL) and few layer (FL) are also easily distinguishable. Due to the large band gap of hBN, only thicker flakes (> 5 nm) are visible on this substrate. Different WSe_2 thicknesses result in different optical contrast though less pronounced as for graphene and hBN.

Zomer et al. [138]. In general, any vdW-crystals can be stacked together but for the sake of simplicity the procedure will be described for a hBN/Gr/ WSe_2 heterostructure. It starts with the preparation of a polycarbonate (PC) film on a glass slide. Using an adhesive tape with a window a PC membrane is transferred and fixed on top of a PDMS stamp placed on glass slide as shown in (a). The glass slide with the PC/PDMS stamp is then mounted on a xyz-stage of a home-built transfer microscope.

The top layer (hBN) of the vdW-heterostructures is exfoliated on clean Si/ SiO_2 wafer and suitable flakes are located optically. After mounting the wafer piece with the desired top flake in the transfer stage, a clean area on the PC film is located and the flake is picked up, see (b). Detailed description of this process will be given for the pickup of the graphene flake (next step).

Similarly, the next layer (graphene) is exfoliated on a clean substrate as well, see (c). Again the flakes are located by optical means and the thickness is estimated from the optical contrast, which works quite reliable for graphene. The wafer piece with the graphene flake is then mounted on the xy-stage, which includes a roll and pitch degree of freedom as well. These two parameters can be used to control the relative alignment of the bottom stage to the top translation stage. The two flakes are then aligned relative to each other and the PC/PDMS stamp is lowered until it touches the bottom wafer. Then, the PC/PDMS stamp is further lowered until the meniscus, separating the region where the PC is in contact with the wafer and where it is just before

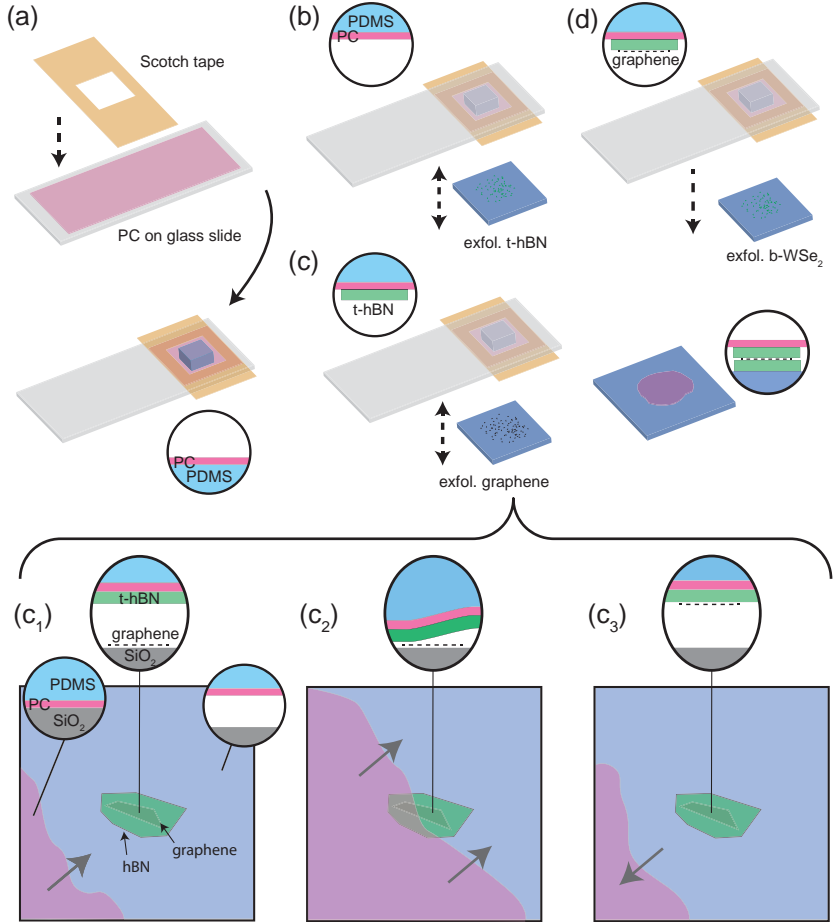


Figure 2.2. Dry stacking of vdW-heterostructures following the method introduced by Wang et al. [137] and Zomer et al. [138] (a) preparation of the PC/PDMS stamp. First, the top hBN is picked up (b), followed by the pick up the graphene (c), which is released on the bottom layer (d) by melting the PC onto the substrate. The circular insets show the detailed stacking order. Figure adapted from Ref. [48]

going into contact with the wafer, is just next to the graphene flake to be picked up. This situation is highlighted in (c_1). Then the stage is heated, which leads to the expansion of the PC film, which in turn leads to a lateral movement of the meniscus across the graphene flake bringing the top hBN into contact with the graphene (this happens around 30 °C to 60 °C, see also (c_2)). Once the meniscus passed both flakes, the temperature is increased to 80 °C, while keeping the meniscus at a fixed position. This is achieved by slowly retracting the PC/PDMS stamp. At 80 °C, the heating is turned off and while the substrate cools down, the PC/PDMS will shrink and hence retract, see (c_3). In doing so, the meniscus slowly moves across the graphene flake, which will be picked up due to the stronger interaction between the graphene and hBN or PC compared to the interaction with the SiO₂. This procedure was also used to pick-up the top hBN layer in the first place.

In a last step (d), the half stack on the PC/PDMS is released on top of the bottom WSe₂ flake previously located on the target substrate. This is done by aligning the half stack with the WSe₂ and bringing them into contact as described in (c_1 to c_2). This time the substrate is heated to 150 °C to detach the PC from the PDMS.

The adhesion of the vdW-heterostructure to the target substrate is increased by heating the complete stack, including the PC, on a hotplate at 180 °C for 3 min. Afterwards, the PC is dissolved in chloroform. An annealing step in forming gas (H₂/N₂) at 200 °C for 100 min is performed to remove polymer residues on the top and to allow the bubbles to move and coalesce in order to obtain a more homogeneous sample. In general, an AFM image is acquired to locate bubble-free regions on the vdW-heterostructure to design the device in these regions. After this treatment, the vdW-heterostructure can be further processed, including shaping into the final device geometry, fabrication of side contacts and the deposition of top gates. For all these steps standard e-beam lithography, reactive ion etching and metallization processes were used. Details can be found in the appendix A.

2.1.3. Suspended graphene samples

Freely suspended graphene samples on a lift-off resist (LOR)⁶ were fabricated following a recipe by Maurand et al. [139], which itself is based on the pioneering work by Tombros et al. [140]. The fabrication process is schematically depicted in Fig. 2.3 (a) to (c). It all starts with the fabrication of a bottom gate structures which afterwards are covered by LOR. Graphene is then deterministically transferred employing a wet transfer method [121] on top of the bottom gates. A double layer system of Dextrane/PMMA is used on which graphene was exfoliated. The dissolution of the dextrane layer in

⁶LOR 5A, MicroChem Corp.

water released the PMMA membrane with the graphene floating on top of the water. This PMMA layer can then be fished out with a volcano, which is later mounted on a transfer microscope to deterministically transfer the graphene on top of the bottom gate structure. Employing standard e-beam lithography palladium contacts are fabricated. If needed, the graphene can be shaped by an oxygen plasma. In order to suspend the graphene devices, the LOR below the graphene and the contacts is exposed in an e-beam step. This procedure results in freely suspended graphene and contacts, which are a key ingredient to achieve ultra-high mobility graphene devices with a large yield (at least in a two terminal configuration).

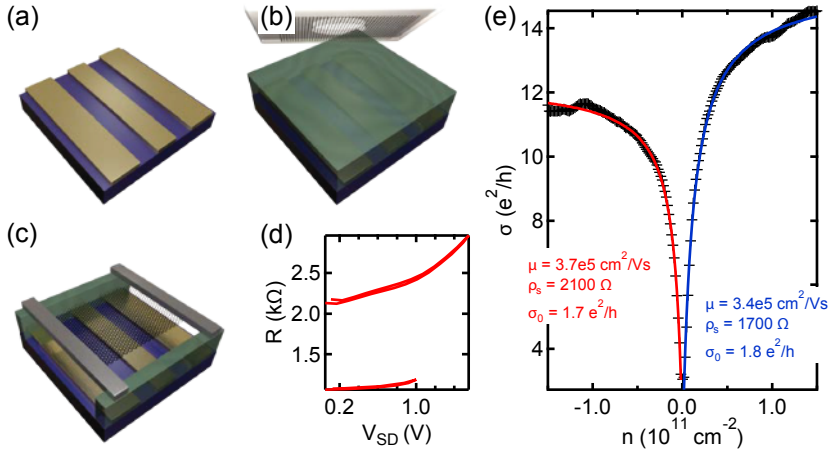


Figure 2.3. Fabrication of suspended graphene following the method introduced by Tombros et al. [140] (a-c) Fabrication of bottom gates on which LOR resist is deposited. Graphene is then transferred deterministically and suspended with free-standing contacts. (d) shows typical current annealing curves and (e) shows a gate dependence after a successful current annealing. Fabrication images are adapted from Ref. [141].

Current annealing was performed at low temperatures in vacuum or in a low pressure He atmosphere by ramping up the DC voltage across the device. A successful current annealing step was confirmed by a gate trace as shown in (e), which yielded field effect mobilities of around $350\,000 \text{ cm}^2 \text{ V}^{-1} \text{ s}^{-1}$. At the same time, clear Fabry-Pérot oscillations were observed in these devices demonstrating ballistic transport over the full device length ($\approx 1.2 \mu\text{m}$). Details on the fabrication and limitations of suspended graphene samples are shown and discussed in Ref. [141].

2.1.4. CVD materials

In this thesis CVD graphene and hBN were used for several different projects. The CVD graphene was grown in-house by Kishan Thodkar on copper substrate. The CVD hBN came either from a commercial source (Graphene Supermarket [142]) or from collaborators (the Zhang group in Beijing [143] or the Hofmann group in Cambridge [144]). The commercial hBN and the hBN from the Zhang group were grown on copper substrate, a weakly interacting growth substrate [145]. In contrast to that, the hBN grown in Hofmann's group came on iron as the growth substrate, which is a strongly interacting catalyst system [145, 146].

The most generic transfer process is schematically shown in Fig. 2.4, often referred to as a wet transfer. It all begins by depositing a supporting layer on top of the CVD material and by removing the CVD material from the other side of the growth substrate (the CVD material grows everywhere on the growth substrate), see also Fig. 2.4 (a). Most often PMMA is used as a supporting layer. In a second step the growth substrate is etched by wet chemical means, see Fig. 2.4 (b). To etch copper ammonium persulfate $((\text{NH}_4)_2\text{S}_2\text{O}_8)$, a very strong oxidizer is often used. Additionally, copper can also be etched by iron chloride or acidic hydrogen peroxide solutions. We mostly etched copper by ammonium persulfate as this lead to the cleanest devices. Once the growth substrate is completely dissolved, the CVD material attached to the supporting layer is brought to deionized water. This step is repeated several times to rinse the CVD material and to remove remaining etchant solution, see Fig. 2.4 (c). In a final step the CVD material is transferred to the target substrate by fishing it out as shown in Fig. 2.4 (d). After the sample is completely dry, the supporting layer can be removed. If it is PMMA it is simply dissolved in acetone. This wet transfer technique has been widely used in several parts of this thesis and detailed fabrication protocols can be found in the appendices A and B.

Many alternative transfer protocols have been developed over time. Another widely used technique is the so called bubbling-technique [147, 148] where the growth substrate is used as an electrode in water hydrolysis. Depending on the polarity of the applied voltage either hydrogen or oxygen is created at the growth substrate. The gas is produced between the conducting growth substrate and the CVD material. The emerging bubbles at this interface separate the CVD material from the growth substrate. This technique was used for hBN grown on iron substrate [144]. Further strategies rely on the weakening of the catalyst/CVD material interaction with subsequent detaching of the CVD material from the growth substrate by mechanical means [149].

Some of the projects required multiple layers of CVD hBN deposited onto the sample. Especially for tunnel barriers used in spin valves (see chapter 5) and for the superconducting tunnel spectroscopy devices presented in chapter 4

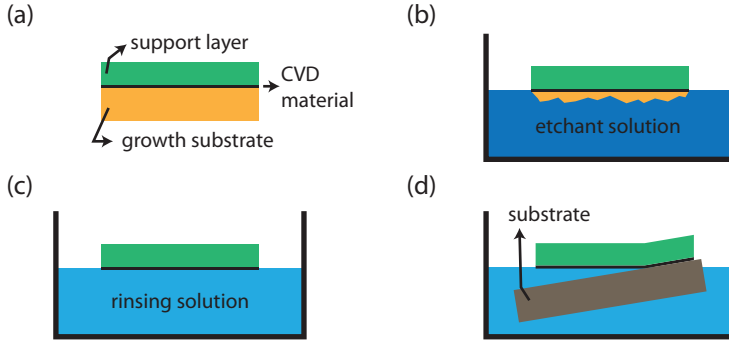


Figure 2.4. Transfer process of CVD materials: A support layer (e.g. PMMA) is deposited on the CVD grown material and on the backside of the growth substrate (e.g. copper) the CVD material is removed by reactive ion etching. (b) the growth substrate is removed in an appropriate etchant solution. After rinsing in water (c) the CVD material can be fished by the target substrate and the support layer can be removed with solvents.

two-layer CVD hBN was used. The first layer of CVD hBN was prepared according to the description above up to the state where it was floating on the water bath before fishing out. Instead of the target substrate, it was fished out by another piece of growth substrate covered with CVD material (in this case copper with CVD hBN). After drying and an additional heating step at 180 °C, the same etching procedure was performed again until a two-layer CVD supported by PMMA was floating on the rinsing water. This could then finally be transferred to the target substrate. In principle this technique would also allow for three-layer CVD structures or even more layers. The advantage over sequential transfers is the reduced usage of PMMA. Only the top most layer of CVD material is in touch with the supporting polymer, whereas the other layers are only in contact with the etchant solution and rinsing water bath. This ensures a cleaner fabrication process than a sequential transfer of each layer.

Recently, a completely new approach based on a dry delamination of the CVD material from the growth substrate was demonstrated for single and bilayer CVD graphene yielding exceptional device quality [150, 151]. This technique is based on a strong vdW interaction between the CVD material and a thick vdW crystal (e.g. hBN, MoS₂, ...) that is used to pick up the CVD material from the growth substrate. Therefore, the CVD material is always buried below a thick vdW crystal and it cannot be used for tunnel barriers for example.

Similarly to the above mentioned fabrication schemes (vdW-heterostructures and suspended samples), the same nanofabrication processes were used to finalize the CVD devices. More details can be found in the appendices A and B.

2.2. Electrical measurements

Sufficiently low temperatures are needed to study various phenomena in graphene based devices. The lattice temperature but also the electron temperature has to be sufficiently low to observe quantum mechanical effects such as coherent transport phenomena or superconductivity. Throughout this thesis several cryogenic measurement set-ups have been used with base temperatures from 20 mK over 4.2 K up to room temperature. Liquid ^4He has a temperature of 4.2 K (at a pressure of 1 bar) and can directly be used to immerse a sample to cool it to 4.2 K. By evaporation cooling, i.e. pumping on the liquid He, latent heat is removed due to the evaporation and temperatures around 1.4 K can be reached. In combination with a heater, various temperatures can easily be achieved. Lower temperatures can only be achieved by using ^3He instead of ^4He . Similarly, evaporation cooling leads to base temperatures on the order of 220 mK. Since ^3He is very rare and therefore expensive, only closed systems exist and therefore continuous operation is not possible. The ^3He has to be recondensed once in a while. A continuous operation and even lower temperatures are possible by $^3\text{He}/^4\text{He}$ dilution refrigerators. Their working principle rely on the fact that a mixture of ^3He and ^4He spontaneously separates into a ^3He -rich and ^3He -poor phase at ~ 870 mK [152]. Essentially the dilution of ^3He from the ^3He -rich to the ^3He -poor phase generates the cooling power [152]. Magnetic fields up to 9 T were applied with superconducting magnets. In some experiments a vector magnet was used to align the magnetic field to the in-plane direction of the sample. At room temperature an electro magnet was used to apply fields up to 500 mT in the in-plane and 800 mT in the out-of-plane direction.

It is not straightforward to connect a nanoscale device to a macroscopic measurement unit. Obviously, commercial, standardized components were used whenever possible. Along the line from the table-top measurement unit toward the device, the last commercial and standardized piece was the chip-carrier, as shown in Fig. 2.5 on the left. The sample chip was glued with silver paint into this 20 terminal chip-carrier that can be plugged into the corresponding chip-sockets in the measurement set-ups. Electrical connections from the chip-carrier to the metallic structures on the Si/SiO₂ wafers were established in a ultrasonic wedge bond process. The on-chip metallic lines then connected to the active device region as shown in Fig. 2.5 on the right for example. In the two experiments where high frequency signals were involved (spin pumping, see

chapter 6, and quantum capacitance and dissipation measurements, see chapter 8) the chip carrier and chip-socket was replaced by custom circuit boards with RF and DC connectors.

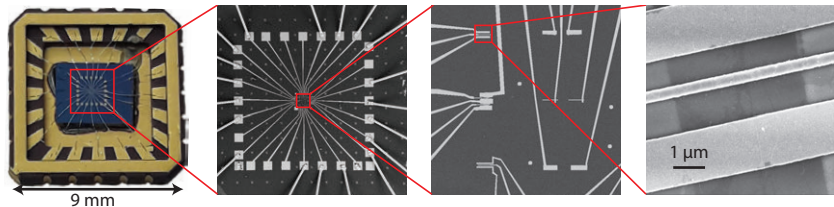


Figure 2.5. How to connect nanoscale samples to the real world: The left shows a wire bonded sample in a chip-carrier. The images to the right show scanning electron micrographs of a typical device at different magnifications. Most of the time, the active device region is on the order of $1\ \mu\text{m}$ with feature sizes down to $\sim 100\ \text{nm}$.

The device in the chip-carrier, mounted into the corresponding chip-socket in the measurement set-up, is then connected through twisted pairs to a break-out box at room temperature where BNC cables were used to connect it to measurement electronics. It is well known that the electron temperature decouples from the lattice temperature at low temperatures if not appropriate thermal anchoring and electrical filtering is performed [152]. Therefore, all measurement lines are well thermalized to the coldest spot in the cryostat (e.g. the mixing chamber in case of a dilution refrigerator). Several filter stages are employed to shield from (thermal) high frequency radiation. We typically use a two-stage filter set-up with a first, commercial filter-stage (cut-off frequency around 1 MHz) directly mounted on the break-out box. A home-built tape-worm filter with a cut-off frequency of 10 MHz is implemented directly at the cold-finger in dilution refrigerators and in the ^3He -system. The sample is shielded from thermal radiation by a Faraday cage in all set-ups. We typically reach electron temperatures below 100 mK in dilution refrigerators.

Standard low-frequency lock-in techniques⁷ were used to measure differential conductance and resistance. A typical schematics of a measurement set-up is shown in Fig. 2.6. Home-built⁸ low-noise and low-drift voltage amplifiers and I/V-converters were used in the detection chain. DC voltages were sourced either by commercially available sources (Yokogawa YK7651) or by a home-built low-noise/high-resolution DAC. AC voltages were superimposed on top of a DC voltage by the usage of a transformer. Additionally, the AC signal

⁷Using Stanford SR830 lock-ins.

⁸Designed and built by the electronics workshop at the Department of Physics, University of Basel[153].

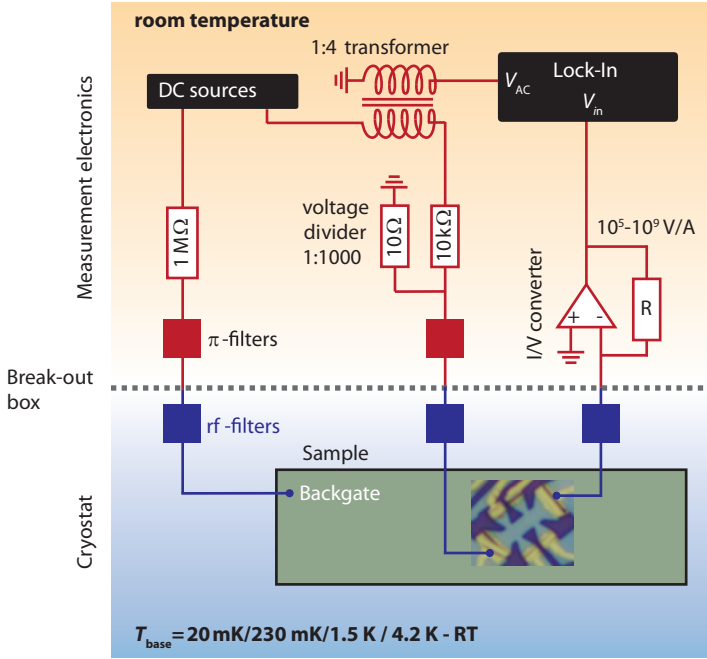
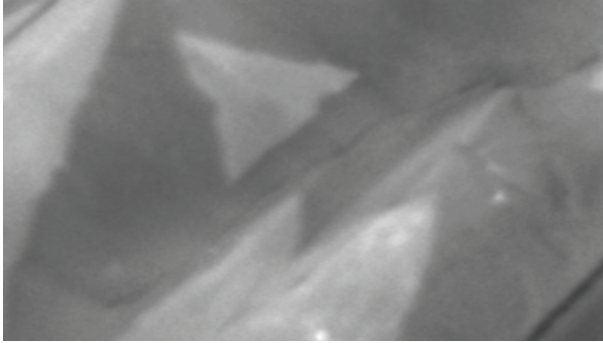


Figure 2.6. Schematics of a cryogenic measurement set-up: Schematic of a typical set-up for voltage biased differential conductance measurements at low temperature indicating the most important components. Image adapted from [84].

could also directly be applied to the device while the DC voltage required for biasing was applied to the offset voltage of the IV-converter. Small magnetic fields as required for localization measurements presented in chapter 7 were generated by replacing the standard current sources at the superconducting magnets with source meters from Keithley (2400). All measurement electronics were controlled by LabView routines or Igor Pro scripts that communicated with the instruments over RS232 or GPIB interfaces.

3 Investigation of building blocks: Ferromagnetic contacts and CVD hBN¹



In this chapter, we investigate essential building blocks for spin valve devices. Ferromagnetic contacts are widely used to inject spin polarized currents into non-magnetic materials such as semiconductors or 2-dimensional materials like graphene. The shape of the nanomagnets as well as their composition can be engineered to tailor their properties for specific applications. However, oxidation of ferromagnetic contacts poses an intrinsic limitation on device performance. In this chapter we characterize nanomagnets with magnetic force microscopy, X-ray magnetic circular dichroism imaging and we study the role of ex-situ transferred chemical vapour deposited (CVD) hexagonal boron nitride (hBN) as an oxidation barrier for nanostructured cobalt and permalloy electrodes. For efficient spin injection tunnel barriers are needed, for which we have used CVD hBN. In this chapter we investigate the quality of CVD hBN from several sources with different imaging techniques.²

¹Parts of this chapter have been published in similar form in Ref. [154].

²A photo emission electron microscopy image of an iron foil on which single layer hBN has been grown partially. The image is recorded at the L₃ edge and the hBN covered regions (e.g. the triangle in the middle) appear brighter since there the iron is less oxidized.

3.1. Introduction

The basic building blocks of a simple spin valve, a prototype spintronics device, were introduced and discussed in section 1.3. In such devices ferromagnetic contacts are used for electrical spin injection. For high performance, the magnetization in the ferromagnetic contacts needs to be controlled accurately: a *single domain structure* of the electrodes is needed, which can be achieved by taking advantage of the shape anisotropy, see section 1.3.1. As shown in section 1.3, the insertion of a *tunnel barrier* between the ferromagnetic contacts and the graphene is of utmost importance for a significant spin injection efficiency. In modern spintronics devices oxide layers are commonly used as tunnel barriers. In magnetic tunnel junctions, which probably are the most widely used spintronics devices, the oxide layer is the key ingredient for achieving large signals [155, 156]. However, high quality oxide tunnel barriers are hard to grow on 2D materials (e.g. graphene) [157, 158]. Spin injection into graphene with exfoliated hBN [159–162] as well as with chemical vapour deposited (CVD) hBN [163–165] has proven to be very efficient and versatile, see also chapter 5.

Moreover, *oxidation of ferromagnetic material* is a challenging problem in spintronics. In commercial devices, the ferromagnetic layers are always protected from oxidation by a layer of a noble metal (e.g. Ru). Recently it has been shown that a single layer of graphene is enough to protect a Ni electrode from oxidation [166]. However, an insulating coating would have the advantage that it could act as a tunnel barrier for spin injection and as an oxidation barrier at the same time. Recent experiments indicate that hBN could serve as an atomically thin oxidation barrier for nanostructured metallic contacts since it was already successfully shown for larger areas (macroscopic) and multiple hBN layers [167, 168].

In this chapter, we try to tackle the above mentioned challenges. To do so, we use different techniques and characterization methods as outlined here. A brief characterization of ferromagnetic contacts by magnetic force microscopy (MFM) and X-ray magnetic circular dichroism is given. These two characterization tools give insight into the domain structure of nanoscale ferromagnetic contacts. Then, the ability of hBN to act as an oxidation barrier for ferromagnetic nanostructures is investigated. As a characterisation tool, X-ray photoemission electron microscopy (XPEEM) was chosen. XPEEM allows to investigate the chemical state (especially the oxidation) as well as the magnetic properties of the ferromagnetic material. In contrast to spatially integrated X-ray photoelectron spectroscopy or X-ray absorption spectra (XAS) methods, XPEEM offers the advantage of high lateral resolution of about 50 nm to 70 nm [169]. Previously, XPEEM was successfully used to determine the oxide thickness of ferromagnetic materials [170, 171]. Since the quality of the involved hBN plays a crucial role, different sources of CVD hBN are compa-

red and their quality is investigated by several imaging techniques in the last section. Electrical characterization of hBN tunnel barriers are presented in chapter 5 and 4.

3.2. Characterization of ferromagnetic contacts

A schematic sketch of the samples investigated in this study is shown in Fig. 3.1 (a). Nanostructured ferromagnetic strips were fabricated by standard e-beam lithography on a Si substrate. After metallisation, half of the strips were covered with a bilayer (BL) of hBN, which was obtained from Graphene Supermarket. In (b) we show a scanning electron micrograph (SEM) of permalloy ($\text{Py} = \text{Ni}_{80}\text{Fe}_{20}$) strips covered with hBN. Having both hBN covered and uncovered regions of ferromagnetic strips on the same sample allowed for direct comparison. Further details on the fabrication procedure can be found in appendix B.

XAS were recorded at the SIM beamline at the Swiss Light Source. Linearly polarized photons with polarization axis perpendicular to the strip axis in grazing incidence were used for symmetric XAS in order to exclude any magnetic contrast. Circularly polarized photons were used for magnetic contrast imaging, probing the magnetization along the strip axis (easy axis of the nanomagnets) by taking advantage of the x-ray magnetic circular dichroism (XMCD) effect. The spectra were recorded by measuring the local intensity of photoemitted secondary electrons using XPEEM.

PEEM images were recorded as a function of photon energy. XAS can then be extracted at any point in these images. An example of a PEEM image is shown in Fig. 3.1 (c), where the Fe containing Py strips appear much brighter than the surrounding background. This image was recorded at the L_3 edge of iron ($E \approx 709 \text{ eV}$). Here, the XAS of the ferromagnetic strips were extracted by averaging over a region on the strips (see black rectangle in Fig. 3.1 (c)). The spectrum is then normalised by dividing the signal from the ferromagnet by the background signal (white rectangle in Fig. 3.1 (c) for every energy in order to compare the XAS from different samples. Furthermore, the spectra is then rescaled such that it is zero at the pre-edge ($\sim 705 \text{ eV}$, no absorption) and one at the post-edge ($\sim 727 \text{ eV}$, finite non resonant absorption), see also Fig. 3.1 (d). This normalization procedure makes the XAS from different samples directly comparable.

For each sample two independent regions were investigated (several hundred μm apart from each other). Four different regions on three different strips were used to extract the XAS signal (as in Fig. 3.1 c)) and the average of these four spectra was then used to extract the oxide thickness.

In Fig. 3.1 (d) XAS at the Fe edge are shown for $\sigma+$ and $\sigma-$ polarized light in red and blue respectively. There are two main peaks corresponding

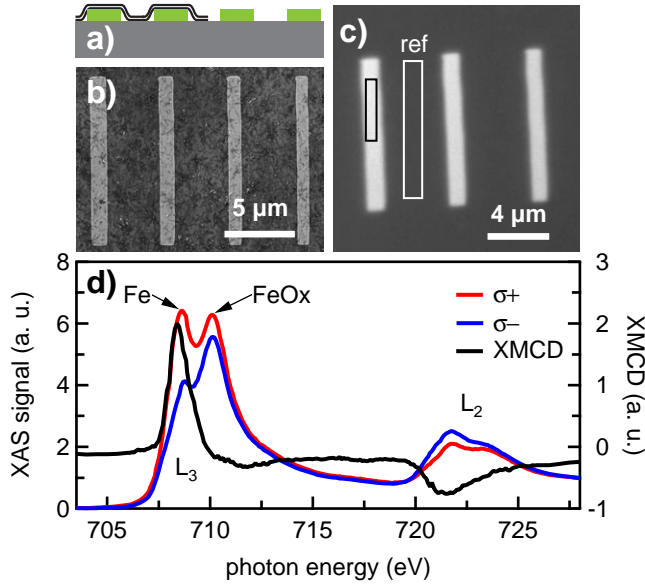


Figure 3.1. Sample design and XMCD spectra. (a) shows a schematic cross section of the samples with the silicon substrate in gray, the ferromagnetic structures in green and the hBN as black solid lines. In (b) a scanning electron micrograph of Py strips covered with hBN is shown. (c) PEEM image of Py strips without hBN at the L₃ resonance of Fe. For further data analysis, spectra (black rectangle) and background spectra (white rectangle) were extracted. In (d), we show an XAS measured with circular polarized light (blue and red curve, left axis) and the corresponding XMCD signal (black, right axis). The L₃ edge shows a double peak with a magnetic contrast only on the left peak which is due to the metallic iron. The right peak at the L₃ edge shows only weak magnetic contrast since it is mostly due an antiferromagnetic iron oxide. As expected, the magnetic contrast is inverted at the L₂ edge compared to the L₃.

to the spin-orbit splitting of the 2p core level, the L_3 edge ($E \sim 709\text{ eV}$) and L_2 edge ($E \sim 722\text{ eV}$). The two circularly polarized photons probe different transition probabilities into the spin-split 3d band and give rise to a magnetic contrast, which is given by the difference of the two XAS and is called XMCD: $(\sigma^+ - \sigma^-)$. The XMCD signal (black line) is positive at the L_3 edge and negative at the L_2 edge as expected since the average spin of the probing electron is inverted at the L_2 edge compared to the L_3 edge [172]. Two sub peaks at the L_3 edge are observed in the σ^+ as well as in the σ^- XAS signal. A large magnetic contrast is observed for the left peak, whereas the right peak only shows very weak magnetic contrast. Metallic iron gives rise to a strong magnetic contrast due to its ferromagnetic nature and therefore we ascribe the left peak to the Fe peak ($E \sim 709\text{ eV}$). Iron can form many different oxides, FeO, Fe_3O_4 , $\alpha\text{-Fe}_2\text{O}_3$ and $\gamma\text{-Fe}_2\text{O}_3$ for example. FeO and $\alpha\text{-Fe}_2\text{O}_3$ are antiferromagnetic and will not show any magnetic contrast. Fe_3O_4 as well as $\gamma\text{-Fe}_2\text{O}_3$ are ferrimagnetic and can contribute to a magnetic contrast, depending on the coupling to the ferromagnet below. Since $\gamma\text{-Fe}_2\text{O}_3$ has a spectral signature similar to Fe_3O_4 [173] it is difficult to distinguish from the latter. Therefore, we do not discriminate between the two here. Furthermore, the XMCD signal in Fig. 3.1 (d) shows a different line shape than expected for Fe_3O_4 and $\gamma\text{-Fe}_2\text{O}_3$ [174, 175]. We conclude that the left peak can be ascribed to metallic Fe and the right peak ($E \sim 711\text{ eV}$) can be ascribed to the iron oxides and therefore we will call the right peak the iron oxide peak.

3.2.1. Magnetization mapping of Py and Co contacts

As mentioned above, the XMCD signal is a measure of the magnetization of the ferromagnetic material. Fig. 3.2 shows XMCD images of Py and Co strips, where the magnetization was probed along the axis of the strips (vertical). These images are ratio images (σ^+/σ^-) and are therefore slightly different from the XMCD signal defined above. The usage of ratio images, however, has advantages as it is normalized and contains only magnetic contrast (e.g. inhomogeneous detector response cancels out).

The homogeneous response in the XMCD images clearly shows the single domain nature of the Py strips, see (a) to (c). As expected, the contrast at the Fe L_2 edge is inverted compared to the Fe L_3 edge as the average spin of the probing electron is inverted. The iron and the nickel are magnetized parallel to each other as can be seen in (c) where an XMCD image at the Ni L_3 edge is shown.

Some variation at the end of wide strips indicate the formation of closure domains. This is especially pronounced in the case of Co (d), which is known to form closure domains more easily. In addition, the magnetization of narrow Co strips breaks up into several domains, visible as segments of opposite contrast. This can be understood since Co is a magnetically harder material than Py

and is therefore less dominated by shape anisotropy. It is important to note that the strips were not magnetized prior to the measurement and a single domain would be expected after magnetizing the strips in an external field larger than their coercive field. The smeared outline of the wide Co strips in (d) can be explained by a slight misalignment of the electron optics in the PEEM.

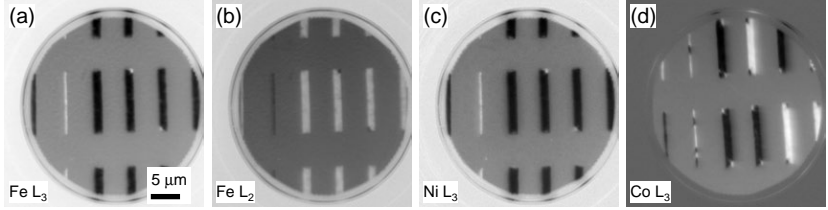


Figure 3.2. XMCD images of Co and Py contacts. (a) to (c) show XMCD images of Py contacts at the Fe L₃, Fe L₂ and Ni L₃ edge respectively. (d) shows the XMCD image of Co contacts taken at the Co L₃ edge. The magnetization was probed along the strip axis and the scale bar in (a) applies to all other sub plots as well.

3.2.2. Magnetic force microscopy

Magnetic force microscopy (MFM) can be used to image the stray field originating from ferromagnetic nanostructures (e.g. contacts for electrical spin injection). Knowledge about the magnetic stray field of ferromagnetic nanostructures can be important in their design as it can influence the properties of the sample. In principle, the direction of the magnetization can be inferred as well from the stray field. Fig. 3.3 shows the out of plane component of the magnetic stray field originating from different contact geometries and materials. The largest stray fields are observed at the end of the Co and Py contacts, see (a) and (c). If two strips face each other the magnetic stray field is strongest in the gap. The bulk of the ferromagnetic nanostructures show negligible stray fields indicating single domain magnetization. The remaining stray field shows that the magnetization does not fully lie in the plane, along the strip axis, but also has a tiny out of plane component that spatially varies. Variations are observed along the strip, but also across the width of the strip for both contact materials, see (b) and (c).

Magnetic stray fields originating from the ferromagnetic contacts itself can lead to spin dephasing if they are not collinear to the spin axis of the injected electrons (e.g. magnetization). Out of plane magnetic stray fields can also lead to orbital effects in the graphene. Therefore, ferromagnetic contacts are

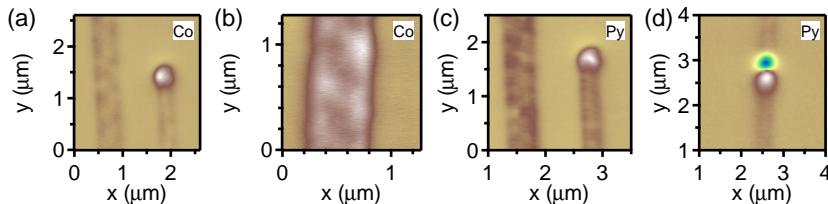


Figure 3.3. MFM of Co and Py contacts. (a) to (d) show MFM images of Co and Py contacts. The out of plane component of the stray field is colour coded in arbitrary units. The background is set to zero. MFM was performed in the Hug lab at EMPA by Johannes Schwenk.

commonly deposited over the full width of the graphene flake in order to avoid the large stray fields originating at the ends of the contacts. This restricts the possible contact configuration.

3.3. Role of CVD hBN in protecting ferromagnetic nanostructures from oxidation

In order to investigate CVD hBN as an oxidation barrier for ferromagnetic nanostructures, the XAS of Py strips at the Fe and Ni edge were recorded after 7 days in ambient conditions (7d), after 84 days in ambient conditions (84d) and after an additional 66 min on a hotplate at 200 °C in ambient conditions (84d*). For this study, devices as introduced in Fig. 3.1 were used.

A direct comparison of the XAS of a covered (w/ hBN) and an uncovered (w/o hBN) Py strip at the Fe edge is shown in Fig. 3.4 (a). The smaller iron peak at the L_3 edge for the uncovered region indicates that there is a thicker oxide layer on top of the uncovered region (black curve) compared to the hBN covered (red). A similar, but smaller effect is also observed at the L_2 edge of the iron. At the Ni edge, there is no noticeable difference between the two different regions and no sign of oxidation, see Fig. 3.4 (b). Altogether, it is clear that there is a significant difference in iron oxidation in Py strips between hBN covered and uncovered regions.

The evolution of the XAS at the Fe edge with time is shown in Fig. 3.4 (c) for an uncovered region and in (d) for a hBN covered region. It is clear that in both cases the oxide peak grows with longer oxygen exposure time. Furthermore, the L_2 resonance of Fe starts to split into two peaks as well, indicating further oxidation. However, it is also clear that the oxide peak of the hBN covered region grows slower, especially for the XAS at 84d.

To quantify the amount of oxidation for the different samples we modelled the XAS signal and fitted the measured spectra. To do so, we assumed that

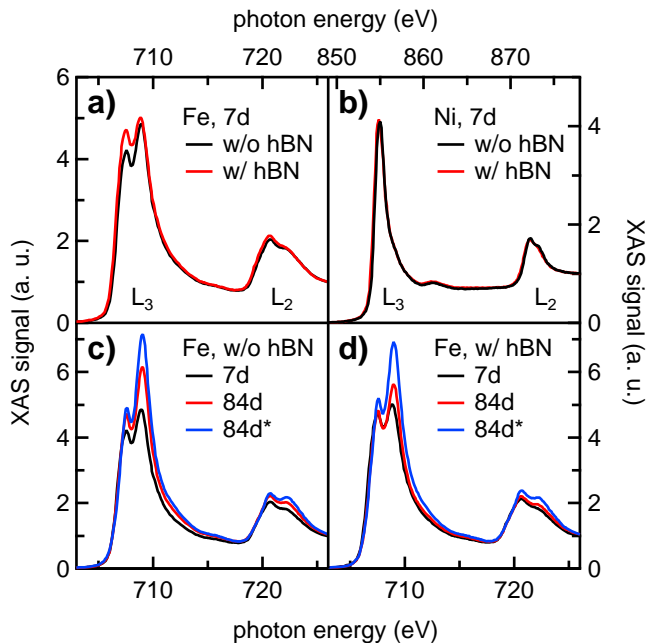


Figure 3.4. XAS spectra of Py strips. (a) and (b) show XAS of Py strips at the Fe and the Ni edge, respectively. A direct comparison of Py strips covered with hBN (red) and uncovered regions (black) are shown after storing the samples for 7 days at ambient conditions. In the case of iron (a), a pronounced difference in the spectra at the L_3 edge is observed. At the Ni-edge (b) no pronounced difference is observed. Temporal evolution of the Fe-edge is shown in (c) for an hBN covered region and in (d) for an uncovered region.

the metallic ferromagnet is covered with a layer of oxide on top. In the case of Py, we treated the iron and the nickel individually. This is justified by the relatively small Fe content of the Py that favours individual oxidation of the elements as supported by our data. In short, oxidised Fe is found to co-exist with metallic Ni in agreement with the higher oxygen affinity of Fe compared to Ni [176].

In the case of iron, a layer of Fe_2O_3 with a thickness $t_{\text{Fe}_2\text{O}_3}$ atop a layer of Fe_3O_4 with a thickness of $t_{\text{Fe}_3\text{O}_4}$ atop a Fe layer of infinite thickness was assumed. FeO was neglected since it is only stable under conditions of limited oxygen availability [170, 171]. Since Fe_2O_3 is the higher oxidised state of iron, we assume that the best model structure is given in Fig. 3.5 (c) where Fe_2O_3 is the topmost layer. Details about the fitting procedure can be found in the appendix B. We were unable to reasonably fit the measured data with a single oxide layer only. In Fig. 3.5 (a) we show a fit to a measured XAS, showing excellent agreement. By fitting the XAS for all different conditions we are able to extract the individual oxide thicknesses, which are shown in Fig. 3.5 (b). The error bars correspond to the standard deviations obtained from least square fits. The statistical error (variance between different regions) is smaller than the error obtained from the fitting and therefore the statistical contribution was neglected.

Our results show that the oxide is always significantly thinner for the hBN covered regions compared to uncovered regions, see Fig. 3.5 (b). It is also obvious that both oxide layers increase in thickness with longer oxygen exposure time. This is the case for hBN covered and uncovered regions, but more significant for the uncovered regions. Whereas $t_{\text{Fe}_3\text{O}_4}$ is similar for hBN covered and uncovered regions, the Fe_2O_3 layer is much thicker for the uncovered regions at 7 d. As the Py strips are further exposed to air (84 d), mainly $t_{\text{Fe}_2\text{O}_3}$ increases with moderate changes in $t_{\text{Fe}_3\text{O}_4}$. The oxidation is promoted by putting the sample on a hotplate at 200 °C as indicated by the increase in the oxide layer thickness and by a modification in the relative weight of the two oxides.

Similar to the Fe edge, the Ni L_3 edge was used to extract the thickness of the NiO. Higher oxidation states of nickel were neglected since they only form at higher temperatures [167]. In Fig. 3.6 (a) we show a fit to a measured XAS after 84 d in ambient conditions, showing also excellent agreement. The individual components are also shown in blue. The metallic Ni is dominating, indicating a thin NiO layer. By fitting the XAS for all different conditions, we were able to extract the individual oxide thicknesses, which are shown in Fig. 3.6 (b).

Initially, one finds no difference between hBN covered and uncovered regions in the oxidation of Ni, see Fig. 3.6 (b) at 7 d. Upon further oxygen exposure, the thickness of the NiO stays the same within the error bars for hBN covered regions. In contrast to that, Ni oxidises further in the case of uncovered Py

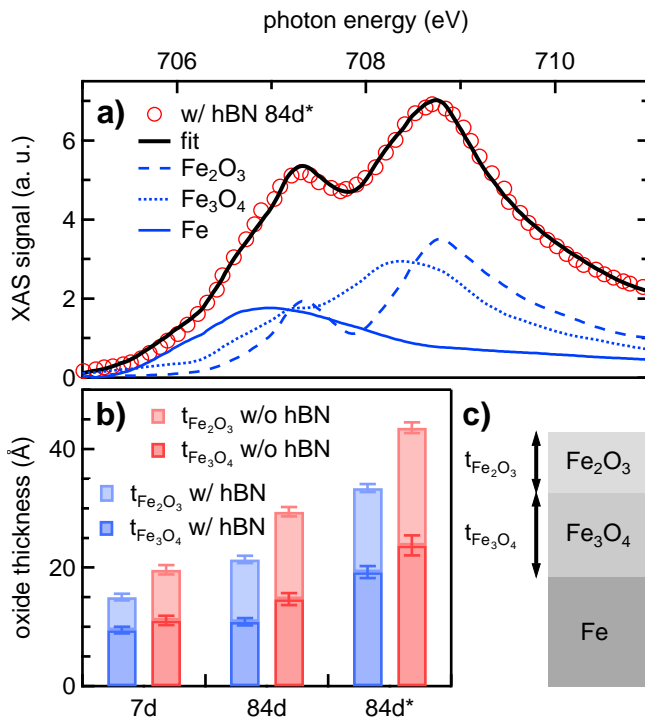


Figure 3.5. Fe oxide thickness of Py strips. The XAS at the Fe-edge for an hBN covered region was fitted as a superposition of Fe, Fe₃O₄ and Fe₂O₃ spectra to extract the corresponding oxide thicknesses $t_{\text{Fe}_3\text{O}_4}$ and $t_{\text{Fe}_2\text{O}_3}$. The individual components are shown in blue. In (b) the extracted oxide thicknesses are shown as a function of oxygen exposure time. In (c) the model structure that was used to fit the XAS is depicted.

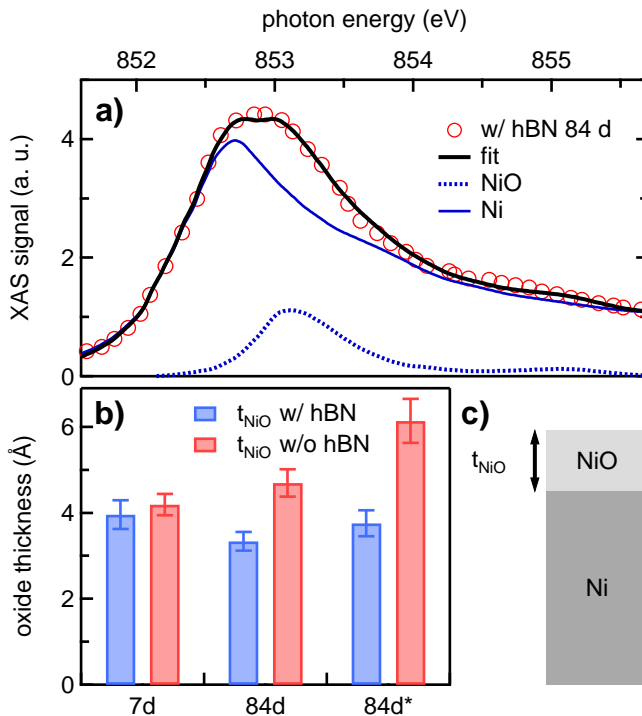


Figure 3.6. Ni oxide thickness of Py strips. The XAS at the Ni-edge for an hBN covered region was fitted as a superposition of Ni and NiO spectra to extract the oxide thickness t_{NiO} . The individual components are shown in blue. In (b) the extracted oxide thicknesses are shown as a function of oxygen exposure time. (c) Model structure used to fit the XAS spectra of the Ni-edge.

strips and t_{NiO} increases by 50 % to $6.1(5) \text{ \AA}$.

We have performed a similar analysis for hBN covered and uncovered cobalt strips, where we extracted the thickness of the CoO (t_{CoO}). Higher oxidation states of cobalt were neglected as in the Ni case. In Fig. 3.7 (a) we show a fit to a measured XAS after 84 d in ambient conditions, showing excellent agreement. By fitting the XAS for all different conditions we are able to extract the individual oxide thicknesses, which are shown in Fig. 3.7 (b).

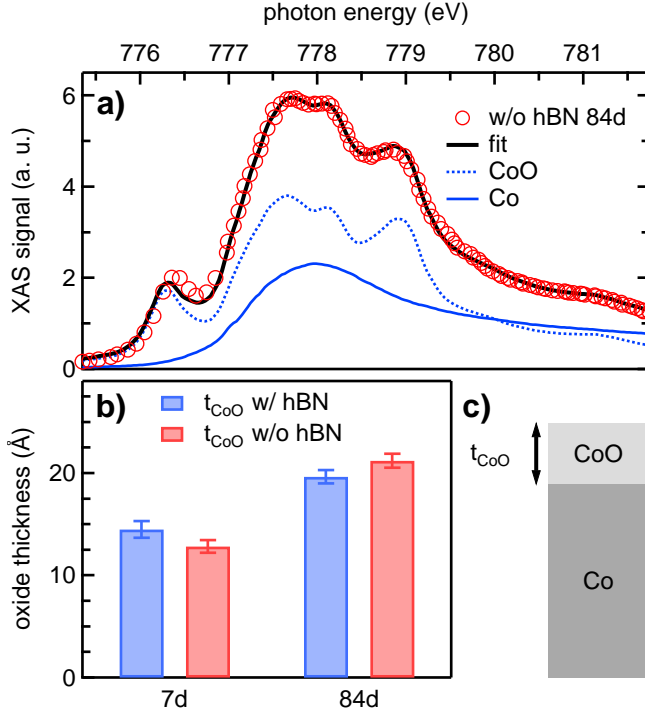


Figure 3.7. Co oxide thickness in Co strips. The XAS at the Co edge for an hBN covered region was fitted as a superposition of Co and CoO spectra to extract the oxide thickness t_{CoO} . The individual components are shown in blue. In (b) the extracted oxide thicknesses are shown as a function of oxygen exposure time. Spectra were normalised with the I_0 counts from a mirror and not with a reference area. (c) Model structure used to fit the XAS spectra of the Co-edge.

Although it is not obvious on first sight that Co strips covered with hBN

oxidise more slowly, the absolute increase of $5.1(10) \text{ \AA}$ is significantly smaller than the increase of $8.4(9) \text{ \AA}$ for the uncovered region. It is important to note that markers on the samples allowed us to look at the same location in different measurements (e.g. 7d and 84d).

Table 3.1 and 3.2 show an overview of the extracted oxide thicknesses for the different elements and samples. The difference (Δ) is calculated by subtracting the oxide thickness with hBN from the oxide thickness without hBN.

Table 3.1. Overview of the extracted iron oxide thicknesses for regions without hBN (w/o hBN), with hBN (w/hBN) and the absolute difference between these regions (Δ).

	$t_{\text{Fe}_2\text{O}_3} \text{ (\AA)}$			$t_{\text{Fe}_3\text{O}_4} \text{ (\AA)}$		
	w/o hBN	w/hBN	Δ	w/o hBN	w/hBN	Δ
7d	8.5(8)	5.6(6)	-3.0(13)	11.1(8)	9.5(6)	-1.6(14)
84d	14.7(8)	10.5(6)	-4.2(14)	14.7(10)	10.8(6)	-3.9(16)
84d*	19.8(9)	14.2(7)	-5.6(15)	23.8(17)	19.2(9)	-4.6(27)

Table 3.2. Overview of the extracted nickel and cobalt oxide thicknesses for regions without hBN (w/o hBN), with hBN (w/hBN) and the absolute difference between these regions (Δ).

	$t_{\text{NiO}} \text{ (\AA)}$			$t_{\text{CoO}} \text{ (\AA)}$		
	w/o hBN	w/hBN	Δ	w/o hBN	w/hBN	Δ
7d	4.2(3)	4.0(3)	-0.2(6)	12.8(6)	14.5(8)	1.7(15)
84d	4.7(3)	3.3(2)	-1.4(5)	21.2(7)	19.6(6)	-1.6(13)
84d*	6.1(5)	3.8(3)	-2.4(8)			

3.3.1. Discussion and interpretation of the oxidation of ferromagnetic contacts

Summarizing the data presented above, we can clearly say that there is a difference in oxidation of Fe and Ni for hBN covered and uncovered strips, namely that the hBN covered strips are less oxidised. This is most obvious when

comparing the increase in oxide thickness from 7 d to 84 d oxygen exposure time.

Ni in close proximity to Fe clearly oxidises slowly and only a very thin oxide layer forms at the top. This can easily be explained by the fact that Fe oxidises first as it has a higher oxygen affinity than the Ni [176]. Ni will then only start to oxidise if all iron in close proximity is fully oxidised.

The thin oxide layer already present at 7 d for all samples is partially due to the fabrication process used here. After evaporation in vacuum, the strips are brought to ambient conditions for around 30 min for lift-off. This is already enough for the ferromagnetic materials to oxidise to a certain depth.

Treating the Py as pure Fe for the fitting of the Fe L_3 edge probably underestimates the thicknesses of the oxides since only 20 % of the atoms in the Py are iron atoms. This might lead to extracted values that are smaller than in reality, but the change over time is still captured well. At the absorption edge of Ni, no Fe related features in absorption are expected, nor vice versa, since the energies of the photons are very different. Furthermore, the electron escape depth is similar for Fe ($\lambda_{Fe} = 15 \text{ \AA}$) and Ni ($\lambda_{Ni} = 22 \text{ \AA}$).

In the case of the Co strips, the protection of the hBN against oxidation is not obvious. The behaviour observed is attributed to the low quality of the hBN layers.

During the heat treatment at 200 °C in ambient conditions, the relative weight of the two iron oxides is most probably changed due to different activation energy in their formation. The ratio of $t_{Fe_2O_3}/t_{Fe_3O_4}$ decreased with the heat treatment indicating a shift towards Fe_3O_4 . In addition, an increased temperature also leads to a faster oxygen diffusion within the Py strip. This might be the reason why there is more Fe_3O_4 after the hotplate treatment.

We have also seen an increase in the oxide thickness for the Fe and Co in the hBN covered regions, although it is less pronounced. A defective layer of hBN with some holes or cracks would surely allow for some oxygen diffusion through the layer. In addition, grain boundaries could also allow oxygen diffusion through the layer. These two issues are related to the quality of the hBN and could be minimized by a higher quality hBN (e.g. more homogeneous layer and larger crystals). The mechanical transfer of the hBN on top of the ferromagnetic strips could also lead to cracks along the edges of the strips. This is possible since the height of the strips (30 nm) greatly exceeds the hBN thickness and therefore the hBN could rupture along this step edge. Heating the sample to elevated temperature could even promote this rupturing since the different materials involved have different thermal expansion coefficients. Moreover, oxygen diffusion along the hBN / SiO_2 interface is possible, even though long distances have to be overcome. A defective hBN layer would facilitate the diffusion along the interface since the distances can be orders of magnitude smaller.

3.4. Characterization of CVD hBN

Since the CVD hBN is a crucial part of the study presented above and it also plays a crucial role as a tunnel barrier in the following chapters, we characterized the hBN with several techniques, including PEEM, SEM and atomic force microscopy (AFM). PEEM images of hBN transferred on top of ferromagnetic strips are shown in Fig. 3.8 recorded at the boron K-edge (a) and at the nitrogen K-edge (b). Both images are edge / pre edge images where the image at the edge is divided by an image at the pre edge. This corrects for unwanted contributions from the detectors stage and it also corrects for surface effects such that the observed contrast is a pure material contrast. Furthermore, the intensity has been normalized. In both images, spatial intensity variations are clearly visible indicating an inhomogeneous hBN layer, largely varying in thickness. Similar structures are also observed in the SEM image (see Fig. 3.8 (c)). This SEM image was taken on the as-received hBN on copper foil and therefore we conclude that this inhomogeneities are not introduced by the transfer, but are rather a sign of a low quality hBN layer. AFM characterisation (not shown) reveal height variations of around 2 nm which are far from the thickness of a single layer ($\approx 3 \text{ \AA}$). From the observations, we conclude that the hBN layers have not only multilayer patches but may also have holes and cracks. The quality of the CVD hBN from Graphene supermarket was found to vary from batch to batch considerably, see Fig. 3.8 (c) and (d). In Fig. 3.8 (d). The SEM image in (d) shows a completely different hBN film of much higher quality than shown in (c). The multilayer patches are nearly absent and single layer regions were found to be much larger.

Due to the poor quality of some batches of the CVD hBN from the Graphene Supermarket, different sources of hBN were investigated. A first alternative is hBN grown on copper foil in the Zhang lab [143], Beijing. As a second alternative we investigated hBN grown on iron in Hofmann's lab [144], Cambridge.

In Zhang's lab, the hBN is grown in a copper enclosure that drastically reduces the nucleation sites and therefore leads to larger single crystals of hBN. Unfortunately, the growth speed is different for different crystal direction of the copper substrate [143]. This leads to the large variation in hBN thickness and coverage over large scales as observed in Fig. 3.9 (a). There the grain boundaries in the copper are highlighted with red arrows. On a small scale, see (b), regions with a continuous single layer hBN can be found. The grain size of the hBN can reach several microns. Few BN particles are visible that originate from the growth in a copper enclosure [143]. The size of the high quality single layer film is finally given by the size of Cu(111) grains.

hBN grown on copper interacts only very weakly with the underlying growth substrate and can therefore easily be transferred by several wet transfer techniques (e.g. etching of the growth substrate, bubbling method, interfacial oxidation of the copper and removal by a thermal release tape and many more,

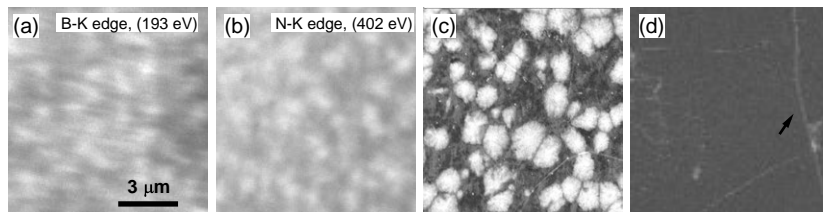


Figure 3.8. Characterization of hBN from Graphene supermarket.

(a) shows a PEEM image of CVD hBN obtained from Graphene Supermarket at the boron K-edge and (b) similarly shows a PEEM image recorded at the nitrogen K-edge. The better image quality in (b) compared to (a) is due to a better adjusted electron optics in the PEEM. The spatial variation in the PEEM images correlates well with the structural features observed in the SEM image (c), which was recorded with an acceleration voltage of 2 kV. (d) shows an SEM image of a different batch of hBN obtained from Graphene supermarket. The scale bar in (a) applies to all sub plots.

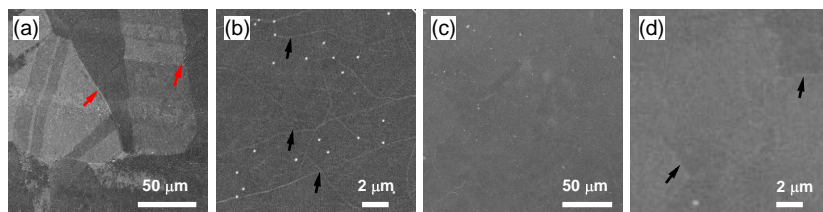


Figure 3.9. SEM images of hBN on growth substrate: (a) and (b) show CVD hBN grown on copper as received from the Zhang group, Beijing. On a large scale, inhomogeneities are observed (a), whereas on a small scale homogeneous layers are found (b). Grain boundaries between different copper crystal with different crystal orientation are indicated by red arrows. The single layer hBN grains are several micro meter large (grain boundaries are indicated with black arrows) and only few BN particles are observed (white dots). (c) and (d) show CVD hBN grown on iron as received from the Hofmann group, Cambridge. The material is grown homogeneously over large scales as well over small scales. The grains are as well several micro meter large and only very few BN particles are present.

see also section 2.1). This is a big advantage and it might lead to the innovation of novel transfer methods that preserve the high quality of the CVD grown material. A dry transfer method that keeps the interface between the CVD hBN and the graphene clean would be highly desirable. Recently, the a novel dry pick-up method for CVD graphene grown on copper was introduced, which lead to very high quality graphene devices [150].

CVD hBN grown on an iron foil by the Hofmann group grows very homogeneous over a large scale [144]. The hBN grain size is on the order of several micro meter and very few BN particles are present. The continuous high quality single layer hBN film is highly desirable for many applications. hBN grown on iron foil strongly interacts with the underlying growth substrate and is therefore hard to transfer to a different substrate. In general the bubbling technique is used [144].

3.5. Discussion, conclusion and outlook

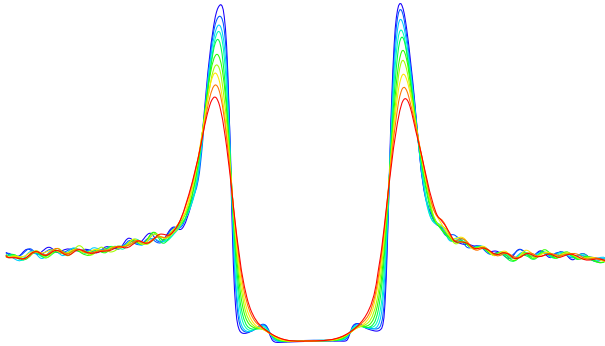
The magnetic structure of ferromagnetic nanostructures is important in the design of spintronics devices as well as in mesoscopic quantum systems. Especially stray fields might have negative influences on the performance of spin valves (source of spin dephasing) but can on the other hand can lead to novel physics. The presence of a periodically modulated magnetic field, generated by an array of nano magnets for example, is predicted to result in a large Rashba spin-orbit coupling in graphene armchair nanoribbons [177]. The contact designs investigated here showed single domain behaviour with very small stray fields along the strip axis and hence are perfectly suited for such experiments.

It was found that oxidation is a serious problem in nanostructured Co and Py electrodes exposed to ambient conditions. CVD hBN has been shown to slow down the oxidation, however full protection is not achieved. In summary, the quality and the ex-situ transfer of hBN on top of the ferromagnetic material limits the effective protection of the hBN. This could possibly be solved by an in-situ transfer of high quality hBN onto pre-patterned and pre-cleaned ferromagnetic electrodes (e.g. transfer in an UHV system with sputter cleaned ferromagnets). The perfect solution would be an in-situ growth of CVD hBN onto pre-patterned electrodes. This has become possible by the demonstration of large single crystal CVD growth of hBN on a Fe catalyst [144] and first implementations of this techniques in magnetic tunnel junctions have shown promising results [178]. This approach could be combined with the technology of inverted spin valves that have been shown the exhibit very long spin relaxation times [179, 180] and a further increase in device performance could be expected.

In general it is very challenging to grow CVD hBN uniformly over a large scale on a weakly interacting substrate. We have found that the quality of

CVD hBN grown on copper (a weakly interacting substrate) can vary from one growth batch to the next considerably. In addition, spatial inhomogeneities have been found. These two findings make it very hard for a reproducible device fabrication. The growth of CVD hBN on a more controlled substrate such as iron would solve these problems. However, it comes with the drawback of a much stronger interaction between the growth substrate and the CVD hBN and hence it is difficult to transfer to a different substrate.

4 Non-equilibrium properties of graphene probed by superconducting tunnel spectroscopy



In this chapter, superconducting tunnel spectroscopy is introduced as a powerful tool to study non-equilibrium phenomena in graphene. After a brief description of the sample and the fabrication process, the extraction of non-equilibrium energy distribution functions is explained. In a first part, this technique is then used to extract the electron temperature as a function of bath temperature. In a second part, Joule heating is applied to the sample and the dominant cooling through electron out diffusion is investigated. We observe that the cooling is mostly dominated by the Wiedemann-Franz law with some minor deviations, which will be discussed. In a third part, the electron-phonon coupling is extracted from a large-area graphene sample. Possible influences on the electron temperature are discussed in the end.

4.1. Sample overview and fabrication

A false colour micrograph of a typical device is shown in Fig. 4.1 (a) with a cross section in (b). It consists of a graphene channel of length L and width W , which is connected to two normal contacts N1 and N2 that act as ideal reservoirs: all incoming quasiparticles are absorbed and the emitted quasiparticles obey a Fermi-Dirac distribution at the reservoir temperature. In the middle of the graphene channel, a superconducting electrode S is tunnel coupled to the graphene. The CVD hBN tunnel barrier is covering the full sample.

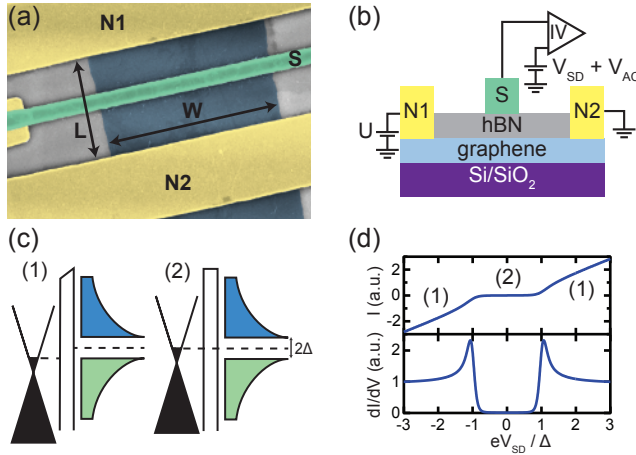


Figure 4.1. Device and working principle of superconducting tunnel spectroscopy: (a) shows a false colour scanning electron micrograph of a typical sample. The superconducting Pd/Pb/In electrode is labelled with S and the normal Cr/Au contacts are labelled with N1 and N2, respectively. (b) shows a cross section of a typical device with the measurement setup indicated. (c) and (d) show the working principle of superconducting tunnel spectroscopy with the energy diagrams in (c) and the resulting current and differential conductance in (d). Current can only flow if the bias $|V_{SD}|$ across the tunnel junction is larger than Δ/e , case (1), otherwise it is suppressed due to the gapped DoS, case (2).

Here, we used CVD graphene that was in-house grown by Kishan Thodkar. After the transfer from the growth substrate to a Si/SiO₂ wafer it was structured by e-beam lithography and reactive ion etching into the desired shape. The CVD hBN layer was transferred after a thermal annealing in forming

gas. Commercial hBN obtained from Graphene Supermarket [142] was used for device A and D, whereas hBN from the Hofmann group [144] was used for device B and C. In the case of device A and D a two layer CVD hBN was used. Single layer hBN was used for device B and C. An overview of all devices can be found in Tab. 4.1. In a next step, the normal contacts were fabricated. Quasi 1-dimensional Cr/Au side contacts were achieved by a short plasma etching before the metal deposition. The CHF_3 based plasma removed the hBN, as well as partially the graphene. It turned out that these quasi 1-dimensional side contacts are less reproducible than the 1-dimensional contacts to "bulk" hBN/Gr/hBN vdW-heterostructures. A significant increase in the number of working contacts was achieved by redeveloping the PMMA mask after the CHF_3 plasma. We attribute this to the fact that the overlap of the metal with the graphene channel is increased. In a last step, the superconducting electrode was deposited. Here, we used an optimized three layer structure consisting of 5 nm Pd as wetting layer, 110 nm of Pb and 20 nm of In as a capping layer [181]. Pb was chosen because of its large superconducting gap that allows thermometry up to several kelvins.

Table 4.1. Overview of all devices: L and W are specified in Fig. 4.1, A_T denotes the area of the tunnel contact and $R_T A_T$ specifies the tunnel resistance area product of the tunnel contact.

	L (μm)	W (μm)	$R_T A_T$ ($\Omega \mu\text{m}^2$)	A_T (μm^2)	hBN source
A	3.4	2	90×10^3	0.7	2-layer, comm. ¹
B	1.3	4	470×10^3	1.4	1-layer, collab. ²
C	100	6	$\leq 40 \times 10^3$	2.1	1-layer, collab.
D	2.5	1	1.8×10^6	0.35	2-layer, comm.

4.2. Working principle of superconducting tunnel spectroscopy

Superconducting tunnel spectroscopy is a powerful tool to access the energy distribution function as introduced by a pioneering work by Pothier et al. [129, 130] on copper wires. Later, this technique was also used to study electron relaxation rates in carbon nanotubes [182]. The current through a superconductor (S)/insulator (I)/graphene (gr) junction is given by

$$I(V) = \frac{1}{eR_T} \int_{-\infty}^{+\infty} dE n_s(E - eV) \cdot n_{gr}(E) \cdot [f_{gr}(E) - f_S(E - eV)], \quad (4.1)$$

¹hBN was obtained from Graphene Supermarket [142].

²hBN was obtained from the Hofmann group, Cambridge [144].

where R_T is the tunnel junction resistance, $n_s(E)$ is the superconducting density of states with an energy gap of Δ , $n_{gr}(E)$ is the density of states of graphene and $f_s(E)$, $f_{gr}(E)$ are the energy distribution functions in the superconductor and in the graphene, respectively [183]. An energy diagram of the tunneling process is shown in Fig. 4.1 (c) next to the tunnel current, see Fig. 4.1 (d). The density of states of the graphene $n_{gr}(E)$ can be assumed as a constant for small biases on the meV-scale. If $k_B T \ll \Delta$, then the energy distribution function in the superconductor is well described by the Heavyside function $\Theta(E - eV)$ instead of a Fermi-Dirac distribution $F(E - eV)$. The differential conductance is then readily obtained as [129, 183]

$$\frac{dI}{dV}(V) = \frac{1}{R_T} \int_{-\infty}^{+\infty} dE \frac{dn_s}{dE}(E - eV) (1 - \Theta(E - eV) - f_{gr}(E)). \quad (4.2)$$

The differential conductance of a S/I/Gr-junction is schematically shown in Fig. 4.1 (d). The energy distribution function $f_n(E)$ can be obtained by a deconvolution of the measured $dI/dV(V)$ using Eq. 4.2. It is obvious from Eq. 4.2 that if the distribution function in the normal metal is also a Heavyside function (i.e. a very cold Fermi gas), then the dI/dV is directly proportional to the DoS of the superconductor. We would like to note here, that the exact form of the distribution function in the superconductor does not alter the $dI/dV(V)$, see also section D.1.

Fig. 4.2 (a) shows the differential conductance measured from the superconductor to the graphene with N1 and N2 grounded as a function of the spectroscopy bias V_{SD} and back gate voltage V_{BG} . A clear superconducting gap is observed. Since there are some resonances tuned by both V_{BG} and V_{SD} , an averaging over 5 V in V_{BG} is performed that is shown on the right. These resonances most probably originate from universal conductance fluctuations (UCFs). As stated above, this measurement resembles the DoS of the superconductor. A zoom in of the same measurement is shown in Fig. 4.2 (c). It is obvious that this DoS cannot be described by a standard BCS DoS as expected for a superconductor. The deviation is attributed to the averaging that is needed to get rid of the fluctuations present in (a). This averaging then leads a much broader peak at the gap edge than predicted by a BCS or a Dynes [184] density of states. We, therefore, use the lowest temperature and zero heating bias U measurement as the DoS of the superconductor, which is a fair assumption as explained above.

All measurements shown in here were carried out in a dilution fridge at very low temperatures of ~ 50 mK. The electrical measurement scheme is described in more detail in section 2.2. Very low AC excitation voltages on the order of $k_B T/e$ have been used in order to maximize the energy resolution.

The presence of a finite heating bias U across the graphene channel (applied between N1 and N2, see Fig. 4.1 (b)) drives the electronic system out-of-

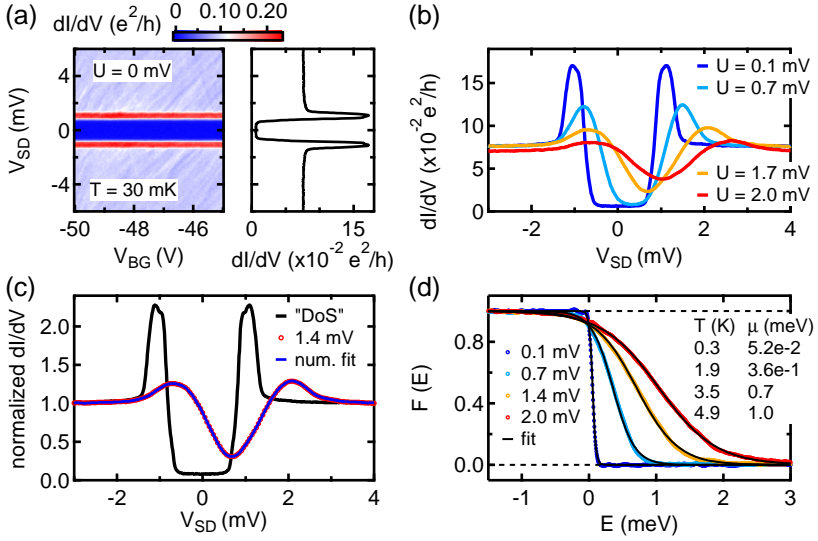


Figure 4.2. Extraction of the distribution function: (a) shows the differential conductance measured through the superconducting electrode to the graphene as a function of gate voltage V_{BG} and bias across the hBN tunnel barrier V_{SD} . A pronounced superconducting gap of the Pd/Pb/In electrode is clearly observed. In addition some resonances tuned by V_{BG} and V_{SD} are visible outside of the gap, which are attributed to universal conductance fluctuations. In order to remove those resonances, an averaging over 5 V in V_{BG} is performed and the average is shown on the right. (b) shows the differential conductance for different values of U applied across the graphene flake to drive it out-of-equilibrium. A clear broadening of the gap due to heating is observed, while the position of the gap shifts by roughly $U/2$. (c) By using the lowest T and $U = 0$ V measurement as the density of states (DoS) of the superconductor, the differential conductance at $U \neq 0$ V can be used to numerically deconvolve the distribution function. (d) shows the numerically extracted distribution functions from the three traces shown in (b). They all resemble a Fermi-Dirac distribution and therefore the electron temperature and the chemical potential can be extracted.

equilibrium. Depending on the scattering length scales and device length, different regimes can be accessed (see section 1.5). Fig. 4.2 (b) shows the tunnelling differential conductance at several values of heating bias U . Two main changes can be observed: First, the superconducting gap smears out and second, the position of the superconducting gap shifts in V_{SD} . The smearing can be explained by a higher electron temperature and the shift in bias is just due to the linear voltage drop of U along the graphene channel that shifts the chemical potential below the superconductor by $eU/2$.

Fig. 4.2 (c) shows the DoS of the superconductor and the tunnelling differential conductance at $U = 1.4$ mV. In a numerical deconvolution, the energy distribution function of the graphene at finite heating bias U can be extracted. To do so, a reasonable guess of the energy distribution function is assumed and according to Eq. 4.2 the resulting tunnelling differential conductance is calculated. The calculated differential conductance is then compared to the measurement and based on the differences, the guess of the energy distribution function is adjusted. This procedure is repeated until it matches the measured dI/dV , see Fig. 4.2 (c). Details about this numerical deconvolution can be found in appendix D.

The corresponding energy distribution functions to the differential conductance measurements in Fig. 4.2 (b) are shown in Fig. 4.2 (d). In the case of device B the energy distribution functions resemble a Fermi-Dirac distribution parametrized by the electron temperature T_e and chemical potential μ . These two parameters were extracted by fitting a Fermi-Dirac distribution function to the numerically extracted energy distribution function.

In the following, all electron temperatures shown were extracted according to the technique described here.

4.3. Temperature dependence

In order to test the ability of the method presented above to extract the electron temperature, the tunnelling differential conductances was measured at different bath temperatures, which is shown in Fig. 4.3 (a). An increased bath temperature results in a smearing of the feature in the differential conductance resulting from the superconducting gap. The electron temperature extracted from fitting a Fermi-Dirac distribution to the numerically extracted distribution function is shown in Fig. 4.3 (b) against the bath temperature measured on the cold finger of the dilution fridge.

A clear linear relation between the bath temperature and the electron temperature is obtained. The electron temperature starts to saturate at low bath temperature and does not decrease further. The negligible change in the tunnel conductance between 23 mK and 98 mK indicates a lower bound of ~ 100 mK for the electron temperature. It is well known that the electron temperature

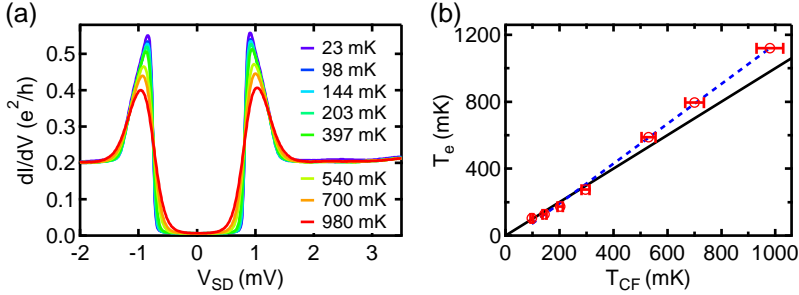


Figure 4.3. Temperature dependence of device A: (a) shows the differential conductance measured through the superconducting electrode to the graphene for different dilution fridge temperatures with $U = 0$ V. The electron temperature extracted from fitting a Fermi-Dirac distribution to the numerically extracted distribution function is shown as a function of the coldfinger temperature of the dilution fridge. The blue dashed line is linear guide to the eye, whereas the black solid line corresponds to $T_e = T_{CF}$. The error bars correspond to an uncertainty of 5 % in fridge temperature.

decouples from the bath temperature if the electrical leads in the fridge are not well thermalized and filtered against high frequency electromagnetic radiation. Even though our set-ups are equipped with RF filters at room temperature and low temperature, a deviation of the electron temperature can still occur.

In addition to the above mentioned deviation at low bath temperature, we face another limitation at low electron temperature. The differential conductance measurement at the base temperature that is used as the DoS of the superconductor contains a finite broadening due to the non-zero electron temperature of this measurement. Therefore, the extracted temperatures close to the base temperature will be underestimated. This effect is negligible at larger temperatures (≥ 1 K) and will therefore not affect the measurements presented in the following part.

Even though there is a linear relation between T_e and T_{CF} , the electron temperature T_e is always a bit above T_{CF} . This could have the following origin. The sample and the thermometer at the cold finger are not exactly at the same position. Furthermore, the thermal coupling of the sample to the cold finger is usually not as good as the one of the thermometer. These two set-up related issues would both lead to $T_e \geq T_{CF}$.

Despite all this complications, the extraction of a Fermi-Dirac distribution with a temperature close to the bath temperature is achieved. Therefore, this method is used in the following sections to study non-equilibrium phenomena

in graphene and to extract the electron temperature as a function of the heating bias U that gives insight into the dominating cooling mechanism at play.

4.4. Hot electron regime

In the hot electron regime, the electron-electron scattering length l_{e-e} is much shorter than the device length L and therefore many inelastic scattering events take place while an electron travels from N1 to N2. This leads to an effective electron temperature that follows the temperature profile along the device as described in Eq. 1.55 and shown in Fig. 4.4. The dominating cooling mechanism in this regime is due to hot electron out-diffusion. It follows that the temperature in the middle of the sample is linearly dependent on bias with the Lorenz number \mathcal{L}_0 as the proportionality factor. This holds for $U^2/\mathcal{L}_0 \gg T_0$, where T_0 is the temperature of the reservoirs.

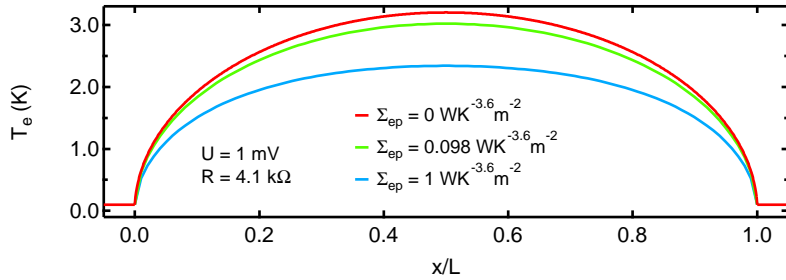


Figure 4.4. Temperature profile in the hot electron regime: $T_e(x)$ is obtained by numerical solving the heat transfer equation 1.53. The device dimensions of device A are used with different electron-phonon coupling strengths as indicated. A power law of 3.6 is used as was observed in device C, see section 4.5. The phonon and reservoir temperature is assumed to be 100 mK.

Fig. 4.5 (a) shows the tunnelling differential conductance for several values of heating bias U . An increased U leads to a smearing of the sharp superconducting gap and the middle of the gap is shifted by $U/2$ since the tunnel probe is located in the middle of the sample. The extracted electron temperature is shown in Fig. 4.5 (b) as function of heating bias U for several values of back gate voltage V_{BG} . It can be seen that T_e depends linearly on U . The inset in (b) shows the gate dependence of the graphene conductance measured from N1 to N2. While the graphene resistance is tuned by roughly a factor of two (by changing the charge carrier density by $\sim 7 \times 10^{12} \text{ cm}^{-2}$), the re-

sulting electron temperature is independent of the graphene resistance. If a large contact resistance would be present, a substantial part of the heating bias would drop on this resistor and a bias smaller than U would drive the graphene out-of-equilibrium. The ratio of the voltage dropping on the graphene and on the contact resistance would depend on the gate voltage as the graphene resistance is tunable. Therefore, different temperatures for the same U would be expected for different gate voltages. However, the measurements show that neither the electrical contact nor the charge carrier density plays a significant role.

A linear dependence of T_e on U is expected in the hot electron regime, where the cooling is given by the Wiedemann-Franz law that relates electrical conductivity to thermal conductivity. As shown in section 1.5 the electron temperature profile can be calculated analytically by Eq. 1.55 and the expected T_e at the location of the superconducting probe electrode is shown as solid black line in Fig. 4.5 (b). All extracted values for T_e fall below the expected value. Possible deviations are discussed later in section 4.7. Increasing \mathcal{L}_0 by 24 % leads to a lower T_e as shown by the solid blue line in Fig. 4.5 (b). A similar effect is observed by including the phonon cooling, see the two solid purple lines. The heat diffusion equation is numerically solved taking into account the electron-phonon coupling extracted in section 4.5. The two lines originate from the largest and smallest device resistance as this influences the total cooling power through the phonons.

Similar results have been obtained for device B, which are shown in Fig. 4.6. The extracted electron temperatures of device B are also independent of the gate voltage. Here, the graphene resistance changes by a factor of three while changing the charge carrier density by $\sim 7 \times 10^{12} \text{ cm}^{-2}$. This again confirms the negligible role of electrical contact resistance. Here, the dependence of the temperature on heating bias U can be divided into two qualitatively different regimes. For $U \leq 1 \text{ mV}$, a linear dependence similar to device A is observed. Again, the extracted values for T_e are smaller than calculated by Eq. 1.55 (solid black line). An increase of 48 % in \mathcal{L}_0 results in lower values of T_e , close to the experimentally observed ones as shown by the solid blue line. For $U > 1 \text{ mV}$, the extracted electron temperature is much lower than expected (even for the larger \mathcal{L}_0). This "kink" is well explained by the onset of electron-phonon cooling which reduces the electron temperature below the expected value. This is visualized by the two solid purple lines that represent the expected electron temperature including phonon cooling. The two lines originate from the largest and smallest device resistance as this influences the total cooling power through the phonons. Further possible explanations are discussed in section 4.7.

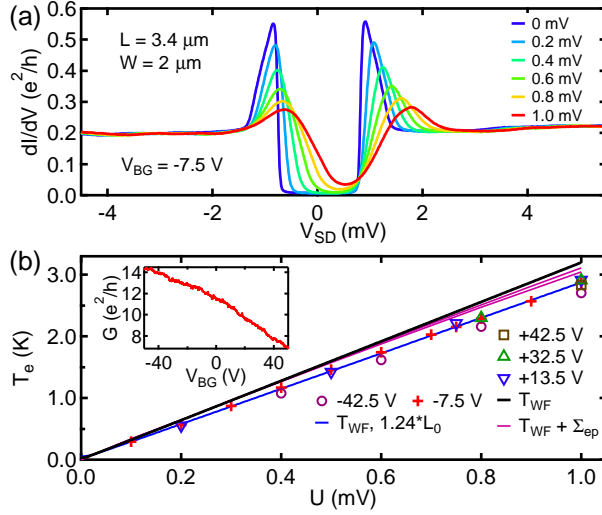


Figure 4.5. Device A in the hot electron regime: (a) shows the differential conductance measured through the superconducting electrode to the graphene for different values of heating bias U at a gate voltage of -7.5 V. (b) shows the extracted electron temperature from fitting a Fermi-Dirac distribution to the numerically extracted distribution function for several values of V_{BG} . The electron temperature increases linear with applied bias as expected by a dominating cooling mechanism due to electron out diffusion. The solid black lines represents the expected temperature based on the Wiedemann-Franz law, whereas the solid blue line represents the Wiedemann-Franz law for an increased Lorenz number. The solid purple line shows a numerical estimate of T_e (using Eq. 1.53) including the influence of the phonon cooling by using Σ_{ep} extracted in section 4.5. The two lines originate from the largest and smallest device resistance. The inset shows the two-terminal conductance through the graphene from N1 to N2 as a function of gate voltage V_{BG} .

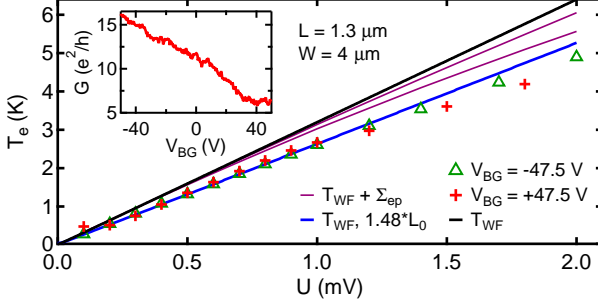


Figure 4.6. Device B in the hot electron regime: The extracted electron temperature from fitting a Fermi-Dirac distribution to the numerically extracted distribution function for two different gate voltages is shown. Typical differential tunnel conductance traces are shown in Fig. 4.2 (b) and (c). The electron temperature increases nearly linear with applied bias as expected by a dominating cooling mechanism due to electron out diffusion. The solid black lines represents the expected temperature based on the Wiedemann-Franz law, whereas the solid blue line represents the Wiedemann-Franz law for an increased Lorenz number. The solid purple line shows a numerical estimate of T_e (using Eq. 1.53) including the influence of the phonon cooling by using the Σ_{ep} extracted in section 4.5. The two lines originate from the largest and smallest device resistance. The inset shows the two-terminal conductance through the graphene from N1 to N2 as a function of gate voltage V_{BG} .

4.5. Phonon cooling

The bigger the graphene area the larger is the cooling power through the electron-phonon coupling. Sample D, which is $100\mu\text{m}$ long is suitable to study the cooling through electron phonon coupling as the cooling by electron out-diffusion is greatly reduced and a flat temperature profile results, see Fig. 4.7.

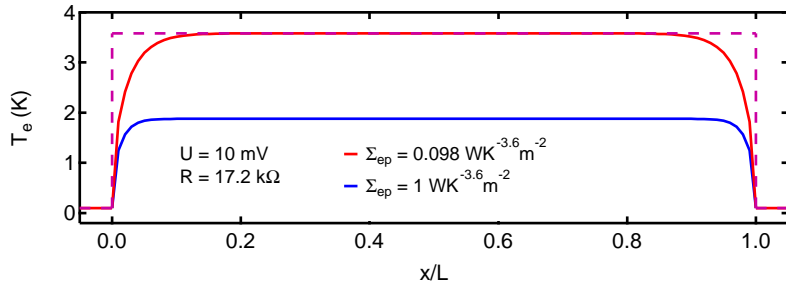


Figure 4.7. Temperature profile in the phonon cooled regime: $T_e(x)$ is obtained by numerical solving the heat transfer equation 1.53. The device dimensions of device C are used with different electron-phonon coupling strengths as indicated. A power law of 3.6 is used as was observed in device C. In the absence of electron cooling through out-diffusion, the temperature profile shown in purple dashed line would be reached with a maximum temperature given by Eq. 1.57. The phonon and reservoir temperature is assumed to be 100 mK.

The differential tunnel conductance through the superconducting electrode to the graphene are shown in Fig. 4.8 (a) for different values heating bias U . All measurements were performed at a high doping of $-5 \times 10^{12} \text{ cm}^{-2}$. The Joule heating power is shown as a function of the extracted T_e in Fig. 4.8 (b). The cooling power through the acoustic phonons is described as $P = A\Sigma_{ep}(T_e^\delta - T_0^\delta)$, with the total area A , the electron-phonon coupling Σ_{ep} , the electron temperature T_e and the phonon temperature T_0 , see section 1.5 for more details. In the dirty limit a power law of 3 is expected, whereas at higher temperatures in the clean limit a power law of 4 is expected. Above 1 K an exponent of 3.6 is extracted with an electron phonon coupling strength of $98 \text{ mWK}^{-3.6} \text{ m}^{-2}$. This lies somewhat between the clean limit (T^4) and dirty limit (T^3). A crude estimation of the crossover from the dirty to the clean limit by Eq. 1.61 yields a crossover temperature of around 1 K using a mean free path of $\sim 30 \text{ nm}$ extracted from the gate dependence of the graphene resistance. It is evident from Fig. 4.8 (b) that at lower temperatures the exponent is smaller. This is expected as the dirty limit is more relevant at lower temperatures, which was

shown in previous measurements on single layer graphene [126].

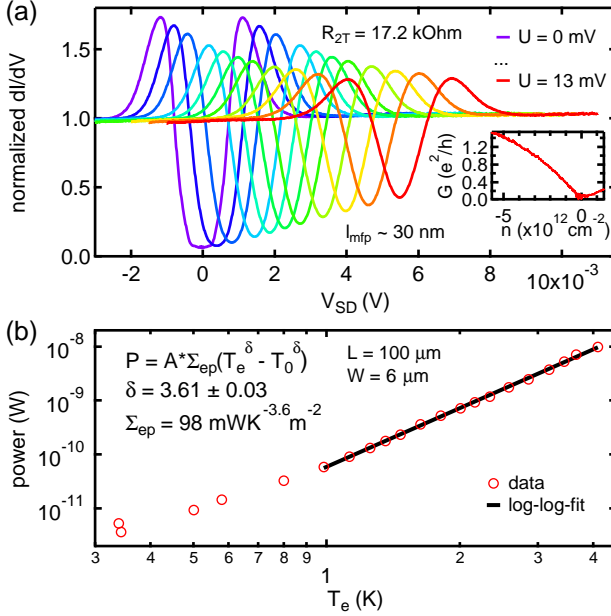


Figure 4.8. Device C in the phonon cooled regime: (a) shows the normalized differential conductance measured through the superconducting electrode to the graphene for different values of heating bias U . The inset shows the two-terminal conductance through the graphene from N1 to N2 as a function of density. (b) shows a log-log plot of the calculated Joule heating power versus the extracted electron temperature from fitting a Fermi-Dirac distribution to the numerically extracted distribution function. A linear fit reveals the exponent of the phonon cooling and the electron-phonon coupling strength.

4.6. Hint of double step

The tunnelling differential conductance of Device D is shown in Fig. 4.9 (a). This device developed a shoulder in the conductance peaks at the superconducting gap edges at moderate biasing $U \sim 0.5$ mV. This shoulder is a first indication of a double step energy distribution function as described in section 1.15 for non-interacting quasiparticles. The corresponding numerically

extracted distribution functions are shown in Fig. 4.9 (b), while the calculated differential conductance based on these distribution functions reproduce the measured differential conductance very well (thin solid black lines), see Fig. 4.9 (a). Hints of a plateau are visible at 0.5 in the energy distribution functions. However, at larger biases, the energy distribution functions start to smear out due to self heating of the electrons.

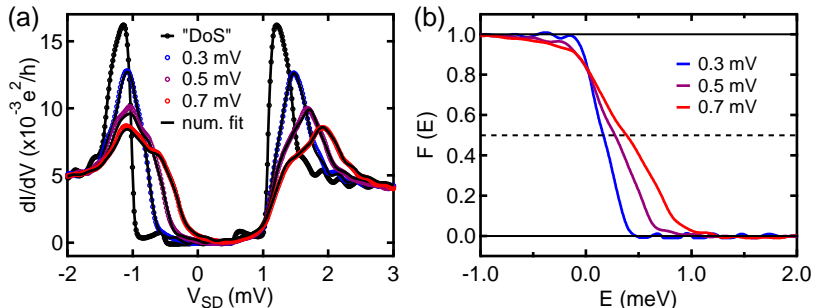


Figure 4.9. Hint of a double step function in Device D: (a) shows the differential conductance measured through the superconducting electrode to the graphene for different values of U . Clear shoulders develop for 0.5 mV and 0.7 mV. The numerically extracted distribution functions are shown in (b). A hint of a double step with a plateau around 0.5 is visible.

There are three limitations present in this data set. First, the differential conductance was only measured within a bias window of ± 3 mV, that complicates the numerical extraction. Ideally, the differential conductance is measured over a bias range that is much larger than the superconducting gap. Far away from the superconducting gap the differential conductance approaches a constant value that is the normal state conductance. If the differential conductance approaches a constant, it can be numerically extended to any bias value that is optimal for the numerical deconvolution. However, this is not the case here and therefore the deconvolution was performed on a limited bias range. In addition, the measured differential conductance contains some wiggles due to UCF, that were not fully average out (not enough averaging over back gate voltage). The presence of these relatively sharp features that even changes with applied bias are a further complication for an accurate extraction of the energy distribution function. A last complication is the additional resonance feature observed within the gap at ~ 0.5 meV. The exact origin of this is unknown but it might originate from the proximitized Pd layer that was used as a sticking layer. This is a further feature that introduces some complications in the numerical deconvolution and even worse, it might change

with bias as well. It was observed that it disappears with increasing temperature and that it is fully absent at 1 K (not shown). Nevertheless, a hint of an additional plateau at 0.5 is observed that is characteristic of non-interacting quasiparticles.

4.7. Discussion

First, the hot-electron regime, then the phonon cooled regime and in a last section the hint of a double step function are discussed. After that some general points are brought up.

4.7.1. Deviation from hot electron regime

This part of the discussion is dedicated to the deviation of the electron temperature from the expected value in the hot electron regime. We consistently observed an electron temperature that is significantly lower than expected by theory, see section 1.5.

First of all, a finite contact resistance between the graphene and the normal metal reservoirs could lead a thermal contact resistance as well. The presence of a thermal contact resistance would lead to a larger electron temperatures in the graphene as the cooling would be less efficient. Similar arguments hold for reservoirs that are at an elevated temperature. Both effects would lead to higher electron temperatures and are therefore ruled out.

In the hot electron regime, $T_e(x)$ is described by a pseudoparabolic profile. Obviously a superconducting electrode with finite width will not only probe the highest temperature in the middle, but will also probe lower temperatures off-centre. In order to estimate this, the width of the superconducting electrode (≤ 400 nm) has to be compared to the device length (3.4 μm for device A and 1.3 μm for device B). Even though the width of the superconducting electrode is a considerable fraction of the device length for device B, its influence is estimated to be smaller than 1.6 %, see appendix D. We therefore, take this as the lower bound of the uncertainty of T_e . In summary, this effect is too small to explain the deviation from the expected electron temperature.

In principle cooling through the superconducting electrode could also occur. However, this effect is ruled out because of two reasons. First, the contact resistance is on the order of 100 k Ω , which is roughly 100 times larger than the total device resistance. Therefore, only correction on the order of 1 % can be expected. Second, the reduced density of states in the superconductor at the Fermi energy efficiently suppresses cooling through electron out diffusion [124, 126].

Obviously, cooling through phonons lowers the electron temperature. In order to account for that the heat diffusion equation 1.53 was solved numerically using the electron-phonon coupling extracted in section 4.5. The influence

for $U \leq 1$ mV is marginal and cannot account for the observed deviation. In contrast the correction is significant for $U > 1$ mV for device B and can be as large as 0.8 K for a device resistance of 5.2 k Ω at $U = 2$ mV. However, the total cooling power through the phonons depends on the device resistance, which is another argument to rule out the phonon cooling as the main origin of the reduced T_e in the first place.

As a last explanation for the reduced T_e at low bias voltages, we propose an increased Lorenz number, which increases the cooling through electron out diffusion. Even though the Lorenz number $\mathcal{L}_0 = \frac{\pi^2 k_B^2}{3e^2}$ is supposed to be a universal constant, different values have been reported for different materials [185] so far. In order to explain our results, the Lorenz number needs to be increased by 24 % to 48 %. Previous reports on single layer graphene have also reported an increased Lorenz number between $1.26\mathcal{L}_0$ and $1.34\mathcal{L}_0$ [124]. It is theoretically predicted that electron-electron interactions might modify the Lorenz number in graphene [185–187]. It was shown theoretically that in the limit $E_F \ll k_B T$ the system becomes quantum critical and interactions between massless electrons and massless holes increase the Lorenz number [186, 187]. However, our samples are clearly not in this regime as $k_B T \ll E_F$ for all temperatures and densities achieved in these experiments. For impurity limited samples, as ours, a modification of the Lorenz number is also expected, but only if screening is weak [186], which means that the electron-electron interactions are not fully screened.

4.7.2. Electron-phonon coupling strength

As described in section 1.5.2, the deformation potential D is describing the strength of the electron-phonon coupling. Since our measurements lay somewhat between the dirty and clean limit a straightforward estimation of D is not possible. Therefore, D is estimated by using the experimentally extracted electron-phonon coupling of 98×10^{-3} W/m²K⁻⁴ once in the clean limit, see Eq. 1.59, and once in the dirty limit, see Eq. 1.59, with $E_F = 260$ meV and $l_{mfp} \sim 30$ nm. In doing so, we extract ~ 18 eV and ~ 16 eV for the clean and dirty limit respectively. These values are within the widely spread literature values ranging from 2 eV to 70 eV [122–125, 131] and agree well with the most reported values around 15 eV. These values are in agreement with theoretical predictions ranging from 5 eV to 13 eV [188–190].

The Joule power was calculated by U^2/R using the zero-bias differential resistance. The differential resistance might change at larger bias and therefore introduce an uncertainty into the Joule power. This effect is expected to be small though.

4.7.3. Discussion of the presence of a double-step distribution function

A clear double-step energy distribution function is only observed if the inelastic scattering length is much longer than the device length L . Since we only observe a hint of a double step-function and the fact that we observe the hot electron regime even in the shortest device, the inelastic scattering length scale must be shorter than $\sim 1 \mu\text{m}$. UCF correlation measurements or weak-localization measurements could shed some light onto these length scales as the phase coherence length is generally limited by inelastic scattering.

4.7.4. General remarks

The usage of CVD graphene and CVD hBN on SiO_2 -substrate is a limiting factor in device quality. Exfoliated graphene supported on hBN or fully hBN encapsulated graphene would be desirable not only for the much longer inelastic scattering length but also the gate dependent properties could be explored. Weak (anti-)localization and UCF measurements have shown phase coherence lengths on the order of the device size (μm -scale), see chapter 7.

The averaging procedure used here could be obsolete in cleaner devices. This would lead to much sharper peaks in the DoS at the superconducting gap edge. Sharper peaks are highly appreciated since they would allow for a much higher energy resolution in the extracted energy distribution function.

A systematic error in the extraction of the electron temperature is ruled out since the extracted T_e at elevated bath temperatures is larger than the bath temperature. If any systematic deviation is present, it would lead to T_e that is too large and not too low.

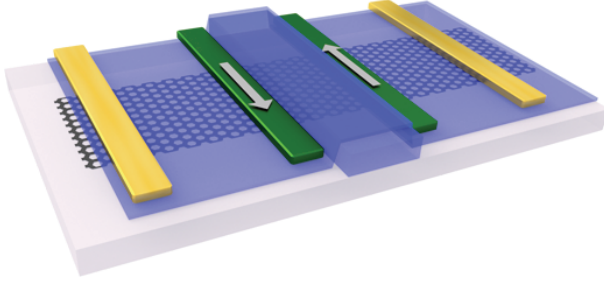
4.8. Conclusion and outlook

Superconducting tunnel spectroscopy was successfully used to locally extract the energy distribution function in graphene driven out-of-equilibrium. In the cases where the extracted energy distribution function resembled a simple Fermi-Dirac distribution the local electron temperature could be extracted. The dependence of the electron temperature on heating bias or Joule heating power respectively, revealed a hot electron regime and a phonon cooled regime. The former regime is dominated by electron out diffusion that is well described by the Wiedemann-Franz law. The latter regime is dominated by phonon cooling, where the electron-phonon coupling in the graphene is the bottleneck that allows us to extract this coupling strength. In the case of the hot electron regime, an increased Lorenz number was found.

Our measurements prove that superconducting tunnel spectroscopy is a powerful tool to locally access non-equilibrium properties of graphene. This

technique is not only limited to graphene but is also readily applicable to other 2-dimensional materials. In principle the density of states could be inferred from such measurements if the channel material is kept at equilibrium with a well known distribution function. Therefore, this could prove useful to study band modifications (e.g. graphene minibands or proximity spin-orbit coupling in graphene/TMDC systems) by locally measuring the density of states.

5 Spin transport in graphene spin valves^{1 2}



In this chapter we present how a layer-by-layer-stacked two-layer CVD hBN barrier is used as a tunnel barrier for spin injection. Hanle measurements were used to extract spin transport properties of the graphene channel. In general, we found typical low quality graphene spin valves with $\tau_s \simeq 400$ ps and $\lambda_s \simeq 2 \mu\text{m}$ for single as well as multi layer graphene devices. We have found that in these devices exfoliated thick hBN does not increase the device quality. Similarly to SiO_2 based devices, spin relaxation rates for the Elliott-Yafet and Dyakonov-Perel spin relaxation mechanism were found to be of similar strength. In addition we investigated the negative spin polarization of high resistive contacts, which showed a DC bias tunability. In a second part, a measurement scheme is introduced and preliminary results are shown that might allow the detection of localized magnetic moments that are believed to result in very short spin lifetimes in graphene based spin valves.

¹Parts of this chapter are results from a collaborative work with Mallikarjuna Gurram, Sidharta Omar and Bart van Wees from the University of Groningen. Some of the figures were prepared by Mallikarjuna Gurram.

²Parts of this chapter have been published in a similar form in Ref. [165].

5.1. Spin transport in two-layer CVD hBN/graphene/hBN heterostructures

The potential of CVD hBN as a tunnel barrier for electrical spin injection into graphene has been recently explored [163, 164, 191, 192]. Electrical injection of spin current using a monolayer CVD hBN tunnel barrier is inefficient [163, 164, 192] due to its low contact resistance-area product $R_c A$ leading to the spin conductivity mismatch problem [95, 193], see also subsection 1.3.3. This can be overcome by increasing the number of layers which would increase the $R_c A$ value leading to a more efficient injection of spin current. Theoretical studies show that the spin injection efficiency is expected to be larger for a bilayer hBN barrier than for a single layer hBN barrier [194]. However, practically, a controlled and direct growth of bilayer or multilayer (> 1 layer) CVD hBN is difficult [148]. Here we prepared a two-layer CVD hBN tunnel barrier via layer-by-layer-stacking of two individual monolayers of CVD hBN. Note that this two-layer CVD hBN is different from a bilayer CVD hBN in that the former is layer-by-layer-stacked using two individual monolayers while the latter is as-grown (i.e. Bernal stacked).

Here we present results of three devices labelled Dev1, Dev2 and Dev3. All devices have a similar geometry as depicted in Fig. 5.1 (a). The CVD hBN for Dev1 and Dev2 was obtained from Graphene Supermarket [142], whereas the CVD hBN for Dev3 is grown by the Zhang lab in Beijing [143]. Moreover, Dev1 and Dev2 are single layer graphene whereas Dev3 is a trilayer graphene. First, a half-stack consisting of graphene on exfoliated hBN is prepared by a dry transfer method similar to the vdW stacking described in section 2.1. After the removal of the transfer polymer in chloroform, the half-stacks were annealed in forming gas to remove any remaining polymer residues. The two layer CVD hBN tunnel barrier was prepared and deposited as described in section 2.1. After removing the supporting PMMA layer in acetone, the devices were again annealed in forming gas to remove further residues. Ferromagnetic cobalt electrodes were patterned by e-beam lithography and subsequent evaporation of Co/Al, see also section 2.1.

All transport measurements were performed at room temperature in vacuum with standard low frequency lock-in techniques. Since the contact resistance plays a crucial role in spin injection, we characterized the contact resistance in a three-terminal configuration. The three-terminal current-voltage (I-V) characteristics are shown in Fig. 5.1(b). The differential contact resistance-area products $R_C A$, measured at zero bias, were found to be in the range of $1 \text{ k}\Omega \mu\text{m}^2$ to $11 \text{ k}\Omega \mu\text{m}^2$, see also Tab. 5.2 for an overview. The $R_C A$ of single layer hBN is reported to fall below $4 \text{ k}\Omega \mu\text{m}^2$ and above $4 \text{ k}\Omega \mu\text{m}^2$ for bilayer hBN [160, 162–164, 195]. Based on these findings, we divide all our contacts into two regimes low resistance LR contacts ($R_C A < 4 \text{ k}\Omega \mu\text{m}^2$) and

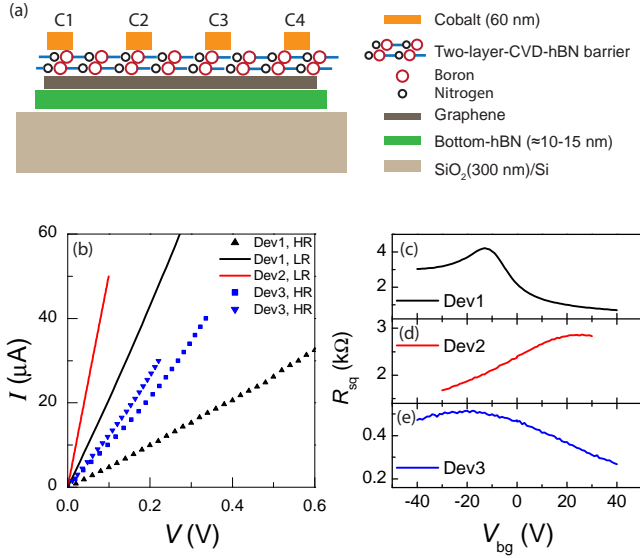


Figure 5.1. Device layout and basic characterization. (a) Schematic drawing of the devices prepared with two-layer-CVD-hBN tunnel barriers. C1-C4 denote the contacts used for the measurements and further contacts are not shown. (b) Representative three-terminal I - V curves for three devices, labelled Dev1, Dev2, and Dev3. High-resistance (HR) and low-resistance (LR) contacts are denoted in the legend with symbols and solid lines, respectively. Within Dev2, all contacts show similar LR behaviour to that shown here. (c), (d), and (e) show the square resistance R_{sq} of the graphene channel as a function of backgate voltage V_{bg} . © 2018 American Physical Society

high resistance HR contacts ($R_{CA} > 4 \text{ k}\Omega \mu\text{m}^2$). For Dev1 and Dev3 we find both LR and HR contacts, whereas for DV2 all contacts were found to be LR contacts. We find linear I-V behaviour for all LR and non-linear I-V behaviour for the HR contacts, see Fig. 5.1 (b). The large spread in R_{CA} values can be explained by the inhomogeneous growth of CVD hBN on the growth substrate (see also section 3.2), cracks or defects induced during the transfer process and the presence of contaminations at all interfaces (Gr/hBN, hBN/hBN, hBN/Co).

The square resistance measured in a four terminal configuration is shown in Fig. 5.1 (c). Field effect mobilities were extracted from the back gate dependence and surprisingly low mobilities were found, $3400 \text{ cm}^2 \text{ V}^{-1} \text{ s}^{-1}$ for Dev1, $120 \text{ cm}^2 \text{ V}^{-1} \text{ s}^{-1}$ for Dev2 and $255 \text{ cm}^2 \text{ V}^{-1} \text{ s}^{-1}$ for Dev3. It was previously shown that the density calculated by a simple capacitance model from the back gate resembles the bulk density measured by the Hall effect for graphene samples up to five layers [196]. The low device quality is attributed to the fabrication procedure as the graphene comes into contact with solvents for several times and an inhomogeneous CVD hBN layer that is in very close proximity.

Standard four terminal non-local spin-valve measurements were employed to characterize the spin transport, see also Fig. 5.2 (a) and section 1.3. In Tab. 5.1 the R_{CA} values of the (inner) injector and (inner) detector electrode pair (C2 and C3 in Fig. 5.2 (a)) are given for each device.

Table 5.1. R_{CA} of the devices: R_{CA} of the injector and detector electrodes of the devices.

	Dev1	Dev2	Dev3
R_{CA} of Inj1 ($\text{k}\Omega \mu\text{m}^2$)	1.7	1.2	4.7
R_{CA} of Det1 ($\text{k}\Omega \mu\text{m}^2$)	10.8	1.0	1.4
R_{CA} of Inj2 ($\text{k}\Omega \mu\text{m}^2$)	-	-	8.6
R_{CA} of Det2 ($\text{k}\Omega \mu\text{m}^2$)	-	-	2.3

An external magnetic field applied in the y direction was used to switch the magnetization of the Co contacts individually. Whenever a contact switches a sharp change in the non-local differential resistance $R_{NL}(B_Y)$ is observed, see Fig. 5.2 (b)-d(d). Dev1 with a LR injector and HR detector showed a regular spin-valve signal with a higher R_{NL} for the parallel (P) configuration than for the anti-parallel (AP) configuration of the involved contacts. In other words, $\Delta R_{NL} = (R_{NL}^P - R_{NL}^{AP})/2 > 0$, Fig. 5.2 (b). Similarly, Dev2 with a LR injector and a LR detector showed as well a regular spin-valve signal ($\Delta R_{NL} > 0$). Interestingly, Dev3 consisting of a HR injector and a LR detector showed an

inverted spin-valve signal with $\Delta R_{NL} < 0$, see Fig. 5.2 (d). Combinations of a HR injector with a HR detector or the combination of a LR injector with a LR detector on this device resulted in regular spin-valve signal with $\Delta R_{NL} > 0$.

Hanle measurements were performed to determine the spin transport parameters with a Hanle field applied perpendicular to the graphene plane in z direction. The Hanle signals measured in parallel and anti-parallel configuration are shown in Fig. 5.2 (e)–(g). The relative injector and detector alignment configuration is indicated with red and black crosses in Fig. 5.2 (b)–(d). In order to eliminate any spurious background the pure Hanle spin signal $\Delta R_{NL}(B_z) = (R_{NL}^P(B_z) - R_{NL}^{AP}(B_z))/2 > 0$ was calculated, which was then used to extract the spin transport parameters using the formula described in section 1.3.6. In doing so, we extracted spin relaxation times τ_s of around 280 ps for Dev1, 80 ps for Dev2 and 100 ps for Dev2.

The LR contacts can have a severe influence on the extraction of the spin transport parameters [193, 199–201]. In order to quantify the influence we calculate the values of R_C/R_s and L/λ_s . The effective spin resistance of the graphene channel $R_s = R_{sq}\lambda_s/w$, where $\lambda_s = \sqrt{D_s\tau_s}$ is the spin relaxation length, compared to the contact resistance quantifies the influence of the contact on the spin transport parameters [193]. For Dev1, Dev2 and Dev3 the following values were found (0.81–12.97, 0.61–1.114), (0.123–3.11, 0.15–2.65) and (13.64–77.81, 0.84–1.19). The low R_C/R_s values of Dev1 and Dev2 indicate a strong influence of the LR contacts on the extracted spin transport parameters. Therefore, the extracted values for τ_s from Hanle measurements are lower estimates and can be corrected according to Ref. [193]. Dev3 on the other hand is not influenced by the contacts and therefore the extracted values from Hanle measurements are believed to represent the true channel properties. The corrected τ_s , and D_s are shown in Fig. 5.3 as a function of carrier density. D_s and D_c reasonably well agree within a factor two confirming the reliability of our analysis [16, 202]

5.1.1. Discussion and interpretation of the spin transport properties

The devices presented here were prepared in a similar way as by Fu et. al. [163] and by Kamalakara et al. [164], except of the additional thick exfoliated hBN that was used as a substrate instead of SiO₂. Even though the hBN substrate should increase the device quality, very low mobilities were found. This very low quality might be attributed to several factors. First of all a very inhomogeneous hBN layer sits directly on top of the graphene channel. In addition, the graphene was directly in contact with the transfer polymer and its solvents as well as it was in direct contact with the rinsing solution of the copper etchant. All these steps can introduce contaminations at several stages that could lead to an inferior device quality.

Even after correcting the spin relaxation times for contact mediated spin

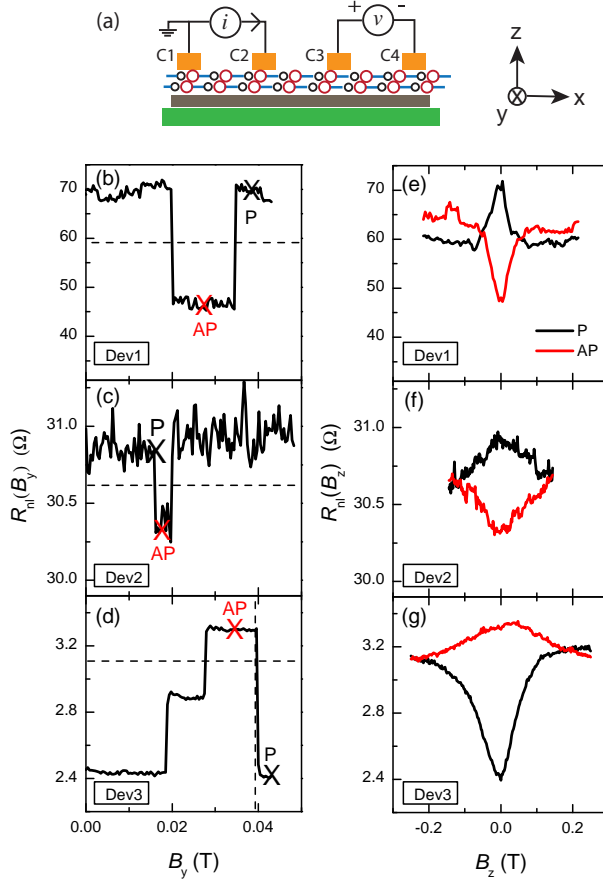


Figure 5.2. Measurement scheme, spin valve and Hanle measurements: (a) Schematic of the four-terminal non-local measurement geometry for the spin valve and the Hanle measurements. (b), (c), and (d) show non-local spin valve signals $R_{nl}(B_y)$ measured at the carrier densities 0, 1×10^{12} , and $4 \times 10^{12} \text{ cm}^{-2}$ for Dev1, Dev2, and Dev3, respectively. Horizontal dashed lines represent the background level of the spin valve signal. Vertical dashed line in (d) represents the magnetization switching field of the (inner)injector contact. Because the outer-detector contact in Dev3 is also sensitive to the spin accumulation three switches are observed in (d). Parallel (P) and anti-parallel (AP) magnetization configurations are denoted by crosses. The Hanle signals $R_{nl}(B_z)$ of the corresponding spin valve in (b), (c), and (d), are shown in parallel and anti-parallel configuration in (e), (f), and (g), respectively. © 2018 American Physical Society

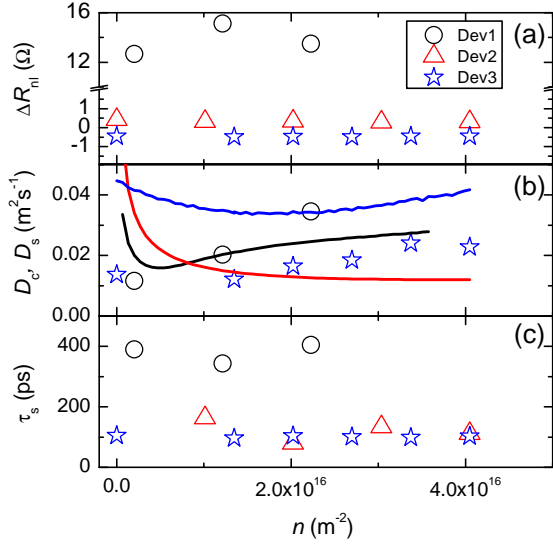


Figure 5.3. Hanle fit parameters: Data extracted from the Hanle spin precession measurements for Dev1, Dev2, and Dev3 at different electron carrier densities. (a) Non-local Hanle spin precession signal $\Delta R_{\text{nl}} = (R_{\text{nl}}^{\text{P}} - R_{\text{nl}}^{\text{AP}})/2$ at $B_z = 0$. Note that ΔR_{nl} for Dev3 remains negative for all densities. (b) Carrier diffusion constants determined from charge transport D_c and from spin transport D_s are shown as lines and symbols, respectively. D_s for Dev2 is not given due to unreliable values obtained from the Hanle fitting. We assumed $D_s = D_c$ [197] for Dev2 and used D_c values to fit the Hanle data $\Delta R_{\text{nl}}(B_z)$ to obtain τ_s . D_c for Dev3 is calculated from the effective density of states of three-layer graphene [198]. (c) Spin relaxation times τ_s . © 2018 American Physical Society

relaxation (low R_c/R_s values) [193], values below 400 ps were found for all three devices as shown in Fig. 5.3 (c). Such low spin relaxation times need an explanation. Several factors influence the device performance, such as the low quality of the graphene due to a wet transfer process of the CVD hBN, a non-uniform CVD hBN tunnel barrier covering the full spin channel, improper interfaces between cobalt and the CVD hBN as well as to the graphene and the proximity of polymer residues origination from the transfer as well as from the lithography process. An inhomogeneous hBN layer and lithography residues might lead to uneven interfacial growth of the ferromagnetic cobalt electrodes on top [161] which can result in enhanced spin dephasing due to randomly oriented magnetic fringe fields near the contacts [203].

In order to investigate the possible spin relaxation phenomenon causing the low spin relaxation times, we analysed the data in Fig. 5.3 by following an approach introduced by Zomer et al. [204]. Considering the Elliott-Yafet (EY) mechanism and the Dyakonov-Perel (DP) mechanism as the two dominating sources of spin relaxation, one can analyse the dependence of τ_s on τ_p using the equation

$$\frac{E_F^2 \tau_p}{\tau_s} = \Delta_{EY}^2 + \left(\frac{4\Delta_{DP}^2}{\hbar^2} \right) E_F^2 \tau_p^2, \quad (5.1)$$

where E_F is the Fermi energy of the graphene, Δ_{EY} and Δ_{DP} are the spin-orbit coupling strengths for the EY and DP mechanisms respectively.

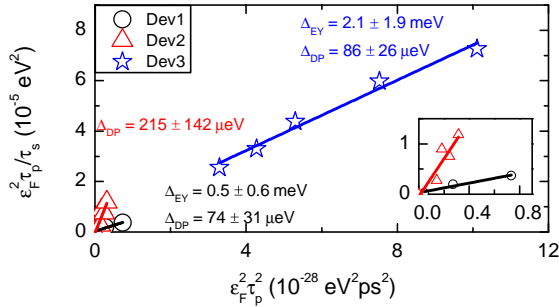


Figure 5.4. Determination of spin-relaxation mechanism: The linear fits (solid lines) of the data using Eq. (5.1) give the spin-orbit coupling strengths of the EY and DP spin relaxation mechanisms. The inset shows the data and fits at small values of τ_p . A reliable value of Δ_{EY} for Dev2 is not obtained due to non-monotonic relation between τ_s and n [204], see Fig. 5.3(c).
© 2018 American Physical Society

Fits to the data of the three devices are shown in Fig. 5.4 using Eq. 5.1. Due

Table 5.2. Overview of the devices: All important information of the three devices are presented.

	Dev1	Dev2	Dev3
$R_C A$ ($\text{k}\Omega \mu\text{m}^2$)	1.7–10.8	0.5–1.2	1.4–8.6
R_C/R_s (1)	0.81–13	0.12–3.1	0.84–1.2
$\tau_{s,EY}^{-1}$ (ns^{-1})	0.2–2.7	-	0.6–1.8
$\tau_{s,DP}^{-1}$ (ns^{-1})	2.0–2.5	10.3–13.8	8.4–9.4

to the small range in τ_p for Dev2 the fitting is not so reliable and we can only extract Δ_{DP} . From the extracted spin-orbit strength, one can obtain the spin relaxation mechanism due to its specific relaxation mechanism as following: $\tau_{s,EY}^{-1} = \frac{\Delta_{EY}^2}{E_F^2 \tau_p}$ and $\tau_{s,DP}^{-1} = \frac{4\Delta_{DP}^2 \tau_p}{\hbar^2}$. The values of $\tau_{s,EY}^{-1}$ and $\tau_{s,DP}^{-1}$ are both found to be on the order of 1 ns^{-1} for all devices and a clear dominance of either mechanism is not found. For an overview of the time scales, please see Tab. 5.2.

The spin valve measurements in Fig. 5.2 unambiguously show that the injector polarization of the HR contacts of Dev3 have opposite sign with respect to the LR contacts at zero DC bias. This is not the case for Dev1, where LR and HR contacts have the same sign of the polarization.

The absolute sign of the spin polarization cannot be determined by non-local spin valve measurements. Here we define that the polarization of the LR contacts is positive. Therefore, for a two layer CVD hBN tunnel barrier we find both positive and negative spin polarizations for HR contacts ($R_C A > 4 \text{ k}\Omega \mu\text{m}^2$) with respect to LR contacts ($R_C A < 4 \text{ k}\Omega \mu\text{m}^2$). There is no clear correlation between the $R_C A$ value and the sign of the polarization as previously reported by Kamalakar et al. [192], where all contacts with $R_C A \leq 25 \text{ k}\Omega \mu\text{m}^2$ showed a positive polarization and all contacts with $R_C A \geq 170 \text{ k}\Omega \mu\text{m}^2$ showed negative polarization. The main difference between the two studies is that the authors in Ref. [192] used a spatially inhomogeneous CVD hBN layer with regions containing single layer and regions with trilayer CVD hBN, whereas here a two-layer CVD hBN tunnel barrier is used. This artificial stacking of two layers does not result in a perfectly Bernal-stacked bilayer hBN but rather in randomly oriented stacking of the two single layers. Therefore, possible spin filtering mechanism that lead to the inversion of the spin polarization might be different.

Gurram et al. [162] reported in a recent study that the spin polarization at zero DC bias can also have a opposite sign for tunnel barriers fabricated from exfoliated bilayer hBN. There the $R_C A$ was in the range of $4.6 \text{ k}\Omega \mu\text{m}^2$ to $77.1 \text{ k}\Omega \mu\text{m}^2$, comparable to the values here. Therefore, the origin of the

different sign of the spin polarization cannot directly be related to hBN crystallographic orientation or number of layers.

In order to be able to study the DC bias dependence of the spin injection into graphene a tunnel barrier at the contact is needed. Only then does the applied voltage drop at the interface between the ferromagnetic contact and the graphene. The applied voltage drops across the graphene channel in the case of transparent contacts and it this leads to carrier drift in the graphene. Recently Gurram et al. [162] showed an enormous tuning of the spin injection polarization by the application of a finite DC bias across a bilayer hBN tunnel barrier. These results are motivating to look into the bias dependence of the devices presented here.

The DC bias dependence of the ΔR_{NL} is shown in Fig. 5.5 for Dev2 and Dev3. The DC bias is applied as a constant current in addition to the AC current applied between the two injector contacts as shown in Fig. 5.2 (a). ΔR_{NL} was measured at zero magnetic field.

Dev2 with LR contacts allowed only for a very small DC bias applied since otherwise large current levels would have destroyed the sample. The small changes in ΔR_{NL} were measured for a p-doping of the graphene channel. Within the bias range of ± 0.07 V, the magnitude of ΔR_{NL} increases (decreases) with positive (negative) bias. This behaviour could be explained with local carrier drift in the graphene due to the low ohmic contacts, which results in a finite voltage drop in the graphene [205].

In the case of Dev3 two sets of injector pairs were investigated, each consisting of a HR injector and a LR detector. At zero DC bias both sets showed an inverted spin valve signal indicating a negative injector polarization, see Fig. 5.2 (d) and (g). An injector current of ± 40 μ A results in an equivalent bias of ± 0.3 V and ± 0.2 V for set1 and set2 respectively. ΔR_{NL} changes in a non-monotonic behaviour with applied bias and does not depend on gate voltage. The absolute value of ΔR_{NL} is largest for negative DC bias. Drift effects can be neglected since the contact resistance is large enough such that the applied voltage drops mostly across the tunnel barrier.

Even though the inverted spin valve signal is a direct evidence of a negative polarization, the dependence of ΔR_{NL} on bias cannot directly be linked to a change in polarization a priori. Its magnitude is given as

$$\Delta R_{NL} = p_{in} p_{det} \left(\frac{R_{sq} \lambda_s e^{-L/\lambda_s}}{2w} \right), \quad (5.2)$$

where p_{in} , p_{det} are the differential spin injection and detection polarizations of the involved contacts. In order to extract p_{in} reliably, Hanle measurements were performed at different bias levels to extract λ_s to accommodate for possible changes in the spin relaxation length. p_{det} and p_{in} are assumed to be equal at zero DC bias and furthermore p_{det} is not expected to change with DC

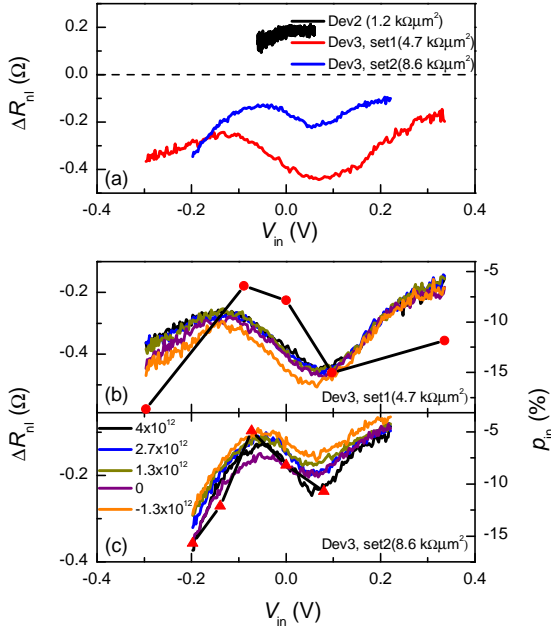


Figure 5.5. DC bias dependence of non-local spin signal:. (a) Non-local spin signal ΔR_{nl} as a function of the injection bias V_{in} for Dev2 with LR injector and detector contacts, and for Dev3 with two different sets of HR-LR injector-detector contacts pairs. Inversion of the spin signal for Dev3 is due to the inverse polarization of the HR injector contact with respect to the LR detector [see Figs. 5.2(d) and (g) for set1]. $R_c A$ values of the respective injector contacts, at zero bias, are given in the legend. The left axis of (b) and (c) shows bias dependent ΔR_{nl} for set1 and set2 contacts of Dev3, respectively, at different carrier densities ranging from electrons ($n > 0$) to holes ($n < 0$). Legend in (c) shows the carrier density in cm^{-2} . The right axis of (b) and (c) shows differential spin injection polarization p_{in} at an electron density of $3.4 \times 10^{12} \text{ cm}^{-2}$ for set1 and $4 \times 10^{12} \text{ cm}^{-2}$ for set2, respectively. © 2018 American Physical Society

bias. The extracted p_{in} as a function of DC bias is shown in Fig. 5.5 (b) and (c) and it closely follows ΔR_{NL} . p_{in} can be tuned within -15% to -5% .

Previously, a sign inversion of the spin valve signal was found for thicker (2-3 layers) CVD hBN [192] over a large range of bias 0.5 V to 2 V. There, the spin signal decreased at larger injection bias and was not measured below 0.5 V. We used a lock-in technique to accurately measure the spin signal at very low injection bias, which is hard in a pure DC measurement [192]. In comparison to the very recent results from Gurram et al. [162] on bilayer exfoliated hBN tunnel barriers, the tunability in two-layer CVD hBN tunnel barrier is much weaker and no sign inversion is found.

In summary, two-layer CVD hBN tunnel barriers were successfully employed for spin injection into single and trilayer graphene. Surprisingly low carrier mobilities and spin life times were found in these devices. Both most likely originate from the low quality of the devices mainly given by the presence of the CVD hBN on top and the many fabrication residues. Neither is the spin relaxation dominated by the Elliott-Yafet mechanism nor does the Dyakonov-Perel mechanism play the dominant role.

Some of the HR cobalt contacts showed a negative spin polarization with respect to the LR contacts. However, a consistent dependence of the $R_C A$ value was not found. The injection polarization stays negative within a bias range of ± 0.3 V and changes between -5% to -15% in a non-monotonic behaviour. The origin of a possible spin filtering effect is still not understood. One possible explanation for the bias dependence could be that the local density of states at the interface of the ferromagnetic cobalt to the CVD hBN tunnel barrier changes in a peculiar way with energy. A larger bias window allows then transport not only at the Fermi energy but also states below and above could then contribute to transport. Therefore, a different spin polarization is not fully unexpected. The findings presented here are in stark contrast to the enormous tunability of spin injection in cobalt/bilayer hBN/graphene systems as previously reported [162].

5.2. Proposal of a measurement scheme to detect the influence of magnetic moments on spin transport

Experiments on weak localization and universal conductance fluctuations in strong in-plane magnetic fields have found a significant contribution to dephasing from magnetic moments [103]. Temperature dependent measurements revealed a g factor around 2 suggesting that the magnetic moments can successfully be pinned by moderate in-plane magnetic fields. Magnetic moments in graphene can form due to carbon vacancies or chemisorbed hydrogen, leading to a sp^3 hybridization [104–107]. Localized magnetic moments acting as resonant scatterers were proposed as an efficient source of spin relaxation [108, 109], see also subsection 1.3.7. The fact that no spin relaxation anisotropy in graphene on SiO_2 was found, points to the direction that magnetic moments indeed are a dominating source of spin relaxation [206].

The direct influence of magnetic moments unintentionally present in pristine graphene on spin transport in graphene has not been shown yet. In the following we propose a measurement scheme to detect the influence of magnetic moments on spin transport. This concept is based on the fact that a static configuration of the magnetic moments aligned collinear to the injecting magnetic contacts will not lead to any dephasing of the electron spin during a resonant scattering event. In general, the direction of the magnetic moments of the resonant scattering sites are random and fluctuate in time. However, in a large magnetic field a Zeeman splitting occurs for the magnetic moments. If temperature is low enough, all magnetic moments will occupy the lowest energy level. This will lead to a static configuration of the magnetic moments aligned with the external magnetic field. Therefore, the combined influence of magnetic field ($E_z = g\mu_B B$) and temperature ($k_B T$) will lead to a clear picture of the contribution of magnetic moments to the spin relaxation. Since large magnetic fields (and obviously low temperatures) are required ($B \geq \frac{k_B T}{g\mu_B}$), the only possible injector and detector configuration will be a parallel alignment of the two electrodes' magnetization. It is obvious that the large magnetic field needs to be applied in-plane as otherwise significant orbital contributions would be expected (Hall effect and Quantum Hall effect). Therefore to address the magnetic moment related spin relaxation the measurement of the non-local resistance as a function of in-plane magnetic field and temperature is needed.

First, the room temperature characteristics of a multilayer graphene spin-valve are discussed. In a second step the low temperature spin transport is presented and the influence of a strong in-plane magnetic field is investigated.

5.2.1. Room temperature characterization of a two-layer CVD hBN/multilayer graphene spin valve

Fig. 5.6 shows the device consisting of a few layer graphene spin transport channel with a two-layer CVD hBN tunnel barrier³. Cobalt electrodes with varying width were used as injectors and detectors of spin polarized current. The sheet resistance $R_{sq} \simeq 200 \Omega$ was found to depend only weakly on gate voltage most probably due to the few layer nature of the graphene. The $R_C A$ was found to be around $3 \text{ k}\Omega \mu\text{m}^2$ to $4 \text{ k}\Omega \mu\text{m}^2$, determined from three terminal measurements. Clear spin valve signals are observed for different contact pairs as shown in Fig. 5.6 (a). The overall signal decreases with length exponentially with a spin relaxation length $\lambda_s = 1.7 \mu\text{m}$. The spin relaxation length is slightly shorter than the contact spacing, which is $2 \mu\text{m}$ (measured from the middle of the contacts). Over a length of $2 \mu\text{m}$ a clear Hanle signal was found, as shown in Fig. 5.6 (c). The data shown here is the difference of the Hanle signal in parallel and in anti-parallel configuration as similarly done above. The extracted spin lifetime $\tau_s = 220 \text{ ps}$ and diffusion constant $D = 0.014 \text{ m}^2 \text{ s}^{-1}$ yields a spin relaxation length of $\lambda_s = 1.8 \mu\text{m}$, which is in good agreement with the length dependence of R_{NL} . Since the spin channel is a few layer graphene flake, the density of states is unknown and therefore the charge diffusion constant D_c is also unknown. We therefore cannot compare the spin diffusion constant D_s to the charge diffusion constant D_c .

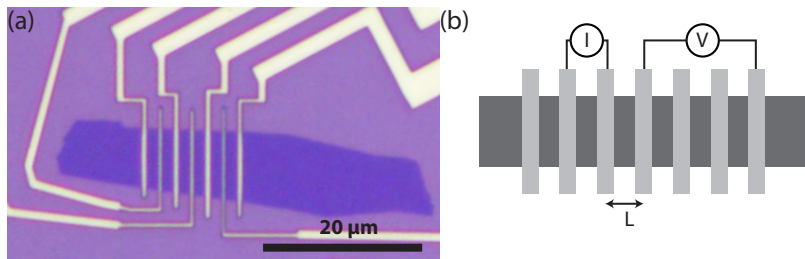


Figure 5.6. Device image and sketch. (a) shows an optical image of the device and in (b) a schematic drawing is shown, indicating the length of the spin transport channel with L .

³Part of the fabrication was performed by Simon Karsten.

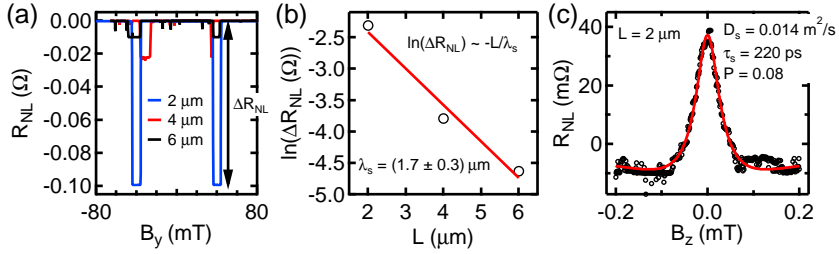


Figure 5.7. Non-local spin valve at RT. (a) shows the non-local spin-valve measurement for different contact pairs (different lengths between injection detection contact pairs). The R_{NL}^P was set to zero for all measurements to compare them on a single graph. The spin signal ΔR_{NL} is shown on a logarithmic scale in (b) as a function of length together with a linear fit to extract λ_s . (c) shows a Hanle measurement, which is the difference of the parallel and anti-parallel configuration.

5.2.2. Low temperature spin transport - signatures of magnetic moments?

As introduced in subsection 1.3.5, the non-local resistance in a spin valve is given by the difference in chemical potential of the spin up component below each detector normalized to the injecting current. Obviously the contact polarization determines how efficient the injection and detection is. However, for the following consideration the absolute value of the polarization does not matter and it is expected to be independent of in-plane magnetic field. In a non-local geometry, the chemical potential is given by the exponential decay with the spin relaxation length λ_s as well as by the effective resistance of the graphene (where λ_s goes into linearly). If the pinning of the magnetic moments results in a significantly longer spin relaxation time τ_s , the spin relaxation length $\lambda_s = \sqrt{\tau_s D}$ is also increased. A longer λ_s will then lead to a larger spin accumulation μ_s^\uparrow in the graphene channel. Fig. 5.8 shows the spin accumulation μ_s^\uparrow for different values of λ_s for the device geometry shown in Fig. 5.6. A moderate increase in λ_s leads to a substantial increase in μ_s^\uparrow below the detector contact C3 and nearly no change below the second detector contact C4. Therefore, an increase in R_{NL} with in-plane magnetic field is expected if magnetic moments are pinned and are a substantial source of spin relaxation. In this very simple argumentation the contacts were assumed to probe exclusively the spin-up chemical potential μ_s^\uparrow . However, the efficiency of each contact to detect μ_s^\uparrow is given by the contact polarization, which is generally not unity. Therefore, the expected change in R_{NL} will be smaller,

but the effect will be present.

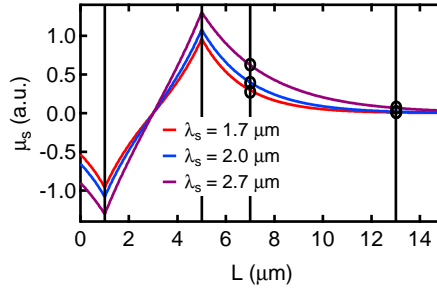


Figure 5.8. Spin up chemical potential for different λ_s : The spin up chemical potential a parallel contact geometry is shown for different values of λ_s as a function of distance. The vertical black lines indicate the position of the four contacts involved in a non-local spin valve.

Measurements at low temperatures

In the following, all transport experiments were carried out in DC. Fig. 5.9 (a) shows spin valve measurements at 4 K and 50 mK, demonstrating spin transport at these temperatures. In (b) the non-local resistance is shown for higher B_y values for 4 K and 50 mK. In principle R_{NL} should not depend on B_y at fields larger than the coercive fields of the involved injector and detector if the influence of magnetic moments is neglected for the moment. However, the measurements in Fig. 5.9 (b) show some dependence of R_{NL} on B_y , which can be due Hall effects of a small out-of-plane component of B_y for example. Hall effects can appear in non-local geometries if the contact is not homogeneously coupled to the graphene channel over the full width of the graphene channel. Pin-holes are an extreme form of such an inhomogeneous contact and have been shown to give rise to field dependent background in spin valve and Hanle measurements [207]. In order to eliminate these influences and to get rid of the large background, the $R_{NL}(4K)$ was subtracted from all other R_{NL} measurements in order to visualize the influence of the in-plane field and temperature on the spin component alone, see Fig. 5.10. The peak in R_{NL} at zero B_y might be explained by weak localization that arises due to a finite out-of-plane component. Small misalignments of the sample plane with respect to B_y were found in other studies (see section 7.5) in the same measurement system.

The normalized R_{NL} curves are shown in Fig. 5.10. Overall, the normalized R_{NL} varies on the order of 1Ω with maxima slightly above 2 T. For positive

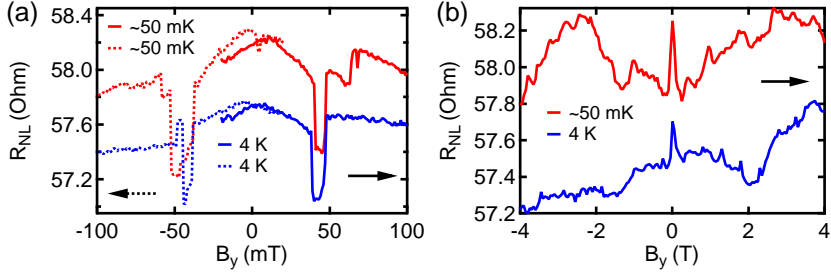


Figure 5.9. Spin valve measurements at low temperature: (a) shows spin valve measurements at low temperature and (b) shows the non-local resistance up to very large in plane fields B_y . The sweep direction of the magnetic field is indicated by black arrows.

B_y , the maximum in R_{NL} shifts to smaller magnetic fields for lower temperatures. In addition the maximum increases in absolute value. This trend is highlighted by the black arrow. For negative B_y a maximum is also observed for all temperatures but no clear trend is visible.

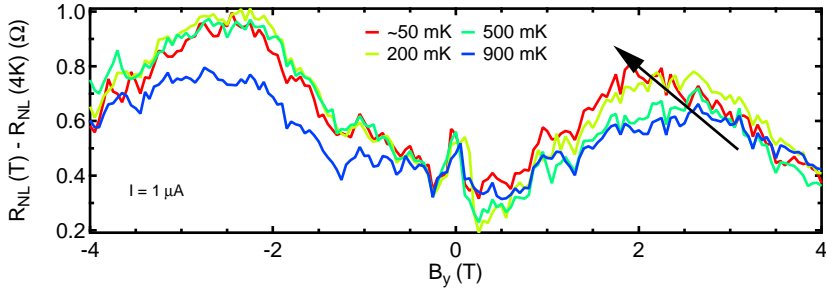


Figure 5.10. Normalized non-local resistance: The normalized non-local resistance is shown for different temperature as a function of in plane magnetic field B_y .

An increase in R_{NL} with increasing $|B_y|$ is indeed expected for the pinning of magnetic moments as this would lead to a longer τ_s and hence to longer λ_s leading to a larger difference in μ_s between contact 3 and 4, as shown schematically in Fig. 5.8. Furthermore, the increase in R_{NL} should happen at lower $|B_y|$ for lower temperatures as the magnetic moments are easier to freeze out at lower temperature.

Since contact 3 and 4 are ferromagnetic (non-local voltage detection), they will be aligned parallel at large $|B_y|$ and therefore both will sense the spin-up chemical potential. For very long λ_s , they will sense both the same chemical potential and hence the R_{NL} will reduce for even larger $|B_y|$. To sum up, all the observations for $B_y > 0$ seem to support the hypothesis of the pinning of magnetic moments.

The fact that the R_{NL} for $B_y < 0$ shows a slightly different behaviour than for $B_y > 0$ cannot confirm the influence of magnetic moments on spin transport. The observed behaviour of R_{NL} with B_y and temperature is therefore most probably due to some other influences. Phase coherent processes could play a role at such low temperatures [208]. Signatures of that are observed as possible WL contribution at very small B_y that can arise from a small out-of-plane component which is a result of a misalignment of the B_y with respect to the sample plane. To sum up, no conclusive picture can be given that would explain the observed line shape in Fig. 5.10.

5.3. Discussion on magnetic moments

Even though hints on the influence of magnetic moments on spin transport at low temperature have been seen, their clear presence could not be proven. In the following I would like to mention some limitations of this experiment and possible improvements.

First of all the condition for the pinning of the magnetic moments is important. As elaborated above, the Zeeman energy should be larger than temperature ($E_z > k_B T$) in order to freeze out the magnetic moments. Even though the lattice temperature is the relevant temperature for the freeze out condition of the magnetic moments⁴, the electronic temperature plays a crucial role as well. If the electronic temperature is much larger than E_z , then a substantial number of electrons carry enough energy to excite the magnetic moment to higher energy states during a scattering event. This will lead to unpolarized magnetic moments that then can lead to spin relaxation again. In conclusion, the electronic temperature has to be small as well. However, this is very challenging to achieve. In typical spin-valve measurements currents of 1 μA are driven across a tunnel barrier on the order of 1 k Ω or higher. Therefore, a bias window of 1 mV is easily opened that leads to the injection of hot electrons into the system. The injection of only a few hot electrons can lead to an electronic temperature well above the lattice temperature. Through multiple scattering events the hot electrons thermalize with the rest of the electronic systems leading to an increased electronic temperature. Furthermore, the presence of tunnel coupled contacts prevent efficient cooling via electron diffusion. We

⁴At least according to a personal communication from Jaroslav Fabian.

therefore think that this is one of the main limitations in the device presented above.

Another crucial part in this experiment is the influence of the contacts on spin relaxation. The fact that the spin relaxation length was found to be around $1.7\,\mu\text{m}$ with a contact spacing of $2\,\mu\text{m}$ (center to center of contact) is a bit problematic. It could very well be that the contacts are the main limiting factors leading to this spin relaxation length and that removing the influence of magnetic moments would not increase the spin relaxation length substantially. As introduced above, the influence of the contact resistance can be estimated by the R_C/R_S . The spin resistance R_S is roughly $70\,\Omega$, mainly given by the low sheet resistance and the wide sample. On the other hand, contact resistances of $\sim 3\,\text{k}\Omega$ lead to $R_C/R_S \sim 20$, which would render the influence of the contact negligible.

One more technical issue is the alignment of the magnetic field with respect to the sample plane and to ferromagnetic contacts. A slight misalignment with respect to the sample plane can lead to orbital effects as observed in a WL signatures at very low fields. In addition, Hall components are also expected, which were shown to lead to substantial non-local signals if the contacts are not homogeneous over the full width of the sample [207].

The device could substantially be improved by replacing contact 1 and contact 4 by two normal contacts, that would not be sensitive to spin. A spin insensitive voltage probe would make the interpretation of the measured R_{NL} easier as it should then change monotonically and no downturn would be expected.

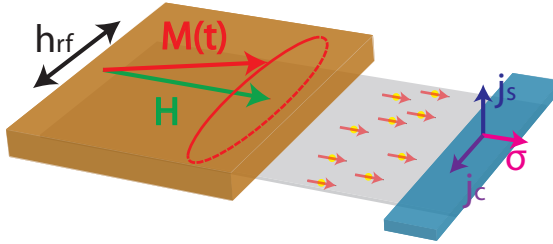
5.4. Conclusion and outlook

Two-layer CVD hBN tunnel barriers can be used for spin injection into graphene. Clear spin valve signals and Hanle precession curves were obtained in such samples at RT and low temperatures. However, the uncontrolled observation of different spin polarization of HR contacts is not understood and complicates things for further studies. The dirty fabrication procedure leads to inferior device performance in charge and spin transport. Therefore, an alternative route to the fabrication of clean spin valve devices is needed. The dry transfer method for CVD grown materials introduced for graphene [150] is an important step towards the integration of CVD materials into clean devices. However, there is still a lack of high quality, uniform large area grown CVD hBN on weakly interacting growth substrate that would allow for such transfer processes. Still considerable effort is needed to push the field of graphene spintronics towards the reliable fabrication of large scale devices. Possible strategies could include in-situ growth of hBN on pre-patterned ferromagnetic electrodes that then could be combined by the inverted fabrication procedure

used in Refs. [179, 180]. It was shown that iron is a well understood catalyst system for the growth of single layer hBN [144]. The proposed fabrication method has already been implemented in magnetic tunnel junctions [178].

In the perspective of fundamental science graphene spin valve devices still lack behind theoretical predictions and the short spin relaxation times are not yet fully understood. Localized magnetic moments could very well explain the short spin lifetimes observed and the weak spin relaxation anisotropy in pristine graphene [206] supports this hypothesis. In addition the WL and UCF measurements revealed a significant contribution of magnetic moments to the dephasing of electrons in graphene [103]. However, there is still a lack of experiments probing the presence of magnetic moments in pristine graphene with pure spin currents. Therefore, the proposed experiment might shed new light onto the short spin relaxation times in graphene.

6 Spin pumping into graphene^{1 2}



Graphene is an ideal material for spin transport as very long spin relaxation times and lengths can be achieved. However, electrical spin injection is challenging due to the conductivity mismatch that is explained in chapter 1 and 5. One way to circumvent this problem is the implementation of a tunnel barrier between the ferromagnetic material and graphene as shown in chapter 5. Spin pumping driven by ferromagnetic resonance (FMR) is another way to circumvent the conductivity mismatch as it produces a pure spin current in the absence of a charge current. In order to achieve this, transparent interfaces between the ferromagnetic and the non-magnetic material are needed [89, 210–213]. We will explore this alternative possibility of spin injection into graphene in this chapter.

¹This chapter is a collaborative work with David Indolese, who also partly prepared the figures.

²Parts of this chapter have been published in a similar form in Ref. [209].

6.1. Introduction into dynamical spin injection into graphene

When a ferromagnet with a precessing magnetization is brought into contact with a non-magnetic material, a pure spin current is emitted to the normal metal across the interface. This effect is called spin pumping, and was first described by Tserkovnyak et al. [89, 210]. A schematic view of this process is shown in Fig. 6.1. A magnetic RF-field is used to resonantly excite the magnetization (green arrow) such that it precesses around the effective magnetic field (blue arrow). This technique is called ferromagnetic resonance (FMR) [214] and can be used for continuous spin pumping. The damping of the FMR can partially be viewed as the transfer of angular momentum across the FM/NM interface in the form of a pure spin current (grey arrows in Fig. 6.1 crossing the FM/NM interface). This spin current consists of a time-dependent component with a spin polarization rotating in the yz -plane (purple arrow) and of a static component with the spin polarization in the x -direction (yellow arrow). Spin pumping can therefore be understood as the reverse effect of a spin current absorbed by a ferromagnet that exerts a torque on the magnetization [211].

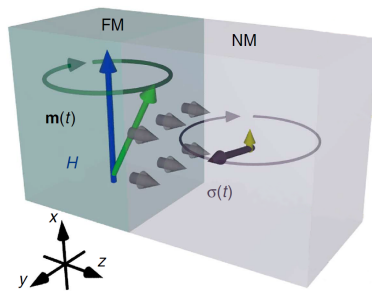


Figure 6.1. Working principle of spin-pumping at FMR: In the case of FMR, the magnetization (green arrow) precesses around the effective field (blue arrow). This leads to the generation of a spin current (grey arrows) at the FM/NM interface due to the magnetization dynamics of the FM. The time dependent spin polarization is shown as a purple arrow and rotates almost entirely in the yz -plane, whereas the time averaged component points along the x -direction (yellow arrow). Image adapted from Ref. [215].

The spin current across the FM/NM interface, which flows in the absence of a charge current, is mediated by the so-called spin mixing conductance that accounts for spin-dependent scattering at the FM/NM interface. In contrast to DC electrical spin injection, spin pumping works at gigahertz frequencies, which leads to the injection of a DC and an AC component of the spin current into the normal metal. Resonant phenomena of the AC component are ex-

pected to occur such as the amplification of the spin signal in AC spin valves [216]. A recent study revealed that the AC component of the spin pumping can be 100 times larger than the time averaged one [215], paving the way for further studies on dynamical spin injection. However, the detection of RF spin currents is very challenging and therefore we will restrict ourselves to the detection of DC spin currents. Furthermore, spin dynamics in graphene at high frequency are expected to play a crucial role in the realization of spin-torque devices for nano oscillators [217].

An enhanced damping of the FMR, proposed by Tserkovnyak et al. [89], has been observed in metallic structures [90, 91] as well as in graphene based devices [92]. Even though first hints on spin pumping into graphene have been observed, the detection of a spin current in the graphene was still missing until recently. Tang et al. [93] demonstrate spin pumping and the detection of a spin current by the inverse spin Hall effect in palladium in macroscopic graphene samples [93]. However, this study was limited to macroscopic samples and high RF power levels (on the order of 100 mW). Furthermore, the experiment was carried out in a microwave cavity that did not allow to change the excitation frequency.

In contrast to the above limited experiments, we show here for the first time spin pumping in micron scale graphene samples at room temperature and we detect the spin currents using the inverse spin Hall effect of a platinum electrode. The usage of on-chip coplanar transmission lines to locally excite micron scale Py pads come with the advantage that this method works over a broad frequency range. Since the samples are brought very close to the transmission line, much smaller power levels can be used compared to the conventionally used microwave cavities.

This chapter is organized as follows: First an overview of the device and its working principle is given. Next, the FMR condition is characterized, which is followed by the measurements and interpretations of an inverse spin Hall voltage at the platinum electrode.

6.2. Working principle of spin pumping

A schematic drawing of the samples is shown in Fig. 6.2. On the left a spin current is dynamically injected into the graphene spin transport channel, whereas on the right (at a distance L) the spin current is detected with a platinum electrode employing the inverse spin-Hall effect. An external magnetic field H defines the equilibrium magnetization direction. A magnetic RF field h_{rf} excites the magnetization of the Py pad that leads to FMR and finally to spin pumping into graphene with a DC component along the external magnetic field. A uniform magnetization (i.e. a macrospin) is ensured by the negligibly small crystal anisotropy of Py ($\text{Ni}_{80}\text{Fe}_{20}$) and the shape that favours in-plane

magnetization [218, 219]. A more detailed description about the anisotropies defining the equilibrium magnetization and the dynamics of a magnetization can be found in section 1.3. The AC component, that follows the RF field, is neglected here since our detection scheme is not capable of detecting signals at gigahertz frequencies. Once the spin polarized electrons are in the graphene they diffuse around and will eventually reach the Pt electrode. Due to a large spin Hall angle, a spin current j_s with a spin orientation σ is converted into a charge current j_c that leads to a finite voltage U in the open circuit configuration, see also section 1.4 for further information on the spin-Hall effect.

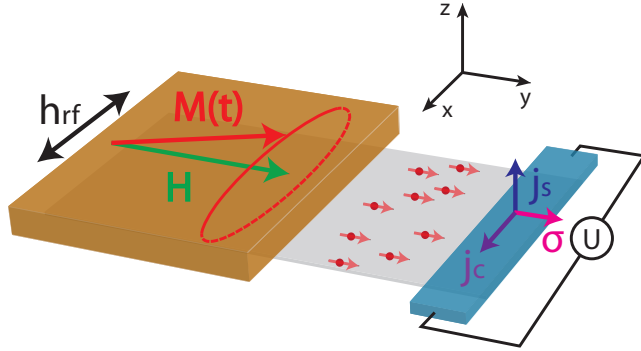


Figure 6.2. Working principle of spin-pumping at FMR: A RF magnetic field h_{rf} is used to drive the magnetization M of the Py pad (orange) at the FMR around the external magnetic field H . This leads to spin pumping into graphene with a DC component schematically depicted as arrows in the graphene plane (grey). The spins can freely diffuse in the graphene and once they are absorbed in the Pt electrode a transverse voltage (U) develops due to the inverse spin Hall effect.

6.2.1. Device fabrication and implementation

The above described working principle is implemented in our devices as shown schematically in Fig. 6.3. The samples consist of the following main parts: (1) a coplanar transmission line that is used to generate the magnetic RF field, (2) a Py/Gr-junction that is used for spin injection into graphene and (3) a laterally separated Pt/Gr junction to detect the spin current.

All samples presented here were fabricated on intrinsic, high resistive silicon wafers to reduce RF losses. The wafer was covered by a 170 nm thick SiO_2 layer. In a first step CVD graphene, grown in house by Kishan Thodkar, was transferred by a conventional wet transfer method using PMMA as a

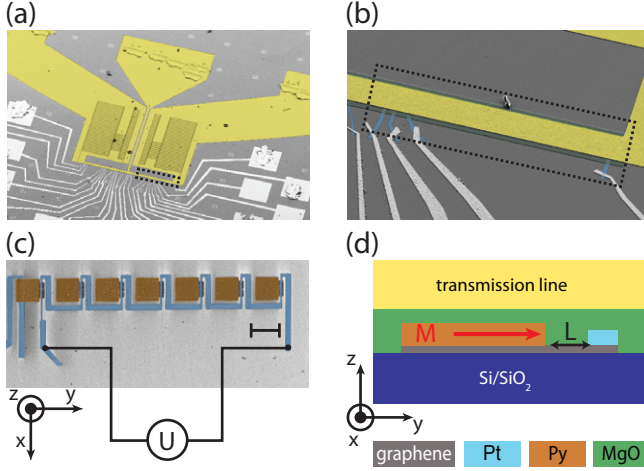


Figure 6.3. Device schematics: (a) - (c) show false-colour scanning electron micrographs of a typical device in various stages of the fabrication. In (a) a finished device is shown, where the launcher for the RF transmission line is clearly visible on top right and the DC lines are visible on the bottom. The zoom-in of the region highlighted by the black dashed line is shown in (b). The active device region, where the Py/graphene and Pt/graphene junctions are located below the transmission line (in yellow). (c) shows a zoom-in of the region highlighted by the black dashed rectangle in (b) before the deposition of the transmission line. The meander structure of the Pt electrode as well as the Py pads and the graphene are visible. The voltage measurement set-up across the Pt electrode is schematically shown. The scale bar is 10 μm . (d) shows a cross section of the device.

supporting layer and ammonium persulfate as the copper etchant. This is described in more detail in section 2.1. In a second step, the graphene sheet was patterned into an array of rectangles with width of $8\mu\text{m}$ and length of $12\mu\text{m}$ by e-beam lithography and reactive ion etching. As a next step the platinum electrodes were deposited either by sputter deposition or by thermal evaporation. The thickness of the Pt electrodes was kept at a maximum of $\approx 10\text{ nm}$ to avoid shunting effects. These effects occur since the spin-to-charge conversion in the Pt electrode happens mostly within a thickness of the spin relaxation length, which is on the order of a few nanometres [112]. Several devices were connected in series employing a meander structure of the Pt electrode, see Fig. 6.3 (c). In doing so, the voltage due to the ISHE of each device is added up, which results in a larger signal. In total, seven devices were connected in series. For a clean fabrication of Py structures, a fabrication procedure based on ZEP resist was used [220]. Py pads of $8\mu\text{m} \times 8\mu\text{m}$ were patterned on top of the graphene, see also Fig. 6.3 (c) for a false-colour electron micrograph of a sample at this fabrication stage.

A layer of MgO was used to insulate the device from the RF transmission line on the top. This fabrication scheme was chosen in order to bring the Py pads as close as possible to the RF transmission line to maximize the magnetic RF-field. A false-colour electron micrograph of this fabrication stage is shown in Fig. 6.3 (b). The RF transmission line consists of 5 nm Ti, 100 nm of Cu to reduce the resistance and a top layer of 45 nm of Au that prevents the copper from oxidation. The RF structure was designed to match 50Ω at the input to maximize the transmitted power. A current anti-node above the active region of the device was ensured by shortening the end of the coplanar transmission line to the ground plane. The planar capacitance structure in the ground plane of the transmission line shown in Fig. 6.3 (a) was used to electrically insulate the signal line from the ground plane. The capacitance was chosen large enough that it provides a short at RF frequencies. This would allow to use the transmission line as a top gate electrode in future experiments.

Here, a total of three devices are discussed. Two of which contain a graphene spin transport channel (sample A and B) whereas a device C serves as a reference device without graphene. All three devices are otherwise equal (except that the Pt in device A and C is sputter deposited whereas it was thermally evaporated for device B).

6.2.2. Measurement technique

A vector network analyzer (ZNB8 R&S) was used to generate the RF magnetic field. At the same time it was also used to detect the ferromagnetic resonance condition by measuring the reflection coefficient S_{11} , which corresponds to the ratio of the reflected and emitted power. At the FMR condition, power is resonantly absorbed by the precessing magnetization, which can easily be

detected in a measurement of S_{11} . The inverse spin-Hall signal was measured with a lock-in employing magnetic field modulation of the external magnetic field. This technique offers the advantage of a better signal to noise ratio and is less susceptible to thermal voltages and drifts during the measurements.

6.3. Ferromagnetic resonance condition

The ferromagnetic resonance condition of a thin ferromagnetic film with the external magnetic field applied in-plane is given by the Kittel formula [214]:

$$f_{res} = \frac{\gamma\mu_0}{2\pi} \sqrt{H_{ext}(H_{ext} + M_s)}, \quad (6.1)$$

where $\gamma = g \frac{\mu_B}{\hbar}$ is the gyromagnetic ratio with g being the g-factor, the Bohr magneton μ_B and the reduced Planck constant \hbar , the vacuum permeability μ_0 , the external magnetic field H_{ext} and the saturation magnetization M_s . The precession frequency is governed by the material properties γ and M_s . Eq. 6.1 assumes a uniform magnetization of the Py as a macrospin, which is justified by the negligible crystal anisotropy and the shape anisotropy favouring in-plane magnetization.

Fig. 6.4 (a) shows S_{11} as a function of external magnetic field and frequency. In order to eliminate the standing wave background due to reflections at each connector and modes, a frequency dependent background was subtracted (100 mT trace). The remaining vertical lines originate from a weak magnetic dependence of the standing wave background. At the FMR condition RF power is absorbed by the precessing magnetization, which is easily detectable in the reflected signal S_{11} . Two equivalent branches for positive and negative magnetic fields were observed, while the resonance condition is well described by the Kittel formula. Fitting the resonance condition with Eq. 6.1 allowed us to extract the saturation magnetization $M_s = 0.96$ T, while fixing $g = 2$ to literature values [212]. The extracted M_s agrees well with literature values [212, 221].

The line width of the FMR is given by the damping term α in Eq. 1.35. Cuts at $f = 4.8$ GHz are shown in Fig 6.4 (b) for sample A with graphene and for a sample C without graphene. The full width at half maximum (FWHM, ΔH) was extracted by fitting a Lorentzian to the data. A significant larger FWHM was observed for the sample with graphene indicating an additional damping term. This additional damping term can be interpreted as spin pumping into graphene [89]. The linewidth of the FMR, ΔH , can be related to the Gilbert damping

$$\Delta H = \frac{4\pi\alpha}{\sqrt{3}\gamma} f_{res}, \quad (6.2)$$

where α is the Gilbert damping constant in Eq. 1.35 [92]. Here, inhomogeneous sample-dependent broadening of the linewidth was neglected since it

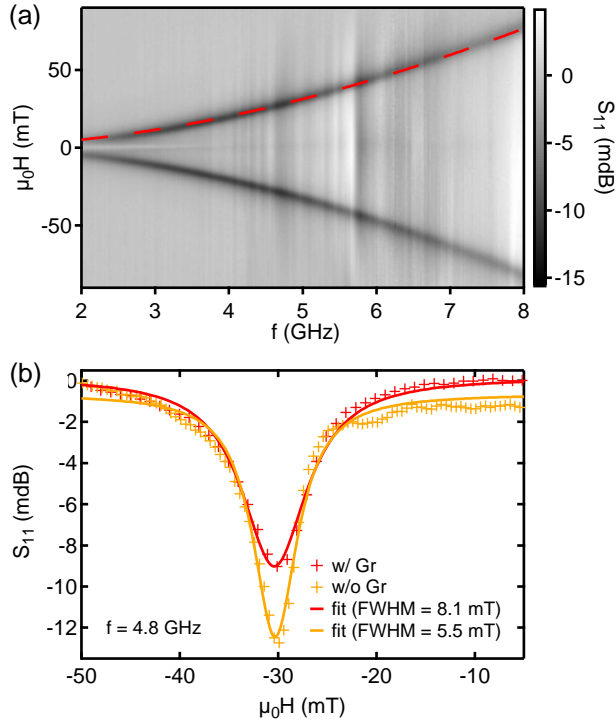


Figure 6.4. Ferromagnetic resonance condition: (a) shows S_{11} as a function of magnetic field and frequency. The two branches of the FMR condition are clearly observed. The dashed red line is a fit to Eq. 6.1. (b) shows S_{11} as a function of magnetic field at $f = 4.8$ GHz for a device without graphene (orange) and for a device with graphene (red). Lorentzian fits are used to deduce the full width at half maximum as indicated in the legend. © 2018 American Physical Society

was shown to be negligible [92]. The difference in linewidth of a sample with graphene and one without graphene can be used to estimate the real part of the effective spin-mixing conductance [222, 223]

$$g_{\uparrow\downarrow} = \frac{4\pi M_s d_{FM}}{g\mu_B} (\alpha_{Py/Gr} - \alpha_{Py}), \quad (6.3)$$

where d_{FM} is the thickness of the ferromagnetic Py layer. The imaginary part of the spin mixing conductance can be neglected since it is much smaller than the real part for metallic ferromagnets [222]. The spin-mixing conductance is a measure of the efficiency of the spin injection and was here estimated to be $2 \times 10^{20} \text{ m}^{-2}$ using $M_s = 0.96 \text{ T}$ as extracted above, $d_{FM} = 30 \text{ nm}$ and a literature value of $g = 2$ [212]. The value of the effective spin-mixing conductance extracted here is substantially larger (roughly one order of magnitude) than previously reported in similar Py/graphene systems [92, 93]. The spin mixing conductance is an important figure of merit if one wants to investigate the spin transport properties of the graphene channel as discussed below.

6.4. Inverse spin Hall voltage

In the section above clear indication of spin pumping into graphene is shown based on the broadening of the FMR in samples where graphene is present. In order to investigate spin transport in graphene, a spin current j_s can be detected with a Pt electrode placed at a distance L (600 nm for device A and 700 nm for device B) from the Py pad, see also Fig. 6.2. The charge current j_c due to the inverse spin-Hall effect can be detected as a voltage in an open-circuit configuration. This voltage changes sign if the direction of the spin polarization σ is reversed ($j_c \sim \sigma \times j_s$, see also section 1.4), while σ is simply controlled by the external field H . The voltage due to the inverse spin-Hall effect follows the line shape of the FMR and is therefore described by a Lorentzian.

Here, the voltage U at the Pt electrode was measured with a lock-in technique employing magnetic field modulation ($\mu_0 dH \sim 2.75 \text{ mT}$) at a frequency of 377 Hz. This technique has the advantage that it is more sensitive and not affected by thermal voltages that can drift over the long time scales of the measurements. Therefore, we recorded $dU/\mu_0 dH$ as a function of frequency and magnetic field as shown in Fig. 6.5 (a). The signal follows the FMR condition, which is indicated by red dots. The slight discrepancy at larger frequencies can be explained by sample to sample variation as the FMR condition was extracted from a different sample. Fig. 6.5 (b) shows $dU/\mu_0 dH$ as a function of magnetic field and reveals the expected lineshape of a derivative of a Lorentzian. Similar results were obtained for sample B, shown in Fig. 6.5 (c). The voltage at the Pt electrode shows for all frequencies the expected symmetry in magnetic field as one can easily see in Fig. 6.5 (a).

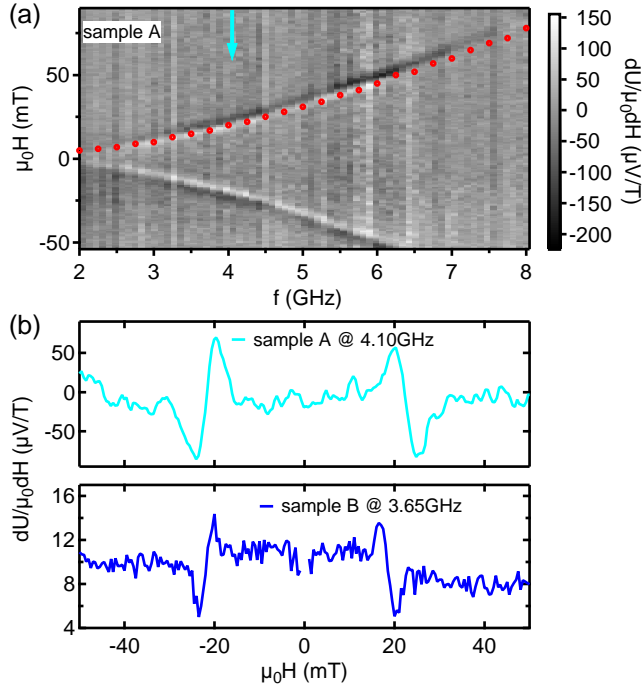


Figure 6.5. Inverse spin Hall voltage at Pt electrode: (a) shows the voltage measured at the platinum electrode as a function of magnetic field and frequency for sample A. The superimposed red dots mark the position of the FMR condition extracted from a measurement of S_{11} of a different sample. (b) shows the cut indicated in (a) and a cut from sample B. The signal clearly shows the mirror symmetry with respect to zero magnetic field. In the case of sample B, the data points around zero magnetic field were removed due to technical limitations.

As motivated above, a magnetic field modulation based measurement technique has its advantages when it comes to sensitivity and influences by spurious effects. However, it can itself lead to a background signal, which we would like to discuss in this paragraph. The small modulation of the magnetic field induces a voltage in the wires connecting the sample to the voltage amplifiers. This voltage depends on the magnetic field due to a field dependent modulation amplitude given by the magnet set-up. This is a result of a non-linear current to field conversion of the magnet set-up used here. In order to remove this background, the voltage at the Pt electrode was once measured with the microwave source turned on and once with the microwave source turned off. The difference of these two measurements is shown in Fig. 6.5 and used in the following analysis.

6.4.1. Influence of spurious effects

It is well known that several spurious effects can appear in spin pumping experiments [223]. Since the voltage at the Pt electrode is measured at low frequency, these effects can either arise due to thermal gradients in the sample or due to RF rectification effects (down mixing).

The effect of thermal voltages can most likely be excluded since the voltage is measured in a field modulation technique that is only sensitive to voltages that depend on the external magnetic field. Therefore, only charge currents within the Py pad could give rise to a magnetic field dependent voltage. However, thermal gradients in the Py pads, creating a charge current within the Py pads, are highly unlikely since a homogeneous RF absorption is expected. We therefore rule out any contributions from thermal effects.

The measurement set-up presented above are only sensitive to voltages that develop in x direction. As far as we know, only the AHE can contribute to a rectification effects that lead to a potential gradient along this direction. The AHE was included into the analysis and its contribution could be quantified due to a different lineshape. The contribution was found to be small and only weakly dependent on RF power.

6.4.2. Power dependence of the voltage at the Pt electrode

The voltage due to the inverse spin Hall effect at the Pt electrode should scale linearly with applied RF power ($j_s \sim h_{RF}^2$). In order to extract the dependence on RF power, the measured $dU/\mu_0 dH$ was fitted with a model containing the signal originating from the inverse spin Hall effect and from the anomalous Hall effect [116]:

$$U(H) = U_{ISHE} \frac{\gamma^2}{(H - H_{FMR})^2 + \gamma^2} + U_{AHE} \frac{-2\gamma(H - H_{FMR})}{(H - H_{FMR})^2 + \gamma^2}. \quad (6.4)$$

Here, U_{ISHE} and U_{AHE} represent the amplitudes of the contribution of the ISHE and the AHE to the signal. H_{FMR} is the field at which the FMR conditions is met and γ describes the width of the resonance, as earlier described. Contributions due to the AHE can be expected since RF eddy currents are induced by the RF magnetic field in the Py pads. These currents flow in the y-z plane in the permalloy and in combination with a varying magnetization in the x-z plane an anomalous Hall voltage (a Hall voltage proportional to the magnetization) can be expected to appear. This voltage will consist of a component at twice the frequency and of a down mixed DC component along the x direction.

Power dependence was performed on sample B and a fit at 8.9 mW is shown in the inset in Fig. 6.6. The contribution due to the ISHE is much larger than the contribution due to the AHE for any microwave power investigated. Both contributions scale linearly with power as indicated by the solid lines that are guide to the eyes. The linear scaling with power is expected for both contributions.

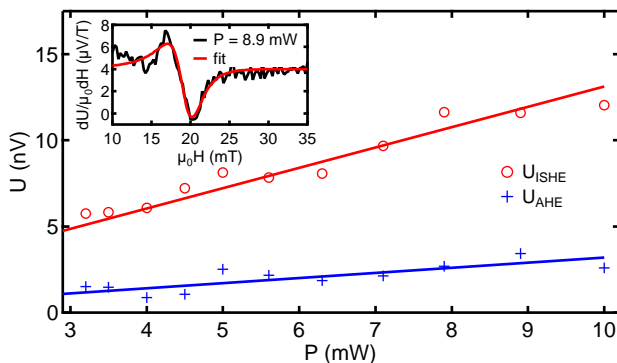


Figure 6.6. Power dependence of the voltage at the Pt electrode: The contribution of the ISHE and the AHE to the voltage at the Pt electrode are shown as a function of microwave power individually. The inset shows an actual measurement with a fit to Eq. 6.4. Both contributions scale linearly with power as indicated by the red and blue lines that are guides to the eye.

6.5. Discussion and interpretation

Here we show for the first time that FMR can be observed in mesoscale Py/graphene heterostructures with on-chip and broadband microwave exci-

tation in a simple reflection measurement. This measurement scheme allows an easy integration of more complex sample structures and measurements at low temperatures.

The observed broadening of the FMR linewidth upon the insertion of a graphene sheet indicates an additional damping channel that can be explained by spin-pumping into graphene. This is further supported by the observation of a voltage at the Pt electrode that is consistent with the expected symmetry of the ISHE. This voltage follows the FMR condition over a broad frequency range and preserves its symmetry in the whole frequency range investigated. Power dependence of this voltage reveals a linear scaling of the ISHE contribution as expected.

Spin transport properties could in principle be inferred from the amplitude of the inverse spin-Hall voltage at the Pt electrode as previously reported by Tang et al. [93]. To do so, the spin mixing conductance $g_{\uparrow\downarrow}$, the rf magnetic field h_{RF} (that can be estimated from the precession cone angle) and the spin-Hall angle of Pt are needed. Even though we have determined an experimental value of $g_{\uparrow\downarrow}$ as shown above, we lack the information about the cone angle. In addition, the magnitude of the reported values of the spin-Hall angle of Pt in literature are wide spread [112]. We, therefore, give not any estimate of the spin transport properties of the graphene channel. Further work is needed to nail down the relevant parameters.

The evaporation of a ferromagnetic material (e.g. Py) on top of graphene can substantially change the band structure of the underlying graphene layer and an exchange coupling induced in the graphene [194, 224] as well as charge transfer [225] can be expected. It is not known how these effects changes the spin pumping into graphene and how spin relaxation is modified below the Py. It is very likely that the spin relaxation is greatly enhanced below the Py and that only a small fraction of the area close to the edge of the Py pad contributes significantly to the spin accumulation in the graphene that is detected laterally by the Pt electrode.

6.6. Conclusion and outlook

The presented detection of a lateral spin current induced by spin pumping through the graphene is a first milestone. Even though remarkable and challenging on its own, it is very hard to extract any spin transport parameters of the graphene such as spin relaxation time τ_s and spin relaxation length λ_s . Due to the shape anisotropy keeping the magnetization in-plane an out-of-plane Hanle field could be applied to measure the Hanle effect. In future experiments, ferromagnetic strips instead of squares could be used. This would facilitate Hanle measurements since no external field is required for FMR. Pioneering work by Costache et al. [212] showed the successful detection of FMR

of a single Py nanomagnet. This would allow to readily characterize the spin transport parameters of graphene.

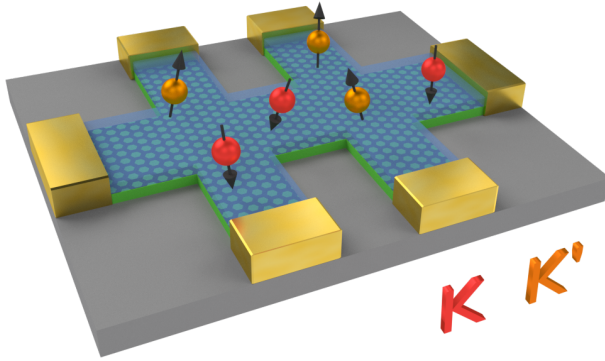
In this work we relied on a platinum electrode to detect the spin current in the graphene. In the future, one could investigate the spin-to-charge conversion in graphene itself. First results were reported by Mendes et al [226] recently. vdW-heterostructures of graphene and TMDC show a greatly enhanced SOC, see chapter 7. These systems are also expected to host very large spin-Hall angles [39] that would allow for a much more efficient spin-to-charge conversion.

Future research could focus on the gate tunability of the spin pumping effect as theoretical studies predict large modulations of the spin pumping efficiency by gate control of the density [227, 228]. This approach is especially interesting in combination with ferromagnetic insulators as a spin current source [226, 229]. The large planar capacitance introduced in the coplanar transmission line allows us to use the transmission line as a top gate electrode to tune the density of the graphene channel. Due to low device yield, the gate dependence of the spin pumping could not be investigated.

In order to gain further insights into the spin dynamics in graphene the AC component of the spin pumping could be investigated in the future. This is especially interesting and important since graphene is a promising candidate for future building blocks in spintronic applications (e.g. spin torque nano oscillators) since it can withstand large current densities [230] and large spin accumulations [162] can be achieved.

The compact measurement scheme presented here can easily be generalized to more exotic material systems such as topological insulators that host spin-momentum-locked edge channels[35]. These edge channels could itself be used to detect the spin-pumping into these systems as they offer a clear spin to charge conversion.

7 Spin-orbit coupling in graphene/WSe₂ heterostructures ¹



Large spin-orbital proximity effects have been predicted in graphene interfaced with a transition metal dichalcogenide layer. Whereas clear evidence for an enhanced spin-orbit coupling has been found at large carrier densities, the type of spin-orbit coupling and its relaxation mechanism close to the charge neutrality point remained unknown. In this chapter, we show for the first time an increased spin-orbit coupling close to the charge neutrality point in graphene, where topological states are expected to appear. Single layer graphene encapsulated between the transition metal dichalcogenide WSe₂ and hBN is found to exhibit exceptional quality with mobilities as high as $100\,000\text{ cm}^2\text{ V}^{-1}\text{ s}^{-1}$. At the same time clear weak anti-localization indicates strong spin-orbit coupling and a large spin relaxation anisotropy due to the presence of a dominating symmetric spin-orbit coupling is found. Doping dependent measurements show that the spin relaxation of the in-plane spins is largely dominated by a valley-Zeeman spin-orbit coupling and that the intrinsic spin-orbit coupling plays a minor role in spin relaxation. In addition, non-local measurements were conducted to investigate the possible presence of a large spin-Hall angle.

¹Parts of this chapter have been published in a similar form in Ref. [231].

7.1. Introduction

It was proposed that graphene in contact to a single layer of a TMDC can inherit a substantial SOC from the underlying substrate [42, 47]. The experimental detection of clear weak antilocalization (WAL) [149, 232–236] as well as the observation of a beating of Shubnikov de-Haas (SdH) oscillations [149] leave no doubt that the SOC is greatly enhanced in graphene/TMDC heterostructures. First principles calculations of graphene on WSe₂ [47] predicted large spin-orbit coupling strength and the formation of inverted bands hosting special edge states. At low energy, the band structure can be described in a simple tight-binding model of graphene containing the orbital terms and all the symmetry allowed SOC terms $H = H_0 + H_\Delta + H_I + H_{VZ} + H_R$ [47, 53]. A complete overview of all terms in the Hamiltonian is given in section 1.1.5.

7.2. Fabrication and characterization of hBN/Gr/WSe₂ heterostructures

The vdW-heterostructures presented here were fabricated as described in detail in section 2. In short, WSe₂/Gr/hBN vdW-heterostructures were assembled using a dry pick-up method [138] and Cr/Au 1D-edge contacts were fabricated [137]. Obviously a clean interface between high quality WSe₂ and graphene is of utmost importance. A short discussion on the influence of the WSe₂ quality is given in the appendix C. After shaping the vdW-heterostructure into a Hall-bar geometry by a reactive ion etching plasma employing SF₆ as the main reactive gas, Ti/Au top gates were fabricated with an MgO dielectric layer to prevent it from contacting the exposed graphene at the edge of the vdW-heterostructure. A heavily-doped silicon substrate with 300 nm SiO₂ was used as a global back gate. An optical image of a typical device and a cross section is shown in Fig. 7.1 (a). In total, three different samples with a total of four devices were fabricated. Device A, B and C are presented here and device D is discussed in the appendix C. Standard low frequency lock-in techniques were used to measure two- and four-terminal conductance and resistance. Weak antilocalization was measured at temperatures of 50 mK to 1.8 K whereas a classical background was measured at sufficiently large temperatures of 30 K to 50 K.

The two-terminal resistance measured from contact 1 to 2 as a function of applied top and bottom gate is shown in Fig. 7.1 (b). A pronounced resistance maximum, tunable by both gates, indicates the CNP of the bulk of the device whereas a fainter line only changing with V_{BG} indicates the CNP from the device areas close to the contacts, which are not covered by the top gate. From the four-terminal conductivity, shown in Fig. 7.1 (c), the field effect mobility $\mu \simeq 130\,000\text{ cm}^2\text{ V}^{-1}\text{ s}^{-1}$ and the residual doping $n^* = 7 \times 10^{10}\text{ cm}^{-2}$ were

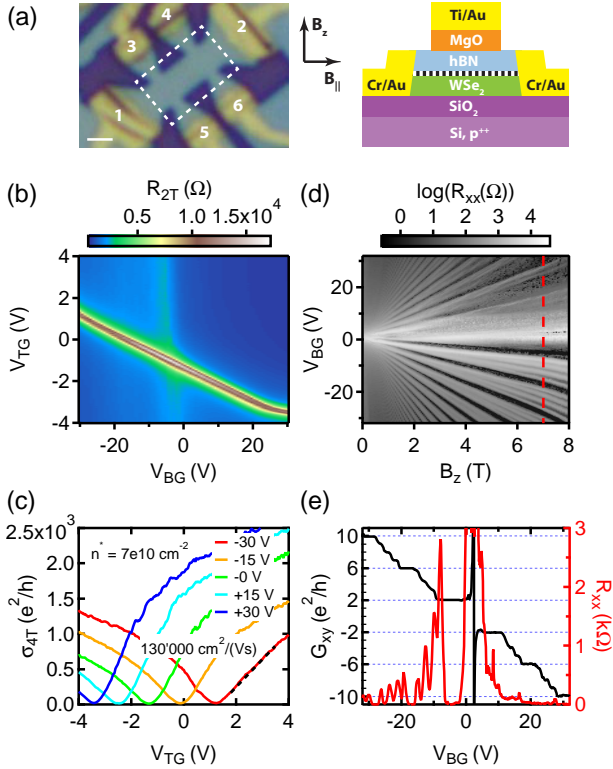


Figure 7.1. Device layout and basic characterization: (a) shows an optical image of device A before the fabrication of the top gate, whose outline is indicated by the white dashed rectangle. On the right, a schematic cross section is shown and the directions of the magnetic fields are indicated. The scale bar is 1 μm . The data shown in (b) to (e) are from device B. The two terminal resistance measured from lead 1 to 2 is shown as a function of top and back gate voltage. A pronounced resistance maximum tunable by both gates indicates the charge neutrality point (CNP) of the bulk device, whereas a fainter line only changing with V_{BG} indicates the CNP from the device area close to the contacts that are not covered by the top gate. Cuts in V_{TG} of the conductivity measured in a four-terminal configuration are shown in (c), which are also used to extract field effect mobility (linear fit indicated by black dashed line) and residual doping as indicated. The fan plot of longitudinal resistance R_{xx} versus V_{BG} and B_z at $V_{\text{TG}} = -1.42 \text{ V}$ is shown in (d) and a cut at $B_z = 7 \text{ T}$ in (e). Clear plateaus are observed at filling factors $\nu = \pm 2, \pm 3, \pm 4, \dots$ and higher, indicating full lifting of the fourfold degeneracy of graphene for magnetic fields $> 6 \text{ T}$. © 2018 American Physical Society

extracted. The mobility was extracted from a linear fit of the conductivity as a function of density at negative $V_B G$. At positive $V_B G$ the mobility is higher as one can easily see from Fig. 7.1 (c). At $V_B G \geq 25$ V, the lever arm of the back gate is greatly reduced since the WSe₂ layers gets populated with charge carriers, i.g. the Fermi level is shifted into some trap states in the WSe₂. Although the WSe₂ is poorly conducting (low mobility) it can screen potential fluctuations due to disorder and this can lead to a larger mobility in the graphene layer, as similarly observed in graphene on MoS₂ [237].

Fig. 7.1 (d) shows the longitudinal resistance as a function of magnetic field and gate voltage with lines originating from the integer quantum Hall effect. At low fields, the normal single layer spectrum is obtained with plateaus at filling factors $\nu = \pm 2, \pm 6, \pm 10, \pm 14, \dots$, whereas at larger magnetic fields full degeneracy lifting is observed with plateaus at filling factors $\nu = \pm 2, \pm 3, \pm 4, \pm 5, \pm 6, \dots$. The presence of symmetry broken states, that are due to electron-electron interactions [77], is indicative of a high device quality. In the absence of interaction driven symmetry breaking, the spin-splitting of the quantum Hall states could be used to investigate the SOC strength [78].

The high quality of the devices presented here poses sever limitations on the investigation of the SOC strength using WAL theory. Ballistic transport features (transverse magnetic focusing) are observed at densities larger than $8 \times 10^{11} \text{ cm}^{-2}$. Therefore, a true diffusive regime is only obtained close to the CNP, where the charge carriers are quasi-diffusive [44].

7.3. SOC characterization through weak antilocalization measurements

The two-terminal magneto conductivity $\Delta\sigma = \sigma(B) - \sigma(B = 0)$ versus B_z and n at $T = 0.25$ K and zero perpendicular electric field is shown in Fig. 7.2 (a). A clear feature at $B_z = 0$ mT is visible, as well as large modulations in B_z and n due to universal conductance fluctuations (UCFs). UCFs are not averaged out since the device size is on the order of the dephasing length l_ϕ . Therefore, an ensemble average of the magneto conductivity over several densities is performed to reduce the amplitude of the UCFs [232], and curves as in Fig. 7.2 (b) result. A clear WAL peak is observed at 0.25 K whereas at 30 K the quantum correction is fully suppressed due to a very short phase coherence time and only a classical background in magneto conductivity remains. This high temperature background is then subtracted from the low temperature measurements to extract the real quantum correction to the magneto conductivity [149].

In addition to WL/WAL measurements the phase coherence time can be extracted independently from the autocorrelation function of UCF in magnetic

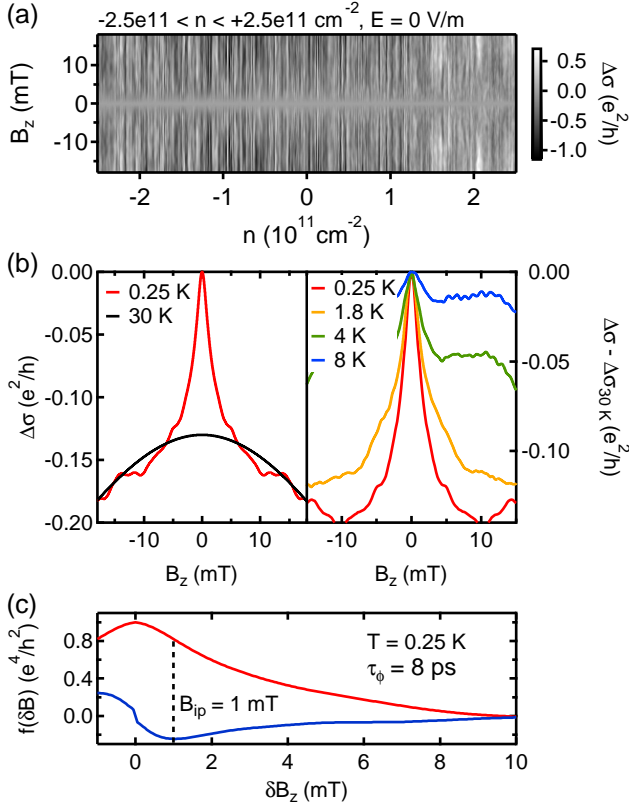


Figure 7.2. Magneto conductivity of device A: (a) Magneto conductivity versus B_z and n is shown at $T = 0.25$ K. A clear feature is observed around $B = 0$ mT and large modulations due to UCF are observed in B_z and n . (b) shows the magneto conductivity averaged over all traces at different n . The WAL peak completely disappears at $T = 30$ K, leaving the classical magneto conductivity as a background. The 30 K trace is offset vertically for clarity. The quantum correction to the magneto conductivity is then obtained by subtracting the high temperature background from the magneto conductivity, see (b) on the right for different temperatures. With increasing temperature the phase coherence time shortens and therefore the WAL peak broadens and reduces in height. (c) shows the autocorrelation of the magneto conductivity in red and its derivative in blue (without scale). The minimum of the derivative indicates the inflection point (B_{ip}) of the autocorrelation, which is a measure of τ_ϕ . © 2018 American Physical Society

field [238]. UCF as a function of B_z was measured in a range where the WAL did not contribute to the magneto conductivity (e.g. 20 mT to 70 mT) and an average over several densities was performed. The inflection point in the autocorrelation (B_{ip}), determined by the minimum in its derivative, is a robust measure of $\tau_\phi = \frac{3\hbar}{2eDB_{ip}}$ [239], see Fig. 7.2 (c).

7.3.1. Fitting

To extract the spin-orbit scattering times we use the theoretical formula derived by diagrammatic perturbation theory [73]. In the case of graphene, the quantum correction to the magneto conductivity $\Delta\sigma$ in the presence of strong SOC is given by:

$$\Delta\sigma(B) = -\frac{e^2}{2\pi h} \left[F\left(\frac{\tau_B^{-1}}{\tau_\phi^{-1}}\right) - F\left(\frac{\tau_B^{-1}}{\tau_\phi^{-1} + 2\tau_{asy}^{-1}}\right) - 2F\left(\frac{\tau_B^{-1}}{\tau_\phi^{-1} + \tau_{asy}^{-1} + \tau_{sym}^{-1}}\right) \right], \quad (7.1)$$

where $F(x) = \ln(x) + \Psi(1/2 + 1/x)$, with $\Psi(x)$ being the digamma function, $\tau_B^{-1} = 4eDB/\hbar$, where D is the diffusion constant, τ_ϕ is the phase coherence time, τ_{asy} is the spin-orbit scattering time due to SOC terms that are asymmetric upon z/z inversion (H_R) and τ_{sym} is the spin-orbit scattering time due to SOC terms that are symmetric upon z/z inversion (H_I , H_{VZ}) [73]. The total spin-orbit scattering time is given by the sum of the asymmetric and symmetric rate $\tau_{SO}^{-1} = \tau_{asy}^{-1} + \tau_{sym}^{-1}$. In general, Eq. 7.1 is only valid if the intervalley scattering rate τ_{iv}^{-1} is much larger than the dephasing rate τ_ϕ^{-1} and the rates due to spin-orbit scattering τ_{asy}^{-1} , τ_{sym}^{-1} . Further discussion on this formula can be found in section 1.2.2.

In the most general case there are three different regimes in the presence of strong SOC in graphene: $\tau_{asy} \ll \tau_{sym}$, $\tau_{asy} \sim \tau_{sym}$ and $\tau_{asy} \gg \tau_{sym}$. Therefore, we fitted the magneto conductivity with initial fit parameters in these three limits. An example is shown in Fig. 7.3, where the three different fits are shown as well as the extracted parameters. Obviously, the case $\tau_{asy} \ll \tau_{sym}$ (fit1) and $\tau_{asy} \sim \tau_{sym}$ (fit2) are indistinguishable and fit the data worse than the case $\tau_{asy} \gg \tau_{sym}$ (fit3). In addition, τ_ϕ extracted from the UCF matches best for fit3. Therefore, we can clearly state that the symmetric SOC is stronger than the asymmetric SOC. The flat background as well as the narrow width of the WAL peak can only be reproduced with the third case. Additionally, measurements at 1.8 K over a larger magnetic field range confirm this finding as shown in the appendix C.

A very similar behaviour was found in device C at the CNP. In device B (shown in the appendix C), whose mobility is larger than the one from device

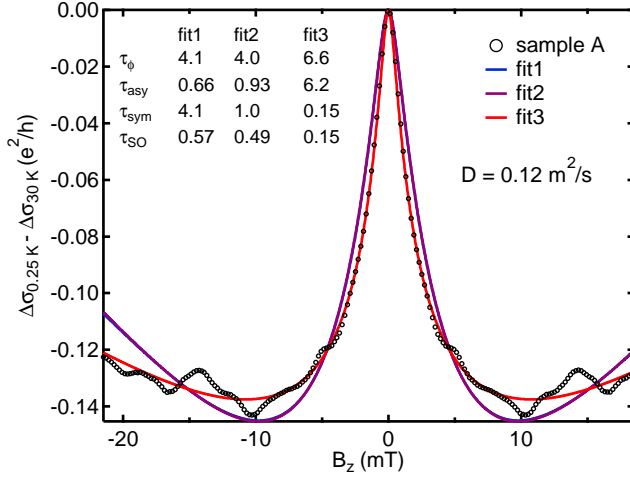


Figure 7.3. Fitting of quantum correction to the magneto conductivity of device A The quantum correction to the magneto conductivity is fit using Eq. 7.1. The results for three different limits are shown and their parameters are indicated (in units of ps). τ_ϕ is estimated to be 8 ps from the autocorrelation of UCF in magnetic field, see Fig. 7.2 (c). © 2018 American Physical Society

A, we cannot clearly distinguish the three limits as the transport field is too low (≈ 12 mT) and the flat background at larger field cannot be used to disentangle the different parameters from each other. However, this does not contradict $\tau_{asy} \gg \tau_{sym}$ and the overall strength of the SOC ($\tau_{SO} \simeq 0.2$ ps) is in good agreement with device A shown here.

Obviously, the extracted time scales should be taken with care as many things can introduce uncertainties in the extracted time scales. First of all, we are looking at ensemble-averaged quantities and it is clear that this might influence the precision of the extraction of the time scales. In addition, the subtraction of a high temperature background can lead to higher uncertainty of the quantum correction. Lastly, the high mobility of the clean devices places severe limitations on the usable range of magnetic field. All these influences lead us to a conservative estimation of a 50 % uncertainty for the extracted time scales. Nevertheless, the order of magnitude of the extracted time scales and trends are still robust.

The presence of a top and a back gate allows us to tune the carrier density and the transverse electric field independently. The spin-orbit scattering rates were found to be electric field independent at the CNP in the range of -0.05 V nm⁻¹ to 0.08 V nm⁻¹ within the precision of parameter extraction. Details are given in the appendix C. Within the investigated electric field range τ_{asy} was found to be in the range of 5 ps to 10 ps, always close to τ_ϕ . τ_{sym} on the other hand was found to be around 0.1 ps to 0.3 ps while τ_p was around 0.2 ps to 0.3 ps, see appendix C for more details. The lack of electric field tunability of τ_{asy} and τ_{sym} in the investigated electric field range is not so surprising. The Rashba coupling in this system is expected to change considerably for electric fields on the order of 1 V nm⁻¹, which are much larger than the applied fields here. However, such large electric fields are hard to achieve. In addition, τ_{sym} , which results from λ_I and λ_{VZ} is not expected to change much with electric field as long as the Fermi energy is not shifted into the conduction or valence band of the WSe₂ [42]. These findings contradict another study [234], which claims an electric field tunability of both SOC terms. However, there it is not discussed how accurately those parameters were extracted.

7.3.2. Density dependence

The momentum relaxation time τ_p can be tuned by changing the carrier density in graphene. Fig. 7.4 shows the dependence of τ_{asy}^{-1} and τ_{sym}^{-1} on τ_p in a third device C. The lower mobility in device C allowed for WAL measurements at higher charge carrier densities not accessible in devices A and B. At the CNP, τ_{asy}^{-1} and τ_{sym}^{-1} are found to be consistent across all three devices A, B and C. Here, τ_{sym}^{-1} increases with increasing τ_p whereas τ_{asy}^{-1} is roughly constant with increasing τ_p . The dependence of the spin-orbit scattering times on the

momentum scattering time can give useful insights into the dominating spin relaxation mechanisms, as will be discussed later. It is important to note that the extracted τ_{asy} is always very close to τ_ϕ . Therefore, τ_{asy} could be longer than the extracted value since τ_ϕ acts as a cut-off.

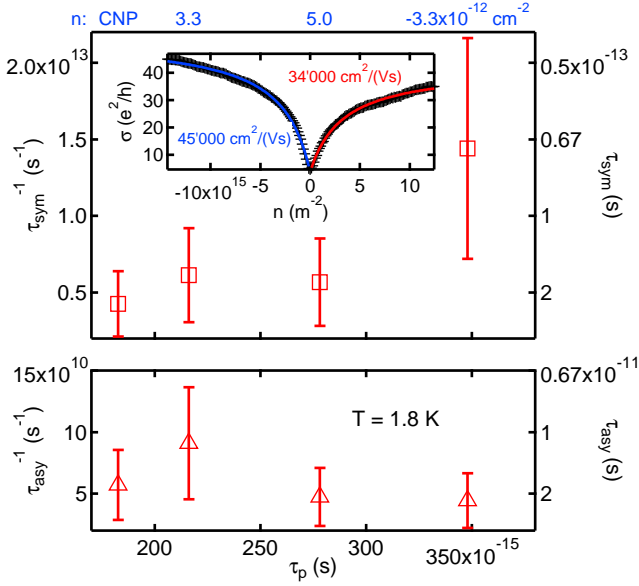


Figure 7.4. Density dependence of device C: The dependence of the spin-orbit scattering rates τ_{sym}^{-1} and τ_{asy}^{-1} as a function of τ_p are shown for device C. The error bars on the spin-orbit scattering rates are given by a conservative estimate of 50 %. The two terminal conductivity is shown in the inset and the extracted mobilities for the n and p side are indicated. The density of each data point is indicated in blue above the top graph. The magneto conductivity was averaged over a density range of $3.3 \times 10^{12} \text{ cm}^{-2}$ centered around the value given at the top. © 2018 American Physical Society

7.3.3. In-plane magnetic field dependence

An in-plane magnetic field (B_{\parallel}) is expected to lift the influence of SOC on the quantum correction to the magneto conductivity at sufficiently large fields. This means that a crossover from WAL to WL for z/-z asymmetric and a crossover from reduced WL to full WL correction for z/-z symmetric spin-

orbit coupling is expected at a field where the Zeeman energy is much larger than the SOC strength [73]. The experimental determination of this crossover field allows for an estimate of the SOC strength.

The B_{\parallel} dependence of the quantum correction to the magneto conductivity of device A at the CNP and at zero perpendicular electric field was investigated, as shown in Fig. 7.5. The WAL peak decreases and broadens with increasing B_{\parallel} until it completely vanishes at $B_{\parallel} \simeq 3$ T. Neither a reappearance of the WAL peak, nor a transition to WL, is observed at higher B_{\parallel} fields (up to 9 T). A qualitatively similar behaviour was observed for device D. Fits with equation 7.1 allow the extraction of τ_{ϕ} and τ_{SO} , which are shown in Fig. 7.5 (b) for B_{\parallel} fields lower than 3 T. A clear decrease of τ_{ϕ} is observed while τ_{SO} remains constant.

The reduction in τ_{ϕ} with increasing B_{\parallel} was previously attributed to enhanced dephasing due to a random vector potential created by a corrugated graphene layer in an in-plane magnetic field [70]. Similar results were obtained for a hBN/Gr/hBN heterostructure, which is shown in the appendix C. The clear reduction in τ_{ϕ} with constant τ_{SO} and the absence of any appearance of WL at larger B_{\parallel} also strongly suggests that a similar mechanism is at play here. Therefore, the vanishing WAL peak is due to the loss of phase coherence and not due to the fact that the Zeeman energy (E_z) is exceeding the SOC strength. Using the range where WAL is still present, we can define a lower bound of the crossover field when τ_{ϕ} drops below 80 % of its initial value, which corresponds to 2 T here. This leads to a lower bound of the SOC strength $\lambda_{SOC} \geq E_z \sim 0.2$ meV given a g factor of 2.

7.4. Interpretation and discussion of WAL measurements

The effect of SOC was investigated in high quality vdW-heterostructures of WSe₂/Gr/hBN at the CNP, as there the effects of SOC are expected to be most important. The two-terminal conductance measurements are not influenced by contact resistances nor pn-interfaces close to the CNP due to the dominance of the intrinsic graphene resistance at the CNP. At larger doping, the two-terminal conductance would need to be considered with care.

Phase coherence times around 4 ps to 7 ps were consistently found from fits to Eq. 7.1 and from the autocorrelation of UCF. It is commonly known that the phase coherence time is shorter at the CNP than at larger doping [68, 70]. Moreover, large diffusion coefficients lead to long phase coherence lengths being on the order of the device size ($l_{\phi} = \sqrt{D\tau_{\phi}} \approx 1 \mu\text{m}$), which in turn leads to large UCF amplitudes making the analysis harder.

In general Eq. 7.1 is only applicable for short τ_{iv} . Since τ_{iv} is unknown in these devices, only an estimate can be given here. WL measurements of graphene on hBN found τ_{iv} on the order of picoseconds [71], see also appendix C.

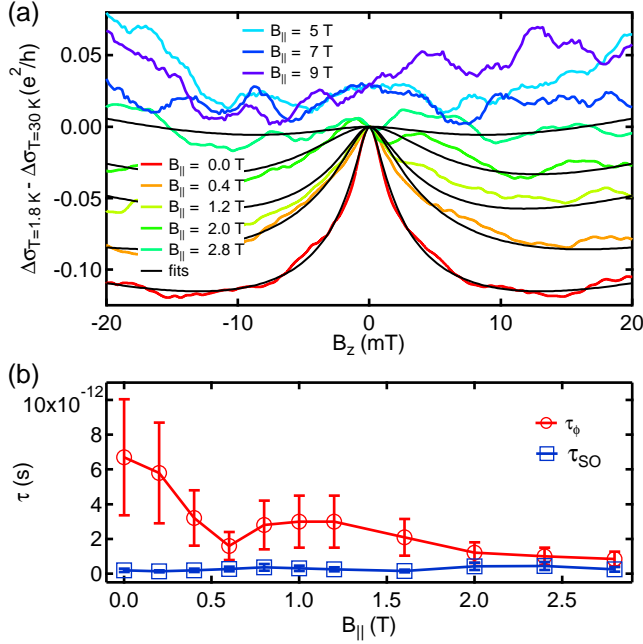


Figure 7.5. In-plane magnetic field dependence of device A: The quantum correction to the magneto conductivity at the CNP and at zero perpendicular electric field is shown for different in-plane magnetic field strengths B_{\parallel} in (a). Here, n was averaged in the range of $-1 \times 10^{11} \text{ cm}^{-2}$ to $1 \times 10^{11} \text{ cm}^{-2}$. The WAL peak gradually decreases in height and broadens as B_{\parallel} is increased. The traces at $B_{\parallel} = 5, 7, 9$ T are offset by $0.03 e^2/h$ for clarity. In (b) the extracted phase coherence time τ_{ϕ} and the total spin-orbit scattering time τ_{SO} are plotted versus B_{\parallel} . τ_{ϕ} clearly reduces, whereas τ_{SO} remains roughly constant over the full B_{\parallel} range investigated. The error bars on τ_{SO} and τ_{ϕ} are given by a conservative estimate of 50 %. © 2018 American Physical Society

Intervalley scattering is only possible at sharp scattering centres as it requires a large momentum change. It is a reasonable assumption that the defect density in WSe₂, which is around $1 \times 10^{12} \text{ cm}^{-2}$ [240], is larger than in the high quality hBN [135]. This leads to shorter τ_{iv} times in graphene placed on top of WSe₂ and makes Eq. 7.1 applicable despite the short spin-orbit scattering times found here. In the case of weaker SOC, Eq. 7.1 cannot be used. Instead, a more complex analysis including τ_{iv} and τ_* is needed. This was used for device D, and is presented in the appendix C.

The following part of the discussion is dedicated to the interpretation of the extracted spin-orbit scattering time scales τ_{asy} and τ_{sym} . First, their magnitude and their relative strength are discussed. Next, the individual spin-orbit components giving rise to τ_{sym} and τ_{asy} are considered and their strengths are estimated. Finally, an overview and a possible band structure are given.

7.4.1. Spin-orbit scattering times and their anisotropy

Spin-orbit scattering rates were successfully extracted at the CNP and τ_{asy} was found to be around 4 ps to 7 ps whereas τ_{sym} was found to be much shorter, around 0.1 ps to 0.3 ps. In these systems, if τ_{iv} is sufficiently short, $\tau_{asy}/2$ is predicted to represent the out-of-plane spin relaxation time τ_{\perp} and τ_{SO} then represents the in-plane spin relaxation time τ_{\parallel} [73]. For the time scales stated above, a lower bound of the spin relaxation anisotropy $\tau_{\perp}/\tau_{\parallel} \sim 20$ is found (see appendix C for detailed calculation). This large anisotropy in spin relaxation is unique for systems with a strong valley-Zeeman SOC [36]. Similar anisotropies have been found recently in spin valves in similar systems [241, 242]. While the measured spin relaxation anisotropy is similar, the time scales extracted from Hanle and spin valve measurements differ by roughly one order of magnitude from the time scales extracted here. This large discrepancy might be attributed to the different measurement techniques that could probe different time scales. However, further theoretical and experimental work is needed to clarify this issue.

In order to link spin-orbit scattering time scales to SOC strengths, spin relaxation mechanisms have to be considered. The simple definition of \hbar/τ_{SO} as the SOC strength is only valid in the limit where the precession frequency is much larger than the momentum relaxation rate (e.g. full spin precession occurs between scattering events). In the following we concentrate on the parameters from device A that were extracted close to the CNP. The dependence on τ_p in device A can most likely be assumed to be very similar to that observed in device C. Within the investigated density range of $-2.5 \times 10^{11} \text{ cm}^{-2}$ to $2.5 \times 10^{11} \text{ cm}^{-2}$, including residual doping, an average Fermi energy of 45 meV was estimated. This is based on the density of states of pristine graphene, which should be an adequate assumption for a Fermi energy larger than any

SOC strengths.

7.4.2. $z \rightarrow -z$ symmetric SOC (τ_{sym})

The symmetric spin-orbit scattering time τ_{sym} contains contributions from the intrinsic SOC and from the valley-Zeeman SOC. Up to now, only the intrinsic SOC has been considered in the analysis of WAL measurements, and the impact of valley-Zeeman SOC has been ignored. However, as we now explain, it is highly unlikely that intrinsic SOC is responsible for the small values of τ_{sym} .

In a first step, we only consider the intrinsic SOC as a source of spin relaxation. The intrinsic SOC is expected to relax spin via the Elliott-Yafet (EY) mechanism [102], which is given as

$$\tau_{sym,I} = \left(\frac{2E_F}{\lambda_I} \right)^2 \tau_p, \quad (7.2)$$

where $\tau_{sym,I}$ is the spin relaxation time stemming from intrinsic SOC only, E_F is the Fermi energy, λ_I is the intrinsic SOC strength and τ_p is the momentum relaxation time [102]. Since the intrinsic SOC does not lead to spin-split bands and hence no spin-orbit fields exist that could lead to spin precession, a relaxation via the Dyakonov-Perel mechanism can be excluded. Therefore, we can estimate $\lambda_I = 2E_F / \sqrt{\tau_{sym,I} \tau_p^{-1}} \sim 110$ meV using $\tau_{sym,I} \sim 0.2$ ps, a mean Fermi energy of 45 meV and a momentum relaxation time of 0.3 ps. The extracted value for λ_I would correspond to the opening of a topological gap of 220 meV. In the presence of a small residual doping (here 30 meV), such a large topological gap should easily be detectable in transport. However, none of our transport measurements confirm this. In addition, the increase of τ_{sym}^{-1} with τ_p , as shown in Fig. 7.4, does not support the EY mechanism. We therefore rule out the intrinsic SOC as the dominant spin relaxation origin.

On the other hand, Cummings et al. have shown that the in-plane spins are also relaxed by the valley-Zeeman term via a Dyakonov-Perel mechanism where τ_{iv} takes the role of the momentum relaxation time [36]:

$$\tau_{sym,VZ}^{-1} = \left(\frac{2\lambda_{VZ}}{\hbar} \right)^2 \tau_{iv}. \quad (7.3)$$

While this equation applies in the motional narrowing regime of spin relaxation, our measurement appears to be near the transition where that regime no longer applies. Taking this into consideration (see Supplemental Material), we estimate λ_{VZ} to be in the range of 0.23 meV to 2.3 meV for a $\tau_{sym,VZ}$ of 0.2 ps and a τ_{iv} of 0.1 ps to 1 ps. This agrees well with first principles calculations [47]. The large range in λ_{VZ} comes from the fact that τ_{iv} is not exactly known.

Obviously, τ_{sym} could still contain parts that are related to the intrinsic SOC ($\tau_{sym}^{-1} = \tau_{sym,I}^{-1} + \tau_{sym,VZ}^{-1}$). As an upper bound of λ_I , we can give a scale of

15 meV, which corresponds to half the energy scale due to the residual doping in the system. This would lead to $\tau_{sym,I} \sim 10$ ps. Such a slow relaxation rate ($\tau_{sym,I}^{-1}$) is completely masked by the much larger relaxation rate $\tau_{sym,VZ}^{-1}$ coming from the valley-Zeeman term. Therefore, the presence of the valley-Zeeman term makes it very hard to give a reasonable estimate of the intrinsic SOC strength and we conclude that $\tau_{sym} = \tau_{sym,VZ}$.

7.4.3. $z \rightarrow -z$ asymmetric SOC (τ_{asy})

The asymmetric spin-orbit scattering time τ_{asy} contains contributions from the Rashba-SOC and from the PIA SOC. Since the PIA SOC scales linearly with the momentum, it can be neglected at the CNP. Here, τ_{asy} represents only the spin-orbit scattering time coming from Rashba SOC. It is known that Rashba SOC can relax the spins via the Elliott-Yafet mechanism [102]. In addition, the Rashba SOC leads to a spin splitting of the bands and therefore to a spin-orbit field. This opens a second relaxation channel via the Dyakonov-Perel mechanism [243]. In principle the dependence on the momentum scattering time τ_p allows one to distinguish between these two mechanisms. Here, τ_{asy}^{-1} does not monotonically depend on τ_p as one can see in Fig. 7.4 and therefore we cannot unambiguously decide between the two mechanisms.

Assuming that only the EY mechanism is responsible for spin relaxation, then $\lambda_R = E_F / \sqrt{4\tau_{asy}\tau_p^{-1}} \sim 5.0$ meV can be estimated, using τ_{asy} of 6 ps, a mean Fermi energy of 45 meV and a momentum relaxation time of 0.3 ps. On the other hand, pure DP-mediated spin relaxation leads to $\lambda_R = \hbar / \sqrt{2\tau_{asy}\tau_p} \sim 0.35$ meV. The Rashba SOC strength estimated by the EY relaxation mechanism is large compared to first principles calculations [47], which agree much better with the SOC strength estimated by the DP mechanism. This is also in agreement with previous findings [233, 235].

7.4.4. Band structure analysis

Since there is a finite valley-Zeeman SOC, which is a result of different intrinsic SOC on the A sublattice and B sublattice, a staggered sublattice potential can also be expected. The presence of a staggered potential, meaning that the on-site energy of the A atom is different from the B atom on average, leads to the opening of a trivial gap of Δ at the CNP. Since there is no evidence of an orbital gap, we take the first principles calculations as an estimate of $\Delta = 0.54$ meV.

Knowing all relevant parameters in model tight-binding Hamiltonian (introduced in section 1.1.5), a band structure can be calculated, which is shown in Fig. 7.6. The bands are spin split mainly due to the presence of strong valley-Zeeman SOC but also due to the weaker Rashba SOC. At very low energies, an inverted band is formed due to the interplay of the valley-Zeeman and Rashba SOC, see Fig. 7.6 (b). This system was predicted to host helical edge states

for zigzag graphene nanoribbons, demonstrating the quantum spin Hall effect [47]. In the case of stronger intrinsic SOC, which we cannot estimate accurately, a band structure as in Fig. 7.6 (c) is expected with a topological gap appearing at low energies. We would like to note here, that this system might host a quantum spin Hall phase. However, its detection is still masked by device quality as the minimal Fermi energy is much larger than the topological gap, see also Fig. 7.6 (a), where the residual doping is indicated by the grey shaded region.

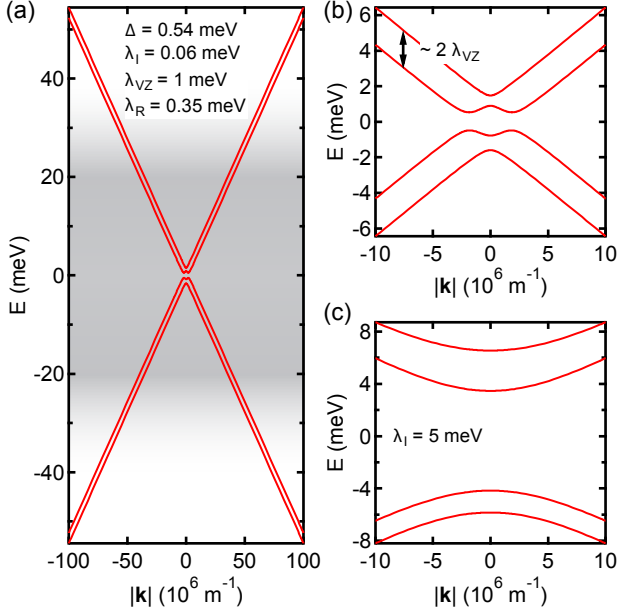


Figure 7.6. Possible low energy band structures: (a) and (b) show the band structures using the Hamiltonian described in section 1.1.5 with the parameters listed in (a). The unknown parameters Δ and λ_I were taken from Ref. [47]. In (a), the band structure is shown in the density range of $-2.5 \times 10^{11} \text{ cm}^{-2}$ to $2.5 \times 10^{11} \text{ cm}^{-2}$ (CNP), which corresponds to the one investigated above. The energy range dominated by charge puddles is indicated by the grey shaded region. (b) shows a zoom in at low energy. In (c), λ_I of 5 meV is assumed to show the changes due to the unknown λ_I at low energy.

Our findings are in good agreement with the calculations by Gmitra et al.

[47]. However, we have to remark that whereas the calculations were performed for single-layer TMDCs, we have used multilayer WSe₂ as a substrate. Single-layer TMDCs are direct band-gap semiconductors with the band gap located at the K-point whereas multilayer TMDCs have an indirect band gap. Since the SOC results from the mixing of the graphene orbitals with the WSe₂ orbitals, the strength of the induced SOC depends on the relative band alignment between the graphene and WSe₂ band, which will be different for single- or multilayer TMDCs. This difference was recently shown by Wakamura et al. [236]. Therefore using single-layer WSe₂ to induce SOC might even enhance the coupling found by our study. Furthermore, the parameters taken from Ref. [47] for the orbital gap and for the intrinsic SOC have to be taken with care.

7.5. Non-local resistances in hBN/graphene/WSe₂ heterostructures

The presence of strong SOC as presented above also implies that a considerable spin-Hall angle might exist in Gr/TMDC systems [39]. The generation of a pure spin current by the spin-Hall effect and its detection via the inverse spin-Hall effect can lead to non-local resistances that cannot simply be explained by current spread in the sample [244]. A brief introduction into SHE and ISHE and their connection to non-local resistances in a H-bar sample can be found in subsection 1.4.1. Previous studies have found very large non-local resistances that were explained by the presence of enhanced SOC in hydrogenated graphene [245], chemical vapour deposited graphene with remaining copper residues [246] and in graphene placed on top of a WS₂ crystal [232, 247]. However, there are, also studies that cannot confirm the spin-Hall effect and inverse spin-Hall effect as the origin of the large observed non-local signals in hydrogenated graphene [248] for example. Therefore, a careful analysis of the non-local signals are required to conclude about the possible enhancement of SOC.

The measurement scheme is shown in Fig. 7.7. A current is passed as indicated and the local resistance (R_1) is then given as $R_1 = V_1/I$. The two non-local voltages (V_2 and V_3) can be converted into non-local resistances the same way ($R_{2,3} = V_{2,3}/I$). The non-local resistance due to current spread can be estimated by:

$$R_{ohmic} = \frac{\rho}{\pi} e^{-\pi \frac{l}{w}}, \quad (7.4)$$

where ρ is the sheet resistance, w the width and l the length between the current path and the non-local voltage detection [244]. It is obvious from Eq. 7.4 that the ratio l/w should be large to suppress the ohmic contribution substantially. The metallic contacts to the graphene that are used to detect the non-local voltage can influence the measurement as they act as equipotential lines over their width. Therefore, the effective length for the device is shorter than L and as a lower bound L^* can be given, see Fig. 7.7 for clarity. Obviously the effect of the contacts depends on the ratio of d/s . The corresponding resistivity ρ can be measured in a four-terminal configuration in such Hall-bars. Therefore, it is possible to estimate the expected ohmic contribution to the non-local signal.

The same devices that were used for the investigation of the SOC via WAL measurements as presented above were also used to investigate the possibility of the creation and detection of spin currents via a combination of spin-Hall and inverse spin-Hall effect. Fig. 7.8 shows the non-local signals R_2 and R_3 as well as the corresponding ρ of this regions for device B. R_2 and R_3 peak when the graphene is tuned to charge neutrality. The largest non-local signals are observed around $V_{BG} = 30$ V, where the back gate is screened. To compare the

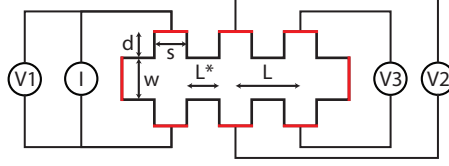


Figure 7.7. Non-local measurement scheme: The out-line of the Hall bar is shown in black and 1D side contacts to the graphene are indicated in red. The width (w), length (L) as well as the segment in between the contacts (L^*) and s and d are indicated. The voltage drop $V1$ is proportional to the local resistance $R1$. The non local resistance $R2$ and $R3$ are proportional to the non-local voltages $V2$ and $V3$.

measured non-local signal to the expected ohmic contributions, two cuts are shown in Fig. 7.8 (e) to (h). To give a bound for the ohmic contribution, R_{ohmic} was once calculated with $l = L = 1.5 \mu\text{m}$ and once with $l=L^*=1 \mu\text{m}$. The width w is $0.9 \mu\text{m}$. It is clear that the aspect ratio of the device is not perfectly suited for this kind of measurements as a substantial ohmic contribution is expected. However, the ohmic contribution is much smaller for most cases. This is especially pronounced for the increased non-local resistance around $V_{BG} \sim 30 \text{ V}$. The screening of the back gate is discussed later.

It is obvious from Fig. 7.8 that current spread alone cannot account for the large non-local resistance observed. In the following the dependence on top and back gate, temperature and magnetic field is investigated. All measurements here were performed in current bias (100 nA) at low frequencies (37.77 Hz). If not otherwise stated, the temperature was $\approx 1.7 \text{ K}$.

7.5.1. Density and electric field dependence of the non-local signal

A gate-gate map of $R1$ and $R2$ of device A is shown in Fig. 7.9. The local resistance $R1$ shows two charge neutrality points (CNPs) that are only tuned by the back gate, which can be associated with the regions close to the contacts as there is no top-gate. The CNP changing with both gates comes from the bulk of the sample. It is only this CNP that gives rise to a substantial non-local signal as observed in $R2$, see (b). $R2$ grows with increasing electric field (or in other words with more asymmetric gating). Two cuts at $V_{BG} = -28 \text{ V}$ and 18 V are shown in (c). The line shape of $R2$ is asymmetric in V_{TG} as a much sharper transition is observed on the unipolar side. At large positive V_{BG} , when the WSe₂ starts to conduct, the non-local signal $R2$ increases substantially. The fact that a kink in the position of the CNP is observed for large positive V_{BG} is a sign that the capacitive coupling of the back gate is

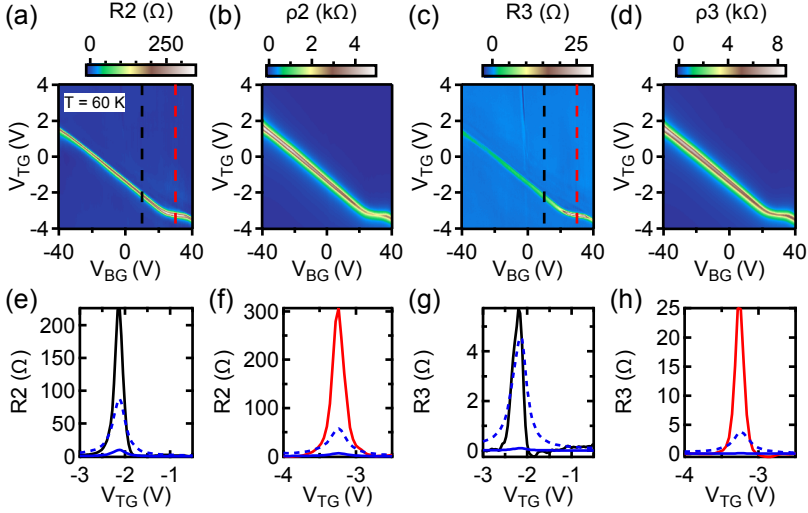


Figure 7.8. Ohmic contribution to non-local signal of device B: (a) to (d) show the non-local signal $R2$ and $R3$ and the corresponding resistivity ρ . Cuts at $V_{BG} = 10$ V (black) and 30 V (red) are shown in (e) to (h). The ohmic contribution for $l=L$ and $l=L^*$ are shown in blue solid and dashed lines respectively. All measurements were performed at a temperature of 60 K.

reduced. We interpret this as a (partial) screening of the back gate voltage by the WSe₂ that starts to conduct. A possible origin of this screening is discussed later in section 7.5.4.

7.5.2. Temperature dependence of non-local signal

Fig. 7.10 shows the local (a) and non-local (b,c) resistances of device B as a function of V_{TG} and V_{BG} for different temperatures. The non-local resistance peaks at the CNP of the bulk. Similarly to the data presented above, it also increases with more asymmetric gating, though less pronounced. The maximum of the non-local resistance $R2$ and $R3$ is found when the WSe₂ is conducting (where the back gate lever arm is reduced). This is especially pronounced in $R3$. As temperature is increased, the magnitude of the non-local resistance does not change much. Only the positions where the WSe₂ is conducting changes and starts to vanish at higher temperatures, which is observed for $R1$, $R2$ and $R3$ simultaneously. At 150 K (not shown) the CNP follows a straight line in the gate-gate map indicating that back gate

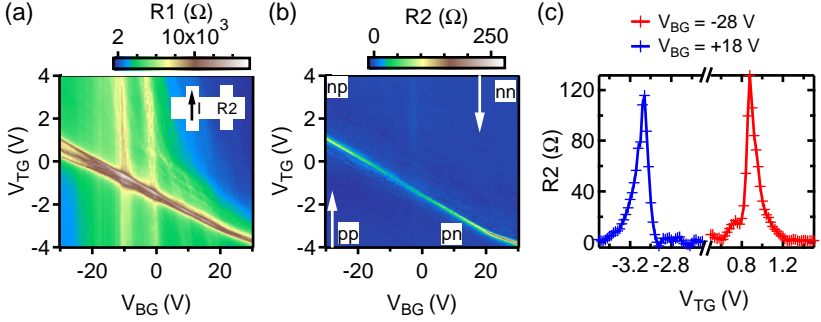


Figure 7.9. Gate-gate map of R1 and R2 of device A: (a) shows the local resistance (R1) as a function of V_{TG} and V_{BG} . The current path and the non-local voltage detection for R2 are indicated in the inset. (b) shows the non-local resistance R2 and two cuts, indicated by white arrows are shown in (c). The magnitude of R2 at the charge neutrality point increases with more asymmetric gating. The cuts in (c) show that the line-shape of R2 in V_{TG} is asymmetric with a sharper transition on the unipolar side. The doping state is indicated by letters in (b) where the first letter denotes the doping state of the top-gated region (bulk) whereas the second letter denotes the doping state of the region close to the contacts without a top gate. R2 increases significantly once V_{BG} is (partly) screened.

is not screened for any gate voltage combinations. The weak temperature dependence of the non-local signal is not supporting the combination of SHE and ISHE as its origin as it is expected that this effect should vanish with higher temperatures.² However, a doping related effect will survive to larger temperatures.

7.5.3. Magnetic field dependence and Hanle measurements

An in-plane magnetic field will lead to a Hanle effect of the out-of plane spin component that is responsible for the non-local resistances due to the spin-Hall and inverse spin-Hall effect. In order to test if the large non-local resistances observed above originate from a combination of spin-Hall and inverse spin-Hall effect, the influence of a magnetic field on the non-local resistance was investigated. Given the out-of plane spin relaxation time extracted from WAL measurements above ($\tau_{asy} \approx 5$ ps), the magnetic field scale at which the spin related signals will decay due to dephasing can be estimated from $\omega\tau_s = 1$ [244,

²Personal communication from Jose H. Garcia

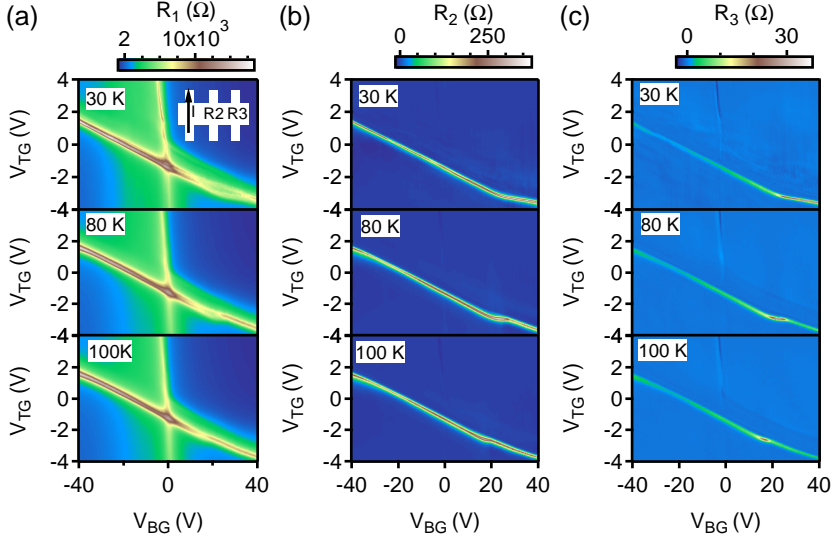


Figure 7.10. Temperature dependence of non-local resistance of device B: (a) The local resistance (R_1) as a function of V_{TG} and V_{BG} is shown for different temperatures. The Hall-bar on the top graph indicates the measurement scheme. A constant current is passed on the left where the local resistance (R_1) is measured. The two non-local resistance R_2 and R_3 are measured to the right. (b) shows the non-local resistance R_2 , that is closer to the current path. In (c) the non-local resistance R_3 is shown. The region in which the back gate voltage is (partially) screened shifts and reduces with increasing temperature until it is fully absent at 150 K

249], where ω is the Larmor precession frequency and τ_s the spin relaxation time. This can be solved for the magnetic field $B = 2m_e/(g\tau_s) \approx 7$ T, where m_e is the electron mass, $g = 2$ the g-factor and e the electron charge.

Since the sample plane is never fully aligned with the external magnetic field axes, there is always a finite out-of plane component if only one magnetic field axis is swept. For large in-plane fields (on the order of T) this can lead to a substantial out-of plane component on the order of 100 mT.

In Fig. 7.11 (a) R_2 of device B is shown as a function of density and B_x , which is mainly in-plane. (b) shows the dependence of R_2 on B_z in the range that is expected due to the finite misalignment of 2.8° . The misalignment was found from the shift of the WAL peak with increasing in-plane field, which is a sensitive measure of zero out-of plane magnetic field. (a) and (b) show

very similar dependencies and the subtraction of (b) from (a) results in the contribution of a pure in-plane magnetic field B_{\parallel} . R2 as a function of B_{\parallel} is shown in (c), which does not show any clear dependence on B_{\parallel} . Similarly one finds the same results for R1 and R3 (not shown here). Therefore, all observed changes in R1, R2 and R3 due to B_x can be explained by a small misalignment of the sample plane with the magnetic field axis.

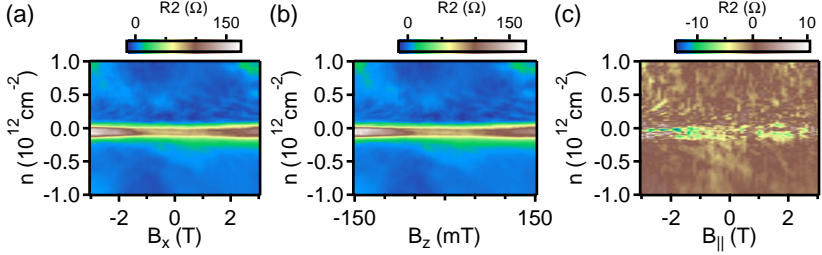


Figure 7.11. Magnetic field dependence of device B: The influence of a magnetic field on the non-local resistance R2 is shown. (a) shows R2 as a function of density and magnetic field in x-direction, whereas (b) shows the dependence of R2 on a magnetic field in z-direction. Here, the x-direction lies in the plane of the graphene and the z-axis is perpendicular to it. Since the sample plane is never fully aligned with the external magnetic field axes, a finite out-of-plane component will be present for any applied field in x-direction. (c) shows the corrected R2, that is only due to a pure in-plane magnetic field (B_{\parallel}). In this case the sample plane was misaligned by 2.8° with respect to the x-axis of the magnet.

Furthermore, the magnetic field dependence of R1 and R2 of device A were investigated as well. There, a misalignment of 0.7° was found between the sample plane and the main in-plane field axis. R2 as a function of V_{TG} and magnetic field is shown in Fig. 7.12 for device A. Similarly, no clear dependence on B_{\parallel} was found in this device. The large remaining fluctuations in R2 are mainly due to the lack of reproducibility and small sample changes in between the measurements.

The above presented findings clearly show that any in-plane magnetic field study has to be taken with care. It is of utmost importance that the field is applied in the plane of the graphene sheet as already a small misalignment of a few degrees can be a problem as it leads to substantial orbital effects.

Similar results were obtained from device D. The non-local signal was larger than expected by simple current spread. The measured non-local resistances were $\sim 200 \Omega$, which are one or two orders of magnitude larger than the contribution expected by current spread $\sim 10 \Omega$ (using $l = L$) and $\sim 1 \Omega$ (using

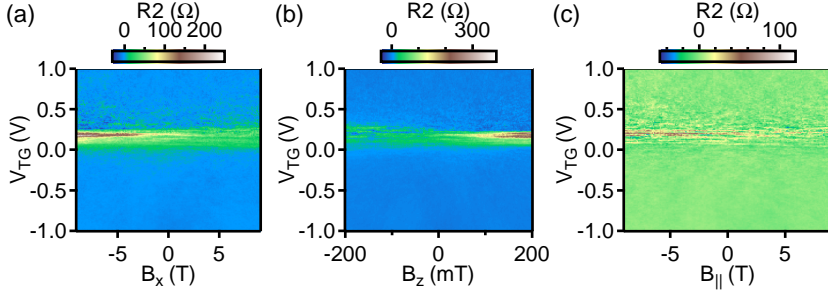


Figure 7.12. Magnetic field dependence of device A: The influence of a magnetic field on the non-local resistance R_2 is shown. (a) shows R_2 as a function of top gate voltage at $V_{BG} = -20$ V and magnetic field in x-direction, whereas (b) shows the dependence of R_2 on a magnetic field in z-direction. The coordinate system is the same as in Fig. 7.11 (c) shows the corrected R_2 , that is only due to a pure in-plane magnetic field ($B_{||}$). In this case the sample plane was misaligned by -0.7° with respect to the x-axis of the magnet.

$l = L^*$). In addition, no dependence on the the in-plane magnetic field was observed ruling out any spin-based contribution (out-of-plane spin that would give rise to spin Hall and inverse spin Hall effect).

The absence of any clear dependence of R_1 , R_2 and R_3 on $B_{||}$ shows that the large non-local signal is not due to the interplay of spin-Hall and inverse spin-Hall effect. This is not so surprising since only very small resistance changes would be expected. For example the local resistivity is expected to change on the order of 1×10^{-5} , depending on spin relaxation time and sample geometry [249]. From the residual resistance fluctuations due to the subtraction procedure and lack of perfect reproducibility, an upper bound of roughly 10Ω can be given for the spin related origin of the non-local resistance. Abanin et al. [244] derived an expression for the magnitude of the non-local resistance due to spin-Hall and inverse spin-Hall effect:

$$R_{nl} = \frac{1}{2} \theta_{SH}^2 \rho \frac{w}{\lambda_s} e^{-L/\lambda_s}, \quad (7.5)$$

where θ_{SH} is the spin-Hall angle, ρ the resistivity, w the sample width, λ_s the spin relaxation length and L the distance between current injection and non-local voltage probes. A rough estimate on the order of magnitude of the non-local signal due to spin-Hall and inverse spin-Hall effect results in $R_{nl} \approx 1 \Omega$ by assuming parameters that are rather optimistic, such as $\theta_{SH} = 4\%$ [39], $\rho = 10 \text{ k}\Omega$, $\lambda_s = \sqrt{D\tau_s} = 1 \mu\text{m}$ (using $D = 0.1 \text{ m}^2 \text{ s}^{-1}$ and $\tau_s = \tau_{asy} = 10 \text{ ps}$), and by using the known sample dimensions of $w = 1.2 \mu\text{m}$ and $L = 2 \mu\text{m}$.

This contribution is very small and if present, it is totally masked by the large background signal.

The origin of the large non-local signal is still unknown. The fact that R_2 and R_3 strongly depend on gate configuration and show an asymmetric line shape in V_{TG} point to the direction that the doping profile in the sample might play an important role. If the density at the edge is pinned or if the residual doping at the edge is larger than in the bulk, large non-local resistances can be expected if the bulk is tuned to the charge neutrality point, where its resistivity is high. A larger residual doping at the edge can readily be understood since disorder is expected to be much larger at the edge. Furthermore, a larger density or even a pinned density could be imagined by chemical functionalization of the edge. This can easily happen during device fabrication as the sample is shaped with reactive ion etching. It was shown that localized states at the edge can form in such samples [56]. In addition, the top gate that overlaps the sample edge could induce larger densities at the edge as there the lever arm is a bit larger than in the bulk, as it also gates from the side and not only from the top.

Close to the CNP, where the largest non-local resistance is observed, the sample is diffusive with a mean free paths below 100 nm. However, the mean free path rapidly increases with doping and ballistic features (transverse magnetic focussing) were observed at larger densities. Nonetheless, the large non-local signals cannot be explained by ballistic effects.

The charge carriers in graphene possess not only a spin degree of freedom, but also a valley degree of freedom. It was shown experimentally that by breaking the sublattice symmetry of the graphene lattice by aligning it with a hBN lattice, large non-local resistances could arise [250]. However, there is still a debate whether this non-local signals are due to topological valley currents or not [251]. In principle, the WSe₂ substrate could break the sublattice symmetry of the graphene as first principles calculations show the appearance of an orbital gap [47]. However, it is unclear how one would distinguish this effect from trivial doping related edge currents and therefore further work is needed to fully understand this behaviour.

7.5.4. Screening of back gate

As shown already above, the back gate in these heterostructure is found to be screened at large positive voltages. The extent of the screening depends on the temperature (screening over larger back gate range for lower temperature). In addition, the non-local resistance shows a clear maximum once the back gate is screened. The origin of this increase is not fully understood. This effect is used to quantify over which gate voltages the back gate is screened. Here we define that for $R_3 > 15 \Omega$ the back gate is screened. From this definition the minimal ($V_{BG,min}$) and maximal ($V_{BG,max}$) value of V_{BG} can be found. This

is shown in Fig. 7.13 together with the difference of gate voltage ($\Delta V_{BG} = \Delta V_{BG,max} - \Delta V_{BG,min}$) that can be converted into a density. One possible explanation for the screening of the back gate is that the Fermi energy is shifted away from the valance band with increasing electric field (positive electric field is pointing from the WSe₂ to the graphene). At some point a trap level is hit and the additional charge induced by the back gate is put into the trap states since the graphene is at the CNP. The number of available trap states is reduced with increasing temperature. This explains the shorter plateau-like feature that is observed at higher temperature.

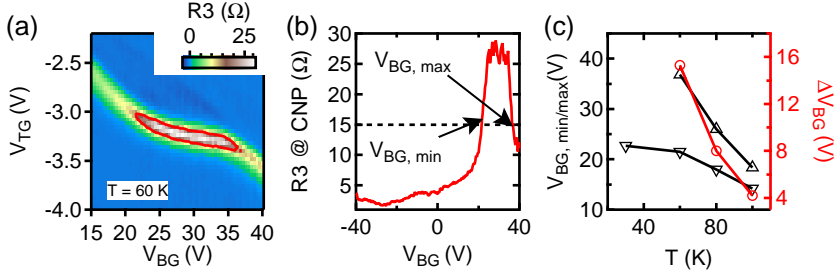


Figure 7.13. Screening of back gate for device B: (a) shows $R3$ at 60 K with a contour line of 15Ω in red. The extracted maximum of $R3$ (at the CNP) is shown in (b), where the cut-off of 15Ω is also indicated. $V_{BG,min}$ and $V_{BG,max}$ are extracted as indicated and plotted together with their difference in (c).

7.6. Alternative WSe₂ source and influence of WSe₂ quality

The interface between the graphene and the WSe₂ substrate is crucial for the observed enhancement of SOC in graphene. Obviously also the quality of the WSe₂ crystal matters as defects and grain boundaries could affect the proximity effect on graphene. Crystals from different sources can have different quality as shown in Ref. [240] where the authors investigated topography and defects in WSe₂ with a scanning tunnelling microscope. We therefore investigated devices with WSe₂ obtained from Nanosurf to compare it to devices with WSe₂ obtained from hq graphene. In general, devices with WSe₂ from Nanosurf showed more gate instabilities than the devices with WSe₂ from hq graphene. In addition, the resistance at the CNP was found to strongly depend on the temperature with a doubling of the resistance at 450 mK compared to 25 K, which was not observed in hBN/Gr/hBN devices nor in hBN/Gr/WSe₂ devices with WSe₂ from hq graphene, see Fig. 7.14. Furthermore, the up and

down sweep do not overlap and a shift of the CNP reveals a hysteretic gate behaviour. At the CNP large resistance fluctuations are observed that are not reproducible.

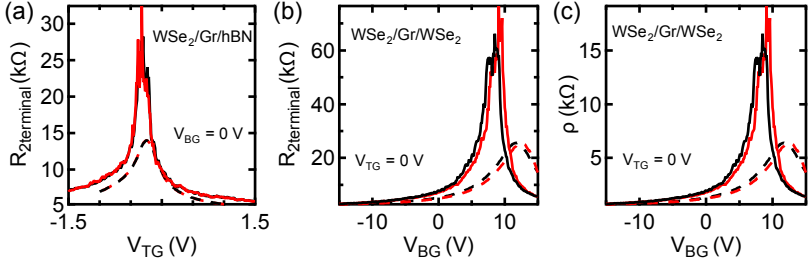


Figure 7.14. Alternative source of WSe₂, temperature dependence, gate instability: Solid lines correspond to a temperature of 450 mK, whereas dashed lines correspond to a temperature of 25 K. (a) shows the two terminal resistance of a WSe₂/Gr/hBN device as a function of top gate voltage. (b) shows the two terminal resistance and (c) shows the resistivity of a WSe₂/Gr/WSe₂ device as a function of back gate. Black traces correspond to up sweeps (from negative to positive voltage) and red correspond to down sweeps.

In Fig. 7.15, further characteristics of the device from Fig. 7.14 (a) are shown. A gate map of the two-terminal resistance is shown in (a). A varying lever arm of the gates indicates less reproducible device behaviour. A mobility of $\approx 17000 \text{ cm}^2 \text{ V}^{-1} \text{ s}^{-1}$ was found. Similar mobilities and changes of the resistance at the CNP were found in the other devices fabricated with this material.

The lower device stability (hysteresis and gate instabilities) can be related to a lower WSe₂ quality that leads to more charge traps than in high quality WSe₂ or hBN crystals. On the other hand, larger resistances at the CNP that are strongly temperature dependent could be explained by strong localization due to disorder [252]. However, a more thorough investigation would be needed to conclude about a possible strong localization.

In order to check for the presence of enhanced SOC, magneto conductivity was measured close to the CNP, see Fig. 7.15 (b) and (c). As previously discussed, an ensemble averaging was performed to average out the influence of UCF. The resulting magneto conductivity shows a clear dip around zero magnetic field and shows no feature of weak antilocalization. The absence of any clear sign of weak antilocalization shows that there is no z/-z asymmetric SOC present in the system. Most likely, there is also no z/-z symmetric SOC

present as this would lead to a reduced weak localization signal. However, it is hard to conclude anything about the SOC in these device as the positive magneto conductance cannot unambiguously be attributed the presence of normal WL or to the presence of z/-z-symmetric SOC.

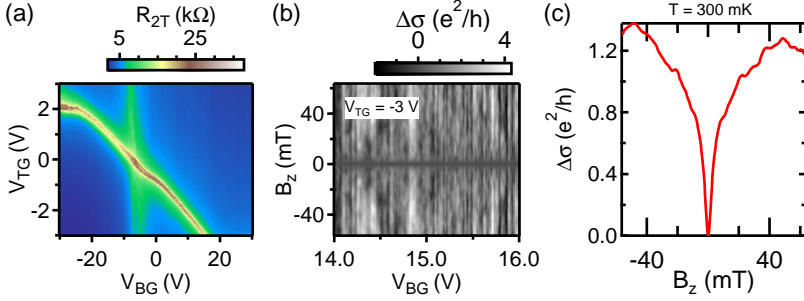


Figure 7.15. Devices with WSe₂ from an alternative source: (a) shows the two terminal resistance as a function of top gate and back gate voltage. (b) shows the magneto conductivity close to the CNP. The back gate voltage was varied within 14 V to 16 V to average out the influence of UCF. (c) shows the average over all gate traces in (b) and a clear weak localization feature is observed. The temperature of all measurements was 300 mK

7.6.1. Fully WSe₂ encapsulated graphene

Graphene encapsulated by WSe₂ on the bottom and on the top is interesting mainly due to two reasons. First, the symmetry in z-direction of the structure is different from hBN/Gr/WSe₂. This could have important consequences on the strength of the different SOC terms. Rashba SOC is expected to be fully absent or at least greatly suppressed [53]. Similar arguments hold for the PIA SOC [53]. On the other hand, one naively could imagine that the other SOC terms would be doubled as the electrons in the graphene experience strong SOC on both sides of the graphene.

To investigate the influence of the symmetry of the structure in z-direction on the SOC, fully WSe₂ devices were fabricated from WSe₂ obtained from Nanosurf. The resistivity of such a device is shown in Fig.7.16 (a). A field effect mobility of $\sim 15\,000\text{ cm}^2\text{ V}^{-1}\text{ s}^{-1}$ and a residual doping of $\sim 8 \times 10^{10}\text{ cm}^{-2}$ was extracted. Due to the lower quality of the WSe₂ only a very broad CNP is observed. In addition, this device showed rather inhomogeneous charge transport. Nevertheless, the magneto conductivity was measured to investigate possible SOC. To reduce the influence of the UCF, the magneto conducti-

vity was measured at different gate voltages close to the CNP as shown in Fig. 7.16 (b). Here, the lower quality of the WSe₂ is also visible since several gate jumps occur during the measurement. The average of this map is shown in Fig. 7.16 (c) that shows a clear dip at $B_z = 0$ mT but no further sign of typical weak localization nor antilocalization.

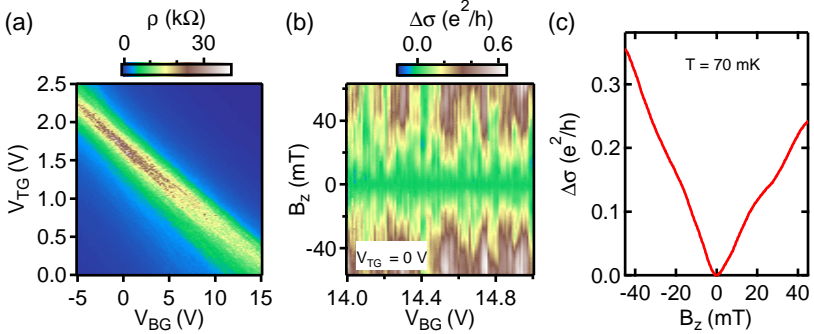


Figure 7.16. Fully WSe₂ encapsulated graphene: The resistivity, obtained in a four terminal configuration, of a fully WSe_e encapsulated device is shown in (a) as a function of top and back gate voltage. (b) shows the magneto conductivity close to the CNP. The back gate voltage was varied within 14 volt to 15 volt to average out the influence of UCF. Several gate jumps are visible in this measurement. (c) shows the average over all back gate traces in (b). The conductivity shows a minimum at $B_z = 0$ mT but does not look like a typical weak localization feature.

In the absence of z/z asymmetry (fully WSe₂ encapsulated graphene), a reduced weak localization is expected in the magneto conductivity that accounts for the presence of $z/-z$ symmetric SOC terms [73]. The fact that the magneto conductivity shown in Fig. 7.16 (c) does not resemble a typical weak localization shape, a clear statement about the presence or absence of any SOC is very hard. Similar results were also found in three further devices that consisted of fully WSe₂ encapsulated graphene.

Since the low field magneto conductivity is not a robust measure to detect SOC in symmetric structures, the investigation of Shubnikov-de-Has (SdH) oscillations could prove useful. It is well known that the spin splitting of single band leads to a beating in the SdH oscillations, which was recently observed in bilayer graphene in contact to WSe₂ [149].

7.7. Conclusion

In conclusion we measured weak antilocalization in high quality $\text{WSe}_2/\text{Gr}/\text{hBN}$ vdW-heterostructures at the charge neutrality point. The presence of a clear WAL peak reveals a strong SOC. Whereas previous studies have also found a clear WAL signal, we present for the first time a complete interpretation of all involved SOC terms considering their relaxation mechanisms. This includes the finding of a very large spin relaxation anisotropy that is governed by the presence of a valley-Zeeman SOC that couples spin to valley. The relaxation mechanism at play here is very special since it relies on intervalley scattering and can only occur in materials where a valley degree of freedom is present and coupled to spin. This is in good agreement with recent spin-valve measurements that found also very large spin relaxation anisotropies in similar systems [241, 242].

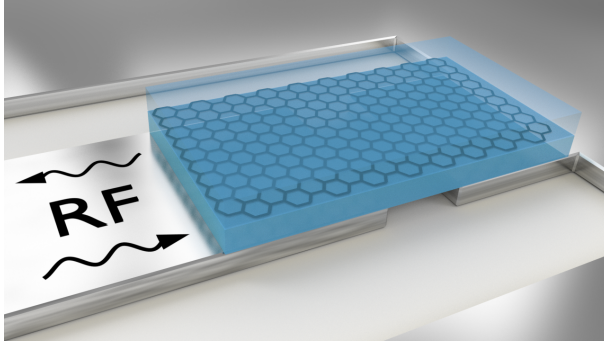
In addition, we investigated the influence of an in-plane magnetic field on the WAL signature. Due to the loss of phase coherence, a lower bound of all SOC strengths of 0.2 meV can be given, which is in agreement with the numbers presented above. This approach does not depend on the accurate fitting of WAL peaks nor on the interpretation of the extracted spin-orbit scattering rates and is therefore a very robust method.

Large non-local resistance signals were found in $\text{WSe}_2/\text{Gr}/\text{hBN}$ vdW heterostructure. Possible contributions of the SHE and ISHE to the non-local resistances were investigated and we found a negligible contribution. This is mainly based on the fact that no dependence on the in-plane magnetic field was found that could confirm the presence of a spin related phenomenon.

It turned out that the quality of the WSe_2 and its interface to the graphene is of utmost importance in enhancing the SOC in graphene. Different sources of WSe_2 lead to different device qualities in terms of charge transport on one side and in terms of induced SOC on the other hand. Only WSe_2 from hq graphene was found to induce a sizeable SOC in graphene.

The coupling of spin and valley opens new possibilities in exploring spin and valley degrees of freedom in graphene. In the case of bilayer graphene in proximity to WSe_2 an enormous gate tunability of the SOC strength is predicted since full layer polarization can be achieved by an external electric field [37, 38]. This is just one of many possible routes for future investigations.

8 Quantum capacitance and dissipation in graphene pn-junctions¹²



In this chapter a new contactless characterization technique of graphene pn-junctions is presented. A superconducting resonant circuit is capacitively coupled to a high quality hBN encapsulated graphene sheet. This allows the simultaneous extraction of the quantum capacitance and the charge relaxation resistance. In contrast to standard transport experiments on graphene devices presented in the previous chapters, this technique offers an alternative way to study intrinsic properties.

¹This chapter is a collaborative work with Vishal Ranjan, who also prepared most of the figures.

²This chapter has been published in a similar form in Ref. [253].

8.1. Introduction

Since the discovery of graphene in 2004, many interesting physical properties of Dirac particles on-chip have been unravelled [26, 43, 44]. The most common technique to characterize graphene remained low frequency lock-in transport measurements, where electrical contacts are an essential part of the device. It is well known that contacts can influence and degrade the device quality by the formation of unwanted pn-junctions at the contacts due to doping [254] and enhanced scattering [255]. Furthermore, resist residues from lithography can degrade metal-graphene interfaces [256] or even the overall device quality. An important example are graphene spin valves, which are discussed in chapter 5. The device quality in graphene spin valves is often limited by the contacts, which cause spin relaxation and decrease of spin lifetime [193, 201, 257, 258]. Therefore, a contactless characterization such as microwave absorption [259] and microwave-impedance microscopy [260] can open up new ways to probe inherent properties of the studied system. Up to now, other contactless schemes such as terahertz spectroscopy [158, 261] and dielectric force microscopy [262] have been employed to study the charge carrier dynamics in graphene. In contrast to the former, microwave response used in this work here precludes any interband or intraband transitions allowing the study of charge carriers at the Fermi level. Most important, our approach allows for a complete on-chip implementation of devices and readout circuit that allows to extract quantum capacitance and charge relaxation resistance in a single measurement even in the absence of any electrical contacts.

In this chapter we present a novel method of characterizing graphene pn-junctions without the need of electrical contacts. High mobility graphene encapsulated between hBN is capacitively coupled to a microwave resonator working at gigahertz frequencies. Here we used a stub tuner as a microwave resonator [263]. Local gating allowed us to probe the internal charge dynamics from which the quantum capacitance (briefly discussed in section 1.1.1 and the charge relaxation resistance can be inferred.

8.2. Device layout

The layout of a typical device investigated here is shown in Fig. 8.1. The stub tuner made out of superconducting niobium is based on two transmission lines TL_1 and TL_2 of lengths l and d , each close to $\lambda/4$ [263]. The working principle of the stub tuner can be understood in a simple analogy to optics. The incoming microwave signal is split at the T-junction that acts as a beam splitter. The microwave signal then travels down both arms and reflects at the open and at the device end. Depending on the device load, different interference conditions are present at the T-junction that provide the resonance condition.

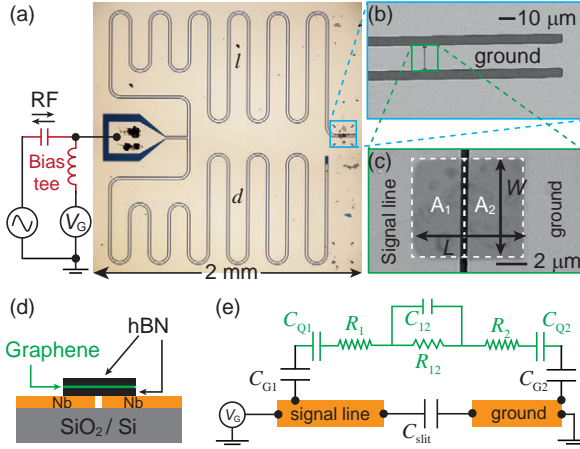


Figure 8.1. Sample layout: (a) An optical picture of the stub tuner with arm-lengths l and d . The central conductor and the gap widths of the transmission lines are $15\ \mu\text{m}$ and $6\ \mu\text{m}$ respectively. Light areas show the Nb film and darker areas are exposed SiO_2 substrate after the Nb is etched away. (b) An SEM image near the l end showing a narrow slit between the signal line and the ground plane. (c) An SEM image of a hBN/Gr/hBN stack for device B placed over the slit. Areas A1 and A2 correspond to the two parts of the graphene lying on the signal line and the ground plane, respectively. (d) A cross section schematic of the device near the slit. (e) An equivalent circuit with lumped capacitance and resistance elements. © 2018 American Physical Society

The circuit is patterned in a 100 nm thick Nb film employing standard e-beam lithography and a dry etching process employing Ar/Cl_2 . In order to minimize microwave loss, the sample is fabricated on an intrinsic, high resistive silicon wafer with a 170 nm thick SiO_2 layer. The signal line of the TL_1 features a narrow slit (450 nm) insulating it from the ground plane to the right, see also Fig. 8.1 (b) and (c). We placed a hBN/Gr/hBN heterostructure across this slit using a dry pick-up method described in more detail in section 2.1. The stack was positioned such that parts of it were lying on top of the signal line (area A1) and parts on the ground plane (area A2). E-beam lithography and reactive ion etching were then used to structure the stack into a well defined rectangular geometry. Details on the fabrication of the niobium resonator can be found in appendix A.

The lack of electrical contacts allowed us to change the shape of the device

while using the same RF circuit. We first fabricated a device with dimensions $W \times L$ of $6.5 \mu\text{m} \times 13 \mu\text{m}$ (device A), with W and L indicated in Fig. 8.1 (c). After measuring device A, the stack was reshaped into the following dimensions of $6.5 \mu\text{m} \times 9.6 \mu\text{m}$ (device B). Both devices consisted of an area A_1 lying on top of the signal line (gate) of $6.5 \mu\text{m} \times 3.4 \mu\text{m}$. The graphene section lying above the ground plane (area A_2) was $6.5 \mu\text{m} \times 9.6 \mu\text{m}$ for device A and $6.5 \mu\text{m} \times 3.8 \mu\text{m}$ for device B. Hence, device A was asymmetric whereas device B was quasi symmetric around the slit. This two devices, using the same resonant circuit, allowed for consistency checks and helped in understanding the gating of these devices. A third symmetric device C of dimension $5 \mu\text{m} \times 12 \mu\text{m}$ fabricated on a separate resonator circuit and a different vdW-heterostructure was also investigated.

8.2.1. Measurement principle

The graphene properties were extracted by measuring the complex reflection coefficient from the stub tuner, which depends on the RF admittance of the load [264]. A vector network analyser is used to measure the reflected part of the probe RF signal fed into the launcher port of the circuit. In order to change the Fermi energy of the graphene a gate voltage V_G is applied to the signal line with the help of a bias tee as shown in Fig. 8.1 (a). The gate voltage changes locally the density and hence the quantum capacitance and also the resistance of the graphene. Careful analysis of the RF response of the circuit at different gate voltages allowed us to extract differential capacitance, related to geometric and quantum capacitance, and dissipation, related to losses and charge relaxation resistance in the graphene. All measurements were performed at a temperature of 20 mK and with an input power of -110 dBm. Even though the Nb resonator could also be operated at higher temperatures (still below T_c), 20 mK was chosen to maximize the quality factor and hence the sensitivity of the RF resonator to changes in C and R of the load impedance.

Since the graphene is not connected to any electrode the total charge on the graphene is conserved and therefore gating works a bit different than in conventional devices. A gate voltage on the signal line induces charge carriers on the graphene part lying on top of it (area A_1). The only source of charge carriers is the graphene area lying on top of the ground plane (area A_2). Therefore, gating will always influence both areas simultaneously. In the case of a pristine graphene sheet (Fermi energy at the CNP without gating), any gate voltage applied to the signal line will lead to the formation of a pn-junction at the slit. However, if a finite offset doping is present, which is generally the case for any graphene device, an offset voltage has to be applied to the gate to drive the graphene charge neutral. The CNP is reached at two different gate voltages, once for each part of the graphene. At voltages larger than this offset voltages (in absolute values) a pn-junction will be present in the

graphene. The charge carrier density is homogeneous within each part of the flake and only changes rapidly close to the slit. Due to different areas A_1 and A_2 , the applied gate voltage results in different charge carrier densities but equal and opposite total charge on the two parts.

In the transmission line geometry, the RF electric field emerges from the signal line and terminates on the ground plane. While the electric field lines are quasi-perpendicular to the graphene sheet far away from the slit, they become parallel and relatively stronger in magnitude close to the slit. The field distribution hence probes the properties of the bulk graphene (homogeneous charge distribution) and the properties of the pn-junction at the slit (inhomogeneous charge distribution). For simplicity, we model the graphene as lumped one dimensional elements of capacitance and resistance as shown in Fig. 8.1 (e). The graphene impedance is then simply given as $Z_G \sim R + 1/(j\omega C)$ with the total series capacitance C and resistance R as

$$\frac{1}{C} = \frac{1}{C_{G1}} + \frac{1}{C_{Q1}} + \frac{1}{C_{G2}} + \frac{1}{C_{Q2}}, \quad (8.1)$$

$$R = R_1 + R_{12} + R_2, \quad (8.2)$$

where $\omega = 2\pi f$ is the angular frequency and j is the imaginary unit. Thus $C_Q = C_{Q1}C_{Q2}/(C_{Q1} + C_{Q2})$ and $C_G = C_{G1}C_{G2}/(C_{G1} + C_{G2})$ are the total quantum and geometric capacitances of the graphene device. We have assumed that the junction capacitance C_{12} is relatively small so that the junction resistance $R_{12} \ll 1/(\omega C_{12})$. Moreover, we ignore the parallel slit capacitance C_{slit} which is relatively small and gate independent. Together with the load Z_G , the reflectance response Γ of the stub tuner can now be described by $[(Z_{\text{in}} - Z_0)/(Z_{\text{in}} + Z_0)]^2$ where the input impedance Z_{in} is given as [265]

$$Z_{\text{in}} = Z_0 \left(\tanh(\gamma d) + \frac{Z_0 + Z_G \tanh(\gamma l)}{Z_G + Z_0 \tanh(\gamma l)} \right)^{-1}, \quad (8.3)$$

with $Z_0 \sim 50\Omega$ the characteristic impedance of the transmission line, $\gamma = \alpha + j\beta$ the propagation constant, α the attenuation constant, $\beta = \sqrt{\epsilon_{\text{eff}}}\omega/c$ the phase constant, ϵ_{eff} the effective dielectric constant and c the speed of light.

8.3. Reflectance results

The reflectance response of device B is shown in Fig. 8.2 as a function of frequency and gate voltage. Large frequency shifts at two gate voltages are observed close to $V_G = 0\text{V}$. These two points can be associated with driving either area A_1 or area A_2 charge neutral. At larger gate voltages a pn-junction forms at the slit separating a homogeneously doped n-doped region

from a homogeneously p-doped region. This behaviour was observed for all three samples investigated and is characteristic for a finite offset doping of the graphene flake. Fig. 8.2 (b) shows two line cuts, where changes in resonance depth, resonance width and resonance frequency are apparent. In a simple picture a pure capacitive load should only shift the resonance frequency while a pure resistive load should only change dissipation and hence the width and depth of the resonance.

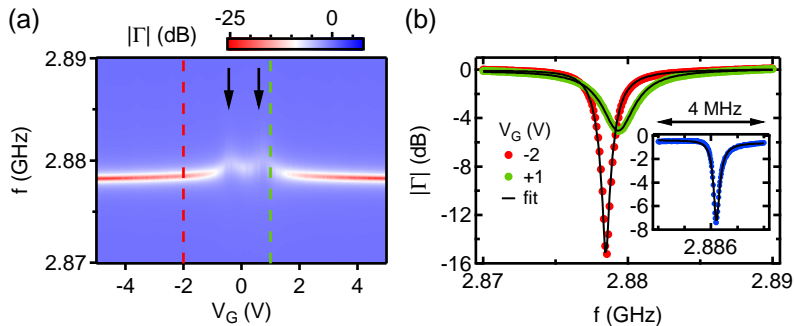


Figure 8.2. Reflectance response of device B: (a) A color map of the measured reflectance power near the resonance frequency versus different gate voltages. Arrows denote the charge neutrality points. (b) Main panel: Cuts of the reflectance curves at two different gate voltages with fits to the Eq. 8.3. Inset: The reflectance response of the same circuit but without any graphene stack. The input RF power is -110 dBm which corresponds to an AC excitation amplitude of $0.7 \mu\text{V}$. Note that the range of frequency is different in the inset.

In order to extract quantitative values of Z_G from fitting Eq. 8.3 to the data presented in Fig. 8.2 one first needs to extract the stub tuner parameters l , d , α and ϵ_{eff} . This can be done by analysing the reflectance response of the same circuit without the hBN/Gr/hBN stack. Therefore, the hBN/Gr/hBN stack was removed by reactive ion etching and the open circuit response, shown as inset in Fig. 8.2 (b), was fitted using Eq. 8.3 with $Z_G = \infty$. We extracted $l \approx 10.57$ mm and $d \approx 10.39$ mm, $\alpha \approx 0.0025 \text{ m}^{-1}$ and an effective dielectric constant $\epsilon_{eff} \approx 6.1$. The extracted lengths are within 1 % of the designed geometric lengths and the loss constant corresponds to an internal quality factor of 25 000, which is commonly achieved with superconducting niobium. The capacitive load of our sample is clearly seen from the resonance frequency of the open stub tuner (2.889 GHz) that is larger than the values in Fig. 8.2 (a). Fixing the extracted stub tuner parameters we can now extract the complex

graphene impedance Z_G containing C and R . As shown in Fig. 8.2 (b), the fitting yields $R = 118 \Omega$, $C = 18.2 \text{ fF}$ for $V_G = -2 \text{ V}$ and $R = 328 \Omega$, $C = 17.2 \text{ fF}$ for $V_G = 1 \text{ V}$. C and R as a function of gate voltage are obtained by fitting the stub tuner response for all gate voltages and the deduced C and R are shown in Fig. 8.3 and 8.4.

8.3.1. Quantum capacitance

We observe for all devices a double dip feature in the extracted capacitance close to $V_G = 0 \text{ V}$, indicating an offset doping. In addition, the capacitance saturates at higher gate voltages as shown in Fig. 8.3. While the two dips have similar widths for device B and device C, these are quite different for device A. This can be understood by considering the asymmetry of device A that results in different charge densities on each part. According to Eq. 8.1, the total capacitance is given by the gate capacitances and the quantum capacitances. The geometric gate capacitance C_{Gi} with $i = 1, 2$ is simply given as $C_{Gi} = \epsilon_0 \epsilon_{hBN} A_i / d$, where ϵ_0 , is the vacuum permittivity, ϵ_{hBN} the dielectric constant of hBN, A_i the area of the graphene flake and d_{hBN} the thickness of the bottom hBN flake estimated by AFM measurements. The quantum capacitance, on the other hand, can be derived from the density of state (DoS) as $C_Q/A_i = e^2 \text{DoS}_i$. The dependence of C_Q in graphene with gate voltage V_G is explicitly given as [266–269]

$$C_{Qi}(V_i) = A_i \frac{4\pi e^2}{h v_F \sqrt{\pi}} \sqrt{n_i(V_i)}, \quad (8.4)$$

with $i = 1, 2$ and v_F the Fermi velocity and h the Planck's constant. Here, we neglect the influence of C_Q on the gating. The gate induced charge carrier density is $n_i(V_i) = (V_i - V_i^0) C_{Gi} / (e A_i)$, where V_i^0 accounts for a finite offset doping and $V_i = V_G \frac{A_i}{A_1 + A_2}$ accounts for the different carrier densities on the two graphene parts due to their different areas. Now, it is straightforward to see from Eq. 8.1 and 8.4 that C is dominated by C_G at large gate voltages leading to the saturation of the capacitance at C_G . Since the devices have different sizes and hence different C_G , the saturation value is different for each device.

In contrast, close to the CNP ($C_Q \leq C_G$), the quantum capacitance starts to dominate. In an ideal system, C should go completely to zero as the DoS vanishes at the CNP. However, residual doping n_i^* resulting from charge puddles [270] prevents this from happening. To account for a finite residual doping we replace $n_i(V_i)$ with a total charge carrier density including this factor $\sqrt{n_i^2(V_i) + n_i^{*2}}$. We now proceed with fitting the total capacitance using Eq. 8.1, where ϵ_{hBN} , n_i^* and v_F are fitting parameters. This is shown by solid red lines in Fig. 8.3. The excellent fit captures not only the width but also the depths of both dips near the CNP of the graphene, justifying the

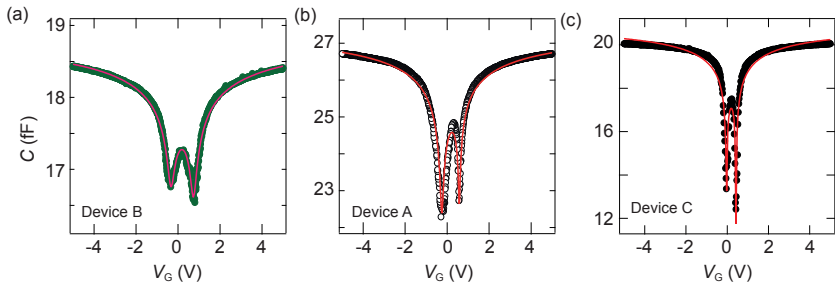


Figure 8.3. Quantum capacitance of graphene: The total extracted capacitance from fitting the reflectance response to Eq. 8.3 for three devices. Solid black lines are fits to Eq. 8.4 showing excellent agreement with the density of states of single layer graphene. Error bars are smaller than the symbol size.

simple lumped element circuit introduced in Fig. 8.1 (e). The extracted fit parameters are listed in Tab. 8.1. The dielectric constant of hBN was found to be around 4 as previously reported [121]. Residual doping levels of around $1 \times 10^{10} \text{ cm}^{-2}$ were found that are consistent with transport measurements reported in hBN/Gr/hBN samples [137, 150, 270]. A very low residual doping in device C goes along with an increased Fermi velocity. In this device the Fermi energy can be tuned to much lower energy than in device A or B as also observed by the much deeper dip in capacitance. Such a renormalization of v_F due to electron-electron interactions close to the CNP has been observed both in capacitance [269] and transport measurements [271–273] in homogeneously doped graphene.

Table 8.1. Overview over capacitance fit parameters: Extracted fit parameters ϵ_{hBN} , n_i^* and v_F for all three devices investigated.

	ϵ_{hBN}	$n_1^* \times 10^{10} \text{ cm}^{-2}$	$n_2^* \times 10^{10} \text{ cm}^{-2}$	$v_F^* \times 10^6 \text{ m s}^{-1}$
device A	4	5	1	1.05
device B	4	7	6	0.95
device C	4.25	0.4	0.35	1.54

8.3.2. Charge relaxation resistance

The extracted real part of Z_G is shown in Fig. 8.4 for device A and B. The resistance of C shows qualitatively the same behaviour and can be found in

the appendix E. We consistently observe a double peak feature in R , which goes along with the double dip feature observed in C that indicates the CNP of either part of the graphene. Even though device A is twice as long as device B, their resistances saturate both at the same value for large gate voltages. Since there are no contacts involved that could lead to resistance saturation, we attribute the observed resistance saturation to the pn-junction formed at the slit between two homogeneously doped graphene parts. Closer to the CNP, the respective bulk parts of the graphene also contribute significantly to the total resistance. These findings are in agreement with the density dependence of the conductivity in the bulk and in pn-junctions in graphene. While the conductivity of a ballistic pn-junction [274] scales with $n^{1/4}$, it scales with n or $n^{1/2}$ for the bulk graphene depending on the relevant scattering mechanism [275].

Transport in the bulk of the graphene can be characterized by the diffusion constant D . Using the Einstein relation, D can be related to the simultaneously measured R and C_Q

$$D = L^2 / (RC_Q). \quad (8.5)$$

Since there is almost always a pn-junction present in our samples, the extraction of D is not as simple as in a homogeneously doped sample. Therefore, we can only give an estimate of D by considering R and C_Q that arise mostly

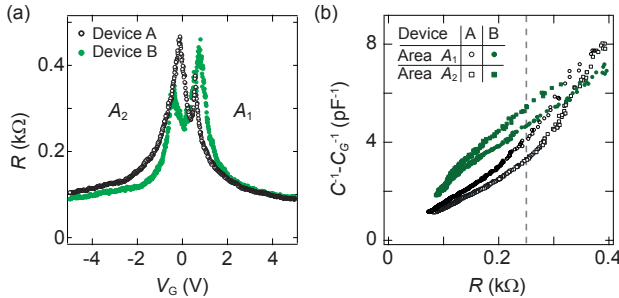


Figure 8.4. Dissipation in graphene: (a) The extracted charge relaxation resistance for devices A and B fabricated on the same hBN/graphene/hBN stack. The same loss constant is used in fitting the reflectance map. (b) The extracted R for device C with a different stack and a different circuit. (c) Inverse quantum capacitance obtained by subtracting the geometric capacitance from the total extracted capacitance is shown as a function of the simultaneously extracted charge relaxation resistance. © 2018 American Physical Society

from one graphene area only (either A_1 or A_2). As previously discussed, R saturates at large gate voltages at the pn-resistance and close to the CNP both areas contribute significantly. Here, we investigate only data points that are strictly on the left (negative V_G) or on the right (positive V_G) of the CNP, as shown in Fig. 8.4 (b). D is extracted at a moderate doping as indicated by the dashed line. Since the contribution from the pn-resistance R_{12} to the total resistance cannot be separated, D will be underestimated since the total R is an upper bound for the bulk graphene resistance. For the graphene area A_1 (lying on the signal line) we extract $D = 0.19 \text{ m}^2 \text{ s}^{-1}$ for device A and $D = 0.21 \text{ m}^2 \text{ s}^{-1}$ for device B. In contrast, D of the graphene area A_2 (lying on top of the ground plane) is $1.2 \text{ m}^2 \text{ s}^{-1}$ for device A and $0.31 \text{ m}^2 \text{ s}^{-1}$ for device B. The large change in D for area A_2 from device A to B is consistent with the substantially increased residual doping for device B. This can be attributed to the additional etching step performed to shape the graphene area A_2 . The mean free path of the charge carriers were estimated as $l_{mfp} = 2D/v_F$ to be around $1.4 \mu\text{m}$ and $0.5 \mu\text{m}$. Similar analysis of device C results in a diffusion constant of $0.44 \text{ m}^2 \text{ s}^{-1}$ and mean free path of $0.92 \mu\text{m}$.

8.4. Discussion

An obvious uncertainty in the extraction of R and C from the reflected microwave signal lies in the determination of the open stub tuner parameters, especially the loss constant α . Here, we rely on the fact that the loss constant α does not change substantially between different cool downs and is also not affected by processing steps such as reactive ion etching. Details of the influence of a varying α on the extraction of R and C can be found in the appendix E. An in-situ determination of α would be possible if the graphene resistance would be known precisely. One way to achieve this is to measure the quantum Hall effect where the conductance of the graphene device is well known. However, superconducting niobium resonators cannot withstand such large magnetic fields and therefore copper resonators [276] would need to be used. Copper resonators would also allow measurements at higher temperatures, however, the quality factor and hence the sensitivity would be reduced.

The variation in ϵ_{hBN} could result from an uncertainty in the thickness estimation of the bottom hBN by atomic force microscopy. However, this will not influence any interpretation of the data as it only enters the gate capacitance.

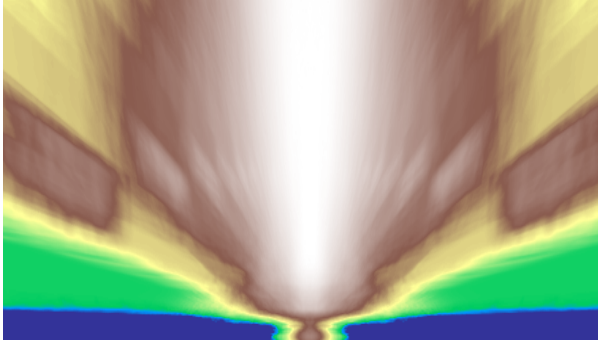
8.5. Conclusion and outlook

In summary, a hBN/Gr/hBN stack was capacitively coupled to a high quality microwave resonator and clear changes in resonance frequency and linewidth

were observed as a response to local gating of the graphene flake. We are able to reliably extract the complex impedance of the graphene device from the frequency response. The extracted capacitance is well reproduced with a simple model taking into account geometrical gate capacitance and quantum capacitance of the graphene. In addition, the charge relaxation resistance can be extracted and the diffusion constant was inferred from both measurements. These results highlight a fast, contactless characterization of graphene pn-junctions and offer an alternative characterization method in addition to standard transport measurements.

The ability of the circuit to measure quantum capacitance and resistance at the same time could be useful to study band modifications of graphene due to proximity spin-orbit effects, see chapter 7, or due to Moiré superlattices [277]. In addition, the contactless nature of this technique could be useful to study more exotic two dimensional materials, on which ohmic contacts are challenging to form.

9 Diamonds in suspended bilayer graphene



In this chapter high quality suspended bilayer graphene devices with local bottom gates are investigated. The local bottom gates can be used to locally tune the charge carrier density and the filling factor in the quantum Hall regime. Within the quantum Hall regime, peculiar conductance enhancements along strictly unipolar gating are observed. In addition, edge state equilibration is investigated and spin selective, partial edge state equilibration is found. At the charge neutrality point and in moderate magnetic field a gapped state is observed originating from electron-electron interaction. The measurements presented here are not fully understood, and we give first ideas, some of which explain parts of the measured features, however fail to describe all the features together.

9.1. Device structure and basic characterization

A scanning electron micrograph of a typical 2-terminal suspended bilayer graphene device is shown in Fig. 9.1 (a). Here, three devices, device A, B and C are presented. If not otherwise noted, all measurements are from device A. All devices were fabricated as explained in section 2.1. Device A, which is the main focus, is $2.6\mu\text{m}$ long and roughly $2\mu\text{m}$ wide and therefore has an aspect ratio close to 1. There are three local bottom gates as one can see in Fig. 9.1 (a). The two bottom gates located partially below the contacts are connected together and form basically one gate, which we will refer to as the outer gate in the following. The local bottom gate in the middle of the device will be referred to as the middle gate.

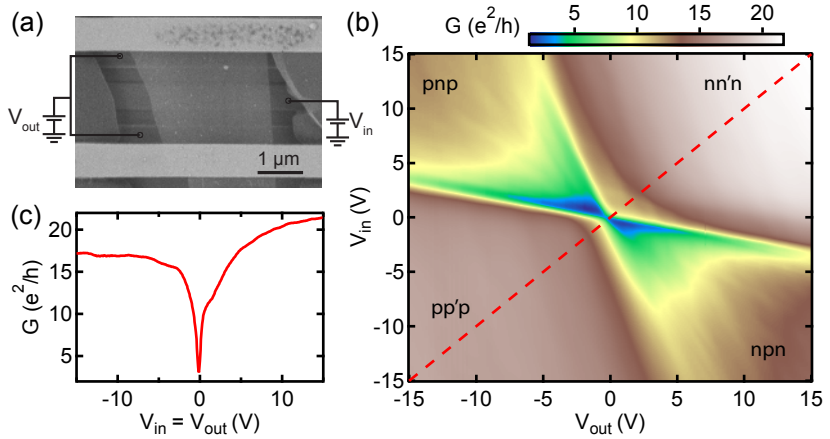


Figure 9.1. Device and basic characterization: (a) Scanning micrograph of a typical suspended 2-terminal graphene device with bottom gates V_{in} and V_{out} as indicated. (b) The two-terminal conductance as a function of V_{in} and V_{out} is shown at a temperature of 800 mK. The four distinct doping regimes are indicated on the map where the first and last letter corresponds to the doping in the outer region, whereas the middle marks the doping in the inner region. (c) unipolar cut with homogeneous doping through the full sample as indicated by the red dashed line in (b).

The two voltages V_{out} applied to the outer gates and V_{in} applied to the inner gate will locally tune the charge carrier density in the graphene sheet above. Therefore, two distinct doping regimes can be accessed. If both gates have the same polarity, a unipolar doping results (e.g. nn'n, where n is the

density in the outer region tuned by V_{out} and n' is the density in the inner region tuned by V_{in}). These two cases correspond to the lower left and upper right corner of the conductance map in Fig. 9.1 (b). If V_{in} and V_{out} have opposite polarity, a bipolar doping profile along the device is formed (e.g. a pnp, where p denotes the hole concentration in the outer region and n denotes the electron concentration in the inner region). Obviously, a npn situation can be realized as well. These two situations correspond to the upper left and lower right corner of the conductance map in Fig. 9.1 (b), where the doping profile is indicated with letters. In the bipolar regimes, the conductance is reduced due to the presence of pn-junctions. The fact that all four regions are well developed confirms that the graphene flake is homogeneously clean, also close to the contacts.

Fig. 9.1 (c) shows the conductance as a function of unipolar doping ($V_{in} = V_{out}$). A very sharp charge neutrality point is observed around zero gate voltage. A kink on the electron doped side around $V_{in} = V_{out} = 1.25$ V corresponding to $\sim 1.25 \times 10^{10} \text{ cm}^{-2}$, which itself corresponds to an Fermi energy of 0.5 meV, is observed. The fact that the conductance extends to larger values on the nn'n side is due to n-doping of the contacts that lead to the formation of an additional pn-junction if the device is tuned to the pp'p regime. A series resistance, that includes contact resistance and line resistances of the setup, is estimated to be around $\sim 900 \Omega$ from the saturation value on the nn'n-side. A very rough estimate of the field effect mobility results in a lower bound of $100\,000 \text{ cm}^2 \text{ V}^{-1} \text{ s}^{-1}$ and a residual doping $n^* \sim 8 \times 10^8 \text{ cm}^{-2}$ yielding a minimal Fermi energy of 30 μeV , both confirming the exceptionally high quality of this device.

9.1.1. Quantum Hall effect

A fan-plot of the conductance as a function of unipolar gating ($V_{in} = V_{out}$) and perpendicular magnetic field is shown in Fig. 9.2. Line cuts at constant magnetic field are shown in (b). The absence of clear plateaus could in principle be explained by a non-quadratic device shape that would lead to the mixing of ρ_{xx} and ρ_{xy} in two-terminal measurements [79, 80]. The filling factors align well with the minimum of the conductance, which would correspond to a wide sample [80]. However, the device presented here has an aspect ratio corresponding to a moderately long sample (close to quadratic) and, therefore we think that the absence of plateaus cannot be explained by the non-quadratic nature of the sample.

9.1.2. Gate-gate maps at finite magnetic field

Fig. 9.3 shows the two-terminal conductance as a function of both gate voltage V_{in} and V_{out} for different magnetic fields. A pronounced conductance enhan-

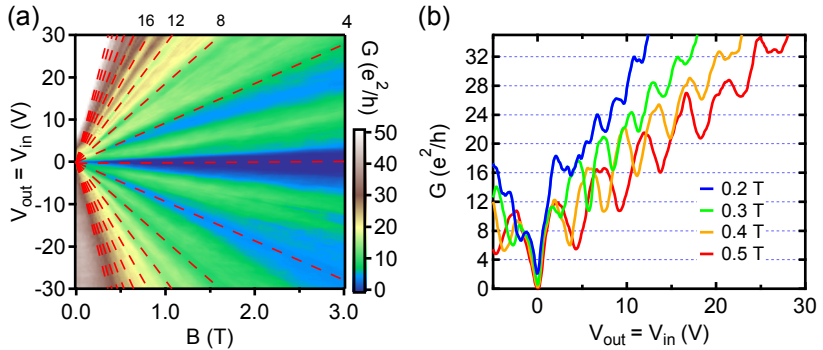


Figure 9.2. Quantum-Hall effect: (a) Conductance as a function of magnetic field and homogeneous doping (fan plot). The dashed lines mark constant filling factors (in steps of 4), and corresponding filling factor values are indicated on top of the figure. (b) Conductance as a function of unipolar gating for different magnetic fields. A series resistance of $800\ \Omega$ was subtracted. Only at high filling factors does the conductance display plateaus.

cement along strictly unipolar gating ($V_{in} = V_{out}$) is found. Within these diamond shaped features the conductance is $\sim 4e^2/h$ to $\sim 8e^2/h$ larger than expected. Next to these diamond shaped features, well developed plateaus with conductance values at multiples of $4e^2/h$ are found. As a guide to the eye, the bulk filling factors of the outer and the inner region are laid over the measurement. Along these nearly horizontal (vertical) lines the charge carrier density and hence the filling factor is constant in the inner (outer) region while the charge carrier density of the outer (inner) region is tuned.

The diamond shaped conductance enhancement appear along strictly unipolar gating $V_{in} = V_{out}$. The extension of those regions is constrained in filling factor to a 4 by 4 region, see Fig. 9.3 where the filling factors are laid over the measurement. At high magnetic field the Landau levels split up due to the lifting of spin and/or valley degeneracy. This can be seen as an internal structure within the diamonds and splitting of the flat plateaus outside the diagonal. See for example Fig. 9.3 (d) where the internal structure of the diamond lines up with filling factor 3. Another example is the two different values of conductance in the area spanned by $0 \leq \nu_{out} \leq 4$ and $4 \leq \nu_{in} \leq 8$ in Fig. 9.3 (b).

The lowest Landau level in bilayer graphene is eightfold degenerate, whereas all the other Landau levels are fourfold degenerate [278]. This leads to plateaus in the Hall conductivity at $\pm 4, \pm 8, \pm 12, \dots \cdot e^2/h$, centred at the corresponding

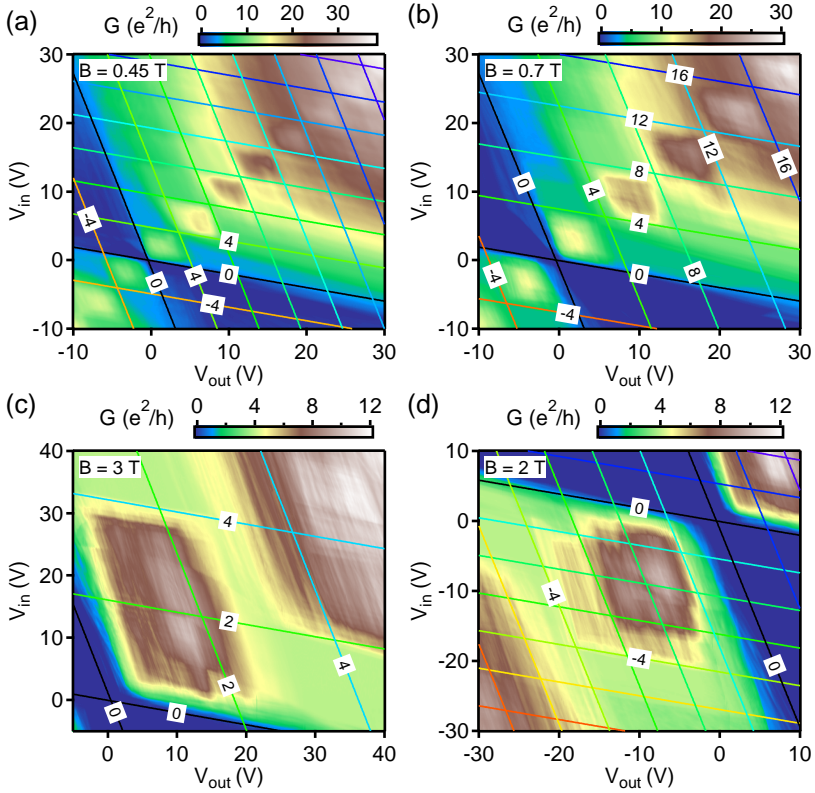


Figure 9.3. Gate-gate map at finite magnetic field: Gate-gate maps of the conductance at various magnetic fields at a temperature of 25 mK. A constant series resistance of 800Ω has been subtracted from all measurements. The solid lines indicate constant filling factors for the inner and outer regions separately. The magnetic field at which the measurements have been performed are indicated on the top left of each panel.

filling factor. Therefore, the lowest two plateaus (± 4) should extend over a larger range in gate voltage compared to all the other plateaus. This also implies that the lowest diamond along strictly unipolar gating should extend over a larger region in gate voltage compared to the other diamonds. However, this is in contradiction with the data that shows equidistant diamonds.

Even though most of the features in the gate-gate maps line up with constant filling factors, there are also a few exceptions. The most prominent are the deviations at large values of V_{out} , where the constant conductance lines are not parallel with the constant filling factors in the inner gate range. This is the case in the area right to the diagonal in the case of n-doping.

These peculiar conductance features persist up to 4.6 K as shown in Fig. 9.4. At larger temperatures some sharp features wash out and the conductance slightly increases for all gate voltages.

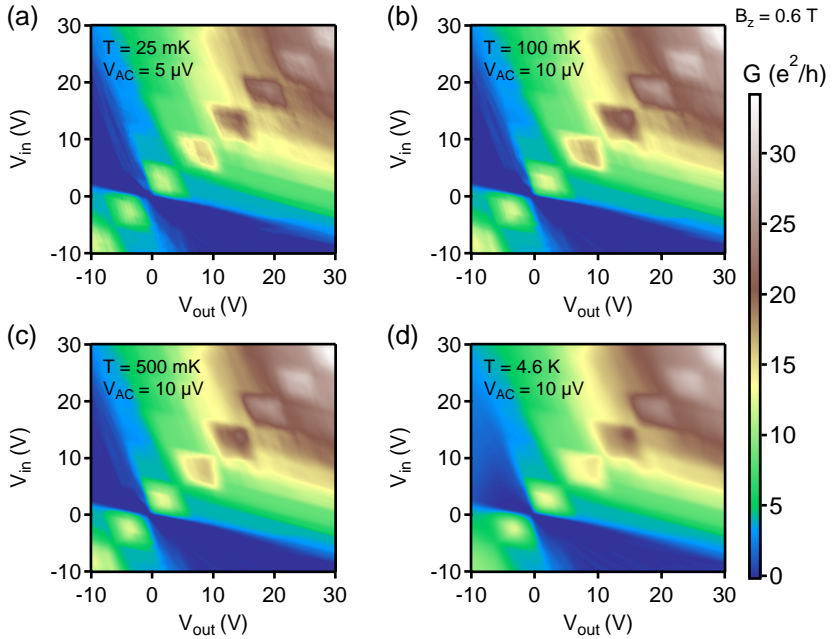


Figure 9.4. Temperature dependence: Gate-gate maps of the conductance at 600 mT for different temperatures. "Diamond" shaped conductance enhancements are present for all temperatures presented as well as the well developed plateaus in the case of $\nu_{out} > \nu_{in}$.

The following discussion on the possible origin of the diamond shaped conductance enhancement along the strictly unipolar gating is limited to the electron side. However, as shown in Fig. 9.3 and 9.4, the same features are also observed on the hole side.

9.2. Possible explanations

In the following a few possible scenarios are presented that could explain some parts of the observed conductance features.

9.2.1. Edge state equilibration

In graphene devices with regions containing different filling factors next to each other, see Fig. 9.5 (a) for a schematic drawing of the three different cases, scattering between different edge states can occur. The edge states can have different chemical potential and the cross-scattering between them can modify the conductance through the device. This effect is called edge state equilibration. In the following different aspects of edge state equilibration are discussed.

Three region model

In the following, the graphene device is treated as three regions with different filling factors. The outer two regions are tuned by the outer gate V_{out} to filling factor ν_{out} and the inner region is tuned by the inner gate V_{in} to filling factor ν_{in} . Both regions can therefore be tuned independently to different charge carrier densities, also of opposite polarity. A schematic view of this is shown in Fig. 9.5 (a) that shows the three distinct cases.

If full equilibration among all edge states in the bipolar regime of a pnp or npn junction is assumed, then the conductance through the device is given as

$$G = \frac{e^2}{h} \cdot \frac{|\nu_{in}||\nu_{out}|}{2|\nu_{in}| + |\nu_{out}|}, \quad (9.1)$$

where $\nu_{in,out}$ denote the filling factors of the inner and outer region of the device [279]. This situation is schematically shown in Fig. 9.5 (a) at the bottom. Full equilibration means that the currents arriving at the pn-junction distribute equally between all channels. Here, we focus on the equilibration in the unipolar regime, since the conductance in the bipolar regime for our device is zero as a gap opens with finite magnetic field at the charge neutrality point (see section 9.3).

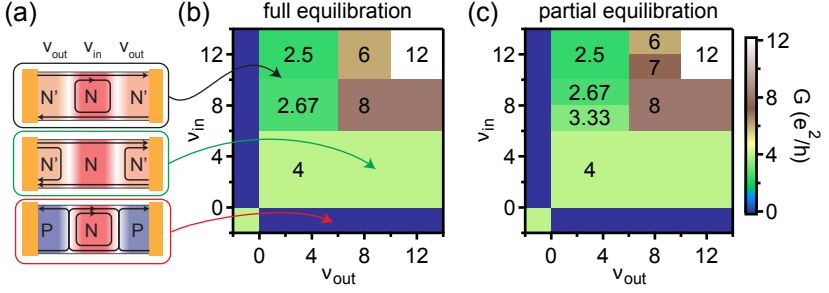


Figure 9.5. Edge state equilibration: (a) Schematic drawing of the equilibration process in the unipolar and bipolar region. Adapted from Ref. [48]. (b) Expected conductance in the unipolar region for full equilibration. (c) Expected conductance in the unipolar region for partial equilibration, where equilibration only happens among edge states with the same spin polarization (see below for details).

In the unipolar regime, there are two distinct situations possible and the conductance through the device is given as follows:

$$G = \frac{e^2}{h} \cdot \frac{|\nu_{in}||\nu_{out}|}{2|\nu_{in}| - |\nu_{out}|} \quad \text{if } |\nu_{out}| \leq |\nu_{in}| \quad (9.2)$$

or

$$G = \frac{e^2}{h} \cdot |\nu_{in}| \quad \text{if } |\nu_{out}| > |\nu_{in}|. \quad (9.3)$$

These two situations are shown in Fig. 9.5 (a) on the top. Now, we can calculate the conductance as a function of ν_{in} and ν_{out} , which is shown in Fig. 9.5 (b). For the sake of simplicity, we restrict ourselves to the nn'n region. Exactly the same results would be expected for the pp'p case.

The expected conductance as shown in Fig. 9.5 (b) shows two qualitatively different dependencies on ν_{in} and ν_{out} . If $\nu_{in} < \nu_{out}$, then ν_{in} edge states are fully transmitted through the sample with $\nu_{out} - \nu_{in}$ edge states being fully reflected at the nn' interface. This results in conductance plateaus at values of $\nu_{in}e^2/h$ for all $\nu_{out} \geq \nu_{in}$. On the other hand, the conductance decreases in well defined steps if $\nu_{in} \geq \nu_{out}$ and conductance values corresponding to fractional multiples of the conductance quantum appear.

Apart from the strictly unipolar doping ($\nu_{in} = \nu_{out}$), this model qualitatively agrees with the measurements. Constant conductance values are found for $\nu_{out} \geq \nu_{in}$, whereas a series of decreasing conductance plateaus are observed in the regime where $\nu_{in} \geq \nu_{out}$. However, careful comparison of the experimental

finding with the expected equilibration plateaus reveal significant discrepancies as one can easily see by comparing the expected conductance shown in Fig. 9.5 (b) with the measured conductance shown in Fig. 9.6. Above the diagonal, additional equilibration plateaus are observed in the measurement that are not expected in this simple model, whereas below the diagonal the conductance does not match the expectations at several places. An example is the first plateau with conductance of $4e^2/h$, which is expected to extend close to filling factor 6, however in the measurement it only extends to filling factor 4.

The equilibration of the edge states relies on scattering from one edge state into another one. Depending on the nature of this scattering event, either valley and or spin can be preserved. The conservation of one of this degree of freedom can restrict the number of possible equilibration processes. If for example spin is conserved during the scattering, a spin-up edge state cannot scatter into a spin-down edge state and therefore half of the scattering processes are forbidden.

Since for the unipolar region equilibration happens at the physical boundary of the sample, valley scattering can readily occur since atomically sharp defects are present. Based on this argument and due to existing experimental evidence of spin selective equilibration in single layer graphene [280, 281], we will consider spin selective equilibration in the next section as an extension of the three region model.

Three region model with spin selective equilibration

Recently, Amet et al. [280] reported the selective equilibration of spin-polarized edges states in single layer graphene. This leads to only partial equilibration, that can be described as the sum of the spin-up and spin-down edge states equilibrating only among themselves in the regime $|\nu_{out}| \leq |\nu_{in}|$, which then defines the conductance as

$$G_{partial} = \frac{e^2}{h} \left[\frac{|\nu_{in,\uparrow}||\nu_{out,\uparrow}|}{2|\nu_{in,\uparrow}| - |\nu_{out,\uparrow}|} + \frac{|\nu_{in,\downarrow}||\nu_{out,\downarrow}|}{2|\nu_{in,\downarrow}| - |\nu_{out,\downarrow}|} \right]. \quad (9.4)$$

Now, the conductance through the device depends on the exact spin state of the Landau levels that are involved in the equilibration process.

As an example, we will now calculate the conductance for the case $\nu_{out} = 4$ and $\nu_{in} = 6$. The lowest Landau level in bilayer graphene is eightfold degenerate and centred around zero energy and half filled by electrons and half filled by holes. First, we will assume that the lowest Landau level splits into two spin-polarized Landau levels leading to a fully spin polarized outer region. Moreover, the second Landau level in the inner region is assumed to be not spin-polarized at half-filling. Therefore, we can write $\nu_{out,\uparrow} = 4$ and $\nu_{out,\downarrow} = 0$ for the outer region and $\nu_{in,\uparrow} = 4 + 1$ and $\nu_{in,\downarrow} = 1$ for the inner

region. The conductance is then calculated using Eq. 9.4 and one obtains $G_{\text{partial}} = 10/3 \sim 3.33 e^2/h$. The same conductance value is obtained if one assumes an unpolarized lowest Landau level in the outer region ($\nu_{\text{out},\uparrow} = 2$ and $\nu_{\text{out},\downarrow} = 2$), but a spin polarized half-filled second Landau level in the inner region ($\nu_{\text{in},\uparrow} = 2 + 2$ and $\nu_{\text{in},\downarrow} = 2$).

There are two more possible configurations. The first configuration involves a spin polarization of the first and second Landau level with $\nu_{\text{out},\uparrow} = 4$ and $\nu_{\text{out},\downarrow} = 0$ in the outer region and $\nu_{\text{in},\uparrow} = 4 + 2$ and $\nu_{\text{in},\downarrow} = 0$ in the inner region. The second configuration involves no spin polarization at all with $\nu_{\text{out},\uparrow} = 2$ and $\nu_{\text{out},\downarrow} = 2$ in the outer region and $\nu_{\text{in},\uparrow} = 2 + 1$ and $\nu_{\text{in},\downarrow} = 2 + 1$ in the inner region. These two configurations lead to a conductance of $3 e^2/h$.

The conductance that results from the equilibration of the filling factors $\nu_{\text{out}} = 4$ and $\nu_{\text{in}} = 8$ can have two different values, depending again on the spin polarization of the lowest Landau level. If the lowest Landau level is spin polarized, then a conductance of $3 e^2/h$ results, whereas $2.67 e^2/h$ is obtained for an unpolarized lowest Landau level. The second Landau level cannot be spin polarized if its completely filled.

Similarly, one can calculate the conductance for partial equilibration for the filling factors $\nu_{\text{out}} = 8$ and $\nu_{\text{in}} = 10$. There the conductance values of the different possible configurations are all close to $7 e^2/h$. At higher filling factors, the different equilibration processes all result in very similar conductance values that make it hard to distinguish the different cases. The expected conductance for a valley polarized lowest Landau level (spin unpolarized) in combination with a spin polarized half-filled second Landau level is shown in Fig. 9.5.

The comparison with the measurement, shown in Fig. 9.6, favours a spin-polarized half filled second Landau level with an unpolarized lowest Landau level. In order to obtain a conductance of $\sim 3.4 e^2/h$ for the filling factors $\nu_{\text{out}} = 4$ and $\nu_{\text{in}} = 6$, a half-filled spin polarized second Landau level is necessary. As mentioned above, this is consistent with the observed conductance of $\sim 2.67 e^2/h$ for the filling factors $\nu_{\text{out}} = 4$ and $\nu_{\text{in}} = 8$. In the case of spin polarized lowest Landau level one would expect a conductance of $3 e^2/h$ for $\nu_{\text{out}} = 4$ and $\nu_{\text{in}} = 8$. Furthermore, the observed conductance for $\nu_{\text{out}} = 8$ and $\nu_{\text{in}} = 10$ is consistent with partial equilibration. Spin polarized Landau levels, especially of half-filled Landau levels, have been reported before [282]. According to this study, the lowest Landau level remains spin polarized at zero electric field [282], which contradicts our finding. However, a different study found a spin unpolarized but valley polarized state [283]. The equilibration measurements point rather to a non-spin polarized lowest Landau level in our sample.

In summary, the conductance in the region where $|\nu_{\text{out}}| \leq |\nu_{\text{in}}|$ is well explained by spin selective partial equilibration of edge states, where the lowest Landau level is not spin polarized. The half filled second Landau level, ho-

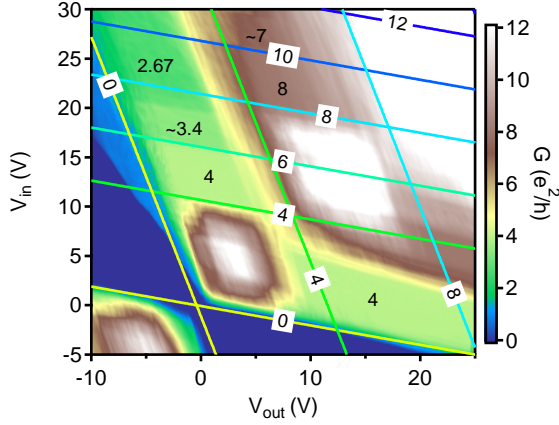


Figure 9.6. Experimental observation of partial equilibration: Conductance in the unipolar region measured as a function of V_{in} and V_{out} at a magnetic field of 1 T. The coloured lines indicated the filling factor and the black numbers indicate the conductance.

wever, is spin polarized. In addition, the constant conductance plateaus for $|\nu_{out}| \geq |\nu_{in}|$ can be understood that only $|\nu_{in}|$ edge states are fully transmitted through the sample. However, the position of these plateaus are not fully correct as one can see for example in Fig. 9.3 (b) where the plateaus are not parallel with lines of constant inner filling factor. In addition, this model totally fails to explain the decrease of the conductance when going from a situation $|\nu_{out}| = |\nu_{in}|$ to $|\nu_{out}| \geq |\nu_{in}|$. In this model, the conductance should no change at all as one can easily see in Fig. 9.5. This very dominant feature appearing for strictly unipolar doping remains to be explained. Some ideas that could result in higher conductance values for $\nu_{in} = \nu_{out}$ are sketched in the following part of this chapter. First an equilibration based idea is presented before possible scenarios involving more sophisticated mechanisms are presented.

Five region model

Due to the bottom gate structure, the charge carrier density profile along the device for unipolar doping is expected to vary smoothly as one can see in Fig. 9.7 (b). The oscillation amplitude of around 15 % could in principle lead to five regions with different filling factor and each hosting a different number of edge states.

This scenario could in principle explain the decrease of the conductance when V_{out} is increased. Starting from a situation depicted in Fig. 9.7 (a) on the top, where $\nu_c = \nu_{out} = \nu_{in}$, an increase in ν_{out} would lead to a situation shown in Fig. 9.7 (a) in the middle. The fact that $\nu_{out} > \nu_c$ leads to equilibration as presented above and hence to a reduction of the conductance compared to the initial case where $\nu_c = \nu_{out} = \nu_{in}$. However, increasing ν_{out} further while keeping ν_c constant, the conductance would reduce further, which is in contradiction to the measurements. Even though five different regions might exist in our sample, it is very unlikely that such a case would lead only once to a reduction in conductance when ν_{out} is increased as observed in the experiment.

Obviously the case $\nu_{in} > \nu_{out}$, as shown in Fig. 9.7 (a) at the bottom, would result in an equilibration process described above.

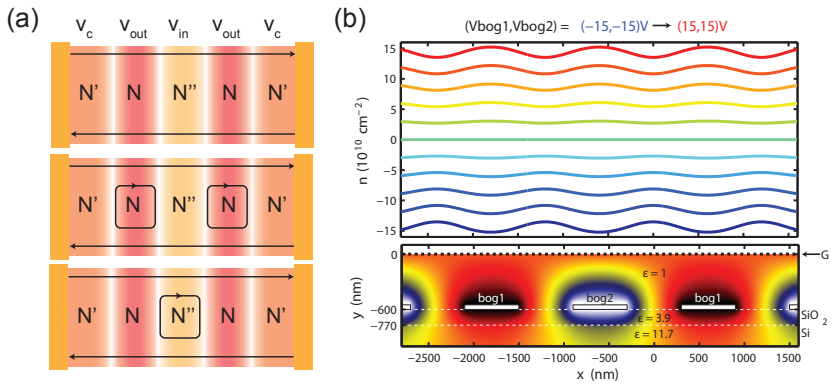


Figure 9.7. Five region model: (a) shows a possible configuration where close to the contact a different filling factor ν_c compared to ν_{out} is obtained. (b) electrostatic calculations show that the density is changing by around 15 % along the device due to bottom gate pattern. The electrostatic calculations, not including the screening of the contacts, were performed by Ming-Hao Liu.

Even though the five-region model could partially explain the decrease of the conductance for $\nu_{out} > \nu_{in}$, it still remains a mystery why the conductance is larger than $\nu_{in}e^2/h$ in the first place. In the following, two scenarios are discussed that could lead to larger conductance values.

9.2.2. Conductance along domain walls in bilayer graphene

Domain walls in bilayer graphene separating AB and BA stacked regions from each other are expected to host topological protected 1-dimensional channels, which have been observed recently in transport experiments [284]. In addition,

these channels can be created artificially by local gating [285]. It was observed that these channels persist in magnetic field [285] and even get more robust.

As shown in Fig. 9.8 (a) a domain wall running along the device connecting the two electrodes will lead to an additional conducting channel carrying $4e^2/h$ in the ideal case. If intervalley scattering is present this value could be reduced to a value below $4e^2/h$. In principle, such domain walls could explain the larger conductance that is observed along unipolar gating. The domain wall is disconnected from the quantum-Hall edge states as long as $\nu_{out} = \nu_{in}$. When $\nu_{out} \neq \nu_{in}$, the edge states will cross the domain wall in the regions of higher filling factor. This is schematically shown for $\nu_{out} > \nu_{in}$ and highlighted by a green dashed circle. If the crossing of the edge state with the domain wall would lead to a complete backscattering of the states running along the domain wall, the overall conductance of the device would drop to $\nu_{in}e^2/h$. It is important to note, that for example by increasing ν_{out} further, the conductance through the device would stay constant at $\nu_{in}e^2/h$ if the complete backscattering of the state at the domain wall would persist to higher doping.

On the other hand, when ν_{in} is increased such that $\nu_{in} \geq \nu_{out}$, normal equilibration as explained above is expected if the crossing of additional edge states and the domain wall would lead to the complete backscattering of the states at the domain wall. These findings are in principle consistent with the measurements. However, we can only speculate about the interaction of the edge states with the domain wall channels, which are crucial in this model. Previous theoretical work showed that quantum Hall edge states could scatter partially back or could be fully transmitted depending on their energy [286].

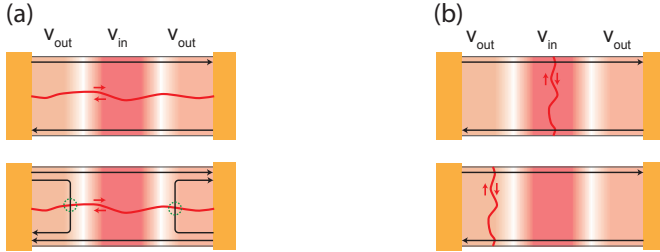


Figure 9.8. Influence of domain walls through the device: (a) a domain wall running along the device connecting the two electrodes would lead to an additional conducting channel carrying $4e^2/h$ in the ideal case. In the case $\nu_{out} > \nu_{in}$ a quantum-Hall edge channel is crossing the domain wall, see lower part where these points are highlighted by a green dashed circle. (b) domain walls running perpendicular to the device will short the opposite edges, independent whether they are located in the inner or outer region.

In principle, domain walls could also run across the device connecting one side to the other as shown in Fig. 9.8 (b). If the domain wall is located in the inner region of the device, an overall decrease of the conductance would be expected for any gate voltage configuration. On the other hand, if the domain wall would be located in one of the outer regions, it is not straightforward to pinpoint the value of the conductance as this would crucially depend on the interaction of the states at the domain wall with the edge states. If the domain wall states do not couple to the edge states that are fully transmitted through the sample, the conductance would simply be given by $\nu_{in}e^2/h$. However, it is more likely, that also some current from these edge states is shorted to the other side and therefore a reduced conductance would result.

9.2.3. Additional conductance channels along the edge

There are several reports in literature about enhanced doping or additional conducting channels along the edge of graphene flakes [260, 287, 288]. This is especially pronounced in bilayer graphene, where the bulk can be gapped by an electric field. Non-local measurements on single layer graphene Hall-bars in chapter 7.5 also point to the direction of an enhanced doping along the edge.

A non-monotonic doping profile at the edge, as schematically shown in Fig. 9.9 (b), could lead to more edge states in the quantum Hall effect. In the bulk of the sample, the filling factor would be ν , whereas it would be larger at the edge, for example $\nu + 1$ as shown in the figure. This larger filling factor directly leads to more edge states as depicted in light blue in Fig. 9.9 (a). In principle there exist as many additional edge channels going from left to right as there are going from right to left. In the absence of any scattering between the counter-propagating edge channels (considering only the light blue ones), two edge channels with a total additional conductance of $8e^2/h$ would result. Since these counter-propagating edge states are sitting very close to each other (spatially), scattering from the right moving to the left moving could in principle occur and the additional conductance could take any value between zero and $8e^2/h$ [260]. To sum up, a non-monotonic density profile at the edge can in principle lead to an enhanced conductance compared to the conductance expected from the bulk filling factor.

Since the filling factor in the outer and in the inner region can be tuned separately, the question arises what will happen to the additional edge states when $\nu_{in} \neq \nu_{out}$. In the case of $\nu_{out} > \nu_{in}$, a schematic picture is shown in Fig. 9.9 (a) at the bottom. If in this case the additional edge channels would be reflected back, the conductance would drop to the expected value defined by ν_{in} . If the additional edge states are also fully reflected for larger ν_{out} conductance and plateaus at $\nu_{in}e^2/h$ would be expected. A similar situation arises when $\nu_{in} > \nu_{out}$. Again, the question would come up what the additional edge states would do. If they would be reflected as well, normal equilibration

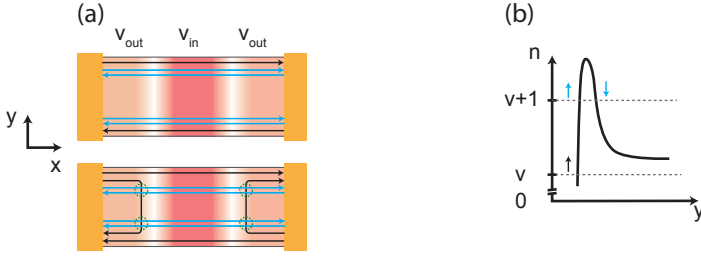


Figure 9.9. Influence of edge doping: (a) an enhanced doping at the graphene edge could lead to additional edge states in the quantum-Hall regime that would lead to an enhanced conductance. In the case $\nu_{out} > \nu_{in}$ a quantum-Hall edge channel is crossing these additional edge channels, see lower part where these points are highlighted by a green dashed circle.

as explained above would define the conductance through the device. In order to clarify the role of additional edge states on the conductance, especially for the case when $\nu_{in} \neq \nu_{out}$, the interaction of the additional edge states with the normal edges states is important. Here, a better understanding of the two-dimensional doping profile could be beneficial and electrostatic simulations could shed some light on that. In addition, scanning probe measurements could reveal the current distribution within the device that could clarify the origin of the enhanced conductance features.

In summary, additional edge states due to a non-monotonic charge density profile at the edge as depicted in Fig. 9.9 (b) could explain the enhanced conductance in the first place. The reduction of the conductance when going away from perfect unipolar doping could be explained if the additional edge states due to gating would lead to back reflection of the additional edge states due to the charge density profile. However, at this point we can only speculate what happens when these edge states meet.

9.3. Evidence of a spontaneous gap formation and Lifshitz transition

The conductance as a function of both gates at small perpendicular magnetic fields are shown in Fig. 9.10 (a) and (b). In addition, the conductance as a function of strictly unipolar gating ($V_{in} = V_{out}$) for small magnetic fields is shown in Fig. 9.10 (c). A conductance ridge at filling factor 4 that changes into a conductance dip around 0.25 mT, see Fig. 9.10 (c) is observed. This crossover goes along with a change of the diamond shaped conductance enhancement along strictly unipolar gating as shown in (a) and (b) in the same figure.

At 200 mT, the first diamond is constrained by the filling factors 0 to 8 for both the outer and inner region, whereas it breaks up into two diamonds at 300 mT, the first being constrained by filling factor 0 to 4 and the second being constrained by the filling factor 4 to 8. This strongly suggests that at low magnetic field the spectrum is eightfold degenerate, whereas it is fourfold degenerate at higher magnetic fields.

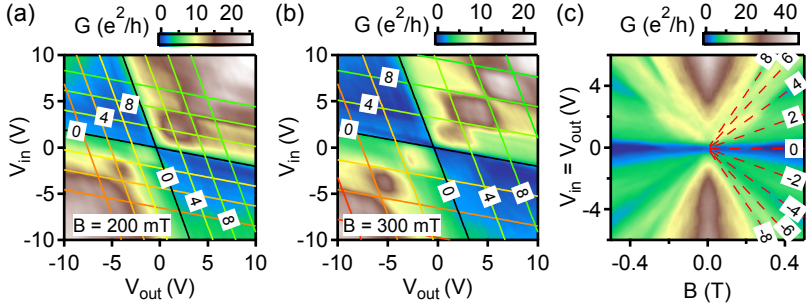


Figure 9.10. Low field maps: (a) and (b) show the conductance through the device as a function of both gate voltages at 200 mT and 300 mT with filling factors in steps of 4 where the black solid lines correspond to $\nu = 0$. Whereas the lowest feature on the electron side is outlined by $\nu_{in} = 8$ and $\nu_{out} = 8$ in (a) it is outlined by $\nu_{in} = 4$ and $\nu_{out} = 4$ in (b). In the fan plot this is also visible as a conductance ridge that evolves into a dip at a magnetic field of around 250 mT.

Spectroscopy measurements around the CNP indicate the formation of a spontaneous gap, see Fig. 9.11 (a) and (b). However, the conductance at zero magnetic field remains finite at a value slightly below $4e^2/h$ within the gap on the order of ~ 2.5 meV. This larger gap rapidly decreases for increased density, whereas a second smaller dip in conductance is observed around zero V_{SD} bias that persist up to larger charge carrier densities. This second smaller gap could arise from Coulomb charging of the whole flake leading to a slight conductance suppression due to weak Coulomb blockade [289, 290]. For magnetic fields larger than ~ 250 mT, a complete gap is observed, that rapidly increase in magnetic field with a slope of ~ 25 meV T^{-1} , see Fig. 9.11 (c) and (d), which is five times larger than in Ref. [291] and roughly 20 times larger than in Ref. [289, 292]. Below 250 mT and at low bias a rich structure in conductance is observed, see Fig. 9.11 (e).

Previous studies also reported insulating states in bilayer graphene [289, 291–293]. Velasco et al. [291] found a gapped phase at the CNP in very clean suspended bilayer graphene. The gap closes with a perpendicular electric field

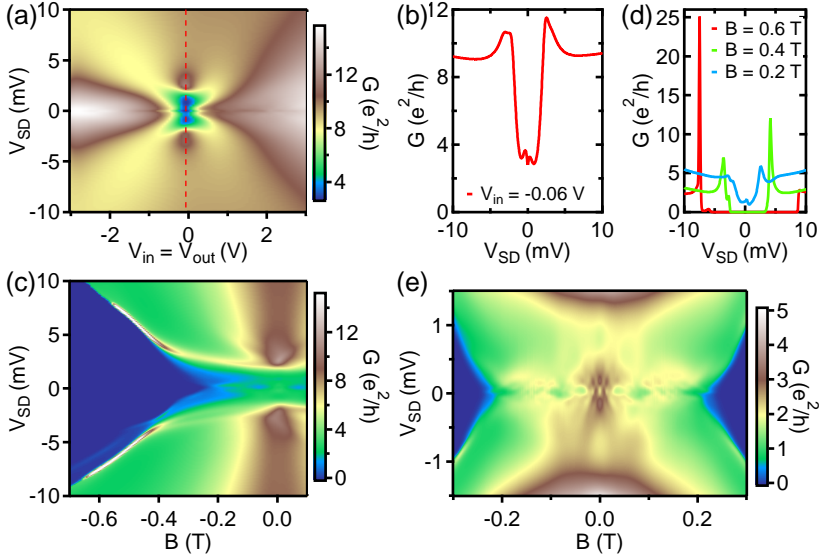


Figure 9.11. Bias spectroscopy: (a) shows the conductance as a function of source-drain bias V_{SD} and gate voltages with a cut at the CNP shown in (b). The conductance as a function of V_{SD} and B in the CNP is shown in (c) and zoom-in is shown in (e). Cuts at different magnetic fields are shown in (d).

of either polarity and a strength of 15 mV nm^{-1} . This state smoothly evolves into the $\nu = 0$ quantum Hall state in magnetic field. They concluded that the gapped state cannot be a spontaneously ordered phase with a net charge imbalance between the layers and therefore the charge layer polarized state has been ruled out. The authors concluded that the ground state of gapped bilayer graphene is either a quantum anomalous Hall phase, a quantum spin Hall phase or a layered antiferromagnet. For details see Ref. [291] and further references therein. Large in-plane magnetic field measurements by Freitag et al. [294] found a spin-symmetric ground state of the gapped bilayer graphene ruling out the quantum anomalous Hall phase. Therefore, only the layer antiferromagnet and the quantum spin Hall phase is left as a possible ground state of bilayer graphene [294].

We would like to note that even though our device does not have a top gate, which would allow independent control of charge carrier density and electric field, the electric field at the CNP is negligibly small and cannot lead to a

substantial layer asymmetry that would result in a gap [289, 295]. In addition, the observed gap disappears around $V_{in} = V_{out} \sim 1$ V, which corresponds to an order of magnitude smaller electric field than was needed to close the gap in Ref. [291], ruling out that absence of a full gap is related to the negligible small electric field as claimed in Ref. [291]. Freitag et al. also found samples called B1, which could only be gapped in magnetic field. The reason for the absence of the full gap, and the connection to the gapped lowest Landau level is still not clear.

The presence of local bottom gates allows us to tune either the inner or the outer region to high charge carrier density, while keeping the other region at the CNP. A transport gap in magnetic field is found in both configurations confirming the homogeneous cleanliness of our device (not shown here).

A Lifshitz transition is expected to occur in bilayer graphene at very low energy. This means that the Fermi surface changes its topology and in the case of bilayer graphene it breaks up from a single circle into four disconnected circles [81]. This effect is due to trigonal warping and arises from the interlayer skew coupling (non-dimer A1 and B1 sites). A Lifshitz transition can be expected at an energy of ~ 1 meV, which we can well resolve with a residual doping of $8 \times 10^8 \text{ cm}^{-2}$ corresponding to $30 \mu\text{eV}$. At energies below ~ 1 meV the parabolic band structure changes into four linear "mini" Dirac cones [50]. Therefore, the degeneracy of the lowest Landau level increases from 8 to 16 (4 Dirac cones $\times 2$ spin $\times 2$ valley) [50]. Above the transition energy, the degeneracy is reduced to 8. In addition, the Lifshitz transition should disappear at small magnetic fields when the magnetic length $l_B = \sqrt{\hbar/eB}$ is comparable to the distance in momentum space between the four points where the valance and conduction bands touch, which was estimated to be around 100 mT [50].

The kink in the conductance on the electron doped side appearing around $1.25 \times 10^{10} \text{ cm}^{-2}$, corresponding to a Fermi energy of ~ 0.5 meV, (Fig. 9.1 (c)) as well as the larger diamond at 200 mT with boundaries at filling factors 8 (see Fig. 9.10 (a)) could be interpreted as a sign of the Lifshitz transition. The larger diamond is directly connected to the increased conductance value for filling factor 4 at low fields in the quantum Hall fan-plot. Increasing the magnetic field or density leads to the transformation to the regular band structure of bilayer graphene. The fact that the enhanced conductance in the fan plot (see Fig. 9.10 (c)) persist up to 250 mT instead of the estimated 100 mT could be related to strain, which is known to affect the Lifshitz transition. Strain could easily arise from current annealing and/or different thermal expansion coefficients of the involved materials. We note, that the device at the CNP becomes fully gapped at similar magnetic fields, however, at this point we are not certain if this is related to the change in the diamond shapes at higher energies.

9.4. Further bilayer devices

In the following, two additional bilayer graphene devices are shown. Both were fabricated on the same flake. In both cases the gate-gate map at zero magnetic field and at 1 T is shown in Fig. 9.12 and Fig. 9.13, respectively. Whereas device B looks very similar to the device presented above with the diamond shaped conductance enhancement around strictly unipolar gating and the opening of a gap at finite perpendicular magnetic field at the CNP, device C is qualitatively different. The conductance enhancements along strictly unipolar doping in magnetic field are absent. In addition, the conductance remains finite in perpendicular magnetic field at the CNP, whereas device B is gapped at the CNP in magnetic field. Both device B and C show a residual doping on the order of $\sim 3 \times 10^9 \text{ cm}^{-2}$ and mobilities of around $100 \times 10^3 \text{ cm}^2 \text{ V}^{-1} \text{ s}^{-1}$ for device B and $50 \times 10^3 \text{ cm}^2 \text{ V}^{-1} \text{ s}^{-1}$ for device C.

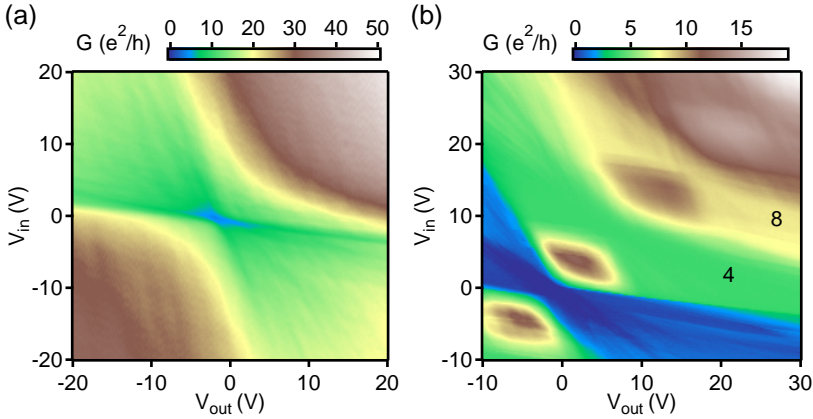


Figure 9.12. Device B: (a) shows the conductance as a function V_{in} and V_{out} at zero magnetic field, whereas (b) shows it at 1 T. The numbers in (b) indicate the conductance value of the plateau. These two measurements were performed at 500 mK. A series resistance of 650Ω has been subtracted.

The quantum Hall fan-plot of device B is very similar to the one of the device presented above with a conductance ridge at small magnetic field that transforms into a conductance dip at larger magnetic field for filling factor 4. This feature is also completely absent in device B (not shown here).

We would like to note here, that previous studies also reported two qualitatively different bilayer samples, some of which were gapped and some of which were not gapped [286, 289, 293].

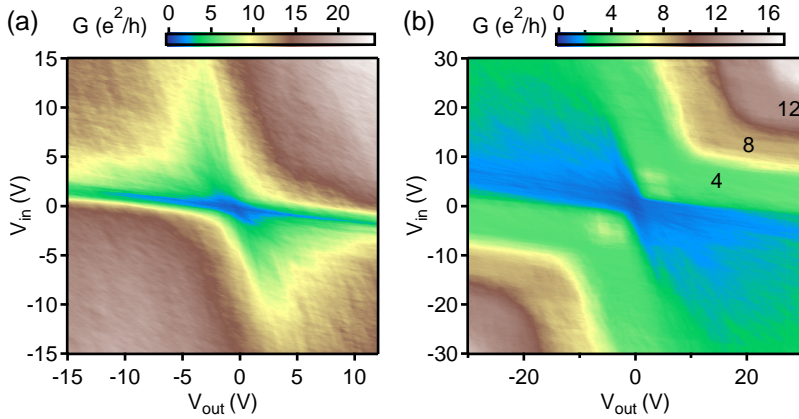


Figure 9.13. Device C: (a) shows the conductance as a function V_{in} and V_{out} at zero magnetic field, whereas (b) shows it at 1 T. The numbers in (b) indicate the conductance value of the plateau. These two measurements were performed at 500 mK. A series resistance of 650Ω has been subtracted.

9.5. Discussion, conclusion and outlook

In summary, exceptionally high quality suspended bilayer graphene devices were investigated. Regions of enhanced conductance along strictly unipolar gating in perpendicular magnetic fields are found, which take the form of "diamonds". In addition, edge state equilibration is observed for $\nu_{out} < \nu_{in}$ and conductance plateaus are found for $\nu_{out} > \nu_{in}$. In addition, a gapped state is found at the CNP at moderate magnetic field, which arises due to electron-electron interaction. Similar results have been previously reported in literature, however it is still an open question what phase governs the ground state in bilayer graphene. Since it is not fully known what determines the low energy spectrum, it is not clear if the observed gap and the enhanced conductance features in the form of diamonds are related. Most likely, these two findings are unrelated as the diamond shaped features persist up to large densities and magnetic fields.

Apart from the conductance enhancement along strictly unipolar gating, trivial edge state physics describes the experimental finding. The edge state equilibration for $\nu_{out} < \nu_{in}$ is governed by spin selective partial edge state equilibration, relaying on a spin-polarized half-filled second Landau level.

Several ideas were presented to explain the special conductance enhancements in the form of "diamonds" along strictly unipolar gating. Trivial con-

cepts such as a non-quadratic device size and five different doping regions in series fail to fully explain the experimental findings. Similarly, more complicated models involving domain walls or non-monotonic doping profiles at the graphene edge also fail to fully account for the experimental findings. The fact that the device is gapped at the CNP in moderate magnetic field makes it incompatible with most of the models presented that could lead to the enhance conductance values. Especially the non-monotonic doping profile at the edge is always present and it is therefore hard to imagine that the device can be gapped. Similarly, it was shown that the additional conductance channels at a domain wall persist in magnetic field, which again is in contradiction with the observed gapped state.

The lowest diamond constrained by the filling factors 0 and 8 at 200 mT that splits up into two diamonds at 300 mT, strongly hints that an eightfold degeneracy is lifted with magnetic field. This is in principle consistent with the Lifshitz transition. However, this is only observed on the electron side and not on the hole side. The reconstruction of the bilayer graphene spectrum due to trigonal warping is expected to be electron-hole symmetric. Since the origin of the diamond shaped conductance feature is unclear, we can only speculate about a possible link to the Lifshitz transition.

Similar transport features were found in device B as well, whereas a qualitatively different behaviour was found in device C. It is important to note that device C is not as clean as device A and, which is readily observed in the gate-gate map at zero magnetic field that shows many random fluctuations due to disorder, see Fig. 9.13 (a).

Further work is needed to fully clarify and to bring all experimental findings into accordance with each other. Dual gated bilayer graphene devices could prove useful as there electric field and charge carrier density could be tuned independently. In addition, capacitance measurements could be used to investigate the density of states for different doping configurations. If the diamond shaped conductance enhancements are due to bulk conduction or due to additional current flowing along domain walls, a scanning technique could prove useful to map the current distribution in this case. In addition, this could also be very interesting at the CNP, where a reduced conductance is observed.

10 Summary and outlook

In this thesis, spin and charge relaxation has been characterized in various graphene devices with different qualities by means of transport experiments as well as high frequency approaches.

A brief introduction to graphene and the experimental methods were given in chapter , 1 and 2.

Ferromagnetic nanostructures were characterized by magnetic force microscopy and X-ray circular dichroism measurements in chapter 3. Well defined single domain structure were found in permalloy and cobalt contacts. In addition, X-ray absorption spectra were used to investigate the role of an ex-situ transferred chemical vapour deposited (CVD) hexagonal boron nitride (hBN) layer in protecting ferromagnetic nanostructures from oxidation. For the first time, we showed that this leads to a slower oxidation process of CVD hBN covered permalloy structures compared to uncovered reference structures.

Superconducting tunnel spectroscopy employing CVD hBN as a tunnel barrier was used as a tool to study non-equilibrium properties of graphene in chapter 4. With this technique we were able to extract the energy distribution function of the quasiparticles, which could then be used as a local thermometer to measure the electron temperature. This allowed us to study heat transport in nanoscale and microscale graphene devices. Cooling through electron diffusion (Wiedemann-Franz law) as well as phonon cooling were identified as the dominating cooling mechanisms in different samples. Deviations from the Fermi liquid value of the Lorenz number were found and the electron phonon coupling strength was extracted.

CVD hBN tunnel barriers were used in chapter 5 for efficient electrical spin injection into graphene. Large injection efficiencies and reversed contact polarizations were found in high resistive contacts made from two-layer CVD hBN barriers. This is a big step towards large scale fabrication of spintronics devices based on CVD materials.

An alternative way of spin injection into graphene was explored in chapter 6. Magnetization dynamics, sustained by a continuous RF drive, is the key ingredient in dynamical spin injection, also called spin pumping. We showed for the first time that dynamical spin injection into graphene can be realized by a compact fabrication scheme that includes a broadband on-chip transmission line for the RF excitation.

Freely suspended graphene devices have proven to be among the cleanest graphene devices reported so far. High quality suspended bilayer graphene was investigated in the quantum Hall regime in chapter 9. Unconventional conductance features in locally gated devices were found alongside with a gapped ground state in small magnetic fields. The spin and valley degree of freedom of the charge carriers in graphene can result in rich transport features and the spin selective equilibration of edge states in the quantum Hall regime demonstrates the robustness of the spin degree of freedom compared to the valley degree of freedom.

The combination of graphene and other two-dimensional materials into vdW heterostructures has proven very useful in preserving graphene's exceptional charge carrier transport properties. In chapter 8, such a vdW heterostructure was capacitively coupled to a superconducting resonator operating at microwave frequencies. Admittance measurements allowed us to extract not only the real part of the impedance but also the complex part, which contains the quantum capacitance. This pioneering approach demonstrates that the important transport parameters of low dimensional systems can be extracted even in the absence of electrical contacts.

By replacing one hBN layer with a WSe₂ layer in these vdW heterostructures, strong spin-orbit coupling (SOC) was induced in graphene as presented in chapter 7. We showed for the first time that substantial SOC is present at low charge carrier concentrations where topological states are expected to emerge. Weak antilocalization measurements were used to quantify the strength of the SOC and revealed a dominating valley-Zeeman SOC term. This directly results in the large spin relaxation anisotropy found in these systems, which could be used as a spin filter in future spintronics applications.

In summary, spin and charge relaxation processes have been investigated in graphene based devices in this thesis. Spin transport measurements and the characterization of the spin-orbit coupling strengths by weak antilocalization measurements reveal the versatile nature of graphene for spintronics applications. In general, these techniques could be applied to other materials, including novel heterostructures as candidates for the future spintronics devices.

10.1. Outlook

It turned out that vdW heterostructures opened up a new field of low dimensional physics. The sheer number of different materials available nowadays offers the possibility of an uncountable number of combinations all with different properties.

Future graphene spin valves could combine the already established inverted fabrication technique, where a graphene/hBN heterostructure is transferred on top of predefined ferromagnetic electrodes [18, 179], with hBN tunnel barriers,

which have proven to be excellent for spin injection [160–162]. A perfect interface between the ferromagnetic material and the hBN tunnel barrier could be achieved by the direct growth of hBN on predefined ferromagnetic contacts [144, 178], which would also solve the oxidation problem of ferromagnetic materials [145, 146, 154]. The combination of these structures with locally patterned TMDC crystals could allow for very precise and gate tunable control of the spin transport properties in these spintronics devices.

Similar structures could be envisaged for superconducting tunnel spectroscopy, which could give direct access to the energy distribution function in various transport regimes. Using normal contacts instead of superconducting electrodes, the local density of states could be directly probed by performing tunnel spectroscopy measurements.

Standard transport measurements probe the average conductance of the sample and give no insight into the current distribution within a mesoscopic sample. However, the understanding of many transport phenomena could benefit from the knowledge of the current distribution within a device. Superconducting interference effects in magnetic field (e.g. Fraunhofer patterns) or scanning probe techniques could shed light onto the underlying mechanism of the large non-local resistance signals at the charge neutrality point in graphene for example. Similarly, the understanding of the unconventional conductance features in the quantum Hall regime of suspended bilayer graphene could profit from the knowledge of the current distribution within the device. Local tunnel probes at the edge in combination with RF capacitance measurements of the bulk could lead to complete understanding of complex mesoscopic devices.

The combination of graphene with other two-dimensional materials will definitely result in more exciting physical properties. One possibility is to combine bilayer graphene with WSe₂ that was theoretically predicted to have a tremendous gate tunability of the spin-orbit coupling [37, 38]. Superconducting electrodes are relatively easy to couple to graphene compared to traditional two-dimensional electron gases. This opens the possibility to combine graphene with engineered spin-orbit coupling with superconductivity resulting in a system that is expected to host novel states.

Apart from graphene based heterostructure, more exotic combinations of vdW heterostructures are possible nowadays, such as the coupling of ferromagnetic layers and superconducting layers to topological insulators.

Bibliography

- [1] J. Bardeen and W. H. Brattain, *Phys. Rev.* **74**, 230 (1948).
- [2] M. M. Waldrop, *Nature News* **530**, 114 (2016).
- [3] R. Blatt and C. F. Roos, *Nature Physics* **8**, 277 (2012).
- [4] Y. Nakamura, Y. A. Pashkin, and J. S. Tsai, *Nature* **398**, 786 (1999).
- [5] I. Chiorescu, Y. Nakamura, C. J. P. M. Harmans, and J. E. Mooij, *Science* **299**, 1869 (2003).
- [6] J. M. Martinis, S. Nam, J. Aumentado, and C. Urbina, *Phys. Rev. Lett.* **89**, 117901 (2002).
- [7] “IBM Q Experience,” <https://quantumexperience.ng.bluemix.net/qx/experience>, accessed: 2018-02-20.
- [8] D. Loss and D. P. DiVincenzo, *Phys. Rev. A* **57**, 120 (1998).
- [9] J. J. Pla, K. Y. Tan, J. P. Dehollain, W. H. Lim, J. J. L. Morton, D. N. Jamieson, A. S. Dzurak, and A. Morello, *Nature* **489**, 541 (2012).
- [10] E. Kawakami, P. Scarlino, D. R. Ward, F. R. Braakman, D. E. Savage, M. G. Lagally, M. Friesen, S. N. Coppersmith, M. A. Eriksson, and L. M. K. Vandersypen, *Nature Nanotechnology* **9**, 666 (2014).
- [11] R. Maurand, X. Jehl, D. Kotekar-Patil, A. Corna, H. Bohuslavskyi, R. Lavieville, L. Hutin, S. Barraud, M. Vinet, M. Sanquer, and S. De Franceschi, *Nature Communications* **7**, 13575 (2016).
- [12] I. Žutić, J. Fabian, and S. Das Sarma, *Rev. Mod. Phys.* **76**, 323 (2004).
- [13] A. Fert, *Rev. Mod. Phys.* **80**, 1517 (2008).
- [14] P. A. Grünberg, *Rev. Mod. Phys.* **80**, 1531 (2008).
- [15] W. Han, R. K. Kawakami, M. Gmitra, and J. Fabian, *Nat Nano* **9**, 794 (2014).
- [16] N. Tombros, C. Jozsa, M. Popinciuc, H. T. Jonkman, and B. J. van Wees, *Nature* **448**, 571 (2007).
- [17] J. Ingla-Aynés, M. H. D. Guimarães, R. J. Meijerink, P. J. Zomer, and B. J. van Wees, *Phys. Rev. B* **92**, 201410 (2015).

- [18] M. Drögeler, C. Franzen, F. Volmer, T. Pohlmann, L. Banszerus, M. Wolter, K. Watanabe, T. Taniguchi, C. Stampfer, and B. Beschoten, *Nano Letters* **16**, 3533 (2016).
- [19] D. Huertas-Hernando, F. Guinea, and A. Brataas, *Phys. Rev. Lett.* **103**, 146801 (2009).
- [20] B. Trauzettel, D. V. Bulaev, D. Loss, and G. Burkard, *Nature Physics* **3**, 192 (2007).
- [21] K. S. Novoselov, A. K. Geim, S. V. Morozov, D. Jiang, Y. Zhang, S. V. Dubonos, I. V. Grigorieva, and A. A. Firsov, *Science* **306**, 666 (2004).
- [22] E. Revolinsky, G. Spiering, and D. Beerntsen, *Journal of Physics and Chemistry of Solids* **26**, 1029 (1965).
- [23] X. Xi, Z. Wang, W. Zhao, J.-H. Park, K. T. Law, H. Berger, L. Forró, J. Shan, and K. F. Mak, *Nature Physics* **12**, 139 (2015).
- [24] B. Huang, G. Clark, E. Navarro-Moratalla, D. R. Klein, R. Cheng, K. L. Seyler, D. Zhong, E. Schmidgall, M. A. McGuire, D. H. Cobden, W. Yao, D. Xiao, P. Jarillo-Herrero, and X. Xu, *Nature* **546**, 270 (2017).
- [25] S. Wu, V. Fatemi, Q. D. Gibson, K. Watanabe, T. Taniguchi, R. J. Cava, and P. Jarillo-Herrero, *Science* **359**, 76 (2018).
- [26] A. K. Geim and I. V. Grigorieva, *Nature* **499**, 419 (2013).
- [27] L. A. Ponomarenko, R. V. Gorbachev, G. L. Yu, D. C. Elias, R. Jalil, A. A. Patel, A. Mishchenko, A. S. Mayorov, C. R. Woods, J. R. Wallbank, M. Mucha-Kruczynski, B. A. Piot, M. Potemski, I. V. Grigorieva, K. S. Novoselov, F. Guinea, V. I. Fal'ko, and A. K. Geim, *Nature* **497**, 594 (2013).
- [28] C. R. Dean, L. Wang, P. Maher, C. Forsythe, F. Ghahari, Y. Gao, J. Katoch, M. Ishigami, P. Moon, M. Koshino, T. Taniguchi, K. Watanabe, K. L. Shepard, J. Hone, and P. Kim, *Nature* **497**, 598 (2013).
- [29] B. Hunt, J. D. Sanchez-Yamagishi, A. F. Young, M. Yankowitz, B. J. LeRoy, K. Watanabe, T. Taniguchi, P. Moon, M. Koshino, P. Jarillo-Herrero, and R. C. Ashoori, *Science* **340**, 1427 (2013).
- [30] M. Lee, J. R. Wallbank, P. Gallagher, K. Watanabe, T. Taniguchi, V. I. Fal'ko, and D. Goldhaber-Gordon, *Science* **353**, 1526 (2016).
- [31] Z. Wang, C. Tang, R. Sachs, Y. Barlas, and J. Shi, *Phys. Rev. Lett.* **114**, 016603 (2015).
- [32] J. C. Leutenantsmeyer, A. A. Kaverzin, M. Wojtaszek, and B. J. van Wees, *2D Materials* **4**, 014001 (2017).
- [33] D. K. Efetov, L. Wang, C. Handschin, K. B. Efetov, J. Shuang, R. Cava, T. Taniguchi, K. Watanabe, J. Hone, C. R. Dean, and P. Kim, *Nature Physics* **12**, 328 (2015).

- [34] L. Bretheau, J. I.-J. Wang, R. Pisoni, K. Watanabe, T. Taniguchi, and P. Jarillo-Herrero, *Nature Physics* **13**, 756 (2017).
- [35] C. L. Kane and E. J. Mele, *Phys. Rev. Lett.* **95**, 226801 (2005).
- [36] A. W. Cummings, J. H. Garcia, J. Fabian, and S. Roche, *Phys. Rev. Lett.* **119**, 206601 (2017).
- [37] M. Gmitra and J. Fabian, *Phys. Rev. Lett.* **119**, 146401 (2017).
- [38] J. Y. Khoo, A. F. Morpurgo, and L. Levitov, *Nano Letters* **17**, 7003 (2017).
- [39] J. H. Garcia, A. W. Cummings, and S. Roche, *Nano Letters* **17**, 5078 (2017).
- [40] S. Konschuh, M. Gmitra, and J. Fabian, *Phys. Rev. B* **82**, 245412 (2010).
- [41] A. H. Castro Neto and F. Guinea, *Phys. Rev. Lett.* **103**, 026804 (2009).
- [42] M. Gmitra and J. Fabian, *Phys. Rev. B* **92**, 155403 (2015).
- [43] A. H. Castro Neto, F. Guinea, N. M. R. Peres, K. S. Novoselov, and A. K. Geim, *Rev. Mod. Phys.* **81**, 109 (2009).
- [44] S. Das Sarma, S. Adam, E. H. Hwang, and E. Rossi, *Rev. Mod. Phys.* **83**, 407 (2011).
- [45] M. O. Goerbig, *Rev. Mod. Phys.* **83**, 1193 (2011).
- [46] M. H. D. Guimarães, *Spin and Charge Transport in Graphene Devices in the Classical and Quantum Regimes*, Ph.D. thesis, University of Groningen (2014).
- [47] M. Gmitra, D. Kochan, P. Högl, and J. Fabian, *Phys. Rev. B* **93**, 155104 (2016).
- [48] C. Handschin, *Quantum Transport in Encapsulated Graphene P-N junctions*, Ph.D. thesis, University of Basel (2017).
- [49] M. S. Dresselhaus and G. Dresselhaus, *Advances in Physics* **51**, 1 (2002).
- [50] A. Varlet, M. Mucha-Kruczyński, D. Bischoff, P. Simonet, T. Taniguchi, K. Watanabe, V. Fal'ko, T. Ihn, and K. Ensslin, *Synthetic Metals* **210**, 19 (2015).
- [51] F. Schwierz, *Nature Nanotechnology* **5**, 487 (2010).
- [52] E. McCann, K. Kechedzhi, V. I. Fal'ko, H. Suzuura, T. Ando, and B. L. Altshuler, *Phys. Rev. Lett.* **97**, 146805 (2006).
- [53] D. Kochan, S. Imer, and J. Fabian, *Phys. Rev. B* **95**, 165415 (2017).
- [54] M. Gmitra, S. Konschuh, C. Ertler, C. Ambrosch-Draxl, and J. Fabian, *Phys. Rev. B* **80**, 235431 (2009).
- [55] K. Nomura and A. H. MacDonald, *Phys. Rev. Lett.* **98**, 076602 (2007).

- [56] B. Terrés, L. A. Chizhova, F. Libisch, J. Peiro, D. Jörger, S. Engels, A. Girschik, K. Watanabe, T. Taniguchi, S. V. Rotkin, J. Burgdörfer, and C. Stampfer, *Nature Communications* **7**, 11528 (2016).
- [57] N. Tombros, A. Veligura, J. Junesch, M. H. D. Guimarães, I. J. Vera-Marun, H. T. Jonkman, and B. J. van Wees, *Nature Physics* **7**, 697 (2011).
- [58] M. I. Katsnelson, K. S. Novoselov, and A. K. Geim, *Nat Phys* **2**, 620 (2006).
- [59] O. Klein, *Zeitschrift für Physik* **53**, 157 (1929).
- [60] P. Rickhaus, R. Maurand, M.-H. Liu, M. Weiss, K. Richter, and C. Schönenberger, *Nature Communications* **4**, 2342 (2013).
- [61] A. L. Grushina, D.-K. Ki, and A. F. Morpurgo, *Applied Physics Letters* **102**, 223102 (2013).
- [62] P. Rickhaus, M.-H. Liu, P. Makk, R. Maurand, S. Hess, S. Zihlmann, M. Weiss, K. Richter, and C. Schönenberger, *Nano Letters* **15**, 5819 (2015).
- [63] P. Rickhaus, P. Makk, M.-H. Liu, K. Richter, and C. Schönenberger, *Applied Physics Letters* **107**, 251901 (2015).
- [64] S. Chen, Z. Han, M. M. Elahi, K. M. M. Habib, L. Wang, B. Wen, Y. Gao, T. Taniguchi, K. Watanabe, J. Hone, A. W. Ghosh, and C. R. Dean, *Science* **353**, 1522 (2016).
- [65] G.-H. Lee, G.-H. Park, and H.-J. Lee, *Nature Physics* **11**, 925 (2015).
- [66] C. Beenakker and H. van Houten, in *Semiconductor Heterostructures and Nanostructures*, Solid State Physics, Vol. 44, edited by H. Ehrenreich and D. Turnbull (Academic Press, 1991) pp. 1 – 228.
- [67] T. Ihn, *Semiconductor Nanostructures* (Oxford University Press, 2010).
- [68] F. V. Tikhonenko, D. W. Horsell, R. V. Gorbachev, and A. K. Savchenko, *Phys. Rev. Lett.* **100**, 056802 (2008).
- [69] F. V. Tikhonenko, A. A. Kozikov, A. K. Savchenko, and R. V. Gorbachev, *Phys. Rev. Lett.* **103**, 226801 (2009).
- [70] M. B. Lundberg and J. A. Folk, *Phys. Rev. Lett.* **105**, 146804 (2010).
- [71] N. J. G. Couto, D. Costanzo, S. Engels, D.-K. Ki, K. Watanabe, T. Taniguchi, C. Stampfer, F. Guinea, and A. F. Morpurgo, *Phys. Rev. X* **4**, 041019 (2014).
- [72] G. Bergmann, *Solid State Communications* **42**, 815 (1982).
- [73] E. McCann and V. I. Fal’ko, *Phys. Rev. Lett.* **108**, 166606 (2012).
- [74] E. H. Hall, *American Journal of Mathematics* **2**, 287 (1879).
- [75] K. v. Klitzing, G. Dorda, and M. Pepper, *Phys. Rev. Lett.* **45**, 494 (1980).

- [76] K. S. Novoselov, Z. Jiang, Y. Zhang, S. V. Morozov, H. L. Stormer, U. Zeitler, J. C. Maan, G. S. Boebinger, P. Kim, and A. K. Geim, *Science* **315**, 1379 (2007).
- [77] A. F. Young, C. R. Dean, L. Wang, H. Ren, P. Cadden-Zimansky, K. Watanabe, T. Taniguchi, J. Hone, K. L. Shepard, and P. Kim, *Nature Physics* **8**, 550 (2012).
- [78] T. P. Cysne, J. H. Garcia, A. R. Rocha, and T. G. Rappoport, *Phys. Rev. B* **97**, 085413 (2018).
- [79] D. A. Abanin and L. S. Levitov, *Phys. Rev. B* **78**, 035416 (2008).
- [80] J. R. Williams, D. A. Abanin, L. DiCarlo, L. S. Levitov, and C. M. Marcus, *Phys. Rev. B* **80**, 045408 (2009).
- [81] E. McCann and V. I. Fal'ko, *Phys. Rev. Lett.* **96**, 086805 (2006).
- [82] J. Stöhr and H. Siegmann, *Magnetism - From Fundamentals to Nanoscale Dynamics* (Springer, 2006).
- [83] M. Getzlaff, *Fundamentals of Magnetism* (Springer Berlin Heidelberg, 2007).
- [84] J. Gramich, *Andreev and Spin Transport in Carbon Nanotube Quantum Dot Hybrid Devices*, Ph.D. thesis, University of Basel (2016).
- [85] W. J. Brown, *Micromagnetics* (Wiley, 1963).
- [86] C. Tannous and J. Gieraltowski, *European Journal of Physics* **29**, 475 (2008).
- [87] L. D. Landau, E. M. Lifshitz, and L. P. Pitaevski, *Statistical Physics, Part 2*, 3rd ed. (Pergamon, Oxford, 1980).
- [88] T. L. Gilbert, *Phys. Rev.* **100**, 1243 (1955).
- [89] Y. Tserkovnyak, A. Brataas, and G. E. W. Bauer, *Phys. Rev. Lett.* **88**, 117601 (2002).
- [90] R. H. Silsbee, A. Janossy, and P. Monod, *Phys. Rev. B* **19**, 4382 (1979).
- [91] S. Mizukami, Y. Ando, and T. Miyazaki, *Phys. Rev. B* **66**, 104413 (2002).
- [92] A. K. Patra, S. Singh, B. Barin, Y. Lee, J.-H. Ahn, E. del Barco, E. R. Mucciolo, and B. Özyilmaz, *Applied Physics Letters* **101**, 162407 (2012).
- [93] Z. Tang, E. Shikoh, H. Ago, K. Kawahara, Y. Ando, T. Shinjo, and M. Shiraishi, *Phys. Rev. B* **87**, 140401 (2013).
- [94] J. Fabian, A. Matos-Abiague, C. Ertler, P. Stano, and I. Žutić, *Acta Physica Slovaca* **57**, 565 (2007).
- [95] G. Schmidt, D. Ferrand, L. W. Molenkamp, A. T. Filip, and B. J. van Wees, *Phys. Rev. B* **62**, R4790 (2000).

- [96] I. I. Mazin, *Phys. Rev. Lett.* **83**, 1427 (1999).
- [97] F. J. Jedema, M. S. Nijboer, A. T. Filip, and B. J. van Wees, *Phys. Rev. B* **67**, 085319 (2003).
- [98] R. H. Silsbee, *Bull. Magn. Reson.* **2**, 284 (1980).
- [99] M. Johnson and R. H. Silsbee, *Phys. Rev. Lett.* **55**, 1790 (1985).
- [100] R. J. Elliott, *Phys. Rev.* **96**, 266 (1954).
- [101] Y. Yafet (Academic Press, 1963) pp. 1 – 98.
- [102] H. Ochoa, A. H. Castro Neto, and F. Guinea, *Phys. Rev. Lett.* **108**, 206808 (2012).
- [103] M. B. Lundberg, R. Yang, J. Renard, and J. A. Folk, *Phys. Rev. Lett.* **110**, 156601 (2013).
- [104] M. M. Ugeda, I. Brihuega, F. Guinea, and J. M. Gómez-Rodríguez, *Phys. Rev. Lett.* **104**, 096804 (2010).
- [105] T. O. Wehling, S. Yuan, A. I. Lichtenstein, A. K. Geim, and M. I. Katsnelson, *Phys. Rev. Lett.* **105**, 056802 (2010).
- [106] R. R. Nair, M. Sepioni, I.-L. Tsai, O. Lehtinen, J. Keinonen, A. V. Krasheninikov, T. Thomson, A. K. Geim, and I. V. Grigorieva, *Nature Physics* **8**, 199 (2012).
- [107] H. González-Herrero, J. M. Gómez-Rodríguez, P. Mallet, M. Moaied, J. J. Palacios, C. Salgado, M. M. Ugeda, J.-Y. Veuillen, F. Yndurain, and I. Brihuega, *Science* **352**, 437 (2016).
- [108] D. Kochan, M. Gmitra, and J. Fabian, *Phys. Rev. Lett.* **112**, 116602 (2014).
- [109] D. Kochan, S. Irmer, M. Gmitra, and J. Fabian, *Phys. Rev. Lett.* **115**, 196601 (2015).
- [110] D. V. Tuan, F. Ortmann, D. Soriano, S. O. Valenzuela, and S. Roche, *Nature Physics* **10**, 857 (2014).
- [111] S. Fratini, D. Gosálbez-Martínez, P. Merodio Cámara, and J. Fernández-Rossier, *Phys. Rev. B* **88**, 115426 (2013).
- [112] J. Sinova, S. O. Valenzuela, J. Wunderlich, C. H. Back, and T. Jungwirth, *Rev. Mod. Phys.* **87**, 1213 (2015).
- [113] N. F. Mott, *Proceedings of the Royal Society of London A: Mathematical, Physical and Engineering Sciences* **124**, 425 (1929).
- [114] Y. K. Kato, R. C. Myers, A. C. Gossard, and D. D. Awschalom, *Science* **306**, 1910 (2004).
- [115] J. Wunderlich, B. Kaestner, J. Sinova, and T. Jungwirth, *Phys. Rev. Lett.* **94**, 047204 (2005).

- [116] E. Saitoh, M. Ueda, H. Miyajima, and G. Tatara, *Applied Physics Letters* **88**, 182509 (2006).
- [117] S. O. Valenzuela and M. Tinkham, *Nature* **442**, 176 (2006).
- [118] H. Zhao, E. J. Loren, H. M. van Driel, and A. L. Smirl, *Phys. Rev. Lett.* **96**, 246601 (2006).
- [119] E. M. Hankiewicz, L. W. Molenkamp, T. Jungwirth, and J. Sinova, *Phys. Rev. B* **70**, 241301 (2004).
- [120] S. V. Morozov, K. S. Novoselov, M. I. Katsnelson, F. Schedin, D. C. Elias, J. A. Jaszczak, and A. K. Geim, *Phys. Rev. Lett.* **100**, 016602 (2008).
- [121] C. R. Dean, A. F. Young, I. Meric, C. Lee, L. Wang, S. Sorgenfrei, K. Watanabe, T. Taniguchi, P. Kim, K. L. Shepard, and J. Hone, *Nat Nano* **5**, 722 (2010).
- [122] A. C. Betz, S. H. Jhang, E. Pallecchi, R. Ferreira, G. Fève, J.-M. Berroir, and B. Plaçaïs, *Nature Physics* **9**, 109 (2012).
- [123] K. C. Fong and K. C. Schwab, *Phys. Rev. X* **2**, 031006 (2012).
- [124] K. C. Fong, E. E. Wollman, H. Ravi, W. Chen, A. A. Clerk, M. D. Shaw, H. G. Leduc, and K. C. Schwab, *Phys. Rev. X* **3**, 041008 (2013).
- [125] C. B. McKitterick, D. E. Prober, and M. J. Rooks, *Phys. Rev. B* **93**, 075410 (2016).
- [126] I. V. Borzenets, U. C. Coskun, H. T. Mebrahtu, Y. V. Bomze, A. I. Smirnov, and G. Finkelstein, *Phys. Rev. Lett.* **111**, 027001 (2013).
- [127] A. S. Price, S. M. Hornett, A. V. Shytov, E. Hendry, and D. W. Horsell, *Phys. Rev. B* **85**, 161411 (2012).
- [128] Z. Chen, W. Jang, W. Bao, C. N. Lau, and C. Dames, *Applied Physics Letters* **95**, 161910 (2009).
- [129] H. Pothier, S. Guéron, N. Birge, and D. Esteve, *Zeitschrift für Physik B Condensed Matter* **103**, 313 (1996).
- [130] H. Pothier, S. Guéron, N. O. Birge, D. Esteve, and M. H. Devoret, *Phys. Rev. Lett.* **79**, 3490 (1997).
- [131] A. C. Betz, F. Vialla, D. Brunel, C. Voisin, M. Picher, A. Cavanna, A. Madouri, G. Fève, J.-M. Berroir, B. Plaçaïs, and E. Pallecchi, *Phys. Rev. Lett.* **109**, 056805 (2012).
- [132] S. Piscanec, M. Lazzeri, F. Mauri, A. C. Ferrari, and J. Robertson, *Phys. Rev. Lett.* **93**, 185503 (2004).
- [133] W. Chen and A. A. Clerk, *Phys. Rev. B* **86**, 125443 (2012).
- [134] K. S. Novoselov, D. Jiang, F. Schedin, T. J. Booth, V. V. Khotkevich, S. V. Morozov, and A. K. Geim, *Proceedings of the National Academy of Sciences of the United States of America* **102**, 10451 (2005).

- [135] T. Taniguchi and K. Watanabe, *Journal of Crystal Growth* **303**, 525 (2007).
- [136] R. V. Gorbachev, I. Riaz, R. R. Nair, R. Jalil, L. Britnell, B. D. Belle, E. W. Hill, K. S. Novoselov, K. Watanabe, T. Taniguchi, A. K. Geim, and P. Blake, *Small* **7**, 465 (2011).
- [137] L. Wang, I. Meric, P. Y. Huang, Q. Gao, Y. Gao, H. Tran, T. Taniguchi, K. Watanabe, L. M. Campos, D. A. Muller, J. Guo, P. Kim, J. Hone, K. L. Shepard, and C. R. Dean, *Science* **342**, 614 (2013).
- [138] P. J. Zomer, M. H. D. Guimarães, J. C. Brant, N. Tombros, and B. J. van Wees, *Applied Physics Letters* **105**, 013101 (2014), <http://dx.doi.org/10.1063/1.4886096>.
- [139] R. Maurand, P. Rickhaus, P. Makk, S. Hess, E. Tóvári, C. Handschin, M. Weiss, and C. Schönenberger, *Carbon* **79**, 486 (2014).
- [140] N. Tombros, A. Veligura, J. Junesch, J. J. van den Berg, P. J. Zomer, M. Wojtaszek, I. J. V. Marun, H. T. Jonkman, and B. J. van Wees, *Journal of Applied Physics* **109**, 093702 (2011).
- [141] P. Rickhaus, *Electron optics in ballistic graphene*, Ph.D. thesis, University of Basel (2015).
- [142] “Graphene supermarket,” <https://graphene-supermarket.com/>, accessed: 2018-02-23.
- [143] X. Song, J. Gao, Y. Nie, T. Gao, J. Sun, D. Ma, Q. Li, Y. Chen, C. Jin, A. Bachmatiuk, M. Rümeli, F. Ding, Y. Zhang, and Z. Liu, *Nano Research*, **1** (2015).
- [144] S. Caneva, R. S. Weatherup, B. C. Bayer, B. Brennan, S. J. Spencer, K. Mingard, A. Cabrero-Vilatelá, C. Baetz, A. J. Pollard, and S. Hofmann, *Nano Letters* **15**, 1867 (2015).
- [145] R. S. Weatherup, L. D’arsié, A. Cabrero-Vilatelá, S. Caneva, R. Blume, J. Robertson, R. Schloegl, and S. Hofmann, *Journal of the American Chemical Society* **137**, 14358 (2015).
- [146] S. Caneva, M.-B. Martin, L. D’Arsié, A. I. Aria, H. Sezen, M. Amati, L. Gregoratti, H. Sugime, S. Esconjauregui, J. Robertson, S. Hofmann, and R. S. Weatherup, *ACS Applied Materials & Interfaces* **9**, 29973 (2017).
- [147] L. Gao, W. Ren, H. Xu, L. Jin, Z. Wang, T. Ma, L.-P. Ma, Z. Zhang, Q. Fu, L.-M. Peng, X. Bao, and H.-M. Cheng, *Nature Communications* **3**, 699 (2012).
- [148] Y. Gao, W. Ren, T. Ma, Z. Liu, Y. Zhang, W.-B. Liu, L.-P. Ma, X. Ma, and H.-M. Cheng, *ACS Nano* **7**, 5199 (2013).
- [149] Z. Wang, D.-K. Ki, J. Y. Khoo, D. Mauro, H. Berger, L. S. Levitov, and A. F. Morpurgo, *Phys. Rev. X* **6**, 041020 (2016).
- [150] L. Banszerus, M. Schmitz, S. Engels, J. Dauber, M. Oellers, F. Haupt, K. Watanabe, T. Taniguchi, B. Beschoten, and C. Stampfer, *Science Advances* **1** (2015), 10.1126/sciadv.1500222.

- [151] M. Schmitz, S. Engels, L. Banszerus, K. Watanabe, T. Taniguchi, C. Stampfer, and B. Beschoten, *Applied Physics Letters* **110**, 263110 (2017).
- [152] F. Pobell, *Matter and Methods at Low Temperatures* (Springer-Verlag Berlin Heidelberg, 2007).
- [153] “Electronics Lab,” <https://www.physik.unibas.ch/departement/infrastruktur-dienstleistungen/elektronik-werkstatt.html>, accessed on 2018-01-05.
- [154] S. Zihlmann, P. Makk, C. A. F. Vaz, and C. Schönenberger, *2D Materials* **3**, 011008 (2016).
- [155] T. Miyazaki and N. Tezuka, *Journal of Magnetism and Magnetic Materials* **139**, L231 (1995).
- [156] J. S. Moodera, L. R. Kinder, T. M. Wong, and R. Meservey, *Phys. Rev. Lett.* **74**, 3273 (1995).
- [157] X. Wang, S. M. Tabakman, and H. Dai, *Journal of the American Chemical Society* **130**, 8152 (2008).
- [158] W. H. Wang, W. Han, K. Pi, K. M. McCreary, F. Miao, W. Bao, C. N. Lau, and R. K. Kawakami, *Applied Physics Letters* **93**, 183107 (2008).
- [159] T. Yamaguchi, Y. Inoue, S. Masubuchi, S. Morikawa, M. Onuki, K. Watanabe, T. Taniguchi, R. Moriya, and T. Machida, *Applied Physics Express* **6**, 073001 (2013).
- [160] M. Gurram, S. Omar, S. Zihlmann, P. Makk, C. Schönenberger, and B. J. van Wees, *Phys. Rev. B* **93**, 115441 (2016).
- [161] S. Singh, J. Katoch, J. Xu, C. Tan, T. Zhu, W. Amamou, J. Hone, and R. Kawakami, *Applied Physics Letters* **109**, 122411 (2016).
- [162] M. Gurram, S. Omar, and B. J. v. Wees, *Nature Communications* **8**, 248 (2017).
- [163] W. Fu, P. Makk, R. Maurand, M. Bräuninger, and C. Schönenberger, *Journal of Applied Physics* **116**, 074306 (2014).
- [164] M. V. Kamalakar, A. Dankert, J. Bergsten, T. Ive, and S. P. Dash, *Sci. Rep.* **4** (2014).
- [165] M. Gurram, S. Omar, S. Zihlmann, P. Makk, Q. C. Li, Y. F. Zhang, C. Schönenberger, and B. J. van Wees, *Phys. Rev. B* **97**, 045411 (2018).
- [166] M.-B. Martin, B. Dlubak, R. S. Weatherup, M. Piquemal-Banci, H. Yang, R. Blume, R. Schloegl, S. Collin, F. Petroff, S. Hofmann, J. Robertson, A. Anane, A. Fert, and P. Seneor, *Applied Physics Letters* **107**, 012408 (2015).
- [167] Z. Liu, Y. Gong, W. Zhou, L. Ma, J. Yu, J. C. Idrobo, J. Jung, A. H. MacDonald, R. Vajtai, J. Lou, and P. M. Ajayan, *Nat Commun* **4** (2013).

- [168] X. Li, J. Yin, J. Zhou, and W. Guo, *Nanotechnology* **25**, 105701 (2014).
- [169] X. M. Cheng and D. J. Keavney, *Reports on Progress in Physics* **75**, 026501 (2012).
- [170] T. J. Regan, H. Ohldag, C. Stamm, F. Nolting, J. Lüning, J. Stöhr, and R. L. White, *Phys. Rev. B* **64**, 214422 (2001).
- [171] C. A. F. Vaz, A. Balan, F. Nolting, and A. Kleibert, *Phys. Chem. Chem. Phys.* **16**, 26624 (2014).
- [172] J. Stöhr, *Journal of Electron Spectroscopy and Related Phenomena* **75**, 253 (1995).
- [173] F. Jiménez-Villacorta, C. Prieto, Y. Huttel, N. D. Telling, and G. van der Laan, *Phys. Rev. B* **84**, 172404 (2011).
- [174] D. J. Huang, C. F. Chang, H.-T. Jeng, G. Y. Guo, H.-J. Lin, W. B. Wu, H. C. Ku, A. Fujimori, Y. Takahashi, and C. T. Chen, *Phys. Rev. Lett.* **93**, 077204 (2004).
- [175] J.-Y. Kim, T. Y. Koo, and J.-H. Park, *Phys. Rev. Lett.* **96**, 047205 (2006).
- [176] T. B. Reed, *Free Energy of Formation of Binary Compounds* (The MIT Press, Cambridge, MA, 1971).
- [177] J. Klinovaja and D. Loss, *Phys. Rev. X* **3**, 011008 (2013).
- [178] M. Piquemal-Banci, R. Galceran, S. Caneva, M.-B. Martin, R. S. Weatherup, P. R. Kidambi, K. Bouzehouane, S. Xavier, A. Anane, F. Petroff, A. Fert, J. Robertson, S. Hofmann, B. Dlubak, and P. Seneor, *Applied Physics Letters* **108**, 102404 (2016), <http://dx.doi.org/10.1063/1.4943516>.
- [179] M. Drögeler, F. Volmer, M. Wolter, B. Terrés, K. Watanabe, T. Taniguchi, G. Güntherodt, C. Stampfer, and B. Beschoten, *Nano Letters* **14**, 6050 (2014).
- [180] M. Drögeler, L. Banszerus, F. Volmer, T. Taniguchi, K. Watanabe, B. Beschoten, and C. Stampfer, *Applied Physics Letters* **111**, 152402 (2017).
- [181] J. Gramich, A. Baumgartner, and C. Schönenberger, *Applied Physics Letters* **108**, 172604 (2016).
- [182] Y.-F. Chen, T. Dirks, G. Al-Zoubi, N. O. Birge, and N. Mason, *Phys. Rev. Lett.* **102**, 036804 (2009).
- [183] T. T. Heikkilä, *The Physics of Nanoelectronics* (OXFORD University Press, 2013).
- [184] R. C. Dynes, V. Narayanamurti, and J. P. Garno, *Phys. Rev. Lett.* **41**, 1509 (1978).
- [185] G. S. Kumar, G. Prasad, and R. O. Pohl, *Journal of Materials Science* **28**, 4261 (1993).

-
- [186] M. Müller, L. Fritz, and S. Sachdev, *Phys. Rev. B* **78**, 115406 (2008).
- [187] M. S. Foster and I. L. Aleiner, *Phys. Rev. B* **79**, 085415 (2009).
- [188] K. M. Borysenko, J. T. Mullen, E. A. Barry, S. Paul, Y. G. Semenov, J. M. Zavada, M. B. Nardelli, and K. W. Kim, *Phys. Rev. B* **81**, 121412 (2010).
- [189] X. Li, E. A. Barry, J. M. Zavada, M. B. Nardelli, and K. W. Kim, *Applied Physics Letters* **97**, 232105 (2010).
- [190] K. Kaasbjerg, K. S. Thygesen, and K. W. Jacobsen, *Phys. Rev. B* **85**, 165440 (2012).
- [191] M. V. Kamalakar, A. Dankert, J. Bergsten, T. Ive, and S. P. Dash, *Applied Physics Letters* **105**, 212405 (2014).
- [192] M. V. Kamalakar, A. Dankert, P. J. Kelly, and S. P. Dash, *Scientific Reports* **6**, 21168 (2016).
- [193] T. Maassen, I. J. Vera-Marun, M. H. D. Guimarães, and B. J. van Wees, *Phys. Rev. B* **86**, 235408 (2012).
- [194] Q. Wu, L. Shen, Z. Bai, M. Zeng, M. Yang, Z. Huang, and Y. P. Feng, *Phys. Rev. Applied* **2**, 044008 (2014).
- [195] L. Britnell, R. V. Gorbachev, R. Jalil, B. D. Belle, F. Schedin, M. I. Katsnelson, L. Eaves, S. V. Morozov, A. S. Mayorov, N. M. R. Peres, A. H. Castro Neto, J. Leist, A. K. Geim, L. A. Ponomarenko, and K. S. Novoselov, *Nano Letters* **12**, 1707 (2012).
- [196] K. Nagashio, T. Nishimura, K. Kita, and A. Toriumi, *Applied Physics Letters* **97**, 143514 (2010), <http://dx.doi.org/10.1063/1.3491804>.
- [197] C. P. Weber, N. Gedik, J. E. Moore, J. Orenstein, J. Stephens, and D. D. Awschalom, *Nature* **437**, 1330 (2005).
- [198] T. Maassen, F. K. Dejene, M. H. D. Guimarães, C. Józsa, and B. J. van Wees, *Phys. Rev. B* **83**, 115410 (2011).
- [199] E. Sosenko, H. Wei, and V. Aji, *Phys. Rev. B* **89**, 245436 (2014).
- [200] H. Idzuchi, A. Fert, and Y. Otani, *Phys. Rev. B* **91**, 241407 (2015).
- [201] G. Stecklein, P. A. Crowell, J. Li, Y. Anugrah, Q. Su, and S. J. Koester, *Phys. Rev. Applied* **6**, 054015 (2016).
- [202] M. H. D. Guimarães, A. Veligura, P. J. Zomer, T. Maassen, I. J. Vera-Marun, N. Tombros, and B. J. van Wees, *Nano Letters* **12**, 3512 (2012).
- [203] S. P. Dash, S. Sharma, J. C. Le Breton, J. Peiro, H. Jaffrès, J.-M. George, A. Lemaître, and R. Jansen, *Phys. Rev. B* **84**, 054410 (2011).
- [204] P. J. Zomer, M. H. D. Guimarães, N. Tombros, and B. J. van Wees, *Phys. Rev. B* **86**, 161416 (2012).

- [205] C. Józsa, M. Popinciuc, N. Tombros, H. T. Jonkman, and B. J. van Wees, *Phys. Rev. B* **79**, 081402 (2009).
- [206] B. Raes, J. E. Scheerder, M. V. Costache, F. Bonell, J. F. Sierra, J. Cuppens, J. Van de Vondel, and S. O. Valenzuela, *Nature Communications* **7**, 11444 (2016).
- [207] F. Volmer, M. Drögeler, T. Pohlmann, G. Güntherodt, C. Stampfer, and B. Beschoten, *2D Materials* **2**, 024001 (2015).
- [208] M. H. D. G. aes, P. J. Zomer, I. J. Vera-Marun, and B. J. van Wees, *Nano Letters* **14**, 2952 (2014).
- [209] D. Indolese, S. Zihlmann, P. Makk, C. Jünger, K. Thodkar, and C. Schönenberger, *Phys. Rev. Applied* **10**, 044053 (2018).
- [210] A. Brataas, Y. Tserkovnyak, G. E. W. Bauer, and B. I. Halperin, *Phys. Rev. B* **66**, 060404 (2002).
- [211] Y. Tserkovnyak, A. Brataas, G. E. W. Bauer, and B. I. Halperin, *Rev. Mod. Phys.* **77**, 1375 (2005).
- [212] M. V. Costache, M. Sladkov, C. H. van der Wal, and B. J. van Wees, *Applied Physics Letters* **89**, 192506 (2006).
- [213] K. Ando, S. Takahashi, J. Ieda, Y. Kajiwara, H. Nakayama, T. Yoshino, K. Harii, Y. Fujikawa, M. Matsuo, S. Maekawa, and E. Saitoh, *Journal of Applied Physics* **109**, 103913 (2011).
- [214] C. Kittel, *Introduction to Solid State Physics*, 7th ed. (John Wiley & Sons, 1996).
- [215] D. Wei, M. Obstbaum, M. Ribow, C. H. Back, and G. Woltersdorf, *Nat Commun* **5**, (2014).
- [216] D. Kochan, M. Gmitra, and J. Fabian, *Phys. Rev. Lett.* **107**, 176604 (2011).
- [217] R. K. Dumas, S. R. Sani, S. M. Mohseni, E. Iacocca, Y. Pogoryelov, P. K. Muduli, S. Chung, P. Dürrenfeld, and J. Åkerman, *IEEE Transactions on Magnetism* **50**, 1 (2014).
- [218] S. Hacia, T. Last, S. F. Fischer, and U. Kunze, *Journal of Physics D: Applied Physics* **37**, 1310 (2004).
- [219] H. Aurich, A. Baumgartner, F. Freitag, A. Eichler, J. Trbovic, and C. Schönenberger, *Applied Physics Letters* **97**, 153116 (2010).
- [220] J. Samm, J. Gramich, A. Baumgartner, M. Weiss, and C. Schönenberger, *Journal of Applied Physics* **115**, 174309 (2014).
- [221] Y.-C. Chen, D.-S. Hung, Y.-D. Yao, S.-F. Lee, H.-P. Ji, and C. Yu, *Journal of Applied Physics* **101**, 09C104 (2007).

- [222] Y. Tserkovnyak, A. Brataas, and G. E. W. Bauer, *Phys. Rev. B* **66**, 224403 (2002).
- [223] R. Iguchi and E. Saitoh, *Journal of the Physical Society of Japan* **86**, 011003 (2017).
- [224] K. Zollner, M. Gmitra, T. Frank, and J. Fabian, *Phys. Rev. B* **94**, 155441 (2016).
- [225] T. Abtew, B.-C. Shih, S. Banerjee, and P. Zhang, *Nanoscale* **5**, 1902 (2013).
- [226] J. B. S. Mendes, O. Alves Santos, L. M. Meireles, R. G. Lacerda, L. H. Vilela-Leão, F. L. A. Machado, R. L. Rodríguez-Suárez, A. Azevedo, and S. M. Rezende, *Phys. Rev. Lett.* **115**, 226601 (2015).
- [227] T. Inoue, G. E. W. Bauer, and K. Nomura, *Phys. Rev. B* **94**, 205428 (2016).
- [228] M. A. Rahimi and A. G. Moghaddam, *Journal of Physics D: Applied Physics* **48**, 295004 (2015).
- [229] S. Dushenko, H. Ago, K. Kawahara, T. Tsuda, S. Kuwabata, T. Takenobu, T. Shinjo, Y. Ando, and M. Shiraishi, *Phys. Rev. Lett.* **116**, 166102 (2016).
- [230] J. Moser, A. Barreiro, and A. Bachtold, *Applied Physics Letters* **91**, 163513 (2007).
- [231] S. Zihlmann, A. W. Cummings, J. H. Garcia, M. Kedves, K. Watanabe, T. Taniguchi, C. Schönenberger, and P. Makk, *Phys. Rev. B* **97**, 075434 (2018).
- [232] Z. Wang, D. Ki, H. Chen, H. Berger, A. H. MacDonald, and A. F. Morpurgo, *Nature Communications* **6**, 8339 (2015).
- [233] B. Yang, M.-F. Tu, J. Kim, Y. Wu, H. Wang, J. Alicea, R. Wu, M. Bockrath, and J. Shi, *2D Materials* **3**, 031012 (2016).
- [234] T. Völkl, T. Rockinger, M. Drienovsky, K. Watanabe, T. Taniguchi, D. Weiss, and J. Eroms, *Phys. Rev. B* **96**, 125405 (2017).
- [235] B. Yang, M. Lohmann, D. Barroso, I. Liao, Z. Lin, Y. Liu, L. Bartels, K. Watanabe, T. Taniguchi, and J. Shi, *Phys. Rev. B* **96**, 041409 (2017).
- [236] T. Wakamura, F. Reale, P. Palczynski, S. Guéron, C. Mattevi, and H. Bouchiat, “Strong Spin-Orbit Interaction Induced in Graphene by Monolayer WS₂,” (2017), [arXiv:1710.07483](https://arxiv.org/abs/1710.07483).
- [237] L. Banszerus, K. Watanabe, T. Taniguchi, B. Beschoten, and C. Stampfer, *Physics Status Solidi RRL* **11**, 1700136 (2017).
- [238] P. A. Lee, A. D. Stone, and H. Fukuyama, *Phys. Rev. B* **35**, 1039 (1987).
- [239] M. B. Lundeberg, J. Renard, and J. A. Folk, *Phys. Rev. B* **86**, 205413 (2012).
- [240] R. Addou and R. M. Wallace, *ACS Applied Materials & Interfaces* **8**, 26400 (2016).

- [241] T. S. Ghiasi, J. Ingla-Aynés, A. A. Kaverzin, and B. J. van Wees, *Nano Letters* **17**, 7528 (2017).
- [242] L. A. Benítez, J. F. Sierra, W. S. Torres, A. Arrighi, F. Bonell, M. V. Costache, and S. O. Valenzuela, *Nature Physics* (2017), 10.1038/s41567-017-0019-2.
- [243] M. I. Dyakonov and V. I. Perel, *Sov. Phys. Solid State* **13**, 3023 (1972).
- [244] D. A. Abanin, A. V. Shytov, L. S. Levitov, and B. I. Halperin, *Phys. Rev. B* **79**, 035304 (2009).
- [245] J. Balakrishnan, G. Kok Wai Koon, M. Jaiswal, A. H. Castro Neto, and B. Özyilmaz, *Nature Physics* **9**, 284 (2013).
- [246] J. Balakrishnan, G. K. W. Koon, A. Avsar, Y. Ho, J. H. Lee, M. Jaiswal, S.-J. Baeck, J.-H. Ahn, A. Ferreira, M. A. Cazalilla, A. H. C. Neto, and B. Özyilmaz, *Nature Communications* **5**, 4748 (2014).
- [247] A. Avsar, J. Y. Tan, T. Taychatanapat, J. Balakrishnan, G. Koon, Y. Yeo, J. Lahiri, A. Carvalho, A. S. Rodin, E. O’Farrell, G. Eda, A. H. Castro Neto, and B. Özyilmaz, *Nat Commun* **5**, (2014).
- [248] A. A. Kaverzin and B. J. van Wees, *Phys. Rev. B* **91**, 165412 (2015).
- [249] M. I. Dyakonov, *Phys. Rev. Lett.* **99**, 126601 (2007).
- [250] R. V. Gorbachev, J. C. W. Song, G. L. Yu, A. V. Kretinin, F. Withers, Y. Cao, A. Mishchenko, I. V. Grigorieva, K. S. Novoselov, L. S. Levitov, and A. K. Geim, *Science* **346**, 448 (2014).
- [251] J. M. Marmolejo-Tejada, J. H. García, M. Petrović, P. H. Chang, X. L. Sheng, A. Cresti, P. Plecháč, S. Roche, and B. K. Nikolic, “Origin of nonlocal resistance in multiterminal graphene on hexagonal-boron-nitride: Fermi surface edge currents rather than Fermi sea topological valley currents,” (2017), [arXiv:1706.09361](https://arxiv.org/abs/1706.09361) .
- [252] J. Moser, H. Tao, S. Roche, F. Alzina, C. M. Sotomayor Torres, and A. Bach-told, *Phys. Rev. B* **81**, 205445 (2010).
- [253] V. Ranjan, S. Zihlmann, P. Makk, K. Watanabe, T. Taniguchi, and C. Schö-nenberger, *Phys. Rev. Applied* **7**, 054015 (2017).
- [254] G. Giovannetti, P. A. Khomyakov, G. Brocks, V. M. Karpan, J. van den Brink, and P. J. Kelly, *Phys. Rev. Lett.* **101**, 026803 (2008).
- [255] A. La Magna and I. Deretzis, *Nanoscale Research Letters* **6**, 234 (2011).
- [256] J. A. Robinson, M. LaBella, M. Zhu, M. Hollander, R. Kasarda, Z. Hughes, K. Trumbull, R. Cavaleiro, and D. Snyder, *Applied Physics Letters* **98**, 053103 (2011).
- [257] F. Volmer, M. Drögeler, E. Maynicke, N. von den Driesch, M. L. Boschen, G. Güntherodt, and B. Beschoten, *Phys. Rev. B* **88**, 161405 (2013).

- [258] W. Amamou, Z. Lin, J. van Baren, S. Turkyilmaz, J. Shi, and R. K. Kawakami, *APL Materials* **4**, 032503 (2016).
- [259] J. Obrzut, C. Emiroglu, O. Kirillov, Y. Yang, and R. E. Elmquist, *Measurement* **87**, 146 (2016).
- [260] Y.-T. Cui, B. Wen, E. Y. Ma, G. Diankov, Z. Han, F. Amet, T. Taniguchi, K. Watanabe, D. Goldhaber-Gordon, C. R. Dean, and Z.-X. Shen, *Phys. Rev. Lett.* **117**, 186601 (2016).
- [261] Z. Q. Li, E. A. Henriksen, Z. Jiang, Z. Hao, M. C. Martin, P. Kim, H. L. Stormer, and D. N. Basov, *Nature Physics* **4**, 532 (2008).
- [262] C. Gomez-Navarro, F. J. Guzman-Vazquez, J. Gomez-Herrero, J. J. Saenz, and G. M. Sacha, *Nanoscale* **4**, 7231 (2012).
- [263] G. Puebla-Hellmann and A. Wallraff, *Applied Physics Letters* **101**, 053108 (2012).
- [264] V. Ranjan, G. Puebla-Hellmann, M. Jung, T. Hasler, A. Nunnenkamp, M. Muoth, C. Hierold, A. Wallraff, and C. Schönenberger, *Nature Communications* **6**, 7165 (2015).
- [265] D. M. Pozar, *Microwave Engineering*, 3rd ed. (Wiley & Sons Inc., 2005).
- [266] Z. Chen and J. Appenzeller, *Electron Devices Meeting, 2008. IEDM 2008. IEEE International* (2008), 10.1109/IEDM.2008.4796737.
- [267] J. Xia, F. Chen, J. Li, and N. Tao, *Nature Nanotechnology* **4**, 505 (2009).
- [268] S. Dröscher, P. Rouleau, F. Molitor, P. Studerus, C. Stampfer, K. Ensslin, and T. Ihn, *Applied Physics Letters* **96**, 152104 (2010).
- [269] G. L. Yu, R. Jalil, B. Belle, A. S. Mayorov, P. Blake, F. Schedin, S. V. Morozov, L. A. Ponomarenko, F. Chiappini, S. Wiedmann, U. Zeitler, M. I. Katsnelson, A. K. Geim, K. S. Novoselov, and D. C. Elias, *Proceedings of the National Academy of Sciences* **110**, 3282 (2013).
- [270] J. Xue, J. Sanchez-Yamagishi, D. Bulmash, P. Jacquod, A. Deshpande, K. Watanabe, T. Taniguchi, P. Jarillo-Herrero, and B. J. LeRoy, *Nature Materials* **10**, 282 (2011).
- [271] L. A. Ponomarenko, R. Yang, R. V. Gorbachev, P. Blake, A. S. Mayorov, K. S. Novoselov, M. I. Katsnelson, and A. K. Geim, *Phys. Rev. Lett.* **105**, 136801 (2010).
- [272] D. C. Elias, R. V. Gorbachev, A. S. Mayorov, S. V. Morozov, A. A. Zhukov, P. Blake, L. A. Ponomarenko, I. V. Grigorieva, K. S. Novoselov, F. Guinea, and A. K. Geim, *Nature Physics* **7**, 701 (2011).
- [273] J. Chae, S. Jung, A. F. Young, C. R. Dean, L. Wang, Y. Gao, K. Watanabe, T. Taniguchi, J. Hone, K. L. Shepard, P. Kim, N. B. Zhitenev, and J. A. Stroscio, *Phys. Rev. Lett.* **109**, 116802 (2012).

- [274] V. V. Cheianov and V. I. Fal'ko, *Phys. Rev. B* **74**, 041403 (2006).
- [275] E. Pallecchi, A. C. Betz, J. Chaste, G. Fève, B. Huard, T. Kontos, J.-M. Berroir, and B. Plaçais, *Phys. Rev. B* **83**, 125408 (2011).
- [276] M. J. Rahim, T. Lehleiter, D. Bothner, C. Krellner, D. Koelle, R. Kleiner, M. Dressel, and M. Scheffler, *Journal of Physics D: Applied Physics* **49**, 395501 (2016).
- [277] G. L. Yu, R. V. Gorbachev, J. S. Tu, A. V. Kretinin, Y. Cao, R. Jalil, F. Withers, L. A. Ponomarenko, B. A. Piot, M. Potemski, D. C. Elias, X. Chen, K. Watanabe, T. Taniguchi, I. V. Grigorieva, K. S. Novoselov, V. I. Fal'ko, A. K. Geim, and A. Mishchenko, *Nature Physics* **10**, 525 (2014).
- [278] K. S. Novoselov, E. McCann, S. V. Morozov, V. I. Fal'ko, M. I. Katsnelson, U. Zeitler, D. Jiang, F. Schedin, and A. K. Geim, *Nature Physics* **2**, 177 (2006).
- [279] B. Özyilmaz, P. Jarillo-Herrero, D. Efetov, D. A. Abanin, L. S. Levitov, and P. Kim, *Phys. Rev. Lett.* **99**, 166804 (2007).
- [280] F. Amet, J. R. Williams, K. Watanabe, T. Taniguchi, and D. Goldhaber-Gordon, *Phys. Rev. Lett.* **112**, 196601 (2014).
- [281] D. S. Wei, T. van der Sar, J. D. Sanchez-Yamagishi, K. Watanabe, T. Taniguchi, P. Jarillo-Herrero, B. I. Halperin, and A. Yacoby, *Science Advances* **3** (2017), 10.1126/sciadv.1700600.
- [282] K. Lee, B. Fallahazad, J. Xue, D. C. Dillen, K. Kim, T. Taniguchi, K. Watanabe, and E. Tutuc, *Science* **345**, 58 (2014).
- [283] A. Kou, B. E. Feldman, A. J. Levin, B. I. Halperin, K. Watanabe, T. Taniguchi, and A. Yacoby, *Science* **345**, 55 (2014).
- [284] L. Ju, Z. Shi, N. Nair, Y. Lv, C. Jin, J. Velasco Jr, C. Ojeda-Aristizabal, H. A. Bechtel, M. C. Martin, A. Zettl, J. Analytis, and F. Wang, *Nature* **520**, 650 (2015).
- [285] J. Li, K. Wang, K. J. McFaul, Z. Zern, Y. Ren, K. Watanabe, T. Taniguchi, Z. Qiao, and J. Zhu, *Nature Nanotechnology* **11**, 1060 (2016).
- [286] P. San-Jose, R. V. Gorbachev, A. K. Geim, K. S. Novoselov, and F. Guinea, *Nano Letters* **14**, 2052 (2014).
- [287] M. T. Allen, O. Shtanko, I. C. Fulga, A. R. Akhmerov, K. Watanabe, T. Taniguchi, P. Jarillo-Herrero, L. S. Levitov, and A. Yacoby, *Nature Physics* **12**, 128 (2015).
- [288] M. J. Zhu, A. V. Kretinin, M. D. Thompson, D. A. Bandurin, S. Hu, G. L. Yu, J. Birkbeck, A. Mishchenko, I. J. Vera-Marun, K. Watanabe, T. Taniguchi, M. Polini, J. R. Prance, K. S. Novoselov, A. K. Geim, and M. Ben Shalom, *Nature Communications* **8**, 14552 (2017).
- [289] F. Freitag, J. Trbovic, M. Weiss, and C. Schönenberger, *Phys. Rev. Lett.* **108**, 076602 (2012).

-
- [290] M. H. Devoret, D. Esteve, H. Grabert, G.-L. Ingold, H. Pothier, and C. Urbina, *Phys. Rev. Lett.* **64**, 1824 (1990).
 - [291] J. Velasco, L. Jing, W. Bao, Y. Lee, P. Kratz, V. Aji, M. Bockrath, C. N. Lau, C. Varma, R. Stillwell, D. Smirnov, F. Zhang, J. Jung, and A. H. MacDonald, *Nat Nano* **7**, 156 (2012).
 - [292] B. E. Feldman, J. Martin, and A. Yacoby, *Nature Physics* **5**, 889 (2009).
 - [293] W. Bao, J. Velasco, F. Zhang, L. Jing, B. Standley, D. Smirnov, M. Bockrath, A. H. MacDonald, and C. N. Lau, *Proceedings of the National Academy of Sciences* **109**, 10802 (2012).
 - [294] F. Freitag, M. Weiss, R. Maurand, J. Trbovic, and C. Schönenberger, *Phys. Rev. B* **87**, 161402 (2013).
 - [295] E. McCann, *Phys. Rev. B* **74**, 161403 (2006).
 - [296] R. Nakajima, J. Stöhr, and Y. U. Idzerda, *Phys. Rev. B* **59**, 6421 (1999).
 - [297] S. Gota, M. Gautier-Soyer, and M. Sacchi, *Phys. Rev. B* **62**, 4187 (2000).
 - [298] V. Chakarian, Y. U. Idzerda, and C. T. Chen, *Phys. Rev. B* **57**, 5312 (1998).

A Fabrication Recipes

Already in the chapter 2, fabrication techniques are discussed. The aim of this appendix is to provide details of the fabrication recipes.

A.1. Fabrication of vdW-heterostructures

A.1.1. Cleaning the wafer for exfoliation

1. Dicing the wafer in appropriate sizes
2. Clean in Acetone, IPA for each ~ 5 min in ultrasonic
3. Blow-dry with N_2
4. UVO or oxygen plasma can be used to increase the yield of the exfoliation.

A.1.2. Markers on Si^{++}/SiO_2 chip (~ 300 nm oxide)

1. Spin-coat full wafer (3 inch) with $\sim 1 \mu m$ AZ 1512 optical resist
2. Bake at $100^\circ C$ for 60 s
3. Expose with marker-grid to UV (wavelength of 365 nm)
4. Develop with MIF 726 for 17 s, stop in DI-water for 30 s
5. Metallization with 5 nm Ti + 40 nm to 60 nm Au
6. Lift-off in warm acetone

A.1.3. Assembly of vdW-heterostructures

In the following the detailed procedure of vdW-heterostructures fabrication following Ref. [138] is presented.

1. PC film preparation by drop casing a solution of PC in chloroform (9 wt%) on a glass slide. A second glass slide is then used to disperse the solution uniformly over both glass slides by pressing/sliding them against each other. Be fast as the chloroform evaporates rapidly.

2. Transfer of the dried PC layer to a PDMS stamp mounted on a glass slide with the help of window in a Scotch tape.
3. Exfoliate top mos layer on Si/SiO₂ substrate
4. Pick up top layer with PC at $\approx 80^\circ\text{C}$
5. Pick up of next layer with PC/top layer, repeat for each layer to be picked up.
6. Release "half-stack" on bottom layer on Si/SiO₂ substrate by heating to 150°C to release the PC layer from the PDMS.
7. Remove PC from the complete stack with chloroform (~ 1 h)
8. Thermal annealing in N₂/H₂ atmosphere (temperature depends on the involved materials)

A.2. E-beam lithography and development

A.2.1. PMMA resist for contacts and etching (negative mask)

1. Spin-coat PMMA (thickness may vary, bake at 180°C for 3 min)
2. Expose with E-beam ($V=20\text{ keV}$; Dose= $450\text{ }\mu\text{C}/\text{cm}^2$)
3. Cold-development in IPA:H₂O (ratio 7:3) at $\sim 5^\circ\text{C}$ for 60 s, blow-dry

A.2.2. PMMA/HSQ resist for etching (positive mask)

1. Spin-coat PMMA (200 nm, bake at 180°C for 3 min)
2. Spin-coat HSQ (100 nm, bake at 90°C for 5 min)
3. Expose with E-beam ($V=20\text{ keV}$; Dose= $100\text{ }\mu\text{C}/\text{cm}^2$, use smallest current possible)
4. Develop HSQ in TMAH (25 wt%):H₂O (ratio 1:1) for 30 s, stop in H₂O for 30 s, blow-dry

A.3. Reactive ion etching

A.3.1. $\text{CHF}_3:\text{O}_2$ plasma

1. Parameters: $\text{CHF}_3:\text{O}_2$ (40 sccm/4 sccm), $P = 60 \text{ W}$, $p = 60 \text{ mTorr}$, $t = 60 \text{ s}$ to 90 s. This plasma is used to shape vdw heterostructure and to define side contacts.
2. Etching rates:
 - hBN: $\sim 20 \text{ nm/min}$
 - SiO_2 : $\sim 14 \text{ nm/min}$
 - PMMA: $< 10 \text{ nm/min}$

A.3.2. $\text{SF}_6:\text{Ar}:\text{O}_2$ plasma

1. Parameters: $\text{SF}_6:\text{Ar}:\text{O}_2$ (20 sccm/5 sccm/5 sccm), $P = 50 \text{ W}$, $p = 25 \text{ mTorr}$, $t = 20 \text{ s}$. This plasma is used to shape vdw heterostructure and it can also be used to define side contacts.
2. Etching rates:
 - hBN: $> 300 \text{ nm/min}$
 - WSe_2 : $> 170 \text{ nm/min}$
 - SiO_2 : $\sim 30 \text{ nm/min}$
 - PMMA: 80 nm/min

It is important to do a short oxygen plasma after each SF_6 plasma as it cross-links the PMMA layer (otherwise cross linked PMMA might be left on the sample after lift-off. The only exception is if the SF_6 based plasma is used to contact the graphene as there the cross linked PMMA is removed with the metal during lift-off.

A.3.3. O_2 plasma

1. Parameters: O_2 (20 sccm), $P = 60 \text{ W}$, $p = 40 \text{ mTorr}$, $t = 4 \text{ min}$. This plasma is used to remove PMMA when HSQ is used as a negative mask. It is also used to define the shape of a vdw heterostructure or graphene/graphite samples.
2. Etching rates:
 - hBN: $\sim 20 \text{ nm/min}$
 - SiO_2 : negligible
 - PMMA: $\sim 100 \text{ nm/min}$
 - graphene: several layers per minute

A.4. Cr/Au leads

1. Type: E-beam evaporation
2. Pumping to base-pressure of $< 2 \times 10^{-7}$ Pa
3. Evaporate away ~ 30 nm of Cr before opening the shutter since the Cr-target was stored in ambient condition (where it oxidises)
4. Open shutter
5. Evaporate 10 nm of Cr (0.7 \AA/s to 1.2 \AA/s)
6. Evaporate 50 nm to 70 nm of Au (0.7 \AA/s to 1.2 \AA/s)

A.4.1. Metal top gates on Hall bar devices

1. Starting with the full stack being on the $\text{Si}^{++}/\text{SiO}_2$ chip with markers
2. Define PMMA mask for contacts (section [A.2.1](#))
3. Expose side-contacts with $\text{CHF}_3:\text{O}_2$ (section [A.3.1](#))
4. Metallize (E-beam evaporation) with Cr/Au (10 nm/70 nm), lift-off in warm acetone
5. Shaping of the device with a 200 nm thick PMMA mask (section [A.2.1](#)) and a $\text{SF}_6:\text{Ar}:\text{O}_2$ plasma (section [A.3.2](#)).
6. Remove PMMA mask in warm acetone.
7. Define PMMA mask for top-gates (section [A.2.1](#))
8. Evaporate a thin MgO layer (12 nm to 14 nm) (E-beam evaporation) to passivate the exposed graphene-edges.
9. Subsequently metallize (E-beam evaporation) with Ti/Au (5 nm/70 nm) using the same PMMA layer, lift-off in warm acetone

A.4.2. ZEP resist for ferromagnetic contacts

1. Spin coat ZEP (300 nm, bake at 180°C for 3 min)
2. Expose with E-beam (10 keV; Dose= $35 \mu\text{C}/\text{cm}^2$)
3. Development in Pentylacetate for 60 s, and in MIBK:IPA (ratio 9:1) for 10 s, blow-dry

A.5. Fabrication of freely suspended graphene samples using the LOR technique

A.5.1. Bottom gate structures

1. Spin coat 500 nm PMMA 950 K, bake at 180 °C for 3 min)
2. Exposure parameters: Acceleration voltage of 20 kV, working distance of 17 mm, Aperture of 10 μm for small structures (250 μm write field) and 120 μm for large structures (2000 μm write field). The following doses are used: 200 $\mu\text{C cm}^{-2}$ for the normal structures, 150 $\mu\text{C cm}^{-2}$ for the bottom gates with a pitch of 600 nm.
3. Development in xylene for 2 min, rinse in hexane
4. Short oxygen plasma to remove resist residues
5. Evaporation of 5 nm Ti and 40 nm Au
6. Lift-off in xylene at 80 °C, rinse with hexane

The bottom gates need to be protected by a dielectric in order to avoid gate leaks.

1. Spin coat 500 nm PMMA 950 K, bake at 180 °C for 3 min)
2. Expose inner gate structure (bonding pads need to remain covered by PMMA), use the same parameters as above.
3. Development in xylene for 2 min, rinse in hexane
4. Evaporation of 100 nm MgO
5. Lift-off in xylene at 80 °C, rinse with hexane

A.5.2. LOR coating and opening of bonding pads

After coating the bottom gates with LOR, the bonding pads need to be opened and "stair" structures allows to pull the metal leads from the bonding pads up onto the LOR

1. Spin coat 600 nm LOR 5A (2200 rpm, 45"), bake at 200 °C for 15 min)
2. Exposure of bonding pads with a dose of 600 $\mu\text{C cm}^{-2}$ with a stepwise decrease (steps of 40 $\mu\text{C cm}^{-2}$ along the direction of the wires to be deposited.
3. Development in ethyl-lactate for 2 min, thorough washing in xylene at 80 °C using a syringe, rinse in hexane

A.5.3. Lithography on LOR

PMMA based electron beam lithography can be performed on top of the LOR by using xylene as a developer and lift-off solvent and hexane as a rinsing solvent. E-gun evaporation (e.g. Ti/Au) proved to be difficult as it exposes the LOR below the contacts. This resulted in contacts floating away while developing the LOR in the last step to suspend the graphene. Therefore, thermal evaporation of palladium was used.

A.5.4. Suspension of graphene

- Exposure of LOR below graphene with $1100 \mu\text{C cm}^{-2}$. This also leads to the suspension of the contacts.
- Development in ethyl-lactate for 2 min, rinse in hexane, blow dry with N_2

A.5.5. ZEP based lithography on LOR for Py contacts

Not only PMMA can be used on top of LOR, but also ZEP proved to work as a resist on LOR. ZEP dissolved in anisole was used for spin-coating and xylene was used as the developer. Due to the reduces backscattering on LOR, the dose needs to be increased compared to the lithography on Si/SiO₂ substrate. Here, an acceleration voltage of 10 kV, a dose of $70 \mu\text{C cm}^{-2}$ to $100 \mu\text{C cm}^{-2}$ and a development in xylene at room temperature for 2 min were used. Lift-off was performed in xylene at 80 °C for 30 min.

A.6. Fabrication of niobium resonators

1. Sputter deposition of 100 nm to 150 nm niobium onto clean substrate (intrinsic silicon, 170 nm of SiO₂) at a rate of 1 \AA s^{-1} using Ar gas at a flow of 40 sccm at a background pressure of 4 mTorr and a RF power of 160 W in a AJA magnetron sputtering system.
2. Define etch mask with standard e-beam lithography using PMMA (see above)
3. Niobium etching in Sentech ICP machine with Ar/Cl₂ at a flow of 25/40 sccm at a background pressure of 1 Pa, DC power of 100 W and a RF power of 125 W resulting in an etch rate of $\sim 4 \text{ nm s}^{-1}$
4. Resist stripping in warm acetone

B Details on the fabrication and XAS analysis of ferromagnetic contacts

The aim of this appendix is to provide details on the fabrication of the samples presented in chapter 3. In addition, details on the analysis of the XAS data presented.

B.1. Fabrication details

First, ferromagnetic strips were fabricated on highly p doped silicon substrate (only native oxide). Standard e-beam lithography with a positive resist (ZEP) was used to pattern the ferromagnetic strips. Py and Co were evaporated from an e-gun target in a UHV system at a pressure of $\leq 5 \times 10^{-10}$ mbar. A total film thickness of 30 nm was deposited at a deposition rate of 0.3 \AA/s . Lift-off was performed in N-Methyl-2-Pyrrolidon (NMP) at 70°C followed by an acetone and a 2-Propanol (IPA) rinse. Directly after lift-off, a bilayer (BL) hexagonal boron nitride (hBN) was transferred on top of the samples such that half of it was covered by hBN. Chemical vapour deposited (CVD) hBN grown on copper foil was purchased from Graphene Supermarket. A thick PMMA layer was spin-coated onto the as received copper foil with hBN. The copper substrate was then etched in a 0.35 mmol/L ammoniumpersulfate solution, leaving an hBN layer with the supporting PMMA layer floating on water. This layer was then transferred onto another piece of hBN covered copper substrate to obtain a BL hBN. Now, a PDMS stamp was added to the PMMA support layer to increase the stability and to make it easier to handle. Again, the Cu substrate was etched in an ammoniumpersulfate solution. After thoroughly washing with water and IPA and drying, the BL hBN was transferred in a dry process onto the ferromagnetic films/strips. Before removing the supporting PMMA and PDMS with a hot acetone bath for 30 min, the sample was cured at 180°C for 3 min to relax the PMMA and to enhance the adhesion of the transferred hBN.

B.2. Fitting procedure of XAS data

The oxide thickness of the ferromagnetic strips was extracted using a procedure introduced by Regan et al. [170], which models the total electron yield (TEY) of an oxide / metal sandwich. In the following, the derivation is given for a stack consisting of Fe with an Fe_2O_3 layer atop a Fe_3O_4 layer atop the metallic iron, but it is analogous for Ni and Co with their oxides. The total electron yield $dN_{\text{Fe}_2\text{O}_3}$ from a layer of Fe_2O_3 of thickness dz at depth z is given by

$$dN_{\text{Fe}_2\text{O}_3} = I_0 \cdot e^{-z\mu_{\text{Fe}_2\text{O}_3}(E)} \cdot \mu_{\text{Fe}_2\text{O}_3}(E) \cdot G_{\text{Fe}_2\text{O}_3}(E) \cdot e^{-z/\lambda_{\text{Fe}_2\text{O}_3}} \cdot dz \quad (\text{B.1})$$

assuming normal incidence of the photons. Here I_0 is the photon flux, $\mu_{\text{Fe}_2\text{O}_3}(E)$ is the absorption coefficient representing the probability of a photon being absorbed, $G_{\text{Fe}_2\text{O}_3}(E)$ is the number of electrons created per absorbed photon and $\lambda_{\text{Fe}_2\text{O}_3}$ is the electron escape depth. The first exponential factor gives the probability of a photon reaching depth z and the second exponential factor gives the probability of a photo electron created at depth z to escape to the surface. Integration of equation B.1 from 0 (surface) to depth $t_{\text{Fe}_2\text{O}_3}$ gives the total electron yield of a Fe_2O_3 layer with thickness $t_{\text{Fe}_2\text{O}_3}$ as follows:

$$N_{\text{Fe}_2\text{O}_3} = \frac{I_0 \cdot G_{\text{Fe}_2\text{O}_3}}{1 + \frac{1}{\lambda_{\text{Fe}_2\text{O}_3} \cdot \mu_{\text{Fe}_2\text{O}_3}}} \cdot e^{-t_{\text{Fe}_2\text{O}_3}(\mu_{\text{Fe}_2\text{O}_3} + 1/\lambda_{\text{Fe}_2\text{O}_3})}. \quad (\text{B.2})$$

Here the energy dependence is not explicitly indicated.

Similarly, one can derive the total electron yield of the Fe_3O_4 layer below, ranging from $z_1 = t_{\text{Fe}_2\text{O}_3}$ to $z_2 = t_{\text{Fe}_3\text{O}_4}$, as follows:

$$N_{\text{Fe}_3\text{O}_4} = \frac{I_0 \cdot G_{\text{Fe}_3\text{O}_4}}{1 + \frac{1}{\lambda_{\text{Fe}_3\text{O}_4} \cdot \mu_{\text{Fe}_3\text{O}_4}}} \cdot e^{-t_{\text{Fe}_2\text{O}_3}(\mu_{\text{Fe}_2\text{O}_3} + 1/\lambda_{\text{Fe}_2\text{O}_3})} \cdot \left[1 - e^{-(t_{\text{Fe}_3\text{O}_4} - t_{\text{Fe}_2\text{O}_3}) \cdot (\mu_{\text{Fe}_3\text{O}_4} + 1/\lambda_{\text{Fe}_3\text{O}_4})} \right]. \quad (\text{B.3})$$

Here the first exponential accounts for the absorption and electron escape losses of the Fe_2O_3 layer.

The total electron yield of the metallic iron (infinite thickness) below these two oxide layers is then given by:

$$N_{\text{Fe}} = \frac{I_0 \cdot G_{\text{Fe}}}{1 + \frac{1}{\lambda_{\text{Fe}} \cdot \mu_{\text{Fe}}}} \cdot e^{-t_{\text{Fe}_2\text{O}_3}(\mu_{\text{Fe}_2\text{O}_3} + 1/\lambda_{\text{Fe}_2\text{O}_3})} \cdot e^{-(t_{\text{Fe}_3\text{O}_4} - t_{\text{Fe}_2\text{O}_3}) \cdot (\mu_{\text{Fe}_3\text{O}_4} + 1/\lambda_{\text{Fe}_3\text{O}_4})}. \quad (\text{B.4})$$

The two exponential account for the absorption and electron escape losses due to the two oxide layers.

The total electron yield of a Fe_2O_3 / Fe_3O_4 / Fe sandwich as shown in Fig. 3 c) in the main text is then given by the sum of equation B.2, B.3 and

B.4. For the fitting, it was assumed that $G_{\text{Fe}_2\text{O}_3}(E) = G_{\text{Fe}_3\text{O}_4}(E) = G_{\text{Fe}}(E) = \text{const}$ (neglecting the difference of the electron yield for different materials and their energy dependence). This results in an overall scaling factor accounting for the photon flux and electron yield. Hence, only $t_{\text{Fe}_2\text{O}_3}$ and $t_{\text{Fe}_3\text{O}_4}$ determine the relative weight of the different chemical species involved and the fit is simply speaking a linear combination of the reference spectra of $\mu_{\text{Fe}_2\text{O}_3}$, $\mu_{\text{Fe}_3\text{O}_4}$ and μ_{Fe} , which were all taken from Ref. [170]. For the electron escape depths we used values from the literature: $\lambda_{\text{Fe}_2\text{O}_3} = 35 \text{ \AA}$ [296], $\lambda_{\text{Fe}_3\text{O}_4} = 50 \text{ \AA}$ [297], $\lambda_{\text{Fe}} = 15 \text{ \AA}$ [298], $\lambda_{\text{Co}} = 22 \text{ \AA}$ [296, 298], $\lambda_{\text{Ni}} = 22 \text{ \AA}$ [296, 298]. To our knowledge, the electron escape depths for CoO and for NiO has not been determined and therefore we used a value of 30 \AA , as suggested by Regan et al. [170].

C Further data and discussions of WSe₂/Gr-heterostructures

The aim of this appendix is to provide further data of the WAL measurements. First, WAL measurements of device A at a higher temperature and over a larger magnetic field range are presented, which are followed by the WAL measurements of device B. Then the detailed analysis of the electric field dependence is presented. Furthermore, the spin relaxation anisotropy and the relaxation due to the valley-Zeeman SOC are discussed in more detail. In addition data from a further device is shown, where the influence of τ_{iv} and τ_* cannot be neglected in the analysis of the magneto conductivity (device D). Furthermore, the influence of an in-plane magnetic field on the WL correction in hBN/Gr/hBN devices is shown, which supports the interpretation of an enhanced dephasing due to the presence of a random vector potential.

C.1. Fitting of magneto conductivity over larger magnetic field range

Fig. C.1 (a) shows the quantum correction to the magneto conductivity of device A over a larger magnetic field scale (± 50 mT), which roughly corresponds to the transport field estimated for this device (70 mT). In order to clarify the relative strength of the two spin-orbit scattering times (τ_{asy}, τ_{sym}) we fit the data with equation 2 from the main text and the best fit is again found for $\tau_{asy} \gg \tau_{sym}$ with very similar results as shown in Fig. 3 in the main text. We consistently find $\tau_{asy}/\tau_{sym} \gtrsim 10$. The reduced τ_ϕ can be explained by the larger temperature on one hand and the fit constraint $\tau_{asy} \leq \tau_\phi$. Without this fit constraint, larger τ_ϕ were found with $\tau_{asy} > \tau_\phi$, which we ruled out.

The evolution of the magneto conductivity with temperature is shown in Fig. C.1 (b). Clearly, the sharp WAL peak around zero magnetic field disappears at higher temperature, whereas the conductivity is not much affected at higher magnetic fields. The curvature around zero magnetic field for 30 K and 50 K is well reproduced by the classical Drude model in magnetic field. The 50 K trace is less negative than the 30 K trace at large magnetic fields, whereas there is nearly no difference between those two traces around zero magnetic field. This would lead to a much flatter background of the quantum correction

to the magneto conductivity at larger fields if the 50 K trace would be used as a classical background instead of the 30 K trace. A flatter background would lead to an even larger anisotropy between τ_{asy} and τ_{sym} .

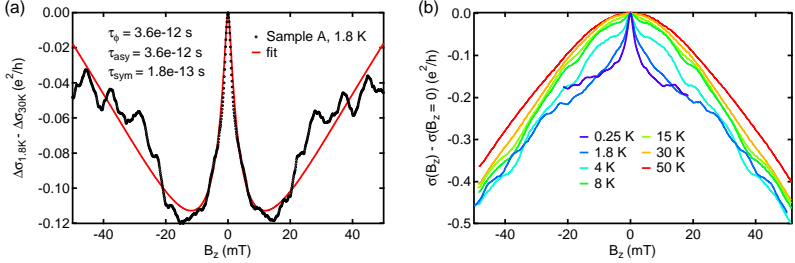


Figure C.1. Fitting over large magnetic field range: (a) shows the magneto conductivity of device A at the CNP at zero perpendicular electric field at a temperature of 1.8 K. The magneto conductivity is fitted with equation 2 from the main text over the full magnetic field range ± 50 mT, with the fit parameters indicated on the graph. (b) shows the evolution of the magneto conductivity with temperature. © 2018 American Physical Society

C.2. Fitting of magneto conductivity data from device B

As mentioned in the main text, a second device B was investigated as well. A gate-gate map of the resistivity of device B is shown in Fig. C.2 (a). A field effect mobility of $\sim 25\,000\text{ cm}^2\text{ V}^{-1}\text{ s}^{-1}$ and a residual doping of $\sim 7 \times 10^{10}\text{ cm}^{-2}$ were found. The quantum correction to the magneto conductivity was measured at the charge neutrality point for different electric fields. The same analysis was performed as mentioned in the main text. The extracted quantum correction to the magneto conductivity was also fit using Eq. 1.23 from the main text considering the three different cases as elaborated in the main text. Since the quality of device B is higher than that of device A, the diffusion constant is larger and hence the mean free path l_{mfp} is longer. This leads to a much smaller transport field as this scales with l_{mfp}^{-2} . Therefore, the fitting range here was limited to 12 mT, which poses serious limits on the quality of the fit. It is very difficult to independently extract the different spin-orbit scattering times as obviously seen in Fig. C.2, where basically all three fits overlap. Only at larger fields would the three fits be distinguishable. However, the time scales extracted here do not contradict the results presented in the main text. The strength of the total SOC, captured in τ_{SO} , is roughly the same for all three fits. As can be seen in Fig. C.2, the total spin-orbit scattering time

τ_{SO} is more robust with respect to different fitting limits. Therefore, we only consider τ_{SO} for device B in the next section.

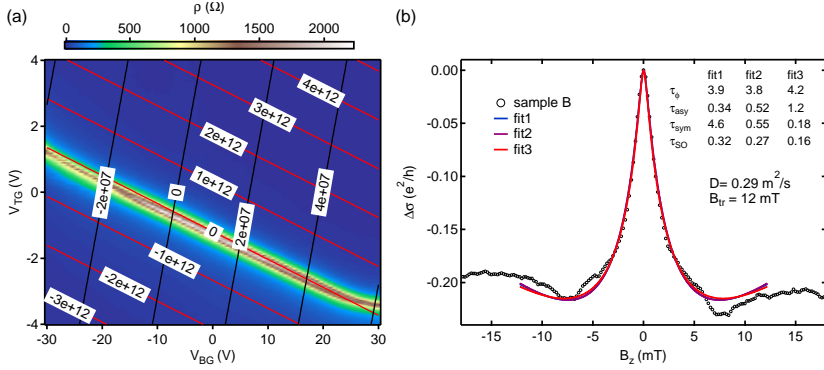


Figure C.2. Data from device B: (a) shows the resistivity as a function of V_{TG} and V_{BG} . Constant density contours are indicated with red solid lines and constant electric field contours is solid black lines. (b) shows the quantum correction to the magneto conductivity of device B at zero electric field within a density range of $-5 \times 10^{11} \text{ cm}^{-2}$ to $5 \times 10^{11} \text{ cm}^{-2}$. The same procedure as described in the main text was used. The results for three different limits are shown and their parameters are indicated. The fitting was restricted to the range of the transport field $B_{tr} = 12 \text{ mT}$. © 2018 American Physical Society

C.3. Electric field dependence of the spin-orbit scattering rates

The presence of a top and a back gate in our devices allows us to tune the carrier density and the transverse electric field independently in devices A and B. The back and top gate lever arms (α_{BG}, α_{TG}) were found from Hall measurements and the charge carrier density in the graphene was calculated using a simple capacitance model,

$$n = \alpha_{BG} (V_{BG} - V_{BG}^0) + \alpha_{TG} (V_{TG} - V_{TG}^0), \quad (\text{C.1})$$

where V_{BG}^0 and V_{TG}^0 account for some offset doping of the graphene. Similarly, the applied electric field (field direction out of plane) was obtained:

$$E = \frac{1}{d_{BG}} (V_{BG} - V_{BG}^0) - \frac{1}{d_{TG}} (V_{TG} - V_{TG}^0), \quad (\text{C.2})$$

where d_{BG} and d_{TG} denote the thickness of the back and top gate dielectric. The thicknesses of the bottom WSe₂ flake and the top hBN flake were determined by atomic force microscopy. To account for the residual doping, the density was corrected in the following way: $n_{corr} = \sqrt{n^2 + n_s^2}$. It was the corrected density n_{corr} that was used for the calculation of the diffusion constant via the Einstein relation and for the estimation of the Fermi energy.

In the case of device A, the SOC strength was found to be electric field independent at the CNP in the range of -5×10^7 V/m to 8×10^7 V/m as shown in Fig C.3. The electric field range was limited by the fact that at large positive gate voltages the Fermi energy was shifted into a trap state in the WSe₂ whereas at large negative gate voltages gate instabilities occurred. Within the investigated electric field range τ_{asy} was found to be in the range of 5 ps to 10 ps, always close to τ_ϕ . τ_{sym} on the other hand was found to be around 0.1 ps to 0.3 ps while τ_p was around 0.2 ps to 0.3 ps for device A. The total spin-orbit scattering time τ_{SO} is mostly given by τ_{sym} . Device B, where only τ_ϕ and τ_{SO} could be extracted reliably, shows similar results as device A. Therefore, we conclude that in the electric field range -5×10^7 V/m to 8×10^7 V/m no tuning of the SOC strength with electric field is observed. From first principles calculations, the Rashba SOC is expected to change by 10 % if the electric field is tuned by 1×10^9 V m⁻¹ and also the intrinsic and valley-Zeeman SOC parameters are expected to change slightly [47]. However, within the resolution of the extraction of the spin-orbit scattering time scales, we cannot establish a clear trend.

These findings are in contrast to previous studies that found an electric field tunability of τ_{asy} and τ_{SO} on a similar electric field scale in graphene/WSe₂ devices [234]. However, it is important to note that the changes are small and since no error bars are given, it is hard to tell if the three data points show a clear trend. Another study found a linear tunability of τ_{asy} of roughly 10 % on a similar electric field scale in graphene/WS₂ devices [233]. There, τ_{sym} was neglected with the argument that it cannot lead to spin relaxation. However, it was shown that τ_{sym} can lead to spin relaxation [36] and therefore it cannot be neglected in the analysis. In our case, it is the dominating spin relaxation mechanism.

C.4. Spin relaxation anisotropy

Cummings et al. have found a giant spin relaxation anisotropy in systems with strong valley-Zeeman SOC that is commonly found in graphene/TMDC heterostructures [36]. They derived the following equation:

$$\frac{\tau_\perp}{\tau_\parallel} = \left(\frac{\lambda_{VZ}}{\lambda_R} \right)^2 \frac{\tau_{iv}}{\tau_p} + 1/2, \quad (\text{C.3})$$

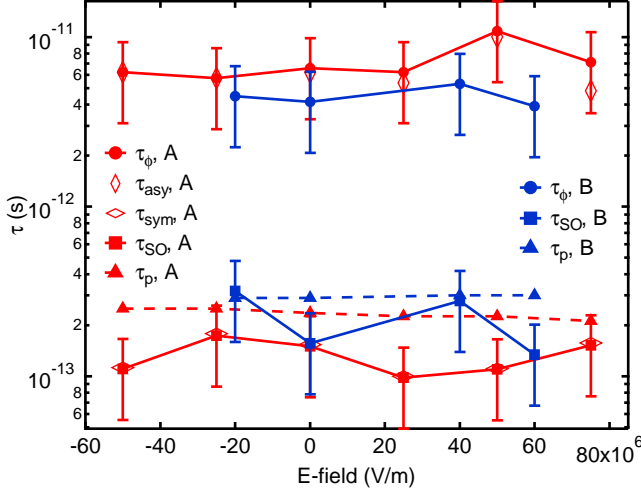


Figure C.3. Electric field dependence of device A and B: The extracted spin-orbit scattering time scales τ_{asy} , τ_{sym} , τ_{SO} and τ_{ϕ} were extracted for different perpendicular electric field around the charge neutrality point. In addition, the momentum scattering time τ_p extracted from the diffusion constant is also shown. In the case of device B, only the total spin-orbit scattering time τ_{SO} is given, as a reliable extraction of τ_{asy} and τ_{sym} was not possible in this device (see discussion above). © 2018 American Physical Society

where τ_{\perp} is the out-of-plane spin relaxation time, τ_{\parallel} the in-plane spin relaxation time, λ_{VZ} is the SOC strength of the valley-Zeeman SOC, λ_R is the SOC strength of the Rashba SOC and τ_{iv} and τ_p represent the intervalley and momentum scattering time, respectively. If a strong intervalley scattering is assumed, which is a prerequisite for the application of the WAL theory [73], τ_{\perp} can be given by $\tau_{asy}/2$ and τ_{\parallel} can be given by τ_{SO} . This can be seen by examining the relaxation rates given in the lefthand side of Table II of Ref. [73]. There the in-plane relaxation rates are given by $\Gamma_x^0 = \Gamma_y^0 = \tau_{SO}^{-1}$, while the out-of-plane relaxation rate is $\Gamma_z^0 = 2\tau_{asy}^{-1}$. The factor of two arises because asymmetric SOC, such as Rashba, relax out-of-plane spins twice as fast as in-plane spins. We therefore extract a lower bound of the spin relaxation anisotropy $\tau_{\perp}/\tau_{\parallel} \approx \tau_{asy}/2\tau_{SO} \approx 20$, which is much larger than what is expected for usual 2D Rashba systems. Furthermore, assuming a ratio of $\tau_{iv}/\tau_p \approx 1$, which corresponds to very strong intervalley scattering, a ratio of $\lambda_{VZ}/\lambda_R \approx 6$ is expected.

C.5. Estimate of valley-Zeeman SOC strength

For a valley-Zeeman SOC strength λ_{VZ} , the spin splitting is $2\lambda_{VZ}$ and the precession frequency is $\omega = 2\lambda_{VZ}/\hbar$. In the D'yakonov-Perel' (DP) regime of spin relaxation, when $\omega\tau_{iv} < 1$, the in-plane spin relaxation rate is $\tau_{s\parallel}^{-1} = (2\lambda_{VZ}/\hbar)^2\tau_{iv}$. However, if $\omega\tau_{iv} > 1$, then the spin can fully precess before scattering randomizes the spin-orbit field, and the spin lifetime scales with the intervalley time, $\tau_{s\parallel} = 2\tau_{iv}$. A plot of these two regimes is shown in Fig. C.4, where we have taken our derived limits of λ_{VZ} are 0.23 and 2.3 meV (see below) as well as the DFT-derived value of 1.19 meV.

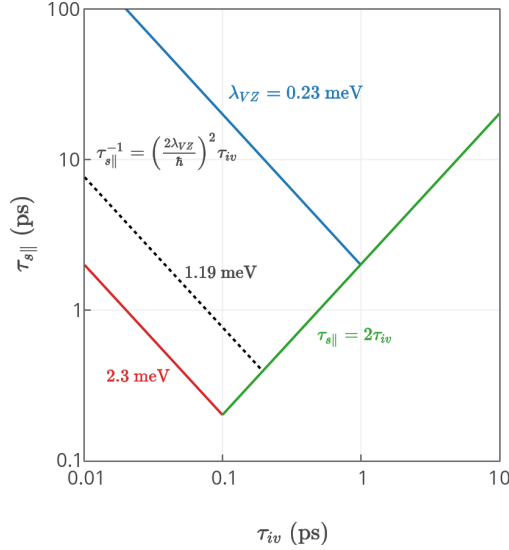


Figure C.4. Estimate of valley-Zeeman SOC strength: Dependence of in-plane spin relaxation time $\tau_{s\parallel}$ on intervalley scattering time τ_{iv} . Red and blue lines show the dependence in the DP regime of spin relaxation, for the largest and smallest estimated values of λ_{VZ} . The black dashed line shows the value derived from DFT [47]. The green line shows the dependence in the coherent spin precession regime. © 2018 American Physical Society

Considering this behavior, the condition $\tau_{s\parallel} \geq 2\tau_{iv}$ should always be satisfied. Meanwhile, our measurements revealed $\tau_{sym} = 0.2$ ps and $\tau_{iv} \approx 0.1 - 1$ ps, which violates this condition for all except the smallest value of τ_{iv} . One way to account for this is to consider the impact of spin-orbit disorder on the in-plane spin lifetime. Assuming that the $\tau_{s\parallel}$ from uniform valley-Zeeman

SOC is given by $2\tau_{iv}$, and the rest comes from spin-orbit disorder, we can estimate an upper bound of $\lambda_{VZ} = \hbar/\sqrt{4(2\tau_{iv})\tau_{iv}} = 0.23 \text{ meV}$ to 2.3 meV .

Another possibility is that since our measurements are right around the transition point $\omega\tau_{iv} = 1$, we could be extracting the in-plane spin precession frequency; $\tau_{sym}^{-1} = \omega$. Doing so would give $\lambda_{VZ} = \hbar/2\tau_{sym} = 1.6 \text{ meV}$, which fits in the range derived above. Overall, since the experiments appear to be close to this transition point, all methods of deriving the strength of λ_{VZ} tend to give similar values, from a few tenths up to a few meV depending on the estimate of τ_{iv} . We would like to note that it is not fully understood how the spin precession frequency enters into the WAL correction and how the corresponding SOC strength would then be extracted. Therefore, further theoretical work is needed.

C.6. Data from device D

The third sample with device D is a $\text{WSe}_2/\text{Gr}/\text{hBN}$ stack with a very thin WSe_2 (3 nm) as substrate. The gate-gate map of the two terminal resistance is shown in Fig. C.5 (a). Due to the very thin bottom WSe_2 the mobility in this device is around $50\,000 \text{ cm}^2 \text{ V}^{-1} \text{ s}^{-1}$ and a residual doping of $2.5 \times 10^{11} \text{ cm}^{-2}$ is found. A typical magneto conductivity trace of this device is shown in Fig. C.5. Mostly, positive magneto conductivity is observed with only a very small feature that shows negative magneto conductivity at 30 mK, which was absent at 1.8 K. The magneto conductivity of device D could not be fitted with the standard WAL formula presented in the main text. However, similar curve shapes could be reproduced by including the influence of τ_{iv} , the intervalley scattering time, and $\tau_* = (1/\tau_{iv} + 1/\tau_z)^{-1}$, that includes intravalley scattering τ_z . A complete formula can be derived from equation 9 of Ref. [73]. If all relaxation gaps are included and if disorder SOC is neglected one arrives at the following form:

$$\begin{aligned} \Delta\sigma(B) = -\frac{e^2}{2\pi h} & \left[F\left(\frac{\tau_B^{-1}}{\tau_\phi^{-1}}\right) - F\left(\frac{\tau_B^{-1}}{\tau_\phi^{-1} + 2\tau_{asy}^{-1}}\right) - 2F\left(\frac{\tau_B^{-1}}{\tau_\phi^{-1} + \tau_{asy}^{-1} + \tau_{sym}^{-1}}\right) \right. \\ & - F\left(\frac{\tau_B^{-1}}{\tau_\phi^{-1} + 2\tau_{iv}^{-1}}\right) - 2F\left(\frac{\tau_B^{-1}}{\tau_\phi^{-1} + \tau_*^{-1}}\right) \\ & + F\left(\frac{\tau_B^{-1}}{\tau_\phi^{-1} + 2\tau_{iv}^{-1} + 2\tau_{asy}^{-1}}\right) + 2F\left(\frac{\tau_B^{-1}}{\tau_\phi^{-1} + \tau_*^{-1} + 2\tau_{asy}^{-1}}\right) \\ & \left. + 2F\left(\frac{\tau_B^{-1}}{\tau_\phi^{-1} + 2\tau_{iv}^{-1} + \tau_{asy}^{-1} + \tau_{sym}^{-1}}\right) + 4F\left(\frac{\tau_B^{-1}}{\tau_\phi^{-1} + \tau_*^{-1} + \tau_{asy}^{-1} + \tau_{sym}^{-1}}\right) \right]. \end{aligned} \quad (\text{C.4})$$

Similar to the main text, we suppose that $\tau_{sym} = (1/\tau_{sym,I} + 1/\tau_{sym,VZ})^{-1}$ captures both the intrinsic and valle-Zeeman SOC and that τ_{asy} captures the Rashba SOC. However, the addition of two more parameters makes it very hard to unambiguously extract all parameters exactly. Therefore, we do not extract any spin-orbit time scales from this device. The influence of τ_{iv} and τ_* are much weaker for the data presented in the main text.

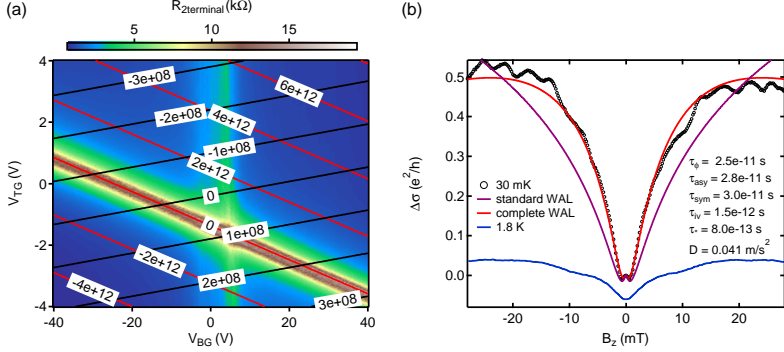


Figure C.5. Data from device D: (a) shows a gate-gate map of the two-terminal resistance of device D. Constant density (red solid line, in units of cm^{-2}) and electric field (black solid lines, in units of V m^{-1}) lines are superimposed on top of that. (b) shows the quantum quantum correction of the magneto conductivity at zero electric field in the density range of $-5 \times 10^{11} \text{ cm}^{-2}$ to $5 \times 10^{11} \text{ cm}^{-2}$. It shows a WL dip with a tiny feature of WAL around zero B_z at a temperature of 30 mK. A possible fit (red) and its parameters, including the influence of τ_{iv} and τ_* , are indicated. The low magnetic field range can be reasonably well described by the standard WAL formula without τ_{iv} and τ_* . As a comparison, the magneto conductivity is also shown at 4 K. This trace is vertically offset by $-0.06 e^2/h$ for clarity. © 2018 American Physical Society

The long phase coherence time $\tau_\phi \sim 25 \text{ ps}$ is attributed to the lower temperature ($T = 30 \text{ mK}$) at which the measurement was performed. At higher temperature (1.8 K), the phase coherence is significantly shorter $\sim 4 \text{ ps}$ (broader dip and reduced overall correction) and the influence of the SOC on the magneto conductivity (WAL) is not observed any longer.

Both τ_{asy} and τ_{sym} seem to be very close to τ_ϕ in sample D. In particular, τ_{sym} is much longer than in the devices presented in the main text. We conclude that even though there is some indication of SOC in sample D, its overall strength must be smaller than in the devices presented in the main

text. Certainly the SOC relevant for τ_{sym} must be smaller as this time scale is two orders of magnitude longer than in device A and B. This large difference cannot be explained by the shorter τ_p that is roughly a factor of 5 shorter in device D than in device A and B.

C.7. WL in hBN/Gr/hBN heterostructures

Weak localization (WL) was measured in single layer graphene encapsulated in hBN to get a handle on the intervalley scattering time τ_{iv} and to understand the influence of an in-plane magnetic field. Fig. C.6 (a) shows the gate dependence of the hBN/Gr/hBN device shown in the inset. Field effect mobilities of around $35\,000\text{ cm}^2/\text{Vs}$ were obtained with a residual doping level of around $2 \times 10^{10}\text{ cm}^{-2}$. A similar procedure as described earlier was employed to extract the proper magneto conductivity (ensemble averaging and subtraction of a high temperature background). In order to extract the scattering times more reliably, the magneto conductivity was measured at different temperatures and a global fit was employed, where only τ_ϕ was allowed to vary for different temperatures. Intervalley scattering times τ_{iv} of around 1 ps were obtained with τ_* being much shorter.

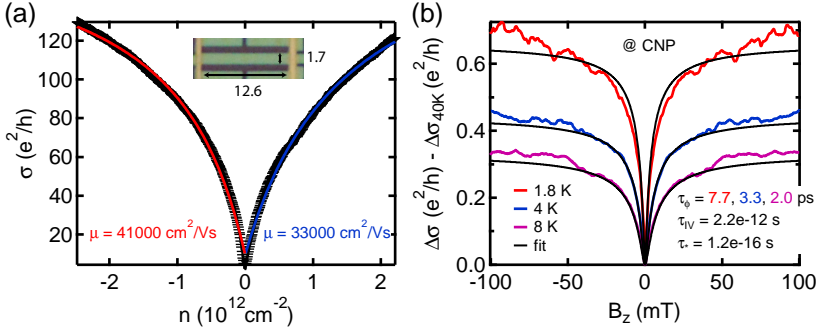


Figure C.6. hBN/Gr/hBN device: (a) shows the conductivity as a function of density of a hBN/Gr/hBN device. The extracted field effect mobilities are indicated. The inset shows an optical image of the device and the dimensions are given in μm . (b) shows the magneto conductivity at the CNP for different temperatures as indicated. A global fit, where only τ_ϕ was allowed to vary for different temperatures is also shown. The error bars in (b) correspond to an uncertainty of 20 %.

A magnetic in-plane field can lead to an enhanced dephasing rate in graphene if ripples are present [70]. This can be explained by the presence of a

random vector potential. We observed a very similar effect here since the phase coherence time τ_ϕ drastically reduces in large in-plane magnetic fields, see Fig. C.7. From the dependence of the dephasing rate in B_\parallel^2 , we can extract a ripple volume of around 125 nm^3 [70]. In order to disentangle the height and width, one would need to investigate the dependence of relative alignment of the current path to the in-plane magnetic field. We attribute the large extracted ripple volume to the presence of bubbles and to the slowly varying thickness of the hBN (even though it is atomically flat on the top it can have some thickness variations due to contaminations below).

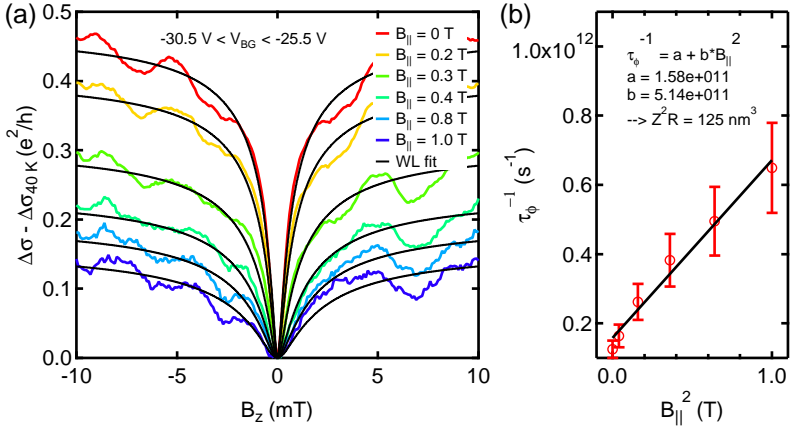


Figure C.7. In-plane magnetic field measurements: (a) shows the magneto conductivity at large hole concentration for different magnetic in-plane fields. A global fit, where only τ_ϕ was allowed to vary for the different magnetic fields is also shown. (b) shows the extracted dephasing rate as a function of B_\parallel^2 . The extracted ripple volume is also indicated following Ref. [70]

D Further information on the superconducting tunnel spectroscopy

D.1. Details on the numerical extraction of the energy distribution function

This section describes the numerical procedure that was used to extract the energy distribution function from the measured differential conductance in more detail. As shown in the main text in Eq. 4.1, the tunnelling current through a superconductor - insulator - graphene (S/I/Gr) can be written as follows:

$$I(V) \propto \int_{-\infty}^{+\infty} dE n_s(E - eV) n_{gr}(E) [f_{gr}(E) - f_s(E - eV)]. \quad (D.1)$$

The two density of states (n_s , n_{gr}) and the two energy distribution functions (f_s , f_{gr}) determine the current. For small bias values eV on the meV-scale, the energy dependence of the graphene density of states can be neglected and assumed to be constant. Therefore, Eq. D.1 can be rewritten

$$I(V) \propto \int_{-\infty}^{+\infty} dE n_s(E - eV) \cdot f_{gr}(E) - \int_{-\infty}^{+\infty} dE n_s(E - eV) \cdot f_s(E - eV), \quad (D.2)$$

where the first integral describes the convolution of the energy distribution function of the graphene $f_{gr}(E)$ with the superconducting density of states $n_s(E - eV)$ and the second integral describes an offset current. The offset current is independent of the bias V and therefore the differential conductance can be written in the following final form:

$$\frac{dI(V)}{dV} \propto \int_{-\infty}^{+\infty} dE \frac{dn_s(E - eV)}{dE} \cdot f_{gr}(E). \quad (D.3)$$

According to Eq. D.3, if $\frac{dn_s(E - eV)}{dE}$ is known, then one can use the measured $\frac{dI(V)}{dV}$ to extract the energy distribution function in graphene $f_{gr}(E)$ by a deconvolution. There are several ways to perform such a deconvolution: 1) direct deconvolution using built-in algorithms in Matlab, Python or anything similar, 2) Fourier transformation and a simple division, or 3) gradient method, that is

a kind of a fitting procedure where the distribution function is calculated in many iterations such that the calculated differential conductance fits the measured data. The first and the second method have the drawback of numerical limitations (basically the differential conductance would need to be measured over the whole energy range $(-\infty$ to $+\infty)$ with very high accuracy. Since this is not possible, we chose to use the third method: the gradient method, as previously used in similar experiments on copper wires [130].

The idea behind the gradient method is to start with a reasonable guess of the distribution function and then to calculate the differential conductance based on the guessed distribution function and the known density of states of the superconductor. The calculated differential conductance is then compared to the measured data and the χ^2 is calculated as defined here:

$$\chi^2 = \sum_V \left(\left. \frac{dI}{dV} \right|^{exp} - \left. \frac{dI}{dV} \right|^{calc} \right)^2. \quad (D.4)$$

Now a new distribution function is calculated point by point by adding a small change which is related to the difference of the guessed and measured differential conductance in the following way:

$$f_{i+1}(E_k) = f_i(E_k) + \lambda \cdot \left. \frac{d\chi_i^2}{df_i(E)} \right|_{E=E_k}. \quad (D.5)$$

Here, λ is a small number ($\ll 1$) and $\frac{d\chi_i^2}{df_i(E)}$ is the gradient of χ_i^2 with respect to the distribution function evaluated at energy E_k (occupation factor at energy E_k) at iteration step i . This assures that the distribution function is changed such that the difference between the measured and guessed differential conductance is minimized in the fastest way. Explicitly written, equation D.5 reads:

$$f_{i+1}(E_k) = f_i(E_k) + \lambda \sum_V \left[\frac{dn_s(E - eV)}{dE} \left(\left. \frac{dI(V)}{dV} \right|^{exp} - \left. \frac{dI(V)}{dV} \right|_i^{calc} \right) \right]_{E=E_k}. \quad (D.6)$$

The distribution function is updated at every energy E_k with a small change which is a sum over the whole voltage range of the derivative of the density of states multiplied with the deviation of the guessed distribution function from the measured distribution function. In this way, the "non-local" effect of the convolution in equation D.3 is reproduced.

This gradient method was implemented in a Python script which uses the differential conductance measured without any bias at the lowest temperature as the density of states of the superconductor. This is justified since the differential conductance of a tunnel junction is basically the superconducting

density of states if temperature is going to zero. In doing so, there is no analytical formula for the superconducting density of states and therefore, a spline of order 3 was fitted to the low temperature limit of the differential conductance. This allowed an easier implementation of the fitting method since the derivative of the superconducting density of states was easy to calculate and was still well behaving (e.g. continuous and smooth (still once differentiable)).

D.2. Influence of the finite width of the superconducting electrode

Since the superconducting electrode has a finite width it does not only probe the electron temperature in the middle of the graphene device. The width of the superconducting electrode was not more than 400 nm, which is a non-negligible part of the full device length (1.3 μm and 3.4 μm). To estimate this influence on the extracted temperature, the expected temperature profile is plotted in Fig. D.1 as a function of normalized device length. Here we take the temperature profile without any electron-phonon cooling as phonon cooling would lead to a flatter temperature profile and hence to a smaller influence of the finite contact width. The relative width of the superconducting electrode of device A and B presented in chapter 4 is indicated by blue and green boxes. The average of the electron temperature within this box deviates by not more than 1.6 % from the value expected in the middle of the device (for the shorter device). The absolute difference is given as Δ in the legend for each device and bias individually. We therefore rule out the finite width of the superconductor as the dominating origin of the lower electron temperature measured in device A and B compared to the expected value by electron cooling through out diffusion.

We would like to note that the above estimate is in principle not fully correct as we are not measuring an average temperature but rather an average over several Fermi-Dirac distributions. However, the order of magnitude of the correction is assumed to be captured by this crude estimate.

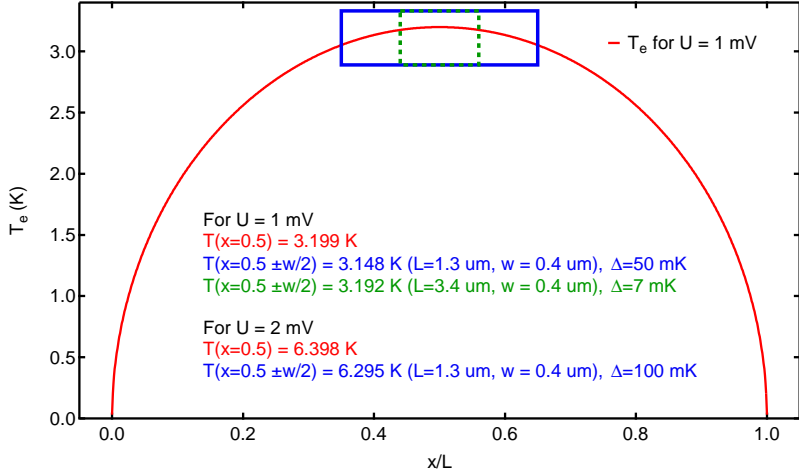


Figure D.1. Influence of finite width of superconducting electrode: Temperature profile in the hot electron regime. The x-axis is normalized by the length L of the graphene channel. The blue and green box indicate the relative extension of the superconductor electrode of device A and B presented in chapter 4. The average temperature within this box is given for 1 mV and 2 mV and the absolute deviation is indicated as Δ .

E Further information on Quantum capacitance and dissipation in graphene pn-junctions

This appendix shows data from a further device that was only partially discussed in chapter 8. Furthermore, the influence of the bare stub tuner properties on the extraction of the graphene impedance are discussed.

E.1. Reflectance measurements of device C

In chapter 8, we presented mainly results on two devices (A and B) fabricated with the same hBN/Gr/hBN stack and the same stub tuner circuit. Here we present qualitatively similar results for a third device C. A separate graphene stack of width $5\text{ }\mu\text{m}$ and length $12\text{ }\mu\text{m}$ is symmetrically transferred across the slit with a width of 250 nm of a different niobium resonator circuit.

Reflectance measurements were performed in the same way at each gate voltage. To fit the resonance response, we again fix the parameters such as the lengths, effective dielectric constant and the loss of the circuit which are independently extracted from the response of the same circuit without the stack. The extracted capacitance C is shown in Fig. 8.3 in chapter 8 and the charge relaxation resistance R are shown in Fig. E.1, next to the raw reflectance data. The characteristic double charge neutrality point feature can be seen again, similar to those in device A and B. We fit the total capacitance using Eq. 8.1 of the main text and extract $\epsilon_{\text{BN}} \approx 4.25$, $v_F \approx 1.54 \times 10^6\text{ m/s}$, $n_{\text{imp},1} = 4 \times 10^9$ and $n_{\text{imp},2} \approx 3.5 \times 10^9\text{ cm}^{-2}$, where we have used the thickness $\sim 26.5\text{ nm}$ of the lower hBN estimated from the AFM measurements.

In order to estimate the diffusion constant, we also plot the inverse quantum capacitance as a function of simultaneously extracted charge relaxation resistance, see Fig. E.2. We find a almost symmetric response for the two areas of graphene, which is consistent with their similar impurity densities and size. At the dashed line, we estimate the diffusion constant $D = 0.44\text{ m}^2\text{ s}^{-1}$ and the mean free path $l_m = 0.92\text{ }\mu\text{m}$.

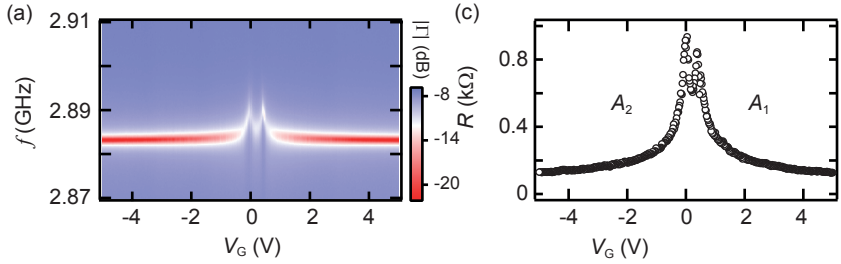


Figure E.1. Reflectance response of device C: (a) A color map of the measured reflectance power near the resonance frequency versus different gate voltages. (b) Extracted charge relaxation resistance from the reflectance data.

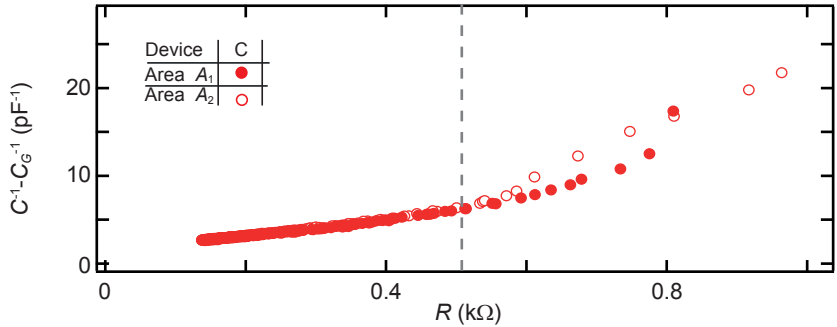


Figure E.2. Extraction of diffusion constant for device C: Inverse quantum capacitance is shown as a function of simultaneously measured charge relaxation resistance. Areas A_1 and A_2 are explained in the main text. The diffusion constant is extracted at the dashed line ($D = 0.44$ $m^2 s^{-1}$). © 2018 American Physical Society

E.2. Details on the parameter extraction for different circuit losses

In our measurements of graphene devices, there is no way to extract the circuit loss constant α simultaneously since device parameters are not known a priori. Therefore we extract α (for devices A/B $\sim 0.0025 \text{ m}^{-1}$ and for devices C $\sim 0.0015 \text{ m}^{-1}$) from the reflectance response of the same circuits after graphene removal (using reactive ion etching). An uncertainty in extracted parameters might arise if the circuit losses do not stay the same from one cool down to another after graphene removal.

To simulate the deviations, we extract R and C at different loss constants from fits of the reflectance response shown in Fig. E.3 (a). The results are plotted in Fig. E.3 (a,b). We see that by increasing the loss constant, the resistance of the device goes down and vice versa. The maximum error in the resistance happens at the largest gate voltage. In case of devices A/B we find deviations smaller than 10% and for device C, smaller than 4% when α is changed by 100%. We do not see any changes in extracted capacitance, as shown in Fig. E.3 (b) for device B.

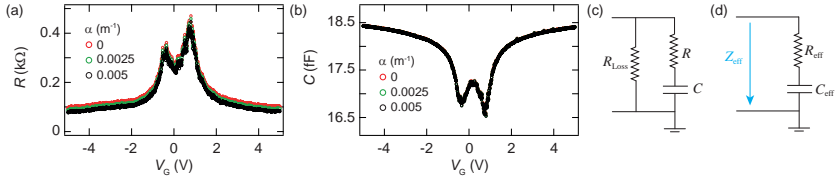


Figure E.3. Response to different loss constants in the parameter extraction: (a) Extracted R for different values of the loss constant from the fits of the reflectance spectra shown in the main text, Fig. 2(a). The loss constant $\alpha = 0.0025 \text{ m}^{-1}$ is obtained by fitting the resonance curve of the same circuit after graphene is removed. (b) Corresponding extracted C . Due to negligible changes, different curves simply lie on top of each other. (c) Equivalent circuit of the device load with the circuit loss denoted by phenomenological parallel resistance R_{Loss} and graphene total resistance R and total capacitance C . (d) An equivalent circuit of panel (c) with an effective series resistance R_{eff} and capacitance C_{eff} . © 2018 American Physical Society

Small deviations in device parameters to the changes in the circuit loss constant can be understood by a simple model shown in Fig. E.3 (c). Here, the gate independent loss constant α is described by a phenomenological parallel resistance R_{Loss} such that α is proportional to $1/R_{\text{Loss}}$. Exact constant of proportionality depends on the stub tuner parameters and is difficult to describe analytically. The effective impedance Z_{eff} seen by the circuit can be described

by Fig. E.3 (d) which is calculated as

$$Z_{\text{eff}} = \frac{R_{\text{Loss}} + \omega^2 C^2 (R + R_{\text{Loss}}) R R_{\text{Loss}}}{1 + \omega^2 C^2 (R + R_{\text{Loss}})^2} - j \frac{\omega C R_{\text{Loss}}^2}{1 + \omega^2 C^2 (R + R_{\text{Loss}})^2}. \quad (\text{E.1})$$

The above equation can be separated into effective R_{eff} and C_{eff} such that

$$R_{\text{eff}} = \frac{R_{\text{Loss}} + \omega^2 C^2 (R + R_{\text{Loss}}) R R_{\text{Loss}}}{1 + \omega^2 C^2 (R + R_{\text{Loss}})^2}, \quad (\text{E.2})$$

$$C_{\text{eff}} = C \frac{1 + \omega^2 C^2 (R + R_{\text{Loss}})^2}{\omega^2 C^2 R_{\text{Loss}}^2}. \quad (\text{E.3})$$

When circuit losses are very small such that $R_{\text{Loss}} \gg R, 1/(\omega C)$, the results are simplified to

$$R_{\text{eff}} \approx R + \left(\frac{1}{\omega C} \right)^2 \frac{1}{R_{\text{Loss}}}, \quad (\text{E.4})$$

$$C_{\text{eff}} \approx C. \quad (\text{E.5})$$

It is evident from the above equation that effective R_{eff} seen by the circuit at two different loss constants are merely offset to each other if C has a weak gate dependence. This can be seen in Fig. E.3 (a) for $|V_G| > 2$ V.

Curriculum Vitae

Simon Zihlmann

Born on 6th August 1988 in Wolhusen (Switzerland)

Education

- | | |
|----------------|---|
| 3/2014–3/2018 | PhD in experimental physics at the University of Basel <ul style="list-style-type: none">- Dissertation in the group of Prof. Dr. C. Schönenberger
<i>“Spin and charge relaxation in graphene”</i> |
| 8/2011–5/2013 | Masters of Science in Nanoscience at the University of Basel <ul style="list-style-type: none">- Master thesis in the group of Prof. Dr. D. M. Zumbühl (University of Basel)
<i>“Hydrogen plasma etching of graphene, Towards crystallographic zigzag edges”</i> |
| 8/2011–12/2013 | ERASMUS semester at the University of Lund, Sweden <ul style="list-style-type: none">- Project work in the group of Prof. Dr. M.-E. Pistol (University of Lund)
<i>“Photoconductivity measurements of semiconductor nanowires”</i> |
| 2008–2011 | Bachelors of Science in Nanoscience at the University of Basel |
| 2007 | Matura Kantonsschule Willisau, Willisau |

Positions

- | | |
|---------------|---|
| 3/2014– | <i>Teaching assistant for physics at the University of Basel</i> |
| 6/2013–1/2014 | <i>Research assistant at the Federal Institute of Metrology, METAS in Wabern, Switzerland</i> |
| 2/2012–1/2013 | <i>Teaching assistant for mathematics at the University of Basel</i> |

Publications

- “Non-equilibrium properties of graphene probed by superconducting tunnel spectroscopy”
S. Zihlmann, P. Makk, S. Castilla, J. Gramich, K. Thodkar, S. Caneva, R. Wang, S. Hofmann, C. Schönenberger
in preparation
- “Dynamical spin injection into graphene by broadband on-chip excitation”
D. Indolese*, **S. Zihlmann***, P. Makk, C. Jünger, K. Thodkar, C. Schönenberger
[Physical Review Applied **10**, 044053 \(2018\)](#)
- “Large spin relaxation anisotropy and valley-Zeeman spin-orbit coupling in WSe₂/Gr/hBN heterostructures”
S. Zihlmann, A. W. Cummings, J. H. Garcia, M. Kedves, K. Watanabe, T. Taniguchi, C. Schönenberger and P. Makk
[Physical Review B **97**, 075434 \(2018\)](#)
- “Spin transport in two-layer-CVD-hBN/graphene/hBN heterostructures”
M. Gurram, S. Omar, **S. Zihlmann**, P. Makk, Q. C. Li, Y. F. Zhang, C. Schönenberger and B. J. van Wees
[Physical Review B **97**, 045411 \(2018\)](#)
- “Anisotropic Etching of Graphite and Graphene in a Remote Hydrogen Plasma”
D. Hug, **S. Zihlmann**, M. K. Rehmann, Y. B. Kalyoncu, T. M. Camenzind, L. Marot, K. Watanabe, T. Taniguchi, and D. M. Zumbühl
[npj 2D Materials and Applications **1**, 21 \(2017\)](#)
- “Contactless Microwave Characterization of Encapsulated Graphene *p-n* Junctions”
V. Ranjan, **S. Zihlmann**, P. Makk, K. Watanabe, T. Taniguchi, and C. Schönenberger
[Physical Review Applied **7**, 054015 \(2017\)](#)

- “Microwave photodetection in an ultraclean suspended bilayer graphene *pn* junction”
M. Jung, P. Rickhaus, **S. Zihlmann**, P. Makk, and C. Schönenberger
Nano Letters **16**, 6988–6993 (2016)
- “Role of hexagonal boron nitride in protecting ferromagnetic nanostructures from oxidation”
S. Zihlmann, P. Makk, C. A. F. Vaz and C. Schönenberger
2D Materials **3**, 011008 (2016)
- “Spin transport in fully hexagonal boron nitride encapsulated graphene”
M. Gurram, S. Omar, **S. Zihlmann**, P. Makk, C. Schönenberger and B. J. van Wees
Physical Review B **93**, 115441 (2016)
- “Guiding of Electrons in a Few-Mode Ballistic Graphene Channel”
P. Rickhaus, M.-H. Liu, P. Makk, R. Maurand, S. Hess, **S. Zihlmann**, M. Weiss, K. Richter and C. Schönenberger
Nano Letters **15**, 5819-5825 (2015)
- “Seeded growth of monodisperse and spherical silver nanoparticles”
S. Zihlmann, F. Lüönd, J. K. Spiegel
Journal of Aerosol Science **75**, 81-93 (2014)

* Equal contribution

Talks

- *Proximity spin-orbit coupling in graphene/WSe₂-heterostructures*
Group seminar, Nanoelectronics research lab, Budapest (Hungary), February 2018
- *Hexagonal boron nitride as an atomically thin oxidation barrier for ferromagnetic nano structures*
Graphene flagship meeting of workpackage Spintronics, Amsterdam (Netherlands), November 2015
- *Ballistic graphene, Towards spintronics with electron optics*
QSIT junior Meeting, Passugg (Switzerland), June 2014

Poster Contributions

- “Spin-orbit interaction in graphene by proximity to TMDC WSe₂”
QSIT General Meeting, Arosa (Switzerland), February 2018

-
- *“Microwave absorption and charge dynamics in clean graphene devices”*
IWEPNM, Kirchberg (Austria), February 2017
 - *“Novel quantum transport features in graphene”*
QSIT General Meeting, Arosa (Switzerland), February 2017
 - *“Superconducting tunnel spectroscopy of graphene”*
Graphene Week 2016, Warsaw (Poland), June 2016
 - *“Novel quantum transport features in graphene”*
QSIT General Meeting, Arosa (Switzerland), February 2016
 - *“Electric transport in locally gated graphene devices”*
Graphene Study 2015, Kaprun (Austria), March 2015
 - *“Spin injection to graphene through layered materials”*
Frontiers of Condensed Matter, San Sebastian (Spain), September 2014

Acknowledgements

All the work presented in this PhD-Thesis would not have been possible without the support and guidance from many exceptional scientist, colleagues, collaborators and friends. Therefore, the following lines are denoted to thank all the people that contributed in various ways to this work.

First of all I thank my thesis advisor Prof. Dr. Christian Schönenberger. Christian gave me the opportunity to pursue the research presented in this thesis. He guided me through the last four years and always encouraged me to do things on my own. His fascination and passion for physics in particular and science in general have always inspired me. I am especially thankful for the many group excursions and events we had the last four years. Canoeing on the Reuss or climbing up a "Klettersteig" certainly were highlights of our group activities. All these events allowed for a relaxed and enjoyable working environment, which I very much appreciate.

Second, I thank Prof. Dr. Bart J. van Wees and Prof. Dr. Christoph Stampfer for taking the effort of reading my thesis. I am very honoured to have two such exceptional physicists in my PhD committee.

I am very grateful to Dr. Péter Makk. Throughout the last four years it was Péter who always had an open door and he supported me whenever help was needed but also let me do things in my own way. His very critical questions always challenged me but lead to a deeper understanding of the science we are doing. It was also him who constantly pushed me and others in the group to do some sports, be it running on Tuesdays or climbing and I am still honoured that he joined the Igloo-weekend I did organize.

Throughout my four years of PhD I could supervise two Bachelor and one Master student. I am very grateful for the work of Sebastian Castilla, Simon Karsten and David Indolese. It was always a pleasure to work with highly interested and motivated students.

With Clevin Handschin I nearly shared my full University career starting from the 1st semester in Nanoscience till the end of my PhD. Clevin introduced me to many fabrication secrets and I always enjoyed discussing science with him. Apart from work, we also enjoyed many outdoor activities together. The many coffee breaks with Christian Jünger were always very welcome during long days in the office or in the lab. We also share the passion for good beers (mostly German), which lead to many deep discussions about "God and the

World" in the "Bierjohann". I am also in debt for his help in the spin-pumping project. I also thank David Indolese and Roy Haller for joining the coffee breaks or beer drinking. Even though I now spent roughly 10 years in Basel, I still got to learn new traditions and places from them. I am especially thankful to Kishan Todkar who grew all the CVD graphene that I could use throughout my PhD. I am also thankful to Vishal Ranjan, who worked with me on the RF admittance measurements of encapsulated graphene. Dr. Gergő Fülöp had always an open ear for questions, especially about programming, and I enjoyed working with him on the graphene relaxation measurements. I also thank him for the nice artistic views of our samples he created. A first and very helpful introduction to fridges I got from Dr. Andreas Baumgartner as well as some inputs on measurement techniques. Furthermore, I thank all further former and current members of the Nanoelectronics group: Peter Rickhaus, Jörg Gramich, Thomas Hasler, Dr. Minkyung Jung, Dr. Wangyang Fu, Samuel d'Hollosy, Lujun Wang, Jan Overbeck, Gulibusitan Abulizi, Frederick Thomas, Dr. Raphaëlle Delagrangé, Maria El Abbassi, Mihai-Cezar Harabula, Anton Vladyka and Arunav Bordoloi, Olivier Faist.

Throughout my four years of PhD I had the opportunity to participate in many collaborations. First, I would like to thank my collaborators Mallikarjuna Gurram, Siddhartha Omar and Bart J. van Wees at the University of Groningen with whom I worked on spin transport in graphene. I very much enjoyed my time in Groningen where I also got in touch with Johannes Christian Leutenantsmeyer, Josep Ingla-Aynés and Alexey A. Kaverzin. Second, the fruitful discussions with Aron W. Cummings, Jose Garcia and Martin Gmitra definitely deepened my understanding in spin-orbit proximity effects in graphene/TMDC systems. Moreover, Ruizhi Wang and Sabina Caneva from the University of Cambridge introduced me to the world of CVD hBN and I enjoyed the many discussions we had on growth and transfer processes. Carlos A. F. Vaz was a great help during the PEEM measurements at the Swiss Light Source and I learnt a lot from him for which I would like to thank him.

There are many people behind the scene at the Physics Department whom I would like to thank. Barbara Kammermann and Astrid Kalt had always a answer to any administrative question I had. Special thanks go to Dominik Sifrig, who always found some helium even when resources were scarce or when I forgot to order in time. Whenever there was a problem with the "Bestec" it was Daniel Sacker who helped me in debugging, cleaning and replacing turbo pumps. Furthermore, I could always rely on the help from the mechanical and electrical workshop at the Department and in particular I would like to thank: Patrick Stöcklin, Sascha Martin and Michael Steinacher.

Apart from science, I am very grateful to my parents Antonia and Hans for supporting me throughout my whole life, be it financially during my studies or with a delicious meal on Sundays in Willisau when I left work in Basel. My sister Barbara knows life as a PhD and therefore understood me when I

was talking about life at University. Many friends outside of science helped me to see the world from a different perspective and scientific problems just look ridiculously small from the top of a mountain in the Alps. Many great skitours, mountain bike trails, challenging rock climbing routes or relaxing canoeing holidays made my life a lot richer.

Without all these people I would not be where I am today.